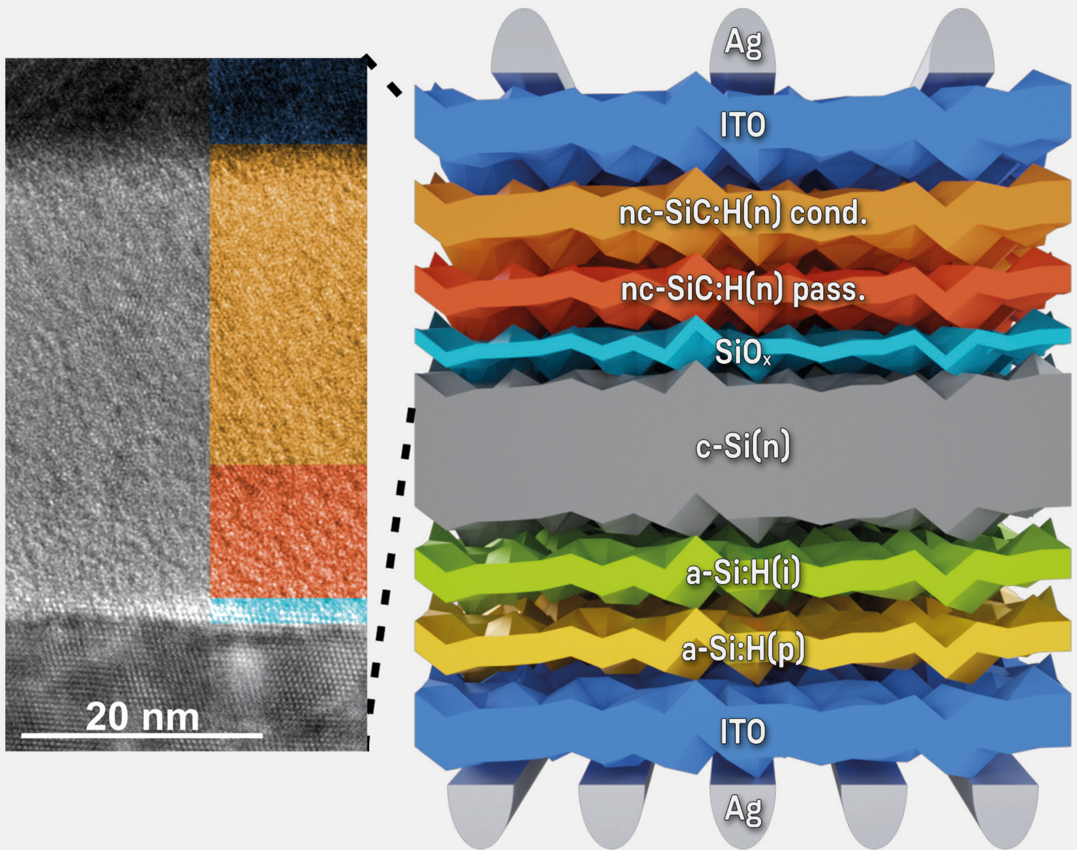

Nanocrystalline Silicon Carbide in Transparent Passivating Contact Solar Cells

Alexander Eberst

Energie & Umwelt / Energy & Environment
Band / Volume 696
ISBN 978-3-95806-891-9

Mitglied der Helmholtz-Gemeinschaft

JÜLICH
Forschungszentrum

Schriften des Forschungszentrums Jülich
Reihe Energie & Umwelt / Energy & Environment Band / Volume 696

Forschungszentrum Jülich GmbH
Institute of Energy Materials and Devices (IMD)
Photovoltaik (IMD-3)

Nanocrystalline Silicon Carbide in Transparent Passivating Contact Solar Cells

Alexander Eberst

Schriften des Forschungszentrums Jülich
Reihe Energie & Umwelt / Energy & Environment Band / Volume 696

ISSN 1866-1793 ISBN 978-3-95806-891-9

Bibliografische Information der Deutschen Nationalbibliothek.
Die Deutsche Nationalbibliothek verzeichnet diese Publikation in der
Deutschen Nationalbibliografie; detaillierte Bibliografische Daten
sind im Internet über http://dnb.d-nb.de abrufbar.

Herausgeber und Vertrieb:	Forschungszentrum Jülich GmbH Zentralbibliothek, Verlag 52425 Jülich Tel.: +49 2461 61-5368 Fax: +49 2461 61-6103 zb-publikation@fz-juelich.de www.fz-juelich.de/zb
Umschlaggestaltung:	Grafische Medien, Forschungszentrum Jülich GmbH
Druck:	Grafische Medien, Forschungszentrum Jülich GmbH
Copyright:	Forschungszentrum Jülich 2026

Schriften des Forschungszentrums Jülich
Reihe Energie & Umwelt / Energy & Environment, Band / Volume 696

ISSN 1866-1793
ISBN 978-3-95806-891-9

Vollständig frei verfügbar über das Publikationsportal des Forschungszentrums Jülich (JuSER)
unter www.fz-juelich.de/zb/openaccess.

This is an Open Access publication distributed under the terms of the Creative Commons Attribution License 4.0,
which permits unrestricted use, distribution, and reproduction in any medium, provided the original work is properly cited.

God made the bulk; surfaces were invented by the devil.

Wolfgang Pauli,
as quoted in *Growth, Dissolution, and Pattern Formation* (1999)

Abstract

Nitrogen-doped hydrogenated nanocrystalline silicon carbide (nc-SiC_X:H)(n) emerges as a superior alternative to hydrogenated amorphous silicon (a-Si:H) as the front contact material in silicon heterojunction (SHJ) solar cells. Its enhanced transparency, significantly reduces parasitic absorption in the front contact layers leading to an increased current generation in solar cells. Furthermore, nc-SiC_X:H(n) exhibits exceptional electrical properties and passivation capabilities, especially when combined with wet-chemically grown silicon oxide (SiO_X). Utilizing the double-layer nc-SiC_X:H(n) transparent passivating contact (TPC) approach as a front contact in SHJ solar cells results in power conversion efficiencies of 23.99% and impressive current densities of 40.9 $\frac{mA}{cm^2}$. However, despite the advanced material properties of nc-SiC_X:H(n), the TPC approach leads to a reduced Fill Factor (FF) and open-circuit voltage (V_{OC}) compared to standard SHJ cells, although with comparable implied open-circuit voltages (iV_{OC}s). Preliminary findings suggest that the reduced FF may lies in limitations imposed by the applied passivating nc-SiC_X:H(n) layer, necessitating further investigation. The contrast between the iV_{OC} of the precursor and the V_{OC} of the solar cell is attributed to the passivation damage induced during the transparent conductive oxide (TCO) sputtering process, an area yet to be fully understood and requiring a deeper analysis. Additionally, methods to restore this induced damage need further exploration.

This thesis re-examines the opto-electrical properties of hot wire chemical vapor deposition (HWCVD)-grown nc-SiC_X:H(n), focusing on a high-quality material. Detailed analyses reveal that conditions favoring low deposition rates improve both the electrical conductivity and the optical bandgap, attributed to larger crystallites in thin films. Hydrogen radical etching emerges as a critical mecha-

nism during layer growth. The investigation extends to the passivation capabilities influenced by the filament temperature and their distance to the substrate, and hydrogen content variations due to changes in the filament temperature, hydrogen dilution, and total gas flow rate. Lower filament temperatures enhance passivation and hydrogen content, with the latter peaking at lower hydrogen dilutions and intermediate total gas flow rates. Subsequently, this thesis investigates the effects of varying layer thicknesses of both conducting and passivating nc-SiC_X:H(n) layers. Although thicker conducting layers marginally affect the *FF* beyond a certain threshold, a notable trade-off between iV_{OC} and *FF* is observed with the passivating nc-SiC_X:H(n) layer. To address this, a gradient layer with gradually shifting properties from passivating to conducting is introduced. This approach can significantly reduce the thickness of the passivating layer, enhancing the best solar cell efficiency to 24.20%.

The second major challenge for TPC solar cells is the reduced V_{OC} post-TCO deposition. A combination of experimental and simulation methods clarifies the damage mechanisms. The microstructure of the nc-SiC_X:H(n) layer is established to remain unaffected during sputtering. Experiments rule out the sputter atmosphere and process heating as sources of degradation. By shielding parts of the sample with filters with varying transmissions, it is determined that plasma luminescence does not deteriorate the passivation quality of the TPC stack. Electron beam simulations and experiments show limited penetration and no degradation impact. Among the ions present during sputtering, oxygen exhibits the deepest penetration into the material, yet is confined to the first nanometers. Various secondary effects of the ion impact are debated. While vacancies are considered to have activation energies too high for low-temperature annealing for passivation restoration, electrons generated from ionization impacts are already excluded as damage sources. The sputter-induced damage is hypothesized to result from a multi-phonon scattering process, displacing hydrogen at the crystalline silicon interface. However, the effect of radiation from ion impacts within the nc-SiC_X:H(n) layer remains unexplored. Remarkably, it is discovered that the previously deemed irreparable sputter damage can be fully restored through thermal annealing. Nevertheless, the temperatures required for nc-SiC_X:H(n) restoration are too high, compromising the passivation quality of a-Si:H.

Zusammenfassung

Als Material für den Frontkontakt von Silizium-Heterostruktur-Solarzellen (engl. silicon heterojunction, SHJ) hat sich Stickstoff-dotiertes hydriertes nanokristallines Siliziumkarbid (nc-SiC:H(n)) als überlegene Alternative zu hydriertem amorphem Silizium (a-Si:H) erwiesen. Seine gesteigerte optische Transparenz minimiert die parasitäre Lichtabsorption in den Frontkontaktschichten signifikant und führt so zu einer gesteigerten Stromerzeugung in der Solarzelle. Zudem weist nc-SiC:H(n) exzellente elektrische Eigenschaften und herausragende Passivierungsfähigkeiten auf, insbesondere in Kombination mit nasschemisch erzeugtem Siliziumoxid (SiO_X). Der Einsatz dieses Doppelschicht-Ansatzes, bekannt als transparenter leitfähiger Kontakt (engl. transparent passivating contact, TPC), ermöglicht Umwandlungseffizienzen von bis zu 23.99% bei hohen Stromdichten von 40.9 $\frac{mA}{cm^2}$.

Trotz der vorteilhaften Materialeigenschaften von nc-SiC:H(n) zeigt der TPC-Ansatz im Vergleich zur herkömmlichen SHJ-Solarzelle eine Verringerung des Füllfaktors (*FF*) und der Leerlaufspannung (V_{OC}), obwohl die implizite Leerlaufspannung (iV_{OC}) auf vergleichbarem Niveau liegt. Vorläufige Analysen deuten darauf hin, dass der reduzierte *FF* durch die passivierende nc-SiC:H(n)-Schicht verursacht wird, was detailliertere Untersuchungen erfordert. Der Unterschied zwischen V_{OC} und iV_{OC} ist auf die Schädigung der Passivierung während der Abscheidung des transparenten leitfähigen Oxids (engl. transparent conducting oxide, TCO) mittels Kathodenzerstäubung zurückzuführen. Dieser Prozess ist noch unzureichend erforscht und bedarf einer umfassenden Analyse.

In dieser Arbeit werden die opto-elektrischen Eigenschaften von hochqualitativem nc-SiC:H(n), deponiert mittels Heißdraht-Gasphasenabscheidung (engl. hot wire chemical vapor deposition, HWCVD), untersucht. Es zeigt sich, dass

Abscheidebedingungen, die zu niedrigen Depositionsraten führen, sowohl die elektrische Leitfähigkeit als auch die optische Bandlücke verbessern, was auf größere Kristallite in den Schichten zurückzuführen ist. Hierbei ist das Ätzen durch Wasserstoffradikale der primäre aktive Mechanismus während der Deposition. Weitere Untersuchungen konzentrieren sich auf die Passivierungseigenschaften in Abhängigkeit der Filamenttemperatur, dem Abstand zwischen Filament und Substrat sowie dem Wasserstoffgehalt der Schichten, der von der Filamenttemperatur, der Wasserstoffverdünnung und dem Gesamtgasfluss abhängt. Eine niedrigere Filamenttemperatur maximiert sowohl die Passivierung, als auch den Wasserstoffgehalt in den Schichten. In weiteren Experimenten werden verschiedene Parameter der Solarzelle in Abhängigkeit von der Dicke der nc-SiC:H(n)-Schichten innerhalb des TPCs analysiert. Es zeigt sich, dass die leitfähige Schicht, nach Überschreitung einer minimalen Grenzschichtdicke, nur einen geringen Einfluss auf die Leistung der Solarzelle hat. Lediglich der *FF* verschlechtert sich leicht mit zunehmender Schichtdicke. Die Dicke der passivierenden nc-SiC:H(n)-Schicht hingegen stellt einen erheblichen Kompromiss zwischen *FF* und iV_{OC} dar, welcher sorgfälltig abgewägt werden muss. Als Lösungsansatz wird eine Gradientenschicht mit kontinuierlich wechselnden Materialeigenschaften, von passivierend zu leitfähig, eingeführt. Dies führt zu einer signifikanten Verringerung der Dicke der passivierenden Schicht und einer Steigerung der Umwandlungseffizienz der Solarzelle auf 24.20%.

Die zweite große Herausforderung für TPC-Solarzellen ist die reduzierte V_{OC} nach der Deposition des TCOs. Um die zugrundeliegenden Prozesse der Schädigung der Passivierung zu untersuchen, werden experimentelle Ansätze und Simulationen kombiniert. Es sind weder Veränderungen der Mikrostruktur festzustellen, noch haben die Gasatmosphäre oder die Substratheizertemperatur während der Kathodenzerstäubung einen negativen Einfluss auf die Passivierung der Proben. Die Abdeckung der Probe mit Filtergläsern unterschiedlicher Transmission für die Plasmalumineszenz führt nicht zu einer Degradierung. Somit kann diese als Schädigungsmechanismus ausgeschlossen werden. Simulationen des Elektronenstrahls auf der Probe zeigen, dass die Elektronen nur begrenzt in die Probe eindringen. Experimentell zeigt sich, dass keine Degradation unter gezielter Bestrahlung mit Elektronen auftritt. Während der Kathodenzerstäubung

dringen Sauerstoffionen, im Vergleich zu anderen vorhandenen Ionentypen, am tiefsten in die Probe ein. Doch auch hier ist die Penetration nur oberflächlich. Zusätzlich werden verschiedene Sekundäreffekte, die unter Ionenbeschuss auftreten können, diskutiert. Erzeugte Leerstellen im Gitter des Siliziumkarbids haben hohe Aktivierungsenergien, weshalb angenommen wird, dass ein Ausheilen des Schadens bei den üblicherweise angewandten niedrigen Temperaturen keinen Einfluss hat. Es wird angenommen, dass durch Ionisation generierte Elektronen eine ähnliche Wirkung wie der bereits untersuchte Elektronenstrahl haben und daher keinen Einfluss auf die Passivierung zeigen. Jedoch könnte ein Multi-Phononen-Streuprozess genug Energie aufbringen, um grenzflächennahen Wasserstoff an der Oberfläche des kristallinen Siliziums zu verschieben und so die Passivierung zu schädigen. Allerdings bleibt ein möglicher Einfluss durch ultraviolette Strahlung, die durch das Auftreffen der Ionen auf die nc-SiC:H(n)-Schicht generiert wird, ununtersucht. Abschließend wird festgestellt, dass die zuvor als unheilbar eingestufte Schädigung der Passivierung vollständig durch thermisches Ausglühen ausgeheilt wird. Allerdings sind die dafür benötigten Temperaturen so hoch, dass sie die Passivierung des a-Si:H auf der Solarzellenrückseite schädigen.

Table of Contents

Abstract v

Zusammenfassung vii

1. Introduction 1

2. Fundamentals of Solar Cell Physics 7

2.1. Working Principles of Solar Cells 7

2.2. Selectivity and Recombination in Solar Cells 19

2.3. Passivating Contacts in Crystalline Silicon Solar Cells 23

2.4. Silicon Carbide in Crystalline Silicon Solar Cells 30

2.4.1. Microstructural and Opto-Electrical Properties of Silicon Carbide Layers 31

2.4.2. Silicon Carbide Layers in Crystalline Silicon Solar Cell . . . 36

3. Sample Preparation, Characterization, and Simulations 41

3.1. Substrates and Experimental Procedures 41

3.1.1. Substrates, Wafers, and Wet Chemical Procedures 41

3.1.2. Deposition of Hydrogenated Nanocrystalline Silicon Carbide 43

3.1.3. Subsequent Processing Steps 44

3.2. Overview of Characterization Techniques 47

3.2.1. Opto-Electrical Characterization Methods 47

3.2.2. Microstructural Characterization Methods 49

3.2.3. Passivation and Solar Cell Characterization 55

3.3. Simulation of Particle Impacts on Thin Films 65

3.3.1. Stopping and Range of Ions in Matter 65

3.3.2. Monte Carlo Simulation of Electron Trajectory in Solid . . . 66

4. Nanocrystalline Silicon Carbide in Transparent Passivating Contact Solar Cells 67
4.1. Single Layer Characterization of Nanocrystalline Silicon Carbide . 68
4.1.1. Effect of Deposition Conditions on Opto-Electrical Properties and Layer Growth Mechanisms 68
4.1.2. Passivating Properties of Nanocrystalline Silicon Carbide . 75
4.2. Nanocrystalline Silicon Carbide Layers in Double-Layer Transparent Passivating Contacts 78
4.3. Gradient Layer for Transparent Passivating Contacts 88
4.4. Summary of Optimized Silicon Carbide Layer Stacks for Enhanced Solar Cell Performance 101

5. Sputter Process-Induced Degradation in Nanocrystalline Silicon Carbide Passivation 105
5.1. Sputter Process-Induced Degradation in Passivating Contacts . . . 106
5.2. Impact of the Sputter Process on nc-SiC:H Material Properties and the Role of Sputter Atmosphere 110
5.3. Assessing the Role of Light, Electrons, and Ions in Sputter Process-Induced Degradation in nc-SiC:H 116
5.4. Annealing Behavior of Transparent Passivating Contact Solar Cells 138
5.5. Summary of Sputter Process-Induced Degradation and Annealing Effects in Transparent Passivating Contact Solar Cells 146

6. Conclusion and Outlook 151

A. On the Lifetime of Hot Wire CVD Filaments 161

B. Evaluation of SRIM Damage Calculation Models 163

C. Evaluating the Optical Band Gap: Choosing an Appropriate Methodology 167

List of Abbreviations 175

List of Figures 193

List of Tables 195

List of Publications 197

Curriculum Vitae 201

References 202

Acknowledgements 223

1. Introduction

In the coming decades, a substantial growth in energy demand is expected, primarily driven by the need to electrify diverse sectors as a careful response to restrain the climate change. The scope of electrification is expanding across multiple domains, ranging from industrial applications to daily life. This includes the progressive electrification in sectors such as the chemical industry and steel production, further enhanced by the growing popularity of electric vehicles in transportation and heat pumps in residential heating. [1–7] Historically, the energy composition has been predominantly fueled by coal and natural gas, with renewable energy sources such as wind and photovoltaics occupying a relatively minor role. [2] This conventional energy mix has been a significant contributor to the increase in global temperatures through greenhouse gas emissions, a phenomenon commonly known as global warming. The Paris Climate Agreement [8] marks a pivotal moment in which nations collectively committed to restricting the increase in global temperatures due to climate change to an upper limit of 2 ℃, but aiming for 1.5 ℃. However, existing policies project a path towards a temperature increase of approximately 3.4 ℃ by the year 2100. On a more optimistic note, certain scenarios present a feasible pathway to achieve the 1.5 ℃ target. [9] Significantly, most nations, particularly those with substantial greenhouse gas emissions, have pledged to reach net zero emissions by 2050 or within the 2060 horizon [10]. In this context, photovoltaics are set to become a fundamental element in the generation of electricity. [5, 11–13]

Crystalline silicon solar cells are at the forefront of the photovoltaic industry because of their well-established technology, superior power conversion efficiency, and cost efficiency. Both the installed capacity and production capabilities of these cells are experiencing rapid growth. As a consequence of the learning

curve in photovoltaics, there is a consistent reduction in the cost per watt peak as the production scales up. [14, 15] Notably, in Germany, electricity generated from large-scale photovoltaic power plants has emerged as the most economical option compared to electricity generated by gas or coal [16]. However, it is observed that the manufacturing costs of solar cells are relatively small when compared to the expenses appearing in producing polycrystalline silicon for the wafers and in the fabrication of solar modules [14]. The most effective strategy to further decrease the cost per watt peak is through the enhancement of the power conversion efficiency, thereby boosting the electrical output of the solar cell and module.

The theoretical efficiency limit for a single-junction solar cell, which is limited by transmission and thermalization losses and known as the Shockley-Queisser limit, is estimated to be around 32-33% for an ideal material band gap between 1.1-1.4 eV [17, 18]. Crystalline silicon aligns well with this optimal band gap range, since its band gap is 1.1 eV, and the theoretical maximum efficiency, including Auger recombination, is determined to be 29.4% [19]. Although its absorption coefficient is lower than that of materials such as gallium arsenide, owing to the indirect nature of its band gap, crystalline silicon remains the predominant choice in the market. This is primarily due to the abundant availability of silicon in the earth's crust, which translates into lower material costs compared to those of other potential materials like gallium arsenide. Despite its availability, it is also on the European Union's list of Critical Raw Materials [20], since large quantities are needed. Therefore, a need to increase the power conversion efficiency of the solar cells arise.

The origin of crystalline silicon solar cells dates back to 1954 with the pioneering work of Bell Laboratories. The initial design comprised an n-type crystalline silicon wafer, boron diffused on the surface, and metal contacts on the rear side [21]. Representing the first industrially applicable solar cell, the aluminium back surface field structure stood as the predominant solar cell architecture for an extended period of time. This design utilized a p-type wafer, integrated with a n-type diffused front emitter surface field and grid electrodes at the front side of the solar cell. The rear surface featured a comprehensive p^+-doping back-

surface field and full area metal contacts. The fabrication process of aluminium back surface field solar cells was advantageous because of its cost effectiveness and simplicity. The process started with a p-type wafer which damaged area due to wafer sawing from the ingot is removed and the surface is textured. In a high-temperature step, phosphorous is diffused over the whole wafer area creating highly doped n^+ regions, but also growing phosphor-silicate glass. This subsequently needs to be removed and edges need to be isolated to avoid shunting. Afterwards, a silicon nitride antireflective coating and passivating layer is deposited using plasma-enhanced chemical vapour deposition and silver front contact fingers and full area rear side aluminium is screen-printed. Finally, a co-firing step is conducted to bring the silver fingers in contact with the crystalline silicon through the silicon nitride and over-dope the parasitic n^+ at the crystalline silicon - aluminium contact creating the name-giving back-surface field. [22] However, this structure was susceptible to intense charge carrier recombination at the crystalline silicon interface, primarily because of the defective metal-silicon contact and the high concentration of dopants in heavily doped areas. To address these recombination losses, a passivation layer with localized contacts, termed passivated emitter rear contact (PERC), was introduced on the rear side. This modification drastically reduced recombination, paving the way for a long-lasting record power conversion efficiencies that reached 25% [23]. The next evolutionary step, the successor of PERC, which still owed the largest market share in the year 2024 [14], incorporates a polycrystalline silicon layer between the metal contacts and a now full area passivating tunnel oxide layer on the rear side. Together with a switch to high-quality n-type wafers, this leads to further reduction in recombination. Further improvements arise from the switch to high-quality n-type wafers. As of the year 2025, tunnel oxide passivated contact (TOPCon) solar cells will dominate the market [24]. Interestingly in these solar cell structures, while the front contact remained relatively unchanged, each successive design evolved from its predecessor. A more radical innovation was the silicon heterojunction solar cell, introduced by Sanyo in 1983, employing intrinsic and doped hydrogenated amorphous silicon layers between the crystalline silicon absorber and metal contacts. This naturally bifacial approach enables both, high V_{OC}s and FFs through excellent surface passivation and electrical properties of the inserted

layers [25, 26]. Detailed insights into passivated emitter rear contact, tunnel oxide passivated contact, and silicon heterojunction solar cells are found in section 2.3.

A notable limitation of the SHJ solar cell, which relies on hydrogenated amorphous silicon, is the parasitic light absorption in these layers. This absorption decreases the light entering the crystalline silicon absorber, consequently reducing the current output of the solar cell. To counteract these losses, more transparent contacting layers are needed. Notable candidates are hydrogenated nanocrystalline silicon or silicon oxide layers [27, 28]. Another promising option, removing all hydrogenated amorphous silicon layers from the front contact, is a TPC structure employing silicon oxide and hydrogenated nanocrystalline silicon carbide on the front side of the solar cell. The further optimization of this contact structure requires a comprehensive investigation into the high-quality hydrogenated nanocrystalline silicon carbide material and its integration behavior in solar cells. A significant challenge in this device configuration is a reduced *FF* in comparison to the SHJ solar cell structure. Furthermore, a notable discrepancy between the implied open-circuit voltage of the solar cell of the solar cell and the open-circuit voltage of the finished solar cell has been identified as a critical limiting factor [29]. This work is dedicated to addressing and overcoming these challenges by further optimizing the nc-SiC_X:H layer material and the TPC layer structure to improve the device's *FF* and by investigating the reason behind the sputter process induced damage. The issue of reduced *FF* is tackled by reducing the low-conductive passivating nc-SiC_X:H(n) layer thickness and inserting a gradient layer with materials properties gradually transitioning from passivating to conducting. The reason behind the sputter process induced is illuminated by combining experimental designs and simulations to separate different effects impacting the sample during the sputter process and a pre-annealing procedure is designed to increase the recoverability of the TPC contact.

This dissertation is structured into six chapters. Chapter 2 gives a comprehensive introduction to the principles of solar cells and provides an in-depth overview of current advances and the status of silicon carbide in the context of crystalline silicon solar cells. Section 2.1 summarizes the fundamental solid state principles essential to understand solar cell operations, defining both the working

mechanism and the characteristic features of solar cells. Following this, section 2.2 ventures into a deeper exploration of the concept of selectivity, charge carrier separation, and the phenomenon of recombination. Subsequently, section 2.3 embarks on an examination of widespread contact schemes used in crystalline silicon solar cells, offering a critical analysis of their merits and limitations while introducing the well-known optimization triangle. The chapter concludes with section 2.4, presenting a comprehensive literature-based survey of the present state of silicon carbide in crystalline silicon solar cells.

Chapter 3, dedicated to the experimental methodologies used in this work, explains the sample preparation procedures and measurement techniques used in this research. Section 3.1 details the substrate selection and various processing methodologies, including wet chemistry, chemical vapor deposition, and physical vapor deposition, among others. Section 3.2 systematically outlines various characterization techniques related to optical, electrical, microstructural, passivation, and solar cell properties. The chapter ends with section 3.3, introducing the simulation tools and input parameters used in chapter 5.

The findings related to the material properties of hydrogenated nanocrystalline silicon carbide and its application in solar cells are presented in chapter 4. This chapter begins with section 4.1, which examines the optical, electrical and passivation characteristics of hydrogenated nanocrystalline silicon carbide deposited under various conditions, also discussing the different effects during layer growth. Section 4.2 examines the performance of different hydrogenated nanocrystalline silicon carbide layers within a transparent passivating contact structure, highlighting the constraints inherent in the double layer approach. To overcome these limitations, the integration of a gradient layer within the stack is introduced in section 4.3. The chapter concludes with a brief summary presented in section 4.4.

The second chapter dedicated to the results of this research, chapter 5, delves into the investigation of the degradation of the passivation quality during the sputter deposition of the transparent conductive oxide layer. This chapter adopts a dual approach, linking both experimental data and simulation insights. Section 5.2 delves into the exploration of material behavior under the specific

conditions prevailing in the sputtering chamber. It provides information on the microstructural changes and a first glimpse on the reversibility of the sputter process-induced damage of the hydrogenated nanocrystalline silicon carbide and transparent passivating contact. The subsequent section 5.3 extends the analysis to the influences exerted during the sputtering process, focusing on the effects of plasma radiation, electrons, ions, and their secondary impacts on the transparent passivating contact. This chapter then transitions to section 5.4, which is dedicated to researching various annealing strategies aimed at reversing the degradation induced during the sputtering process. The chapter ends with a comprehensive summary presented in section 5.5.

This thesis concludes with a summary and further research outlook, chapter 6, in which the results of the various studies are summarized. This chapter projects potential future research pathways concerning the material hydrogenated nanocrystalline silicon carbide, the transparent passivating contact, and the broader thematic area of sputter-induced damage. This final chapter aims to set the stage for further studies and advancements in this field.

2. Fundamentals of Solar Cell Physics

This chapter establishes a fundamental understanding of the physical principles of solar cells and elaborates on the principle of passivating contacts. In addition, it presents an overview of the recent advancements in silicon carbide applications within the field of crystalline silicon solar cells.

2.1. Working Principles of Solar Cells

A solar cell functions by absorbing light and transforming it into electrical energy through the photoelectric effect [30]. The absorption of a photon with a specific energy excites an electron to a higher energetic state. Within the band structure of the solar cell material, the valence band energy (E_V) represents the highest energy level fully occupied by electrons at a temperature of 0,K. This full occupancy restricts the mobility of electrons, rendering them inactive in processes such as electrical conductivity (σ). The conduction band energy (E_C) is the subsequent higher energy band, which may be partially or completely unoccupied at a temperature of 0,K, allowing electron mobility and thus facilitating electrical conductivity. The energy difference between these energy bands is called the band gap (E_G) and materials can be classified according to their E_G. These energy bands are an overlap of atomic energy potentials and the bandwidth and band gap is dependent on inter-atomic distance in the crystalline lattice, as sketched in figure 2.1 a). Based on the gap between E_V and E_C, materials can be classified in metals, semiconductors and insulators. In metals, the E_V and E_C overlap with no E_G, creating an energetic continuum. This enables electrons of the valence band

to directly move to the conduction band, leading to a partly unoccupied valence band. These readily available electrons lead to the high σ distinct to metals. On the contrary, materials with a substantial gap between the E_V and E_C require considerable energy for electrons to be excited to the E_C and partake in electrical conductivity, classifying them as insulators. Semiconductors, materials with intermediate band gaps, permit electron excitation, by, for example, absorbing a photon with energies corresponding to the solar spectrum and exciting it to the E_C or, for very low band gaps even room temperature, facilitating electron mobility. Graphic representations of the band structures for metals, semiconductors, and insulators are shown in figure 2.1 b). [31–33]

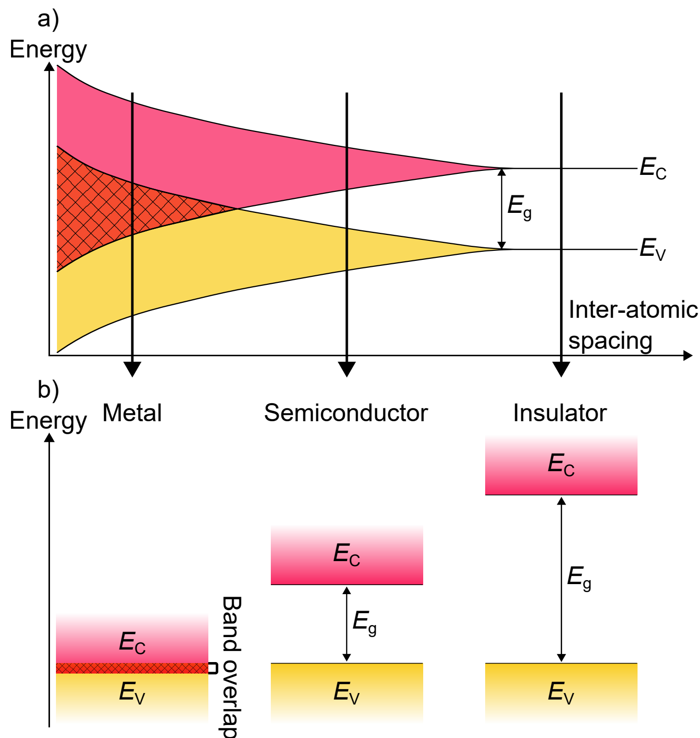

Figure 2.1.: *a) Sketch of continuum of energy bands depending on the inter-atomic spacing, adapted from [32] and b) snapshots for classifications of, from left to right, schematic representations of band structures for metals, semiconductors, and insulators, highlighting the band overlap in metals and the distinct band gaps in semiconductors and insulators.*

Semiconductors are the materials of choice for solar cell applications as their E_V electrons are excitable by light. The electron and hole occupation probabilities in thermal equilibrium and in the dark, as a function of the energy (E), are given by the Fermi-Dirac statistics. When $E - E_F > 3k_B T$, where k_B is the Boltzmann constant, E_F represents the Fermi energy, the theoretic chemical potential at which the occupation probability of electrons would be 0.5, and T is the temperature, the equilibrium concentrations of electrons (n_0) and holes (p_0) at the band edges can be approximated using the Boltzmann distribution as

$$n_0 = N_C e^{\frac{E_F - E_C}{k_B T}} \tag{2.1}$$

and

$$p_0 = N_V e^{\frac{E_V - E_F}{k_B T}}, \tag{2.2}$$

respectively, where N_C and N_V denote the density of states in the conduction and valence band edges, respectively. Combining the equilibrium electron concentration (n_0) in equation (2.1) and equilibrium hole concentration (p_0) in equation (2.2) to

$$n_0 p_0 = N_C N_V e^{\frac{E_V - E_C}{k_B T}} = n_i^2 \tag{2.3}$$

yields the charge carrier concentration intrinsic to the material (n_i). For crystalline silicon at 300 K, n_i equals $1x10^{10}$ cm^{-3}, with a band gap of $E_G = 1.1$ eV. [31]

In intrinsic semiconductors, the E_F is positioned in the center of the band gap if a similar effective mass for electrons and holes is assumed. Introducing additional elements that either add energetic states slightly below the conduction band minimum and donate electrons or add energetic states sightly above the valence band maximum and accept electrons leads to a shift in the Fermi energy as the occupation of electrons or holes changes due to the additional energetic states, a process known as doping. When the donors add electrons, E_F shifts towards the conduction band energy as more free electrons are brought into the system. These additional electrons shift the theoretically occupied energy levels at $T = 0$ K and thus the E_F. This is called n-type doping. On the contrary, the acceptor elements cause E_F to shift towards the E_V, as free electrons are removed from the system the theoretically occupied energy levels at $T = 0$ K is

lowered. This is termed p-type doping. Excessive doping can cause E_F to enter the E_V or E_C, transitioning the semiconductor to a degenerate state with metallic electrical properties. For silicon, which is in group four of the periodic system of elements, group five elements such as phosphorus or antimony act as donors, while group three elements like boron or gallium function as acceptors. Figure 2.2 a)-c) illustrates the impact of doping on the band structure for intrinsic, p-type, and n-type conditions, respectively. [31, 33]

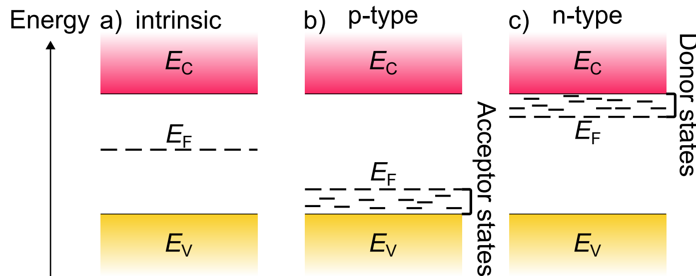

Figure 2.2.: *Depiction of the Fermi-level positioning within the band gap for a) intrinsic, b) p-type doped, and c) n-type doped scenarios.*

When light illuminates a semiconductor, such as crystalline silicon (c-Si), absorption occurs only if the energy of the incident photon is equal to or exceeds the band gap energy of the semiconductor. Insufficient energy results in light transmission through the material, as electrons do not gain the necessary energy to be excited to the conduction band energy. When the photon energy exceeds the band gap, the electrons are excited above the lowest energy level of the conduction band energy, requiring the release of surplus energy as heat, a process called thermalization. These inherent losses, thermalization due to high-energy light absorption and transmission due to sub-band gap incident energies, are unavoidable but require a careful balance in choosing the semiconductor with its specific band gap. If the band gap, and therefore maximum device voltage, is reduced, a wider spectrum of light is absorbed, which will lead to a larger current in the solar cell. On the other hand, this will also reduce the device voltage. For solar cell applications, the ideal semiconductor band gap lies within 1.1-1.4 eV [34], optimizing sunlight absorption throughout the spectrum with a single material and balancing the device's current and voltage. [31, 35]

Light absorption in a semiconductor excites electrons to the conduction band energy, creating electron vacancies or 'holes' in the valence band energy. This generation of these electron-hole pairs enhances the densities of electrons in the conduction band energy and holes in the valence band energy. Given that the generation of an electron and a hole always occurs in pairs, the principle of charge conservation holds true, denoted as $\Delta n_e = \Delta p$, where Δn_e indicates the excess electron concentration and Δp the excess hole concentration. The augmented carrier densities for electrons and holes in thermal equilibrium are then represented as

$$n = n_0 + \Delta n_e \text{ and } p = p_0 + \Delta p, \tag{2.4}$$

respectively. Introducing additional charge carriers shifts the Fermi energy, as is known from doping. However, the simultaneous generation of electrons and holes from light absorption poses a challenge, as the Fermi energy should theoretically shift towards both the conduction band energy due to excess electrons and the valence band energy due to excess holes. This dilemma is resolved by a splitting of the Fermi energy into two quasi-Fermi levels: The quasi-Fermi level of electrons ($E_{F,e}$) and quasi-Fermi level of holes ($E_{F,h}$). Incorporating equation (2.3) in equation (2.4), together with the excess charge carrier densities, the quasi-Fermi levels, and the conservation of charge, yield in

$$np = (n_0 + \Delta n_e)(p_0 + \Delta p) = n_i^2 e^{\frac{E_{F,e} - E_{F,h}}{k_B T}}. \tag{2.5}$$

The quasi-Fermi level difference, $E_{F,e} - E_{F,h}$, corresponds to the product of the implied voltage (V_{imp}), which is the maximum voltage achievable with the solar cell, and elemental charge (q). [31, 35]

For these charge carriers generated by light absorption to be used, the electron/hole pair needs to be separated before the electron 'falls' from the conduction band back into the valence band hole, a process called 'recombination'. The different kinds of recombination will be discussed in more detail in the following section. Separating the electron/hole pair can happen if, for example, a n-type and a p-type doped semiconductor are in contact with each other, and a pn-junction is formed.

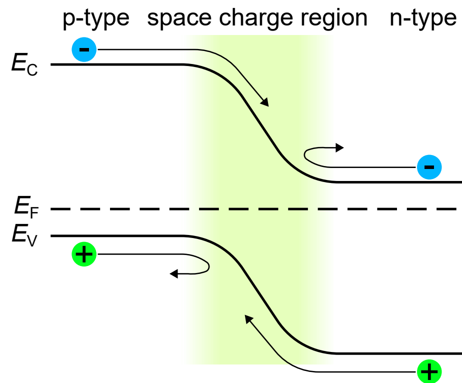

Figure 2.3.: *Depiction of a pn-junction in a non-illuminated state with a generated electron/hole pair in the p-type and n-type material. At the pn-junction, an electron can migrate from the p-type to n-type region, but not vice versa. The hole, on the other hand, can move from n-type to p-type material but is blocked to move from p-type material to n-type material.*

When a n-type and a p-type material in thermal equilibrium are brought in contact with each other, a pn-junction is formed. The E_F of both materials align and electrons diffuse from the n-type material to the p-type material and holes from the p-type material to the n-type material, recombining in the other material. This diffusion and recombination processes lead to the depletion of charge carriers close to the intersection and leaves the immobile charged doping atoms, creating a space charge region in the junction area, which leads to the band bending at the intersection of the two differently-doped materials, as illustrated in figure 2.3. At this intersection, if an electron/hole pair is generated in the p-type material, electrons ('-') in the conduction band from the electron/hole pair will move to the n-type material, as it is energetically favorable. The holes ('p') on the other hand remain in the p-type material, as they are blocked by an energy barrier, leading to the separation of the charge carriers. If the electron/hole pair is generated in the n-type material, the electron is blocked from moving into the p-type materials due to an energy barrier, while it is energetically favorable to move to the p-type material. [31]

After separation, the charge carriers can be extracted by the solar cell's contacts. This leads to the basic structure of a crystalline silicon solar cell as given in figure 2.4. The base of the solar cell is the doped absorber material,

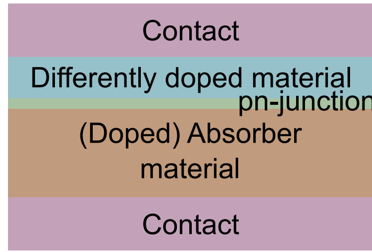

Figure 2.4.: *Basic structure of a crystalline silicon solar cell consisting of an absorber material for light absorption and electron/hole pair generation, which can already be doped. On top needs to be a doped layer of different polarity for charge carrier separation and some contacts for charge carrier extraction.*

in which the light is absorbed and electron/hole pairs are generated. To form a pn-junction and separate the charge carriers, a material of different polarity is needed, topped by a contacting material for charge carrier extraction, which also participates in absorption and charge carrier generation.

The current generated by the solar cell (J_{gen}) depends on the equilibrium between the generation rate of electron-hole pairs (G) and their recombination. Functionally, the solar cell behaves like a diode, where J_{gen} shifts the diode JV (current density-voltage) characteristics along the J axis by J_{gen}, resulting in negative currents, making the solar cell a power generator. In real solar cells charge carriers face various resistances, such as contact and sheet resistances, summarized as the series resistance (R_S), and shunt resistance (R_{sh}), as discussed later. The resulting J-V curve is mathematically expressed with a one-diode equation as

$$J(V) = J_0(e^{\frac{q(V-R_S J)}{n_{id} k_B T}} - 1) + \frac{V - R_S J}{R_{sh}} - J_{gen} \tag{2.6}$$

with J_0 representing the recombination current density and n_{id} as the diode ideality factor. n_{id} can be extracted from the slope of the JV-curve and is defined as

$$n_{id} = \frac{q}{k_B T} \frac{dV}{d\ln(J)}. \tag{2.7}$$

It is a fitting parameter in the one diode model and gives information about the recombination mechanisms at play, as discussed in the next section. Equation (2.6) defines the JV-curve of the solar cell, as depicted in figure 2.5. From this curve,

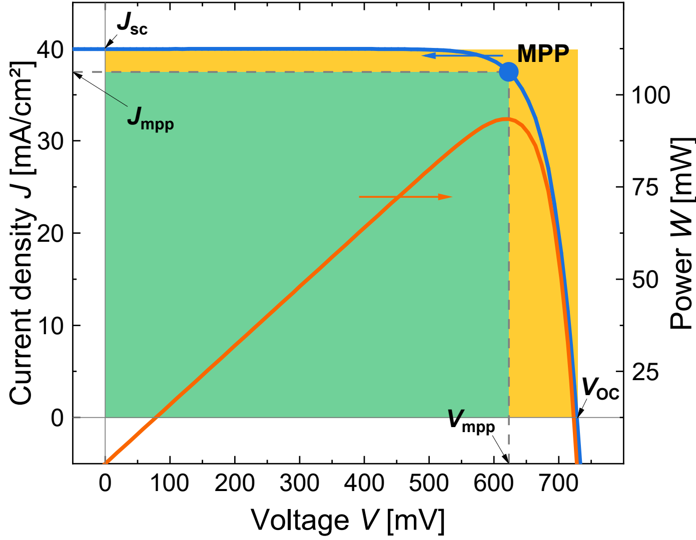

Figure 2.5.: *Illustration of a JV-curve (blue) and the corresponding power (orange) of a solar cell under one sun illumination. Key solar cell parameters are highlighted. The curve is mirrored to positive currents for clarity.*

the fundamental solar cell parameters can be deduced [31, 35], which are also marked in the exemplary *JV*-curve in figure 2.5:

- **Short-circuit current density (J_{SC}):** Denotes the short-circuit current density, the current density at zero voltage:

$$J(V = 0\,V) = J_{SC} = J_{gen}. \tag{2.8}$$

  It mainly reflects the optical properties, including optical losses, within the solar cell, including front side reflection, reducing light incorporation into the solar cell, and parasitic absorption in the front contact layers that does not contribute to current generation. Additionally, it can also be reduced by strong recombination.

- **Open-circuit voltage (V_{OC}):** The open-circuit voltage from the one-diode equation is defined at zero current flow as

$$V(J = 0\,A) = V_{OC} = \frac{n_{id} k_B T}{q} \ln\left(\frac{J_{SC}}{J_0} + 1\right), \tag{2.9}$$

which depends on J_0 and the diode ideality factor (n_{id}), two parameters depending on the passivation and recombination mechanisms at play in the solar cell. These parameters will be further explored in the subsequent section, focusing on various types of recombination and their mitigation strategies.

The V_{OC} can also be expressed as

$$V_{OC} = \frac{k_B T}{q} ln(\frac{np}{n_i^2}) \tag{2.10}$$

and is a more implied value, as it can be determined form charge carrier concentration measurements without applying metal contacts to the solar cell [36].

- **Maximum Power Point (MPP):** This point in the *JV* curve represents the maximum power output of the solar cell. The power at the maximum power point (P_{MPP}) is defined using the voltage at the maximum power point (V_{mpp}) and the corresponding current density at the maximum power point (J_{mpp}), is given by:

$$P_{mpp} = V_{mpp} J_{mpp} \tag{2.11}$$

The solar cell resistances, R_S and R_{sh}, influence the shape of the *JV* curve and therefore affect the MPP.

- **Fill Factor (*FF*):** The *FF* is the fraction of the extracted power at MPP conditions compared to the maximum possible current density or voltage and is significantly impacted by R_S and R_{sh}. Its mathematical definition is

$$FF = \frac{V_{mpp} J_{mpp}}{V_{OC} J_{SC}}. \tag{2.12}$$

High series resistances and low shunt resistances flatten the *JV*-curve, shifting the MPP, and reducing V_{mpp} and J_{mpp}, thereby diminishing *FF*. The ratio of the green area to the yellow area in figure 2.5 visually represents the mathematical definition. Additionally, the *FF* depends on V_{OC} and therefore the passivation quality, as the upper resistance-free limit of *FF* (FF_0) is given

by the empirical relation

$$FF_0 = \frac{\nu_{OC} - \ln(\nu_{oc} + 0.72)}{\nu_{oc} + 1}. \quad (2.13)$$

Here, ν_{oc} denotes the normalized open-circuit voltage $\nu_{oc} = \frac{qV_{OC}}{n_{id}k_B T}$. [37]

- **Power conversion efficiency (η):** The η is defined as the maximum extractable power of the solar cell compared to the incident power (P_{in}). It combines the aforementioned parameters and correlating them with the P_{in}, yielding the power conversion efficiency (η) as

$$\eta = \frac{P_{MPP}}{P_{in}} = \frac{V_{OC} J_{SC} FF}{P_{in}}. \quad (2.14)$$

Standardizing P_{in} is crucial for consistent η measurements, facilitating comparative analyses. Under standard test conditions of 25 °C and an Air Mass (AM)1.5 solar spectrum, P_{in} is defined at an one sun intensity as 1000 $\frac{W}{m^2}$. The AM 1.5 represents the number of atmospheres light traverses, correlating to a solar incidence angle of approximately $\sim 48^{\circ}$, commonly observed in various European regions.

- **Resistances:** Solar cells exhibit two critical resistances: The series resistance and shunt resistance. R_S encompasses resistances encountered by the charge carriers within the layers, influenced, for example, by the electrical conductivities of any interlayers between the metal contacts and absorber material and the contact resistivities between layers, the silicon absorber, and metal contacts. Minimizing electrical losses requires keeping R_S as low as possible, which can be determined by measuring the *JV* curve with varying light intensities. Mathematically, R_S reduces FF_0 to [37]

$$FF_S = FF_0 (1 - R_S \frac{J_{SC}}{V_{OC}}). \quad (2.15)$$

R_{sh} relates to resistance against unintended parallel current flows, similar to short circuits, which reduce the power output. A high R_{sh} is essential to prevent parasitic current paths, which can arise, for example, from n-type contacts wrapping around the wafer and connect to the p-type contacts.

Determining R_{sh} requires fitting the JV curve. Its impact on the FF can be expressed as [37]

$$FF_{sh} = FF_S(1 - \frac{\nu_{OC} + 0.7}{\nu_{OC}} \frac{FF_S}{R_{sh}\frac{J_{SC}}{V_{OC}}}). \tag{2.16}$$

The experimental determination of these values is explained in section 3.2.

- **Dependence of FF on V_{OC}:** As visible in equation (2.13), equation (2.15) and equation (2.16), the various FFs are depending on the ideality factor of the solar cell and its V_{OC}. As visible in equation (2.6), the n_{id} impacts the slope of the JV-curve at V_{OC} and therefore also MPP and FF. If passivation is limited by the three-carrier process Auger recombination, as discussed in the next chapter, the lowest n_{id} =2/3 is achievable [38]. As visible in equation (2.9), a high V_{OC} is achievable by a low J_0, which is a measure for recombination. This reduced recombination leads to less free energy losses at MPP, which shifts MPP conditions and increases FF. This leads to a higher upper limit of FF_0 for higher V_{OC}. In figure 2.6, the maximum achievable FF for given V_{OC} values is visualized for n_{id} of 2/3 in the Auger-limited case and 1 in the ideal diode case, which attainable for different conditions as discussed in the next chapter. Additionally, both cases are shown for R_S values of 0 Ω, 0.5 Ω and 1 Ω. The star marks the combination of the maximum achievable FF and V_{OC} for wafers of certain thickness and doping concentration which are used in this work according to the Richter parametrization [39]. While a higher n_{id} steadily decrease the FF for a given V_{OC}, the impact of series resistance is more severe and strengthened the impact of V_{OC} on FF. The Richter limit slightly deviates from the ideal FF due to usage of a doped wafer which increases recombination.

The one-diode model in equation (2.6) is a computational easy approach to fit to measured data and extract parameters. To improve the accuracy and better account for different recombination mechanisms and physical processes within the solar cell, this model can be extended to a two-diode by adding an additional

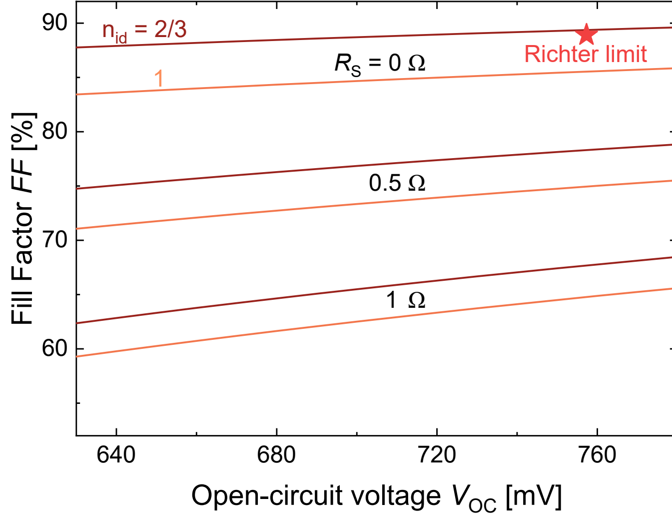

Figure 2.6.: *Calculations of the dependence of FF on V_{OC} for n_{id} of 2/3 and 1 and different R_S of 0 Ω, 0.5 Ω and 1 Ω. The star marks the maximum achievable FF-V_{OC} combination for wafer thicknesses and dopant concentrations used in this thesis. The impact of R_{sh} is neglected.*

parallel diode. This extends equation (2.6) to

$$J(V) = J_{01}\left(e^{\frac{q(V+R_S J)}{n_{id,1}k_B T}} - 1\right) + J_{02}\left(e^{\frac{q(V+R_S J)}{n_{id,2}k_B T}}\right) + \frac{V - R_S J}{R_{sh}} - J_{gen}, \tag{2.17}$$

which separates the recombination current density into J_{01} and J_{02}, one for each diode. The same is true for n_{id}, which separates into $n_{id,1}$ for the first diode and $n_{id,2}$ for the second diode. Here, the first diode represents diffusion currents in the quasi-neutral regions, while the second diode accounts for recombination in the depletion region. [40–42]

More information about the solid state physics background and the operating principle of solar cells can be found in refs. [31, 32, 34, 35, 43].

2.2. Selectivity and Recombination in Solar Cells

For solar cells, the generation of an electron/hole pair via light absorption and their extraction is the essential working principle of the device. The subsequent challenge lies in the efficient separation and extraction of these charge carriers before they recombine and are lost for power generation purposes: extracting one type (say, electrons) while repelling the other (holes), minimizing resistances for the desired carrier, and simultaneously passivating surface defects in crystalline silicon to suppress recombination. This section delves into the principle of selectivity before exploring charge carrier recombination and passivation.

The currents of electrons and holes can be expressed as

$$J_e = \mu_n n \frac{\delta}{\delta x} E_{F,e} \tag{2.18}$$

and

$$J_h = \mu_p p \frac{\delta}{\delta x} E_{F,h}, \tag{2.19}$$

respectively. These currents are determined by the respective electron or hole mobilities (μ_n,μ_p), the charge carrier concentrations (n;,p), and the gradients in quasi-Fermi levels ($E_{F,e}$;$E_{F,h}$). For charge carrier separation, a *pn* junction can be utilized, as discussed before. [31] A measure to quantify the charge carrier recombination and taking the resistance each charge carrier faces into account is the selectivity (S). It is quantified by the ratio of the minoriy carrier resistance (ρ_m) to majority carrier resistance (ρ_M), as introduced by Brendel and Peibst [44]. The minoriy carrier resistance can be derived from the recombination current density at $V = 0\,V$, while ρ_M depends on the contact resistivity (ρ_c). Consequently, a simple definition of the selectivity is given by

$$S = \frac{k_B T}{q J_0 \rho_c}. \tag{2.20}$$

This definition breaks the selectivity down to two easily measurable parameters: The contact resistivity (ρ_c) and J_0. Optimizing the contact resistivity for selective contacts involves increased levels of appropriate doping and alignment of the respective energy bands of the contact layers with the work function of the metal

contact, thereby circumventing energy barriers. Furthermore, the contact layers should exhibit high σ for the specific charge-carrier polarity, while blocking charge carriers of the other polarity.

Both J_0 and n_{id} are influenced by the recombination dynamics of the generated electron-hole pairs. Nature's tendency to minimize the energy of a system demands that the excited electron seeks a lower energy state, typically achieved by relaxing back to a free state, a hole, in the E_V. This phenomenon, known as recombination, manifests itself in various forms, as illustrated in figure 2.7 together with an illustration of light absorption:

- **Radiative recombination** is the counterpart to absorption. It involves a conduction band electron reuniting with a valence band hole, emitting the energy difference as a photon with $E = E_G = h\nu$. The process in unavoidable and the radiative recombination rate (R_{rad}) is defined as proportional to the charge carrier concentrations $R_{rad} = Bnp$, with B being the radiative recombination constant. At open-circuit conditions and steady state, generation (G) equals recombination $G = R_{rad} = Bnp$. Assuming high level injection, where the generated excess charge carriers exceed the dopant density with $n = p = \Delta n$, this relation can be simplified to $G = R_{rad} = B\Delta n^2 \Rightarrow \Delta n^2 = \frac{G}{B}$. Putting this relation to equation (2.10), one gets

$$V_{OC} = \frac{k_B T}{q} \ln(\frac{np}{n_i^2}) = \frac{k_B T}{q} \ln(\frac{\Delta n^2}{n_i^2}) = \frac{k_B T}{q} \ln(\frac{G}{Bn_i^2}) \tag{2.21}$$

  for V_{OC} and

$$n_{id} = \frac{q}{k_B T} \frac{dV_{OC}}{d\ln(G)} = 1 \tag{2.22}$$

  as ideality factor for this case.

  For the low level injection case, implying a low charge carrier concentration, where to total charge carrier concentration can be approximated by the dopant density with $p \ll n \approx N_D$ for n-type material, G can be approximated as $G = R = Bnp \approx BN_D p$, yielding the same results for V_{OC} and n_{id}.

- **Auger recombination**, a nonradiative process, is a three-particle process where an electron-hole recombination transfers energy to another charge

carrier, for example a conduction band electron, resulting in thermalization of the excess energy. The intensity of this mechanism correlates with the doping concentration, as it heavily relies on one charge carrier polarity and the Auger recombination rate (R_{Auger}) can be expressed as $R_{\mathrm{Auger}} = C(n^2p + p^2n)$, where C is the Auger recombination constant. In the high injection case, this simplifies to $G = R_{\mathrm{Auger}} = 2C\Delta n^3$ and yields

$$n_{\mathrm{id}} = \frac{2}{3} \tag{2.23}$$

and

$$V_{\mathrm{OC}} = \frac{2k_{\mathrm{B}}T}{3q}\ln(\frac{G}{2Cn_{\mathrm{i}}^3}). \tag{2.24}$$

For the low level injection case, one gets $G = R = CN_{\mathrm{D}}^2p$, leading to

$$n_{\mathrm{id}} = 1 \tag{2.25}$$

and

$$V_{\mathrm{OC}} = \frac{k_{\mathrm{B}}T}{q}\ln(\frac{G}{CN_{\mathrm{D}}n_{\mathrm{i}}^2}). \tag{2.26}$$

- The third variant, **Shockley-Read-Hall (SRH)** recombination, is rooted in defects within the bulk, such as impurities, dislocations, vacancies, or interstitials in the crystalline lattice of crystalline silicon, or at the crystalline silicon interface through silicon dangling bonds. In crystalline silicon, bulk defects are generally well managed, yet surface dangling bonds are pivotal in limiting the voltage of the solar cell, requiring passivation. These defects create intermediate band gap states necessary for SRH recombination. At the interface, these intermediate states can be avoided by removing, or 'passivating', the dangling bonds of the un-bonded surface silicon atoms in the crystal. The Shockley-Read-Hall recombination rate (R_{SRH}) is given by $R_{\mathrm{SRH}} = \frac{np}{\tau_{\mathrm{p}}n+\tau_{\mathrm{n}}p}$, depending on the charge carrier lifetime of both types. For high level injection, this simplifies to $G = R_{\mathrm{SRH}} = \frac{\Delta n}{\tau_{\mathrm{p}}+\tau_{\mathrm{n}}}$, which gives an ideality factor of

$$n_{\mathrm{id}} = 2 \tag{2.27}$$

and a V_{OC} of

$$V_{OC} = \frac{2k_B T}{q} \ln(\frac{G(\tau_p + \tau_n)}{n_i}). \tag{2.28}$$

In the low level injection regime, the generation can be approximated as $G = R_{SRH} = \frac{p}{\tau_p}$, leading to

$$V_{OC} = \frac{k_B T}{q} \ln(\frac{N_D G \tau_p}{n_i^2}), \tag{2.29}$$

with

$$n_{id} = 1. \tag{2.30}$$

In summary for crystalline silicon solar cells, radiative recombination is nearly negligible due to the indirect band gap of the material, making the involvement of a phonon during the recombination process necessary. As this is the only non-avoidable recombination mechanism, it impacts the upper efficiency limit, the Shockley-Queisser limit, for solar cells. Auger recombination strongly depends on the doping of the material and further reduces the upper power conversion efficiency limit for crystalline silicon solar cells to 29.4%, according to Richter et al. [19]. It requires three charge carriers, two majority and one minority charge carriers, leading to n_{id} of 2/3 for the high injection case, which is the lower bound for n_{id} and, at sufficiently low R_S, enables string gains in *FF* if Auger recombination is the limiting factor [38]. Finally, SRH recombination is strongly depending on defects and their population, and therefore the charge carrier lifetime of electrons and holes. In the high injection case with n_{id} of 2, the recombination is limited by both majority and minority charge carriers, which shifts to only minority charge carrier limited for the low injection case with $n_{id} = 1$. It is the limiting factor for low-quality silicon wafers or insufficient surface passivation, yielding in a high density of defects available as recombination centers. In recent world record solar silicon heterojunction solar cells, SRH recombination is well under control due to near-perfect surface passivation and very well-balanced doping densities, in addition to high-quality monocrystalline silicon wafers [38].

More detailed information about recombination and the *pn*-junction can be found in refs. [31, 35, 37]

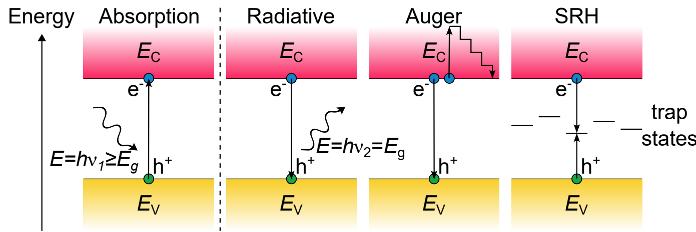

Figure 2.7.: *From left to right, schematic representation of light absorption, radiative recombination, Auger recombination and Shockley-Read-Hall recombination.*

2.3. Passivating Contacts in Crystalline Silicon Solar Cells

A critical aspect of enhancing the solar cell efficiency is the mitigation of SRH recombination, particularly at the semiconductor interfaces. This necessitates 'passivation' of defects to neutralize them as recombination centers. Passivation can be realized either electrically through field effects or chemically. Field-effect passivation employs a build in electric field to repel one type of charge carrier, thereby reducing recombination by depleting this type of charge carrier. However, this approach presents challenges: The introduced free charge carriers can absorb light that would otherwise contribute to electron-hole pair generation, and elevated doping concentrations inevitably amplifies Auger recombination, as previously discussed. Alternatively, chemical passivation targets the neutralization of energetic trap states within the band gap, without preferentially repelling charge carriers. This approach often involves additional layers on top of the absorber, such as silicon oxide in the case of crystalline silicon, where the oxygen atoms bond with open silicon bonds, or hydrogenated layers that utilize the introduced hydrogen atoms to bond to the open silicon bonds, removing their energetic state in the band gap.

In crystalline silicon, radiative recombination is relatively rare due to the indirect nature of its band gap. With controlled doping and growth processes, bulk Auger and SRH recombination can be minimized. However, surface SRH recombination persists as a critical issue. The passivated emitter rear contact (PERC) solar cell, as depicted in figure 2.8 a), utilizes p-type wafers with silicon

nitride for front side passivation, also serving anti-reflective purposes. A phosphorus diffusion process creates a n^+ region on the front of the p-type wafer, establishing the *pn*-junction. This region is further doped to n^{++} beneath the silver contacts for an enhanced conductivity and field-effect passivation in the contact region. The rear side employs an aluminum oxide and silicon nitride passivation, with openings for the aluminum contacts and local aluminum back surface fields. While the majority of the surface is passivated by these oxide layers, a direct metal-to-silicon contact is vital for a low contact resistivity, relying solely on the field effect from the doped area as passivation. These heavily doped areas are prone to Auger recombination, and free carrier absorption issues are present in the doped regions. PERC's direct metal-silicon contact introduces numerous interface defects, necessitating electron-hole pair separation before reaching these defect-laden interfaces. Despite these challenges, the front side's transparent, anti-reflective coatings yield higher generated currents compared to those of other structures. [22, 45]

While PERC solar cells utilize p-type gallium doped wafers, new passivating contact approaches switched to n-type phosphorous or antimony doped wafers. Historically, p-type wafers were used as boron doping used at that time is easier to achieve than phosphorous doping and the p-type substrates showed higher resistivity to space radiation. With more advanced fabrication techniques, the phosphorous doping became the mainstream technology as the quality of wafers is higher as remaining metal impurities in silicon are positively charges an have a larger capture cross-section in p-type materials, increasing the recombination at the impurity [46]. Currently, antimony doping seems a promising next n-type wafer dopant and is making its way as industrial mainstream. Furthermore, the passivating contact technology circumvents the direct metal-crystalline silicon contact through intermediate layers that provide selective charge carrier conduction and passivation, while maintaining transparency for efficient light absorption in the crystalline silicon absorber. These interlayers must furthermore form a low-resistive contact with the metal. Additionally, with the move to passivating contacts, the aluminum metal contacts are replaced by silver contacts. Aluminum is an excellent p-type dopant for silicon, which could be utilized in PERC solar cells as hole-selective contact. This doping from the metal contact is not desired

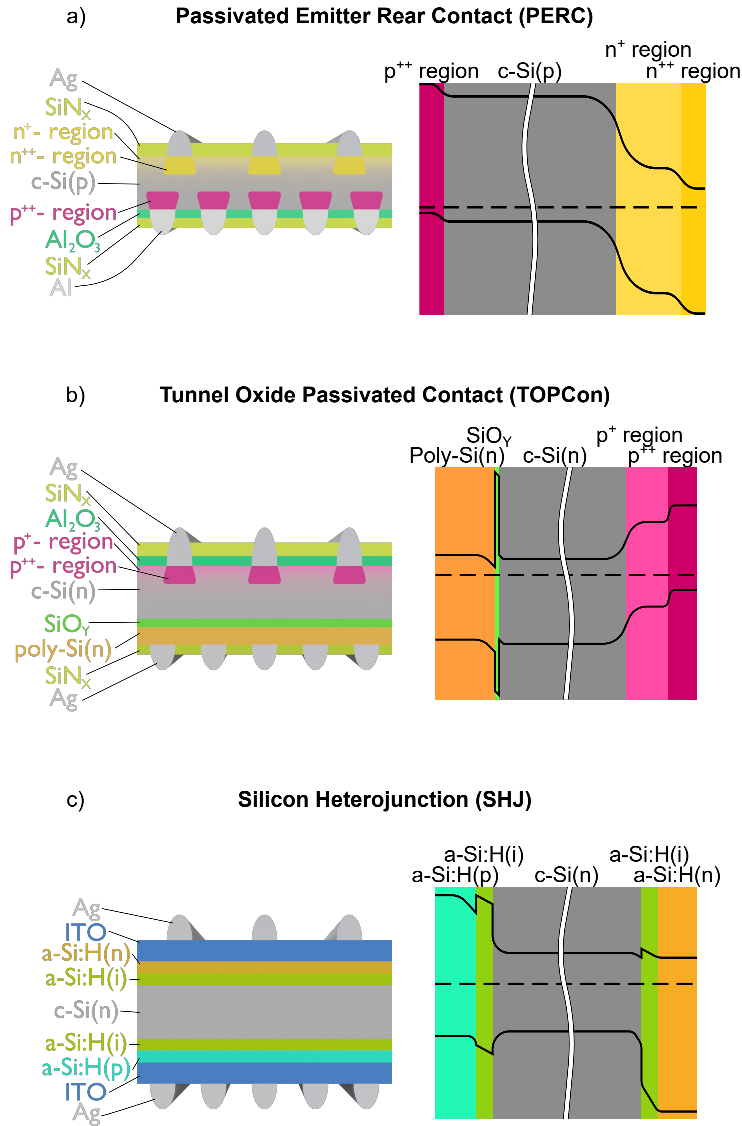

Figure 2.8.: *Illustrations of prevalent solar cell technologies: a) The passivated emitter rear contact (PERC) structure, b) a tunnel oxide passivated contact (TOPCon) structure utilized on the rear side, and c) a hydrogenated amorphous silicon (a-Si:H)-based silicon heterojunction (SHJ) contact. An illustration of the structure is shown on the left side, while a sketch of the corresponding band diagrams is shown on the right side.*

for passivating contacts, making the move to silver necessary. Additionally, the aluminum paste could punch through the emitter and lead to shunt paths. [22, 45]

The field of passivating contacts in crystalline silicon solar cell technology is dominated by two approaches: The silicon heterojunction (SHJ), which leverages a-Si:H, and the silicon oxide-polycrystalline silicon passivating contact known as tunnel oxide passivated contact (TOPCon). The latter, depicted in figure 2.8 b), is a direct evolution from the PERC solar cell, employing silicon oxide for additional interface passivation. A layer of polycrystalline silicon is applied on top of the silicon oxide layer, enabling lateral charge carrier transport and creating a low-resistive contact to the metal contacts. This polycrystalline layer is typically grown by depositing amorphous silicon, followed by a high-temperature annealing process that crystallizes the material. This high-temperature step not only crystallizes the layer but also expels most of the hydrogen vital for chemical passivation. To bolster this chemical passivation in addition to the silicon oxide, a subsequent rehydrogenation step is employed, involving the deposition of silicon nitride followed by annealing, effectively diffusing hydrogen back into the polycrystalline silicon and silicon oxide layers. Furthermore, phosphorus plays an essential role in this architecture; during the crystallization phase, it diffuses from the polycrystalline into the crystalline silicon, leading to a pronounced band bending at the interface with the silicon oxide, thus enabling an efficient field-effect passivation and enhancing the contact properties. [22, 45]

A critical aspect of the TOPCon approach is maintaining an optimal thickness of the polycrystalline silicon (poly-Si) layer, crucial to avoid the need for an additional TCO layer and also to avoid that the metallization is fired into the poly-Si. However, its application is generally restricted to the rear of the solar cell due to significant parasitic absorption issues, an inherent consequence of the poly-Si band gap mirroring that of crystalline silicon. As a rear contact, it is often paired with a diffused junction front contact, similar to that featured in PERC technology. The band diagram in figure 2.8 b) reveals how the silicon oxide, an insulator, introduces an energy barrier for charge carriers due to its large band gap. To navigate this barrier, charge carriers must quantum-mechanically tunnel

through the barrier, a process heavily influenced by the thickness of the barrier. Consequently, the thickness of the oxide layer is limited to below 2 nm to optimize the tunneling probability. [22, 45, 47]

In contrast, the polycrystalline silicon on oxide (POLO) contact differs from TOPCon primarily in terms of oxide thickness. In the POLO contact, the oxide can exceed the 2 nm threshold, but this requires annealing at even higher temperatures, typically above 800 °C. At these elevated temperatures, the silicon oxide undergoes a transformative restructuring, forming more stoichiometric regions, and consequently creating oxide-free zones known as pinholes. These pinholes emerge as vital channels for charge carriers, facilitating their movement through the oxide layer and enhancing the diffusion of phosphorus. This phenomenon compensates for the reduced chemical passivation in pinhole-rich areas with a robust field-effect passivation mechanism. [22, 45, 47]

In the SHJ approach, illustrated in figure 2.8 c), the intrinsic a-Si:H is utilized as the passivation layer, laying the basis for an enhanced solar cell performance. Subsequently, doped a-Si:H is stacked on top of the intrinsic layer to enable an effective contact with subsequent layers and achieve high charge carrier selectivity. However, a notable challenge in this design is the inherent property of amorphous silicon to significantly absorb light, thereby impeding the generation of electron-hole pairs within the crystalline silicon absorber. To mitigate this issue, the thickness of these layers is precisely controlled, limited to just a few nanometers, effectively minimizing parasitic light absorption. [22, 45]

However, these thin layers result in a high sheet resistance, which often requires the integration of an additional TCO layer. This layer not only plays a crucial role in enabling lateral charge carrier transport but also doubles as an anti-reflective coating, enhancing light entering the solar cell and ensuring a low-resistive contact with the silver contacts. The SHJ thus achieves outstanding passivation and *FF*s, albeit at the cost of a reduced current output due to parasitic absorption in both the a-Si:H and TCO layers. [48]

This heterojunction structure, characterized by the formation of the name-giving heterojunction between amorphous and crystalline silicon, is visible in the band diagram in figure 2.8 c), showing two distinct band gaps. Unlike tradi-

tional methods, the *pn*-junction here emerges not through diffusion but through the deposition of, for example, p-type doped a-Si:H onto an n-type c-Si wafer, complemented by an intrinsic a-Si:H interlayer. [22, 45]

Current research in this domain is exploring innovative materials to replace the doped a-Si:H layer, with the aim of achieving a higher transparency. Promising candidates include nanocrystalline forms of silicon, silicon oxide, and silicon carbide. In a more radical approach, there is a growing interest in completely replacing the doped layers with metal oxides such as titanium oxide, molybdenum oxide, or tungsten oxide. These materials offer new possibilities for improving the efficiency of solar cells. [22, 45]

Additionally, the solar industry faces the challenge of increasing silver use for metallization and the dependence on indium, a scarce and therefore expensive material, for the most effective TCOs. In response, researchers are concentrating on developing alternative strategies, such as substituting copper for silver as metal contacts [49] and employing indium-free doped zinc oxides as a potential replacement for indium-based TCOs [50, 51].

Lastly, the interdigitated back contact (IBC) approach maximizes light entry by integrating all contacts at the back, eliminating shading through metallized areas on the front side and increasing current generation. This design demands closely spaced alternating n-p contacts on the rear, with stringent separation to prevent shunting, posing considerable manufacturing challenges. [22]

These different challenges and requirements for an high-quality passivating contact lead to the optimization triangle, shown in figure 2.9, which links key solar cell parameters to the functionalities discussed. The J_{SC} is influenced by light absorption in the absorber material, which can be enhanced by additional anti-reflective coatings or more transparent or thinner contact layers. In SHJ solar cells, this could be achieved by a reduced TCO layer thickness. The V_{OC} depends on the suppression of charge carrier recombination, as indicated by equation (2.9), where V_{OC} is closely related to the recombination current density J_0. The *FF* is affected by various resistances in the layers and the metal-c-Si contact interface. If additional layers are present between metal contacts and c-Si, their electrical conductivity should be maximized for minimal resistance to

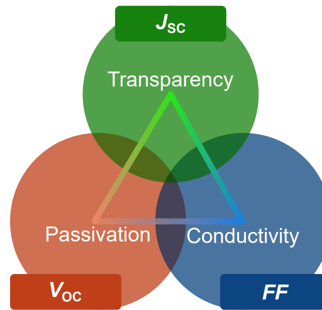

Figure 2.9.: *Optimization triangle for front passivating contacts, illustrating the interplay and trade-offs between the short-circuit current density (J_{SC}), open-circuit voltage (V_{OC}), and the Fill Factor (FF).*

charge carrier movement. The trade-offs and challenges along the optimization triangle axis include:

- J_{SC}-V_{OC} axis: Challenges include optimizing the thickness of the crystalline silicon absorber. A thicker absorber material allows for increased light absorption, improving J_{SC}, while simultaneously increasing the bulk defects, reducing V_{OC}. Furthermore, the doping concentration below the finger area for PERC solar cells could also pose a challenge, as previously discussed.
- J_{SC}-FF axis: A balance between doping concentration and free charge carrier absorption is crucial in TCO layers in SHJ. Higher doping improves the conductivity, reducing resistive losses, and improving FF, but also increases free charge carrier absorption, reducing the J_{SC}.
- V_{OC}-FF axis: In TOPCon structures, the passivation effect of silicon oxide and the transport of the charge carrier through the oxide layer present a trade-off. Thicker oxide or fewer pinholes improve the passivation, and therefore the V_{OC}, but hinder charge carrier extraction, reducing the FF. A similar trade-off exists in SHJs with the thickness of the intrinsic a-Si:H layer, affecting both passivation and charge carrier extraction.

Optimizing one parameter often affects others, adding complexity to solar cell development. The evolving landscape of solar cell technology continually seeks to enhance the power conversion efficiency. A snapshot of current champion solar cell parameters for solar cells contacted at the front and rear side is given in ta-

Table 2.1.: *Key solar cell parameters for each technology type as of December 2024. Data taken from ref. [52].*

Contact	η [%]	J_{SC} [$\frac{mA}{cm^2}$]	V_{OC} [mV]	*FF* [%]
PERC	25.0	42.7	706.0	82.8
SHJ	26.8	41.5	751.4	86.1
TOPCon	25.8	42.9	724.1	83.1

ble 2.1. Further information on passivating contacts and the different approaches can be found in refs. [22, 47, 53–57]

2.4. Silicon Carbide in Crystalline Silicon Solar Cells

Silicon carbide, a well-known material with a long-standing reputation in the semiconductor industry, has its applications in various domains. These range from power electronics, where it is utilized in devices such as metal–oxide–semiconductor field-effect transistors and diodes [58–61], to high-voltage equipment such as solid-state circuit breakers [62, 63] and grid transmission applications [64, 65]. Its utility also extends to sensor technology [66–68]. The pathway of amorphous silicon carbide in solar cell applications began in 1981, serving as a window layer in silicon thin film solar cells [69]. Its widespread adoption in the sector of thin film solar cells is traceable to its wide and adjustable band gap, together with its superior electrical properties [70–72]. However, its integration into crystalline silicon-based solar cells presents challenges, primarily because of the subpar performance of silicon carbide layers compared to pure silicon layers. Research into the incorporation of silicon carbide in various forms, amorphous, nanocrystalline, or polycrystalline, and in different doping states, like intrinsic, n-type or p-type continually progresses. Techniques for depositing silicon carbide thin films are diverse, including chemical vapor deposition (CVD) methods such as HWCVD [73–75], halide CVD [76], plasma-enhanced chemical vapor deposition (PECVD) [77–79], low pressure CVD [80], and combinations thereof [81]. Physical vapor deposition (PVD) techniques, such as sputtering [82–84] and pulsed laser deposition [85–87], are also employed. For solar cell applications, the main focus is

on HWCVD and PECVD, with some studies exploring sputtering processes. For crystalline silicon solar cell applications, two process temperature regimes can be defined: High-temperature regimes for polycrystalline silicon carbide layers in TOPCon-like structures and temperatures above 750 ℃, and low-temperature regimes with structures similar to SHJ solar cell and applied temperatures below 300 ℃.

2.4.1. Microstructural and Opto-Electrical Properties of Silicon Carbide Layers

As depicted in figure 2.9, the deposited thin film must exhibit excellent optical and electrical properties and should additionally effectively passivate the surface of crystalline silicon for use in passivating contact schemes. Adjustments in the carbon content of the material can widen the optical band gap [88–91], as well as modulations in the hydrogen content [92, 93] and the crystalline volume fraction of the layer, including defect adjustments [94, 95]. The electrical attributes of the film are closely related to its microstructure, including factors such as crystallite size and grain boundaries that can hinder the movement of the charge carriers, as well as defects that can trap charge carriers [95, 96]. Tuning of these electrical properties can also be achieved by doping, with boron [74, 97] and aluminum [98] commonly used for p-type doping, while phosphorous [97, 99–101], nitrogen [95, 102], and oxygen [95, 103] are utilized for n-type doping. In general, the charge carrier mobility in silicon carbide is depending on its polytype, but in all cases it is lower than in crystalline silicon [104, 105]. The passivation mechanism in silicon carbide can be attributed either to field-effect or to chemical passivation. Together with doping, field-effect passivation is influenced by fixed charges within the first nanometers of the silicon carbide [106], which are amphoteric in nature, implying their ability to be either positive or negative depending on the substrate doping [107–110]. Furthermore, the high hydrogen content in the silicon carbide layers facilitates effective chemical passivation [95, 111].

Given their enhanced opto-electrical characteristics, nanocrystalline or polycrystalline materials are preferred, akin to silicon or silicon oxide materials. Re-

garding optical and electrical properties, silicon carbide grown via HWCVD surpasses layers produced by PECVD. This is due to the higher density of hydrogen radicals at lower energies during the HWCVD process [95, 112, 113], leading to larger crystallite sizes in nanocrystalline materials [95] and reduced damage to the surface of crystalline silicon, a concern with parallel plate PECVD depositions [114]. In PECVD, larger crystallites can be achieved by decreasing the total flow rate or increasing the process temperature, generator power, or hydrogen dilution of the precursor gases [95, 115, 116]. For HWCVD-grown films, reducing the filament temperature or the total flow rate and increasing the hydrogen dilution of the precursor gases enhance grain sizes. Furthermore, minimizing the distance between the substrate and the catalytic filament increases the grain size as well. [95, 113] In general, deposition conditions that achieve larger crystallites create harsher environments, potentially damaging the crystalline silicon surface. Thus, monitoring the passivation quality of the substrate is crucial. Compared to pure silicon layers, introducing carbon into the silicon network enhances etch resistance against wet chemicals like potassium hydroxide [90], hydrofluoric and hydrochloric acid, it improves thermal stability, shifts hydrogen effusion peaks to higher temperatures, and traps hydrogen [89, 90, 109, 117, 118], reducing blistering [89, 107, 119, 120]. However, films with carbon are more porous [107, 117] and less dense [121]. The impact of carbon on stress within the layer is ambiguous, potentially increasing [88, 119] or decreasing [89, 107, 120] it. The release of hydrogen during annealing is assumed to increase the stress in the layer [90]. This stress can lead to the formation of an amorphous interlayer for relaxation close to the crystalline silicon interface [89]. The overall hydrogen content increases with carbon incorporation [107, 117], but the silicon-hydrogen bond concentration decrease as hydrogen bonds to carbon [110]. Furthermore, carbon inhibits high-temperature crystallization, reducing film crystallinity [89, 119, 120, 122–125], and higher annealing temperatures are needed to achieve the same crystallinity as in carbon-free films [88, 107, 123, 125].

The first corner of the optimization triangle focuses on the electrical properties of the material to enable an efficient contact, as well as vertical and lateral charge carrier transport. Generally, more crystalline materials with large grains enhance the mobility of the charge carriers by reducing grain boundary scattering

and lowering the activation energy for conductivity, thus increasing the conductivity of the material [95, 113, 116]. An alternative method to improve conductivity involves the introduction of dopants. The material inherently exhibits n-type characteristics [95], so introducing a p-type dopant initially reduces its electrical conductivity before the p-type character becomes prominent [126]. Consequently, n-type doping typically results in conductivities higher than those of p-type doping [127]. But the introduction of dopants into the process influences the growth mechanisms of the layer, where an increase in the dopant concentration could reduce the grain size [97, 128]. Therefore, finding an equilibrium between the introduction of dopants to improve electrical properties and the potential reduction of grain size is essential. Among n-type dopants, nitrogen doping has been shown to be more efficient than phosphorus doping [122, 128], since carbon suppresses phosphorous doping activation [89]. Nitrogen, for example, can passivate defects at the grain boundaries [102], potentially increasing the mobility of the charge carrier by reducing the trapping of the charge carrier at the grain boundaries [96]. However, phosphorous doping still remains more effective than boron acceptor doping [121], which encounters similar activation challenges [122]. Annealing at elevated temperatures, or in the case of HWCVD, depositions at elevated filament temperatures, can enhance dopant activation in the material [90, 111, 129–132]. The high-temperature approach also uses an increase in the firing temperature during metal contact firing to improve the crystallisation of the layer during this firing step [122, 131, 133, 134]. Moreover, the carbon content affects the band gap of the material. A large band gap can result in high valence or conduction band offsets, causing S-shapes in the JV-curve [118, 135–137]. Narrowing the band gap through increased hydrogen dilution during the deposition reduces the offset [29, 118] and an improved transport, for example through the valence band spike, can be achieved by higher doping, trap states, or a thinner intrinsic interlayers before the doped layer [135, 138]. Experimentally, this has been demonstrated with increased FFs and reduced R_Ss for increased doping concentration and lower carbon content [88, 119, 120, 122, 130, 134, 139, 140].

The second aspect of the optimization triangle encompasses the optical properties of the layers, with a particular emphasis on the front and rear contact layers. These layers are crucial, as they must absorb minimal light to reduce

parasitic absorption of incident light and reduce the reflection of incident light which maximises the light reaching the crystalline silicon absorber material. Incorporating carbon into silicon layers broadens the band gap of the material [89–91, 125, 133, 141], thus decreasing light absorption in the material and improving its transparency. The optical band gap also depends on the crystallinity and grain sizes within the layer, aspects previously discussed. Both the optical band gap and the sub-band gap absorption increase with the grain size [95, 113]; therefore, to optimize optically, adjusting the layer thickness and waging the layer reflection and absorption against each other is necessary [142]. Additional doping can increase the band gap [90] but can also increase the absorption coefficient in the infrared spectrum due to free-carrier absorption. This effect is more pronounced for p-type dopants than for n-type dopants [124] and it might be related to the inherent n-type nature of the material, which requires over-doping and thus potentially decreases the crystallinity, lowering the mobility of charge carriers and making higher doping concentrations necessary [74, 95, 126]. Furthermore, carbon incorporation reduces the reflection of the layer [127, 136, 143] by decreasing the refractive index [84, 91]. Forming gas annealing or thermal treatments, vital for applications such as TOPCon solar cells, tend to reduce the band gap [132, 144]. With such high-temperature treatments, it is observed that increased carbon content leads to stronger absorption. Although carbon introduction widens the band gap, the decreased crystallinity of the material increases the light absorption. Consequently, the wider band gap can be overshadowed by the reduced crystallinity of the material [88, 124]. In solar cell applications, thicker layers can lower the J_{SC} by an increased parasitic light absorption [136, 137, 145].

For the final corner of the optimization triangle of passivating contacts, attention turns to passivation, particularly with a focus on hydrogen content, doping and fixed charges for field-effect passivation. Generally, passivation can be enhanced by introducing dopants such as nitrogen, phosphorous, or boron [90, 99, 108, 121, 133, 146–148], increasing the deposition temperature [83, 99, 146, 149–151], reducing the plasma power in films prepared by sputtering [83], or lowering the filament temperature in HWCVD [29, 95, 132, 152, 153]. The use of buffer layers, such as amorphous silicon carbide before the nanocrystalline

form or silicon oxides [95, 114, 116, 152, 153], and the adjustment of the carbon content in silicon carbide also play a role. Thicker layers, while reducing the J_{SC} of the solar cell, improve the passivation of the crystalline silicon [106, 130, 144, 145, 148]. In scenarios without high-temperature annealing, the reports regarding the carbon content are inconclusive, as both a higher carbon content [121, 147] and a lower [110, 118] carbon content are reported to improve the passivation, making definitive conclusions difficult. For high-temperature approaches, a lower carbon content is preferable for passivation [122, 123, 133, 137].

Fixed charges in silicon carbide layers are amphoteric, meaning that they can be positive or negative, depending on the polarity of the substrate. They may originate from the majority charge carriers trapped in the dangling bonds of the silicon carbide [108–110, 147, 154]. The amount of fixed charges can be influenced by the substrate doping [121, 146], the layer doping [99, 147], and, if present, the doping of the capping layer [154]. Increasing the number of dangling bonds in silicon carbide enhances the number of fixed charges [99], achievable through phosphorous introduction or by raising the substrate temperature during deposition, leading to hydrogen effusion and leaving unsaturated dangling bonds [99]. In addition to the influence of fixed charges, the accumulation of charge carriers can significantly affect the field-effect passivation. Specifically, when highly p-doped silicon carbide is employed in conjunction with an n-type substrate, the valence band offset can lead to an accumulation of holes at the crystalline silicon interface. Consequently, this accumulation can decrease the efficacy of the field effect of silicon carbide [138]. Additionally, majority charge carrier accumulation at the crystalline silicon interface can improve field-effect passivation [29].

The hydrogen content of the layer depends on the deposition conditions and the microstructure of the material. In nanocrystalline silicon carbide, hydrogen is speculated to be located at grain boundaries rather than within grains, making smaller grains more advantageous for hydrogen incorporation [95]. For HWCVD silicon carbide, the hydrogen content increases with a reduced hydrogen dilution, an increased total flow rate of the precursor gases, a smaller distance between the catalytic filaments and the substrate, or a reduced filament temperature [29, 95, 132, 152, 153]. In the case of PECVD silicon carbide, the hydrogen content

can be similarly augmented by increasing the total flow rate of precursor gases, or in non-stoichiometric films, by increasing the carbon content and introducing nitrogen, which increases both the carbon and the hydrogen content in the layer [95, 147]. While a lower hydrogen content is said to improve the density of dangling bonds, thus increasing the number of fixed charges and enhancing field-effect passivation, chemical passivation relies on hydrogen. Therefore, a balance between these two effects may be necessary.

2.4.2. Silicon Carbide Layers in Crystalline Silicon Solar Cell

In solar cell structures with high-temperature processing steps, additional hydrogenation is required to reintroduce hydrogen into the layer for passivating purposes. A forming gas anneal can be employed [106, 122, 144, 150, 155], but its effect is thought to originate more from a restructuring of hydrogen within the layer, leading to more dangling bonds and an increased fixed charge density, thus resulting in increased field effect passivation, rather than from additional hydrogen introduction. A similar outcome is observed for annealing in a nitrogen atmosphere, and a higher deposition temperature, hence a lower hydrogen content in the layer, diminishes the effect of a forming gas anneal. [106, 146, 150] A higher carbon content enhances the passivation following the forming gas anneal [123, 125]. Hydrogenation using hydrogen diffusion from a deposited silicon nitride layer appears to be more effective than a forming gas anneal [134], and even capping with amorphous silicon can hydrogenate the silicon carbide [118, 154, 156]. However, capping with a p-type amorphous silicon layer might reduce the temperature stability compared to a n-type amorphous silicon capping, as the Fermi energy shifts closer to the valence band, promoting hydrogen effusion [154]. Even for low-temperature approaches, an annealing step can be beneficial to repair any damage to the passivation caused by subsequent processing steps [29, 157].

Buffer layers such as silicon oxide significantly impact the passivation capabilities of overlying layers. For silicon carbide, they can act as a protective barrier against hydrogen radical bombardment on the crystalline silicon surface

[114, 152] and serve as regions for hydrogen accumulation, essential for chemical passivation [29, 158]. Thicker buffer layers, such as silicon oxide or amorphous silicon carbide under gentle deposition conditions, are known to improve passivation as well [88, 106, 116, 131]. Particularly in high-temperature firing steps, silicon oxide layers often rupture [137], and the present carbon may react with oxygen, leading to the dissolving of the silicon oxide [131]. In addition, buffer layers can reduce impurities or carbon migration from the silicon carbide layer during the high-temperature annealing [122].

From the discussion above, it is apparent that integrating silicon carbide into crystalline silicon solar cells is complex, as resolving one issue can lead to another. Increasing the carbon content in the layer broadens the optical band gap, enhancing layer transparency, but this can result in significant band offsets which impede effective charge carrier transport. The effect of an increased carbon content on layer stress and low-temperature passivation capabilities remains uncertain. However, when combined with an additional hydrogenation step, a higher carbon content improves the passivation in high-temperature processing schemes. Moreover, increased carbon content hinders crystallization at high temperatures, necessitating higher annealing temperatures. This impeded crystallization leads to higher absorption in the layer, countering the benefits of a widened band gap with a more amorphous material. Additionally, a higher carbon content boosts the hydrogen content in the layer, enhancing the thermal stability, but it might also dissolve any interfacial silicon oxide as the carbon reacts with oxygen. A thicker layer enhances the passivation but also reduces the current of the solar cell.

The integration of silicon carbide into solar cells is challenging, as balancing the properties of the material is a difficult task. The evolution of the efficiencies of solar cells that feature silicon carbide layers is depicted in figure 2.10. High-temperature solar cells typically use PECVD-grown amorphous silicon carbide, later crystallized to a polycrystalline state and hydrogenated. The initial integration by Glunz et al. employed silicon-rich passivating layers with carbon-rich capping layers at the rear of the PERC structure [143, 159]. Subsequent developments saw silicon layers in TOPCon structures alloyed or doped with carbon

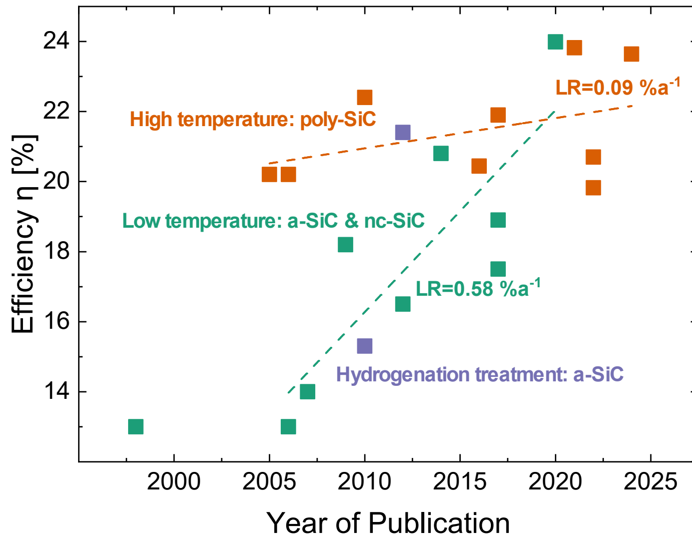

Figure 2.10.: *Evolution of the power conversion efficiency (η) of silicon carbide-based solar cells based on their publication date. High-temperature solar cells mostly employ a plasma-enhanced chemical vapor deposition (PECVD) silicon carbide with a crystalliaztion step and additional hydrogenation, while low-temperature solar cells employ either PECVD or hot wire chemical vapor deposition (HWCVD) to grow amorphous or nanocrystalline silicon carbide. The solar cells marked as 'Hydrogenation treatment' employ a low-temperature approach, but utilize an additional hydrogenation treatment of temperatures around 400 ℃. The learning rate (LR) of the high- and low-temperature approach are given in the graph as well. Efficiency data taken from refs. [29, 89, 116, 117, 119, 120, 127, 128, 130, 131, 134–136, 143, 159–163]*

to improve their thermal stability and address blistering issues in polycrystalline silicon layers, leading to efficiencies of up to 23.82% in 2021, as reported by Lin et al. [89]. Even though starting on a higher efficiency level than the low-temperature approaches, the learning rate (LR) over the years is only at an efficiency improvement of 0.09% per year. In some low-temperature approaches with subsequent hydrogenation techniques, amorphous silicon carbide is used to activate passivation in Al_2O_3, achieving efficiencies up to 21.4%, as demonstrated by Ferre et al. [162]. The low-temperature approach utilizes amorphous or nanocrystalline silicon carbide for the passivating contacts. The prominent TPC approach uses HWCVD-grown near-stoichiometric nanocrystalline silicon carbide for both passivation and contacting, requiring a double layer approach to achieve both qualities, allowing efficiencies up to 23.99% by Köhler et al. [29]. If

only including the publications focussing on solar cell developments, an impressive LR of the efficiency of 0.58% per year has been achieved. Furthermore, another application in solar cells is the use of HWCVD-grown nanocrystalline silicon carbide as a hydrogenation source for polycrystalline silicon, which successfully rehydrogenates polycrystalline silicon after silicon carbide deposition [158].

Both low- and high-temperature methods incorporate a wet-chemically grown silicon oxide layer at the crystalline silicon surface for passivation and protection. However, both approaches report damage to the passivation during the sputter process [29, 134, 137, 153]. In the low-temperature, HWCVD-grown double layer approach, the passivating material exhibits a low conductivity, thus limiting the *FF* of the solar cell and introducing a substantial R_S [29, 113, 164]. Furthermore, a minimum thickness of the conductive silicon carbide layer is required to achieve low contact resistivities [113, 158].

3. Sample Preparation, Characterization, and Simulations

This chapter outlines the methodologies employed in the preparation and characterization of the samples, as well as the simulation tools used in this work. Initially, a detailed description of the substrates utilized is presented. This is followed by an explanation of the deposition technique used to prepare the nc-SiC_X:H using the HWCVD technology. Subsequently, the chapter details the following processing steps and describes the various measurement techniques utilized. Lastly, an introduction to the simulation tools used to analyze the effects of ions and electrons, as discussed in chapter 5, is provided.

3.1. Substrates and Experimental Procedures

This section offers an overview of the sample preparation procedure. It starts with a description of the substrates used, proceeds to detail the HWCVD process for nc-SiC_X:H deposition and finally describes the conditions under which further sample processing was conducted.

3.1.1. Substrates, Wafers, and Wet Chemical Procedures

The experimental samples were prepared using two different types of substrates, c-Si wafers and glass substrates. For the purposes of conductivity and

Ultraviolet/Visible spectroscopy (UV/VIS) measurements, Corning EAGLE XG glass substrates were employed. The glasses were cleaned in an ultrasonic bath using DeContam® at 70 °C for 120 min. Subsequently, the substrates were rinsed with deionized water until a wastewater resistance of 12 MΩ was achieved. Lastly, the substrates were dried in a laminar air flow.

The c-Si wafers designated for Fourier-Transform Infrared Spectroscopy and secondary ion mass spectroscopy analyses were floatzone-grown and exhibit a double-side polished surface. These wafers were either n-type or p-type c-Si with a crystallographic orientation of <111>. They possess a resistivity range between 1-5 Ωcm and were available in thicknesses of either 280 ± 20 µm or 525 ± 20 µm. The wafers used for secondary ion mass spectroscopy (SIMS) measurements are cleaned and oxidized as well, while the wafers for other methods remain untreated.

For Quasy-Steady State Photoconductance (QSSPC), photoluminescent lifetime (PL), and transfer length method (TLM) measurements, as well as for the fabrication of solar cells, Czochralski-grown double-sided textured n-type c-Si wafers were utilized. These textured wafers, supplied by LONGi, were characterized by a <100> crystallographic orientation, a resistivity of 1 Ωcm, and a thickness of 135 µm. Originally, these wafers were of M2(+)-size and were subsequently laser cut into quarters, each measuring 78x78 mm^2.

The initial step in the processing of textured wafers involves a DIO_3 cleaning. For this, the silicon substrates were immersed in a hydrofluoric acid (HF)/hydrochloric acid (HCl) solution containing 15 ppm ozone (O_3) with a following 3 min treatment step with pure HCl solution enriched with 15 ppm O_3. Subsequently, the wafers were treated with a 1% HF solution for 5 min to eliminate any oxide layers formed during the cleaning process. The subsequent step involves immersing the wafers in Piranha acid, a mixture consisting of 2 parts hydrogen peroxide (H_2O_2) and 1 part sulfuric acid (H_2SO_4), for 10 min to facilitate the growth of a defined SiO_X layer of 1-1.5 nm thickness [165]. After the treatment, the samples can be preserved in a nitrogen atmosphere for a duration of up to two months without any discernible impact on their performance.

3.1.2. Deposition of Hydrogenated Nanocrystalline Silicon Carbide

The fabrication of nc-SiC_X:H employs the HWCVD technique, using a custom-built hot wire system developed by MRG. In general, the process involves the use of 5% monomethylsilane (MMS) (CH_6Si) diluted in hydrogen (H_2), further diluted in H_2 gas, supplemented by nitrogen (N_2) as the doping agent. Standard flow rates were set at 70 sccm for H_2, 7 sccm for MMS, and 25 sccm for N_2. When calculating the hydrogen dilution (c_H), the nitrogen flow rate (F_{N2}) was omitted, and c_H was calculated as

$$c_H = \frac{F_{H_2}}{F_{H_2} + F_{MMS}} \tag{3.1}$$

The filament-substrate distance ($d_{f\text{-}s}$) was maintained at 71 mm. The deposition pressure (p_{depo}) was controlled at 0.75 mbar, and the chamber heater temperature (T_{heater}) was set to 250 ℃. The temperature of three rhenium filaments, crucial for the deposition process, was regulated by the current passing through them. As a result of the manual preparation of these filaments, which involves cutting and curling of the filaments, slight variations in deposition conditions were inevitable after each filament replacement. Consequently, the standard deposition parameters were presented as a range, which recognizes these potential deviations. An extensive discussion on filament lifetime is given in appendix A.

For the initial passivating nc-SiC_X:H layer, a filament temperature (T_f) of approximately 1700 ℃, equating to 32 ± 4 A, was utilized. Subsequently, the conducting nc-SiC_X:H layer requires a higher T_f, ranging from 1950 to 2000 ℃, given by a current of 46 ± 2 A. The respective deposition durations for these layers were 4-6 min and 30 min, respectively. Before activating the filaments, a 10-minute stabilization period for both the chamber atmosphere and the heater temperature was introduced. Unless otherwise stated, the adjustment of the filament current was carried out at a rate of $2\,\frac{\text{A}}{\text{s}}$. The resulting silicon carbide layers are expected to have a stoichiometry of approximately $Si_{0.55}C_{0.45}$ [95].

The HWCVD system setup is depicted in figure 3.1, with crucial deposition parameters highlighted for clarity. Once operational, the precursor gases were effectively decomposed by the filaments, facilitating the growth of the film on

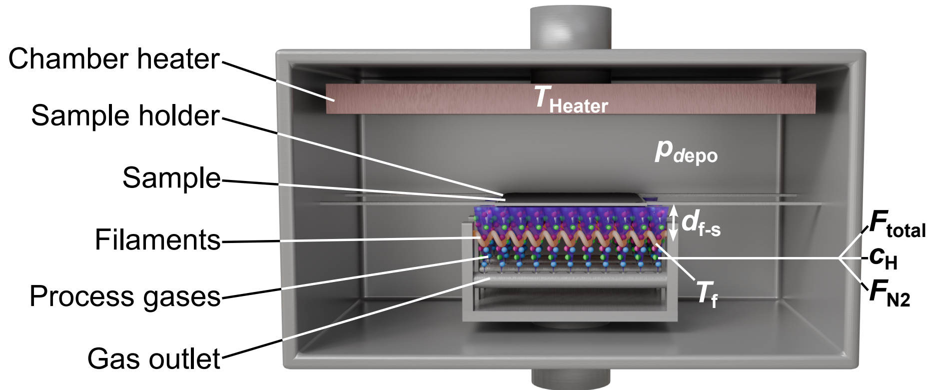

Figure 3.1.: *Illustration of the hot wire chemical vapor deposition (HWCVD) chamber, pinpointing the key deposition parameters in bold.*

the substrate's downward-facing surface. More information on the process of HWCVD can be found in ref. [112].

Specific deposition parameters relevant to the opto-electrical studies discussed in section 4.1.1 are described in table 3.1. Variations within these series are indicated in bold. Unless otherwise specified, the standard process conditions, as previously described, were adhered to. Symmetrical samples and solar cells utilized in chapter 5 stick to the standard conditions described above.

3.1.3. Subsequent Processing Steps

After the wafer and TPC preparation, a full solar cell is produced with the following additional steps.

Formation of the Rear Junction: Given that the oxide layer previously grown was symmetrically applied on both sides of the wafer, it becomes essential to remove the rear oxide. This was achieved through a 10-minute immersion in a 1% HF solution after the nc-SiC_X:H deposition, ensuring no interference with the growth of the a-Si:H layers. The deposition of the a-Si:H layers occurs in a Meyer Burger AK 1000 Inline PECVD reactor. Upon loading the sample into the chamber, it was preheated in a H_2 environment to the needed processing

Table 3.1.: *Overview of the deposition parameter series presented in section 4.1.1. The variation of each series was marked in bold letters.*

Series	F_{MMS} [sccm]	F_{H2} [sccm]	F_{N2} [sccm]	F_{total} [sccm]	T_{heater} [°C]	p_{depo} [mbar]	$d_{f\text{-}s}$ [mm]	I [A]	T_f [°C]
p_{depo}	7	70	25	77	250	**0.5 - 1**	71	49	1995 ± 55
T_f	9	94	30	103	250	0.75	79	**34 - 50**	1670 - 1965
$d_{f\text{-}s}$	9	94	30	103	250	0.75	**69 - 81**	49	1975 ± 13
T_{heater}	7	70	25	77	**200 - 300**	0.75	71	49	1993 ± 66
c_H	**7 - 30**	**70 - 37**	25	77	250	0.75	71	49	1987 ± 7
F_{N2}	9	94	**24 - 39**	103	250	0.75	79	50	1989 ± 5
F_{total}	3 - 13	31.3 - 135.5	10 - 43.3	**34.3 - 148.8**	250	0.75	79	46	1933 ± 4

temperature. The deposition of the intrinsic a-Si:H layer begins with a 2-second power surge at 300 W in the reactor, utilizing flow rates of 145 sccm silane (SiH_4) and 650 sccm H_2. This was followed by a sustained deposition phase with the H_2 flow rate increased to 900 sccm and the reactor power reduced to 50 W. During this phase, SiH_4 flows for the initial 9 seconds, followed by a 20-second H_2 treatment with the SiH_4 off, and then another 9 second cycle SiH_4 on followed by 9 seconds H_2 without SiH_4. For the p-type a-Si:H deposition, the process spans 44 seconds at 80 W, with flow rates of 550 sccm H_2, 50 sccm SiH_4, and 150 sccm 1% diborane (B_2H_6) diluted in H_2 as the doping gas. The chamber pressures were set at 2.7 mbar for the intrinsic a-Si:H and 3.5 mbar for the p-type layer deposition.

Transparent Conductive Oxide Application: Following the PECVD process, a

layer of indium tin oxide (ITO) was sputtered as the TCO in a VISS 300 system by Von Ardenne. Initially, a milder deposition method was employed, which was later substituted with the standard process used for reference solar cells to enhance sample throughput. Both ITO layers, despite the process variations, exhibit comparable opto-electrical characteristics. The ITO thickness was maintained at 70 nm to optimize its anti-reflective properties. The solar cell area was defined by sputtering ITO through a 2x2 cm^2 shadow mask. The deposition processes utilize an ITO 97/3 tube target at a sample-target distance of 8 cm in a vertical system. The softer process uses a power setting of 3.35 kW, a deposition pressure of 15 µbar, a heater temperature of 250 °C, and a target rotation speed of 5.5 $\frac{\text{rounds}}{\text{minute}}$, with gas flow rates of 197 sccm argon and 3 sccm oxygen. The standard process, also applied to the rear side of the solar cell, uses a power of 5 kW, a deposition pressure of 3 µbar, the same heater temperature, and a target rotation speed of 9 $\frac{\text{rounds}}{\text{minute}}$. The last set of samples in this study utilizes ITO from a new horizontal HISS200 system by Von Ardenne. It also employs a 97/3 ITO target. The front contact ITO was sputtered at 1 kW power, 2.5 µbar pressure, and 2.83 $\frac{\text{rounds}}{\text{minute}}$ target rotation speed, with gas flow rates comprising 112 sccm 2.8% hydrogen in argon and 4 sccm oxygen. The rear-side process uses a generator power of 4 kW, 3.5 µbar pressure, 11.33 $\frac{\text{rounds}}{\text{minute}}$ target rotation speed, and gas flow rates of 108 sccm 2.8% hydrogen in argon and 8 sccm oxygen. The solar cells are defined on the wafer by sputtering the ITOs through a shadow mask.

Screen Printing for Metallization: The process of screen printing for silver metallization uses a Micro-tec Co. MT-650TVC printer. The twelve printed fingers, measuring approximately 30 µm in height and 55 µm in width, were contacted through two triangular contact pads adjacent to the cell area. The rear side features 30 fingers with identical contact pads. For this purpose, a low-temperature paste from Kyoto Elex was used. Post-printing on the front side, the paste undergoes a 10-minute drying phase at 150 °C. The rear side was treated similarly, followed by a 40-minute curing at 170 °C. The highest performing cells additionally receive a full-area silver back reflector via sputtering.

Annealing and Heat-Assisted Light Soaking: After the TCO deposition,

the samples are annealed on a Präzitherm TR 28-3 T hot plate at 230 °C in ambient air. Light soaking is done in a GLR-4Z light soaker from Gsolar Power Co., Ltd. The internal hot plate is set to 190 °C, with a process temperature of 175 °C. The light intensity is 55 $\frac{kW}{m^2}$ for a process duration of 180 seconds.

Application of an Anti-Reflective Coating: For the best performing cells, a 120 nm thick layer of magnesium fluoride (MgF_2) was applied as an additional anti-reflective coating. The process was executed using electron beam evaporation in a Leybold system. The contact pads were shielded with tape during the deposition to ensure proper electrical contact during measurements, since MgF_2 acts as an insulator.

3.2. Overview of Characterization Techniques

This section summarizes the characterization methodologies employed in this study and explains the fundamental working principles of each technique.

3.2.1. Opto-Electrical Characterization Methods

Conductivity measurements and spectroscopic analysis are utilized to evaluate electrical and optical properties of the materials studied. If not mentioned otherwise, all measurements described in this subsection are conducted on as-deposited single layers.

Conductivity Measurements: The lateral electrical conductivity of thin films with a known thickness is assessed directly from current-voltage measurements, as described in Ref. [166], using an in-house developed setup. Two coplanar silver electrodes are evaporated onto the layers that were deposited on a glass substrate. The conductivity of these layers was calculated based on several critical dimensions:

- $d_{spacing}$: the distance between the electrodes

- l_{pad}, the length of each electrode
- d, the thickness of the layer under test

The specific resistance ρ of the layer, which is a pivotal parameter in determining the conductivity, was calculated from the current and voltage values recorded during the measurements. These values were interpreted through Ohm's law, enabling the calculation of the resistance R. The subsequent calculation of conductivity takes into account the spatial dimensions of the contact pads and the derived resistance as

$$\sigma = \frac{1}{\rho} = \frac{1}{R}\frac{d_{\text{spacing}}}{l_{\text{pad}}d} = \frac{I}{V}\frac{d_{\text{spacing}}}{l_{\text{pad}}d}. \tag{3.2}$$

While this method is direct and easy to apply, one must also consider unwanted conducting surface channels, like condensed water from the atmosphere, which makes the measurements of low-conductive samples challenging. Additionally, the metal contacts might form junctions with the semiconductor layer under test, leading to extraction barriers and the geometry of the contact pads needs to be precisely known for exact calculations of the layers conductivity. The error of the measured conductivity was estimated to be one order of magnitude from experience.

Ultraviolet/Visible Spectroscopy Analysis: The Ultraviolet/Visible spectroscopy (UV/VIS) was a critical technique used to gather data on the optical properties of the samples, specifically their transmission and reflection characteristics. This information was essential for calculating the absorption coefficients and other related optical parameters. A detailled description can be found in Refs. [167, 168].

The UV/VIS spectroscopic process involves the use of a monochromator to convert polychromatic into monochromatic light. This light was subsequently split into two distinct paths: one directed towards a reference and the other towards the sample. The spectral width of both beams was finely adjusted using a slid.

For the measurement of the transmission (T) and reflection (R), the sample layers on a glass substrate were placed either in front of or inside an Ulbricht

sphere, respectively. In contrast, the reference beam was channelled directly into the sphere. To ensure temporal separation of the beams reaching the detector, a chopper was employed, effectively modulating both beams so that only one beam enters the sphere at any given moment.

The detector inside the Ulbricht sphere quantifies the intensity of the sample beam. This measured intensity was then normalized against the intensity of the reference beam to obtain accurate data. The absorption (A) of the sample was derived using the relation

$$1 = T + R + A. \tag{3.3}$$

Furthermore, the Lambert-Beer law, in conjunction with the known layer thickness d, enables the calculation of the absorption coefficient (α) as

$$\frac{T}{1-R} = e^{-\alpha d}. \tag{3.4}$$

The optical band gap (E_{04}) was subsequently determined as the energy where α equals $10^4\,\text{cm}^{-1}$. An in-depth discussion on the calculation of the absorption coefficient and the method of choice for the optical band gap can be found in chapter C.

For the purposes of this work, the optical analyses were performed using a PerkinElmer Lambda 950 UV/VIS spectrometer. The error in E_{04} was determined by five different R and T measurements each, yielding 25 different combinations for α calculations. The error was then given by the standard deviation of these αs. This was done for an initial sample, and the error was assumed to be constant for all samples. While this technique is quick an non-destructive, the thickness of layers under test need to avoid any interference effects. Additionally, the accuracy of the measurement setup is limited for intermediate and high wavelength, making evaluation challenging.

3.2.2. Microstructural Characterization Methods

In the following, spectroscopic and other characterization methods that were essential to analyse the intricate microstructure of the materials under study. If

not stated otherwise, all characterisation methods are applied on as-deposited single layer. SIMS measurements are conducted as-deposited single layers or layer stacks, as marked accordingly.

Fourier-Transform Infrared Spectroscopy: Fourier-Transform Infrared Spectroscopy (FTIR) stands as a crucial tool to quickly identify the structural attributes of the materials analysed. This technique uses the interaction of infrared radiation with dipolar bonds within the material, causing them to absorb the radiation at distinct resonance frequencies [169]. This interaction leads to various molecular vibrations, such as stretching, rocking, and wagging, each characterized by unique absorption energies specific to the bond. Further information can, for example, be found in Ref. [170].

The absorption spectra collected by FTIR provide helpful information on the microstructure of the material. For example, the width of a peak in the spectrum can be an indication for the atomic disorder in the material. This was because a more disordered material typically exhibits a wider range of bond lengths, thereby broadening the absorbed energy spectrum. To ensure the accuracy of the spectral data, background noise and the absorbance due to the crystalline silicon wafer were mitigated through preliminary background measurements on a bare silicon wafer.

The normalization of the background-corrected spectrum to the thickness of the layer, as defined by Langford et al. [171], yields the FTIR absorption coefficient. This study employed a Thermo Fisher Scientific Nicolet 5700 FTIR spectrometer, operating within a nitrogen atmosphere. The spectrometer scans wavenumbers ranging from ν = 400 cm^{-1} to 4000 cm^{-1} in transmission mode, using a Michelson interferometer.

The methodology involves a polychromatic light source emitting onto a beam splitter, which divides and directs the light towards both a stationary and a moving mirror. The reflected beams recombine at the beam splitter, leading to constructive or destructive interference that depends on the position of the moving mirror. The interfered beam, after interacting with the sample, was then relayed to a detector. This setup allows for the acquisition of spectral data across all

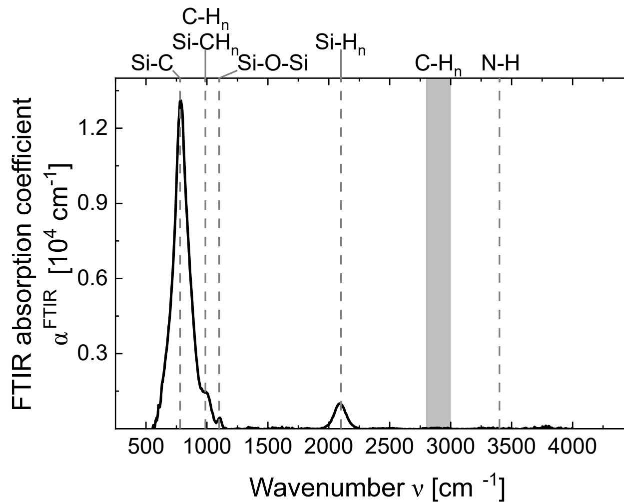

Figure 3.2.: *Exemplary FTIR spectrum of a hydrogen-rich nc-SiC$_X$:H. The peak positions were identified according to values given in literature. [170, 173–175]*

wavelengths simultaneously. The Fourier transformation of the signal against the mirror position provides an intensity spectrum as a function of wavenumbers. The spectrum of the sample was normalized against a prerecorded background spectrum to negate the influences of the crystalline silicon wafer and ambient conditions.

An exemplary absorption spectrum of nc-SiC$_X$:H is shown in figure 3.2. The silicon-carbon peak typically manifests at wavenumbers around ν = 780 cm^{-1}, while the excitation of the silicon-hydrogen bond occurs at about ν = 2100 cm^{-1}. The presence of carbon alters the peak position of the Si-H bond compared to a-Si:H, shifting it to higher wavenumbers. The extent of this shift was dependent on the specific bonding configurations. [172] Additional peaks were visible at ν = 987 cm^{-1} for either silicon-hydrocarbon or carbon-hydrogen bonds and at ν = 1100 cm^{-1} for silicon-oxygen bonds. The carbon-hydrogen peak, generally observed between ν = 2800-3000 cm^{-1}, merges with the background for all the samples in this study. Notably, no nitrogen-hydrogen bond peaks around ν = 3400 cm^{-1} were detected, suggesting that all dopant atoms were seamlessly integrated into the SiC matrix without forming NH$_X$ clusters. [170, 173–175]

The error in the integrated peak values given later on was determined by

the error in the data fit.

Profilometry Analysis: Profilometry is a technique similar to atomic force microscop, as described in Ref. [176]. A delicate needle is placed in contact with the surface of the sample. The force exerted on the needle was regulated to maintain a consistent contact pressure throughout the measurement, ensuring precise thickness readings.

In the preliminary stages of the experiments, before the establishment of an ellipsometry model, thickness measurements to determine layer thickness (*d*) on glass and polished crystalline silicon wafers were carried out using a Veeco DEKTAK 6M Stylus Profiler. In the process, the substrate is marked with dots using a permanent marker before the nc-SiC_X:H deposition, which were subsequently removed with isopropanol post-deposition. The film thickness was determined by conducting a line scan at the periphery of these marked areas and measuring the height discrepancy at the edge of the dot.

The layer thickness error was determined by the standard deviation obtained from three different measurement points.

Spectroscopic Ellipsometry: Spectral ellipsometry (SE) serves as a non-intrusive technique to determine various parameters such as *d*, the refractive index (*n*), and extincition coefficient (*k*). Key components of this technique include a light source and a polarizer to polarize the incident light. This light then interacts with the sample, changing its phase and polarization, and the polarization of either the reflected or transmitted is measured by an analyzer, while the intensity is measured by a detector.

The altered polarization of the reflected light was analyzed to deduce the amplitude ratio Ψ and the phase difference Δ that it experienced during its interaction with the sample. An effective medium approximation model based on an in-house developed model of hydrogenated amorphous silicon and a 4H-SiC model supplied by the software is used to fit the measurement data and parameters such as film thickness and optical properties can be accurately extracted. In this study, substrate models integrated into the ellipsometers software, designed for

either corning glass or crystalline silicon, were employed. To accurately represent nc-SiC_X:H, a dual-material model, incorporating both models for a-Si:H and 3C-SiC supplied by the software, was calibrated against samples with known thicknesses determined by profilometry. More information on SE can be found in Ref. [177].

The spectroscopic ellipsometer utilized in this research was a J. A. Woollam M-2000. The layer thickness error was determined by the standard deviation obtained from three different measurement points.

Secondary Ion Mass Spectroscopy: SIMS measurements were critical for acquiring depth profiles of elements within the layer and were carried out on polished crystalline silicon wafers, as described in Ref. [178]. This technique involves bombarding the sample with cesium ions (Cs^+), which sputter the layer under test and release secondary ions. These ions, accelerated by an electric field, exhibit velocities corresponding to their mass-to-charge ratio. The time taken by these ions to traverse a predefined distance to the detector was precisely measured, allowing for the identification of the ions on the basis of their flight time and other experimental parameters. The different layers in the layer stack were identified by the hydrogen signal, which accumulates in the silicon oxide [29].

These measurements were carried out at the central institute for engineering and analysis 3 (ZEA-3) at Forschungszentrum Jülich, using a ToF-SIMS 5.NCS from IonTof GmbH. The operational parameters include a 1 kV acceleration voltage for Cs^+ ions, a sputter raster of 300 µm x 300 µm, and a sputter current of 87.4 nA, within a chamber pressure of 1.5×10^{-9} mbar.

Effusion Measurements: Effusion measurements were executed using an in-house developed system. The sample was placed inside a quartz glass tube under vacuum conditions. Then it was uniformly heated at a rate of 20 °C per minute. A vacuum pump channels the effusing gases to a quadrupole mass spectrometer, which performs an analysis of the effusing gas species. On the basis of the known elements in the layers and their respective masses,

the effusion profiles of specific elements or compounds were identified across varying sample temperatures. Furthermore, the effusion rates measured can be normalized to the actual atomic contents using a reference sample, thus providing a more detailed understanding of the composition of the material and its properties.

Raman Spectroscopy: The Raman effect, based on the inelastic scattering of light by matter, was first observed by C. Raman [179]. As described in Ref. [180], a monochromatic light source like a laser is directed at a sample. Most photons undergo elastic (Rayleigh) scattering, while a small fraction experience inelastic (Raman) scattering. Here, the energy of scattered photons change due to interactions with molecular vibrations or other excitations. The scattered light is analyzed by a spectrometer, yielding the intensity of light as a function of its frequency shift.

During Raman scattering, a laser photon, characterized by a specific frequency (ω), interacts with the lattice. In elastic Rayleigh scattering, no energy transfer occurs, and the ω of the incident photon resembles that of the outgoing photon. However, in inelastic scattering, energy transfer results in a Stokes or anti-Stokes shift in the frequency of the emitted photon. The absorption of a laser photon generates an electron/hole pair, which, through electron-phonon interactions, produces or annihilates a phonon and alters the energy of the electron or hole. The recombination of this electron/hole pair leads to the emission of a photon, shifted in frequency by the transferred energy. If a phonon was created and the energy of the emitted photon is reduced, it was termed a Stokes shift, while its annihilation and thus the energy increase results in an anti-Stokes shift. [32]

This work used a laser with a 532 nm excitation wavelength and a Renishaw inVia Radar spectrometer in a backscattering configuration. Due to the wavelength of the laser and the photon absorption length of the material under investigation, a prominent peak of the crystalline silicon substrate was observed at wavenumber (ν)= 516 cm^{-1} [181]. Furthermore, ambient nitrogen results in a peak at ν= 2330 cm^{-1} since measurements were carried out in an ambient

atmosphere [182].

3.2.3. Passivation and Solar Cell Characterization

This subsection details the methods used to evaluate the passivation quality of symmetric TPC samples and solar cell precursors, and the optical and electrical characteristics of complete solar cells. QSSPC measurements are conducted after both sides of the wafer are passivated, i.e. after both HWCVD and PECVD depositions in a solar cell precursors, but before an TCO is sputtered. In chapter 5, QSSPC measurements might be obtained after a full-area TCO is applied. The same procedure holds true for PL imaging. TLM and various solar cell parameters are gathered from the fully processed solar cells.

Quasi Steady-State Photoconductance Method: The Quasy-Steady State Photoconductance (QSSPC) method provides an efficient, non-contact approach for measuring preliminary data on solar cell precursors related to its passivation [36, 183]. This technique enables the determination of parameters such as the effective minority carrier lifetime (τ_{eff}) dependent on the excess charge carrier concentration (Δn), the iV_{OC}, and the J_0. As this method does not need external contacts, these values can be tracked after different processing steps such as PECVD or sputter processing.

In steady-state conditions, the J_{gen} equals the current density from charge carrier recombination (J_{rec}), which can be calculated from Δn, q and the thickness of the silicon wafer (W). This relationship is given as

$$J_{gen} = J_{rec} = \Delta n q \frac{W}{\tau_{eff}}. \tag{3.5}$$

Δn can be derived from the photoconductance (σ_L), incorporating the excess electron and hole carrier densities (Δn_e and Δp, respectively) and their respective mobilities (μ_n and μ_p), as

$$\sigma_L = q(\Delta n_e \mu_n + \Delta p \mu_p) W, \tag{3.6}$$

which, taking the conservation of charge $\Delta n_e = \Delta p = \Delta n$ into account, leads to

$$\sigma_L = q(\mu_n + \mu_p)\Delta n W. \tag{3.7}$$

For many semiconductors, and crystalline silicon especially, the charge carrier mobilities are very well known for varying dopant densities and injection levels [184, 185]. Equation (3.7) can be iterated to find both Δn_e and $(\mu_n + \mu_p)$ which are consistent with the measured σ_L. Therefore, this technique is nearly directly a method to probe the excess charge carrier density.

With equation (3.5) and equation (3.7), τ_{eff} was then determined as

$$\tau_{eff} = \frac{\sigma_L}{J_{gen}(\mu_n + \mu_p).} \tag{3.8}$$

J_{gen} and σ_L can be measured by using a reference solar cell or photodiode and a calibrated device, respectively.

As a general expression not only relying on the steady-state, the change in Δn with time (t) can be expressed as

$$\frac{\mathrm{d}}{\mathrm{d}t}\Delta n(t) = G(t) - U(t) = G(t) - \frac{\Delta n(t)}{\tau_{eff}}, \tag{3.9}$$

where G is the generation and U is the recombination rate of charge carriers. From here, τ_{eff} can be expressed as

$$\tau_{eff}(\Delta n) = \frac{\Delta n(t)}{G(t) - \frac{d\Delta n(t)}{dt}}. \tag{3.10}$$

Photoconductance measurements can be performed in quasi steady-state mode or transient mode, which were both utilized in this work depending on the calculated τ_{eff}. The conditions of transience or quasi steady-state depend on the duration of the light pulse (τ_{pulse}) in relation to τ_{eff}. For transient conditions with τ_{eff} significantly greater than τ_{pulse}, $G = 0$ is true and a simplified version of equation (3.10) applies as

$$\tau_{eff}(\Delta n) = -\frac{\Delta n(t)}{\frac{d\Delta n(t)}{dt}}. \tag{3.11}$$

Conversely, for quasi steady-state conditions with τ_{eff} much smaller than τ_{pulse}, a different simplification arises with $\frac{d}{dt}\Delta n = 0$ as

$$\tau_{eff}(\Delta n) = \frac{\Delta n(t)}{G(t)}. \tag{3.12}$$

With generation rates determined from reference solar cells or photodiodes, an accurate determination of τ_{eff} over a wide range was possible. In this work, τ_{eff} was evaluated at $\Delta n = 1x10^{15}\,cm^{-3}$.

Another valuable insight from the QSSPC method is the iV_{OC}, which sets an upper boundary for the final voltage of the device limited by the quasi-Fermi level splitting of electrons and holes. This parameter can mathematically be expressed as

$$iV_{OC} = \frac{k_B T}{q} \ln(\frac{\Delta n(\Delta n + N_\circ)}{n_i^2}), \tag{3.13}$$

where $N_\circ$ denotes the doping concentration in the silicon wafer, either as N_A for acceptor doping in p-type wafers or N_D for donor doping in n-type wafers. Equation (3.13) holds true across various doping concentrations and injection levels of the sample, in contrast to the expression for τ_{eff}, which might be ambiguous due to alterations in device physics at different injection levels.

It is critical to note that iV_{OC} is not a real voltage, as a voltage is defined as the potential difference between two contacts. QSSPC measurements do not need any contacts and, therefore, the iV_{OC} is not a voltage in a stricter sense. It can rather be understood as difference between the chemical potentials of electrons and holes, as defined by their respective quasi-Fermi levels.

Furthermore, the J_0, a critical metric for assessing the passivation quality of the wafer and a component of the selectivity definition in equation (2.20), was derived from the slope of the linear segment of the inverse lifetime curve. This relationship was established as

$$J_0 = \frac{1}{2} q W n_i^2 \frac{d}{d\Delta n} \frac{1}{\tau_{corr}}, \tag{3.14}$$

with the Auger-corrected lifetime (τ_{corr}) defined as

$$\frac{1}{\tau_{corr}} = \frac{1}{\tau_{eff}} - \frac{1}{\tau_{Auger}} - \frac{1}{\tau_{SRH}}. \tag{3.15}$$

In these equations, τ_{Auger} and τ_{SRH} denote the lifetimes associated with Auger and Shockley-Read-Hall recombination processes, respectively. [186] The determination of J_0 was done at $\Delta n = 5x10^{15}$ cm^{-3} in this work.

In the Sinton WTC-120 set-up employed for this study, a coil, part of a bridge circuit linked to a Medium Frequency (MF) generator, was inductively coupled to the silicon wafer under test. The resulting signal was analyzed through specialized software. The light intensity was determined by a calibrated reference solar cell adjacent to the test sample. Using this light intensity and the known J_{gen} from the reference, along with the wafer thickness and its optical constant, the software estimates the J_{gen} for the silicon wafer under test. The signal of the inductively coupled coil, which measures the σ_L of the sample, was adjusted for any baseline conductivity. From this signal, Δn was calculated and τ_{eff} and iV_{OC} were determined, as described above.

Due to the long duration of the light pulse relative to the τ_{eff} of the sample, a wide range of illumination levels can be assessed simultaneously without inducing temperature changes in the sample. This prolonged light pulse ensures that the sample remains in a quasi steady-state. The software iteratively determines the mobilities of electrons and holes to obtain self-consistent values for mobilities and Δns.

Key inputs for the software include the thickness of the silicon wafer, its doping concentration, and optical constant, all of which significantly influence the aforementioned calculations. While the wafer thickness and doping concentration were typically straightforward to determine or were provided by the manufacturer, the optical constant integrates effects from front-surface reflection, light-trapping features, the illumination spectrum, and potential parasitic absorption by any front contact layers. Consequently, any additional layer applied on the silicon wafer requires a specific optical constant, which was not always determined in this study due to time constraints, potentially leading to minor discrepancies between

measured and actual values. Moreover, the integration of a TCO, serving as an anti-reflective coating and parasitically absorbing light, alters the optical constant and introduces an extra conductance, possibly detectable by the coupled coil. At the time of writing this thesis, no literature explicitly discusses the impact of this additional conductance. It was plausible that the elevated charge carrier concentrations in the TCO might modulate the space charge region of the sample, potentially causing an overestimation of the lifetime, similar to Depletion Region Modulation effects [187]. Similarly, effects such as the trapping of minority carriers at defect sites, such as grain boundaries in multicrystalline silicon wafers, could artificially increase majority charge carriers, potentially leading to an overestimation of τ_{eff} at low Δn levels.

The error associated with iV_{OC} was determined as the standard deviation of ten prepared samples, with this error value then being presumed consistent for all subsequent sample preparations and measurements. No additional error was factored in for samples with an applied TCO. More details on the determination of τ_{eff} and iV_{OC} are available in the documentation of the WTC-120 lifetime tester [187] and in refs. [36, 183].

Transfer Length Method: The transfer length method (TLM) can be employed to determine the contact resistivity (ρ_c) in solar cell contact structures [188, 189]. This method involves screen printing eight silver contact pads onto a similar ITO structure, with varying distances between them. The contact pads have a width (W) of 1 cm, a length (L) of 0.2 cm and spacings between 0.5 mm and 1.1 mm with a step size of 0.1 mm. To measure ρ_c through the whole contact stack, the ITO area is confined to beneath the silver contact pads with gaps between each contact pad. The test structure was then subjected to the standard preparation steps used in the fabrication of full solar cells. Given that c-Si possesses the highest conductivity among the layers as the metal contacts and ITO has a gap between pads and the utilized contact layers show low lateral conductivity compared to c-Si, a significant portion of the current flows from one contact pad through the entire front layer stack and c-Si, reaching the opposite contact pad and is extracted after passing the contact layers, ITO and metal contact. For

each measurement between contact pads, the total resistance is then given by

$$R = 2R_c + \rho_{Si} d_{contact}, \tag{3.16}$$

where $d_{contact}$ is the distance between the two contact pads and R_c being the contact resistance.

By applying a voltage between two neighbouring contact pads and measuring the IV-curve, R can be determined through a linear fit for varying $d_{contact}$, the data can then be extrapolated to $d_{contact} = 0$, yielding only the contribution of the vertical resistance of passing the contact stack twice, $2R_c$. This depends on the vertical resistance of each different layers, and the contact resistance between each layer, the layers and the crystalline silicon bulk and the layers to the metal contacts. The length at a resistance of $0\,\Omega$ is the called transfer length (L_T) and is defined as $L_T = \sqrt{\rho_c / R_{sh}}$, where R_{sh} is the sheet resistance of the wafer. With this, the contact resistivity ρ_c can be calculated as [190]

$$\rho_c = R_c L_T W coth(\frac{L}{L_T}) \approx R_c L_T W. \tag{3.17}$$

The resistance was determined through a four-point probe current-voltage measurement conducted between the differently spaced contact pads. In this work, an in-house developed setup was used. Potential errors during the measurement arise at in reality, some fraction of the current might flow though the non-structured contact layers, even though their conductivity is low. Additionally, for the ideal conditions, the measurement area is cut from the c-Si wafer to avoid current flowing outside the contact pad area. Therefore, the error was assumed to be 15%.

Photoluminescence Lifetime: Luminescence measurements are a flexible method to gain spatially resolved information about charge carrier recombination in silicon wafers. Charge carriers can be either injected (electroluminescence, as discussed in the next section) or photo-generated (as discussed in this section). A general description of electro- and photoluminescence developed by U. Rau can be found in ref. [191]. In this work, samples are in open-circuit conditions,

meaning that all injected charge carriers need to recombine. For the fraction recombining radiatively, a photoluminescent lifetime (PL) signal can be detected by a camera. Radiative recombination in silicon is, as previously discussed, a non-dominant recombination mechanism due to the silicon's indirect band gap, preferring non-radiative recombination channels. Therefore, a high radiative PL intensity signals low non-radiative recombination channels, which is desired.

PL measurements can be conducted in a quasi steady-state [192] or dynamic [193–195] conditions. The dynamic measurements, which are used in this work, allow to obtain minority charge carrier lifetimes without calibration to the light intensity. In this approach, four images are captured at different times, as shown in figure 3.3. The first image (*im1*) was captured as the light was activated and records the charge carrier concentration during the rise time ($\Delta n_{\mathrm{rise}}(t)$), the second (*im2*) during steady-state capturing steady-state conditions, the third (*im3*) as the light was deactivated depending of decreasing charge carrier concentration ($\Delta n_{\mathrm{fall}}(t)$), and the fourth (*im4*) in complete darkness giving the background. This gives the PL intensity parameter (I_{PL}) as

$$I_{\mathrm{PL}} = \frac{im2 - im4}{im1 - im3}. \tag{3.18}$$

Here, I_{PL} is proportional to $\Delta n_{\mathrm{e}}(\Delta n_{\mathrm{e}} + N_{\mathrm{D}})$ [196] and the excess charge carrier density is time-dependent, based on the continuity equation equation (3.10) [193]. For the simulations of the PL signals in im_1 to im_4, the quadratic dependence of the PL signals on Δn_{e} and the solution of equation (3.10) for Δn_{rise} and Δn_{fall} need to be considered:

$$\begin{aligned} I_{\mathrm{PL}} &= \frac{\int_0^{t_{\mathrm{int}}} \Delta n_{\mathrm{rise}}(\Delta n_{\mathrm{rise}} + N_{\mathrm{D}})\mathrm{d}t - \int_0^{t_{\mathrm{int}}} \Delta n_{\mathrm{fall}}(\Delta n_{\mathrm{fall}} + N_{\mathrm{D}})\mathrm{d}t}{\int_0^{t_{\mathrm{int}}+t_{\mathrm{stat}}} \Delta n_{\mathrm{rise}}(\Delta n_{\mathrm{rise}} + N_{\mathrm{D}})\mathrm{d}t} \\ &= \frac{t_{\mathrm{int}} + 2\tau_{\mathrm{eff}} \exp(-\frac{t_{\mathrm{int}}}{\tau_{\mathrm{eff}}}) - 2\tau_{\mathrm{eff}}}{t_{\mathrm{int}}}, \end{aligned} \tag{3.19}$$

where t_{int} denotes the time interval used for integration of the signal and t_{stat} the time at which the steady-state image $im2$ is captured. [195] This gives a direct relation between the measured I_{PL} and τ_{eff}.

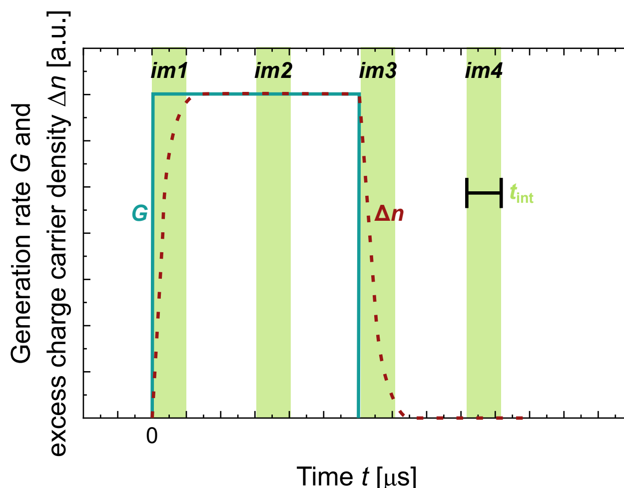

Figure 3.3.: *Generation rate (G) and excess charge carrier concentration (Δn) during the illumination flash in a PL imaging setup. The time points for image capture were indicated, with broader marks denoting the integration of the image signal over time.*

For this study, an in-house build setup was used, featuring LED arrays for a sample illumination over 200 ms, with a 1-second break. The PL emissions were recorded using a Xenics Cheetah 640-CL InGaAs camera. To enhance the signal-to-noise ratio, 460 images were combined for the final image. Additionally, the PL lifetime images are calibrated to the lifetime as measured by QSSPC. The pixel values in the measurement area of QSSPC measurements are averaged and normalized to the QSSPC lifetime. The resulting factor is then applied to the whole PL lifetime image, making the images directly comparable to the τ_{eff} values as given by QSSPC.

Solar Simulator: The solar simulator plays a vital role in evaluating the performance of fully processed solar cells by providing key parameters such as η, J_{SC}, V_{OC}, FF, pseudo Fill Factor (pFF), and R_S.

Current-Voltage Characterization: In the standard measurement procedure, multiple IV sweeps with identical spectra at 25 °C are conducted. These include IV scans in dark conditions and under 1-sun illumination, as well as at illumination

levels of 0.8- and 1.2-suns (multi-light *IV*) and a short-circuit current (I_{SC})-V_{OC} curve. The latter comprises two distinct sweeps: The first measures I_{SC} under varying light intensities, while the second performs the same for the V_{OC}. The data from both sweeps, correlated by light intensities, yields a quasi-R_S-free *IV*-curve. No spectral mismatch correction is applied.

To derive parameters such as η, J_{SC}, V_{OC}, and *FF*, an *IV* sweep under standard 1-sun illumination at 25 ℃ conditions was conducted. The individual parameters can subsequently be directly derived from the *IV* curve as described in section 2.1. To facilitate comparisons between different solar cell structures, the current is normalized to the area of the solar cell, yielding the current density of the solar cell.

R_S can be derived from the dark *IV* curves by examining the bending of the semi-logarithmic curve and fitting it with the one-diode model presented in equation (2.6). This fit subsequently also yields R_{sh} [197, 198]. In the multi-light method, a point on the *IV* curve with a fixed distance in current is selected. If the solar cell adheres to a simple exponential law and the saturation current is independent of the cell voltage, the connecting line of the chosen points should form a straight line, from which R_S can be derived based on its slope [199]. The dark *IV* curve eliminates any influence from the photogenerated current, while the multi-light method determines the resistances as a function of the current, which is more representative of actual solar cell behavior and the method of choice in this thesis. Another method to determine R_S involves combining the 1-sun *IV*-curve with the I_{SC}-V_{OC} curve, from which R_S can be derived as the voltage shift between both curves. R_{sh} can again be derived by fitting the curve data, but in this case, the impact of R_S can be disregarded, thereby reducing the fitting parameters. [197, 200] The I_{SC}-V_{OC} curve additionally provides the p*FF*, which represents the upper limit of *FF* when $R_S = 0$.

Spectral Response of Solar Cells: Determining the spectral response of solar cells, such as external quantum efficiency (*EQE*) or reflection, provides detailed insights into the behavior of the solar cell under different wavelengths of illumination. This analysis can offer into different losses within the solar cell.

External Quantum Efficiency: The *EQE* quantifies the proportion of charge carriers collected per incident photon. To get the *EQE* of the device under test, the short-circuit (SC) response under monochromatic light is determined for each wavelength and compared to the known *EQE* and measured short-circuit response of a reference device, normalized to the signal of a monitor device during both device under test and reference measurements to avoid any impact of small light fluctuations during measurements. Mathematically, this is calculated as [201]

$$EQE_{\text{sample}}(\lambda) = EQE_{\text{ref}}(\lambda)\frac{S_{\text{SC, sample}}(\lambda)}{S_{\text{SC, ref}}(\lambda)}\frac{S_{\text{mon, ref}}(\lambda)}{S_{\text{mon, sample}}(\lambda)}. \tag{3.20}$$

Here, EQE_{sample} denotes the desired *EQE* of the device under test, EQE_{ref} represents the known *EQE* of the reference device, $S_{\text{SC, sample}}$ and $S_{\text{SC, ref}}$ describe the short-circuit responses of the device under test and reference device, respectively, and $S_{\text{mon, ref}}$ and $S_{\text{mon, sample}}$ the signal of the monitor device during reference device and device under test measurements, respectively.

Reflection Measurement: *R* was measured by scanning the specified wavelength range with a monochromatic light beam, and the reflected light was captured in an integrating sphere. The reflectance, including the calibration, is subsequently determined as[201]

$$R = (R_{99} - R_0)\frac{S - S_0}{S_{99} - S_0}\frac{1}{M_{\text{R}}}. \tag{3.21}$$

R_{99} and R_0 represent the given 99% reflectance standard and dark reference, respectively. S denotes the measured sample signal, S_{99} and S_0 indicate the measured 99% reflectance standard and measured dark reference, respectively, and M_R represents the correction factor for the average sphere reflectance.

Internal Quantum Efficiency: From the *EQE* and *R*, the internal quantum efficiency (*IQE*), which signifies the charge carrier collection efficiency per absorbed photon, can be deduced as

$$IQE = \frac{EQE}{1 - R}. \tag{3.22}$$

The *IQE* offers vital information regarding the charge carrier extraction and passivation quality of the solar cell.

The solar simulator employed in this research was a class AAA LOANA sun simulator from pv-tools, coupled with a wavelabs Sinus 220 LED light source. The temperature of the solar cell was regulated, and the light intensity was calibrated using a known reference solar cell to ensure adherence to standard testing conditions. For *EQE* and *R* measurements, monochromized xenon and tungsten lamps were utilized. To obtain a spatially averaged signal and maintain adequate signal intensity, a measurement spot size of 20x20 mm^2 was employed. This inevitably incorporated parts of the contact finger metallization, increasing *R* and reducing *EQE* due to inactive area beneath the metallization. To minimize measurement error, a consistent number of contact fingers was illuminated across all measurements.

3.3. Simulation of Particle Impacts on Thin Films

This section details the simulation tools utilized in this study and explains the ion, electron, and material conditions given as input parameters.

3.3.1. Stopping and Range of Ions in Matter

Stopping and Range of Ions in Matter (SRIM), a Monte Carlo simulation software, was capable of modeling the interactions of ion bombardment with various materials. It enables the customization of incident ions by element, atomic mass, energy, and angle of incidence. In this study, oxygen (O), indium (In), tin (Sn) and argon (Ar) ions were primarily used with incident energies of 270 eV, correlating with the target voltage of 270 V, and a direct 0°-angle approach.

The targeted layers in the simulations were a composite stack comprising 30 nm silicon carbide, 1 nm silicon dioxide, and 135 μm crystalline silicon. A stoichiometric silicon carbide with 13at% hydrogen content was assumed. Given that SRIM considers layers to be amorphous, the crystallinity was mimicked through

density variations; 3.21 $\frac{g}{cm^3}$ for crystalline silicon carbide [202] and 2.4 $\frac{g}{cm^3}$ for the amorphous counterpart [203], with an assumed linear correlation inbetween. A crystalline volume fraction (X_C) of 80%, with an assumed density of 3.04 $\frac{g}{cm^3}$ was the standard SiC material, unless otherwise specified. For silicon dioxide, stoichiometric Si_1O_2 with a density of 2.65 $\frac{g}{cm^3}$ [204] was assumed. In these simulations, the crystalline silicon was pure silicon with a density of 2.32 $\frac{g}{cm^3}$ [205].

To maintain computational efficiency, the number of simulated ions was limited to 50000, yielding results comparable to those from simulations with 5000000 ions but with marginally deeper ion penetration for more simulated ions. SRIM outputs include the depth profile of ion implantation, with d_{max} indicating the maximum penetration depth found in the layer. The simulations also provides details on energy losses to the target material's electrons (ionization), lattice vibrations (phonons), and vacancy generation, additionally giving the depth dependence of these events. A vacancy was generated if the collision of the incident ion transfers more energy than the lattice displacement energy specified in the layer material. If less energy was transferred, the energy was lost to phonons as the layer atom cannot leave its site. The energy loss to the electrons was calculated by the interaction of the impinging ion with the electrons of the target layer. The displacement energy and other parameters were kept at the program's default settings because of the unavailability of specific values for most materials. More information on SRIM can be found in Ref. [206]. To limit the computation time for simulations, the simple Kinchi-Pease damage model was chosen. A discussion on the influence of the damage model on the results can be found in chapter B.

3.3.2. Monte Carlo Simulation of Electron Trajectory in Solid

Monte Carlo Simulation of Electron Trajectory in Solid (CASINO) v3.3 was a Monte Carlo simulation tool designed to analyze electron beam interactions within solid samples. The layer properties mirror those used in the SRIM simulations. Here, the focus was on a 270 eV electron beam incident at a 0°-angle, with secondary electron generation activated. Default settings were used for most parameters. Further information on CASINO can be found in Refs. [207–210].

4. Nanocrystalline Silicon Carbide in Transparent Passivating Contact Solar Cells

The development of transparent passivating contacts (TPCs) stands as a novel alternative to traditional a-Si:H-based silicon heterojunctions as the front contact of crystalline silicon solar cells. The improvements from TPCs are mainly driven by the superior transparency, excellent passivating quality, and high conductivity of n-type nc-SiC_X:H(n). This approach effectively addresses the challenge of parasitic absorption losses that significantly decrease the J_{SC} in SHJ solar cells [211, 212], particularly within the a-Si:H layers. To increase the performance of nc-SiC_X:H(n) materials in TPC solar cells, a deeper understanding of the deposition process and its impact on the optical and electrical properties of the material, as well as microstructural properties, is essential. This chapter aims to undertake a thorough re-examination of the nc-SiC_X:H(n) material properties with a device-level quality. Furthermore, this chapter delves into the behavior of different nc-SiC_X:H(n) layers within the transparent passivating contact structure, highlighting the constraints of the current double layer structure, and proposing new strategies to overcome these challenges.

Results from this chapter contained in section 4.1.1 and section 4.2 are featured in a peer-reviewed publication [113]. The findings from section 4.3 are published in [213].

4.1. Single Layer Characterization of Nanocrystalline Silicon Carbide

In this work, nc-SiC_X:H(n) is used as single layer or light-facing contact in crystalline silicon solar cells. Therefore, the optical and electrical properties of the material are of significant importance. Therefore, this section analyzes the impacts of deposition conditions during the HWCVD deposition on the electrical and optical performance of the material, as well as its passivating capabilities. Furthermore, different growth mechanisms and their impact on layer properties are discussed.

4.1.1. Effect of Deposition Conditions on Opto-Electrical Properties and Layer Growth Mechanisms

An essential aspect of this investigation is to show the connection between the electrical conductivity (σ) and various deposition parameters, as illustrated in figure 4.1. This is done using well-known correlations between the microstructural properties of the material and its σ [95]. The most significant variations in conductivity, which span nine orders of magnitude, are observed in response to changes in the filament temperature (T_f) and hydrogen dilution (c_H). Following this, the total gas flow rate (F_{total}) emerges as the third critical parameter, influencing the conductivity by more than five orders of magnitude, with a notable decrease in conductivity observed at very low flow rates. The F_{N2} demonstrates a relatively modest impact, altering conductivity within one order of magnitude, while the deposition pressure (p_{depo}), filament-substrate distance ($d_{f\text{-}s}$), and chamber heater temperature (T_{heater}) appear to have minimal effects within the examined range. The observed decrease in conductivity at low F_{total} is attributed to a reduced layer thickness. Since the deposition time remains constant across all experiments, the layer thickness is reduced with decreasing flow rates, as the deposition rate decreases. However, a certain minimal thickness is necessary to maintain a constant conductivity, below which the conductivity decreases [95]. It is anticipated that increasing the layer thickness would further enhance the conductivity,

particularly at lower flow rates, following the trend previously observed for higher F_{total}. The T_f and c_H are expected to significantly increase the grain size in the nc-SiC$_X$:H(n), leading to an increase in the conductivity [95, 111]. The flow rate of the dopant gas N_2 yields a minor influence within the tested range. Due to the applied T_fs, it is assumed that the dopant activation is high [111]. Doping in silicon carbide, whether with nitrogen, oxygen, or boron, typically yields reduced crystallite sizes [95, 97]. As a result, the increased doping gas flow could reduce the grain size and introduce impurities, potentially counterbalancing the benefits of increased charge carrier concentration, as indicated by the minor increase in conductivity observed with increased F_{N2}. In contrast, $d_{f\text{-}s}$, p_{depo}, and T_{heater} do not appear to significantly influence the conductivity, and thus crystallite size, within the parameter range investigated. However, it is worth noting that the conductivity might be nearing saturation, thereby rendering changes undetectable and thus overshadowing the effect of these deposition parameter variations.

In addition to electrical characteristics, the optical properties of the material are equally important. Figure 4.2 shows the optical band gap (E_{04}) as a function of conductivity for the series of the presented deposition parameters. A trend of increasing E_{04} is observed with increasing σ, suggesting that nc-SiC$_X$:H(n) gains transparency as conductivity improves. This attribute is particularly advantageous for solar cell applications, where both transparency and conductivity are crucial. However, it is also anticipated that parasitic sub-band gap absorption may increase due to the higher free charge carrier density [95], which is not reflected in the E_{04}. The trend towards higher transparency with increasing σ, and thus larger crystallites, can be explained by the reduced light scattering and less band tails in more uniform crystalline materials [95, 97].

As highlighted earlier, the electrical conductivity and the optical band gap of nc-SiC$_X$:H(n) are linked to the crystallite size of the material. In particular, the crystallite size is influenced by the growth rate of the material [95]. In order to further explore this relationship the conductivity is plotted against the growth rate in figure 4.3. This analysis reveals a significant increase in the conductivity at reduced growth rates, suggesting that slower deposition conditions are favorable to achieve higher conductivities. The deposition parameters that most signifi-

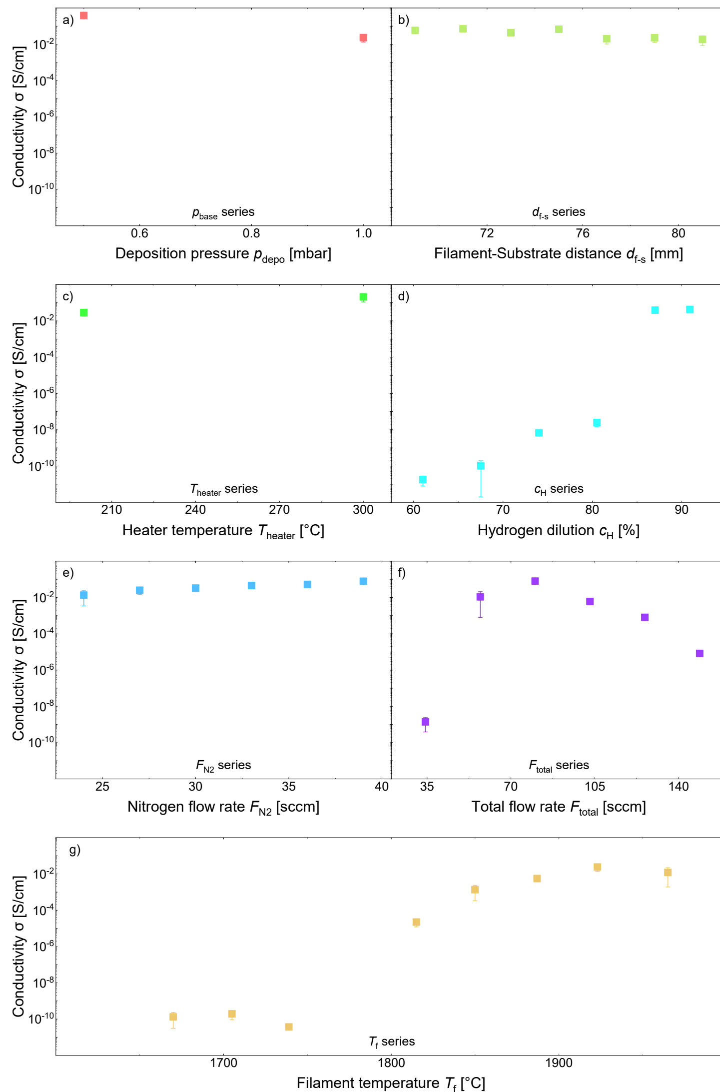

Figure 4.1.: *Dependence of the lateral electrical conductivity (σ) on various deposition parameters a) deposition pressure (p_{depo}), b) filament-substrate distance ($d_{f\text{-}s}$), c) chamber heater temperature (T_{heater}), d) hydrogen dilution (c_H), e) nitrogen flow rate (F_{N2}), f) total gas flow rate (F_{total}), and g) filament temperature (T_f). The parameters that most affect σ, with variations of more than nine orders of magnitude, are T_f and c_H, followed by a five orders of magnitude shift in σ due to F_{total}. Reproduced with permission from John Wiley & Sons - Books, from [113]; permission conveyed through Copyright Clearance Center, Inc.*

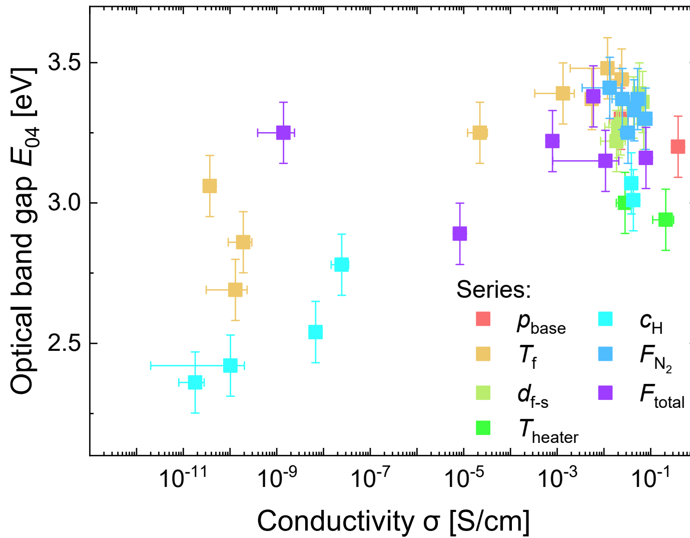

Figure 4.2.: *Correlation between the optical band gap (E_{04}) and electrical conductivity (σ) for the previous series of deposition parameters. An increase in conductivity is usually accompanied by an increase in E_{04}. Reproduced with permission from John Wiley & Sons - Books, from [113]; permission conveyed through Copyright Clearance Center, Inc.*

cantly impact the conductivity also exert a considerable influence on deposition rate (r), thereby warranting a detailed examination of the growth mechanisms. One exception to this trend at high conductivity levels is observed, where an unusually high conductivity coincides with a quadrupled r under reduced heater temperatures. This outlier will be addressed in the following discussion.

Three primary effects govern growth during deposition: hydrogen radical-induced etching of the deposited material, the concentration of reactive species on the sample surface, and the sample temperature , which are also visualized in figure 4.4 a) ot c) respectively. During deposition, hydrogen radicals can etch the already deposited material [112]. The less-ordered amorphous bonds, which are expected to be weaker, are more susceptible to etching than the well-ordered crystalline bonds within growing grains. An increase in hydrogen radical density, induced by higher filament temperatures [112] or an increased hydrogen concentration relative to the material-depositing gas, shifts the equilibrium between the deposition of new material and the etching of already deposited material towards the material removal. This shift facilitates grain growth by reducing the space

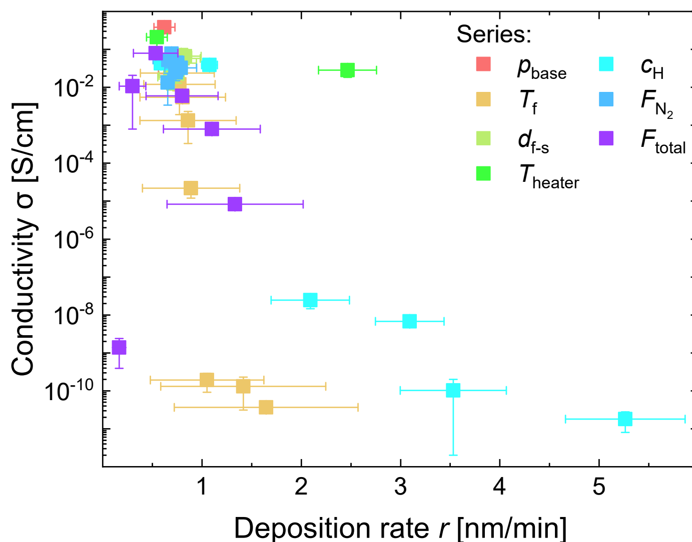

Figure 4.3.: *Dependence of electrical conductivity (σ) on the deposition rate (r) across various deposition parameter series. Lower r tends to yield higher σ, though the increased deposition rate from the chamber heater temperature (T_{heater}) series may be an exception. Reproduced with permission from John Wiley & Sons - Books, from [113]; permission conveyed through Copyright Clearance Center, Inc.*

occupied by amorphous material, leading to larger grains and a simultaneous reduction in nucleation sites. Larger grains also imply a higher etch rate for amorphous material, resulting in a slower overall deposition rate.

The total flow rate and deposition pressure dictate the number of precursor molecules within the chamber, influencing the molecular coverage of the sample by decomposed precursor gas molecules. Increased pressure leads to a density of precursor molecule and reactive species in the chamber, possibly affecting the reactions within the gas phase and amount of reactive species that settle on the surface of the sample. A higher total flow rate increases the availability of decomposed precursor molecules, yielding more reactive species on the sample. As these species move to settle on the sample, their movements can be impeded by each other, preventing them from inhabiting an energetically favorable growth site. This can either promote amorphous growth or increase the nucleation of new crystallites, potentially leading to smaller overall crystallite sizes. Therefore, a reduction in the flow rate and deposition pressure should decrease the number

of reactive species on the sample's surface, subsequently lowering the growth rate and increasing its conductivity.

Finally, the substrate temperature plays a crucial role. At elevated temperatures, molecules and reactive species possess more energy, allowing greater mobility before settling at a growth site. This enhanced mobility facilitates their incorporation into growing crystallites, leading to larger grain sizes. Conversely, higher substrate temperatures may also cause deposited reactive species to desorb more readily as a result of their increased energy. The substrate temperature can be adjusted through the chamber heater temperature, filament-substrate distance, and, to some extent, the filament temperature. An increase in the chamber heater temperature raises the baseline chamber temperature, while a decrease in the filament-substrate distance might increase heat transfer to the substrate. Higher filament temperatures could also contribute additional heat to the substrate through radiation. Following this logic, a reduced chamber heater temperature should correlate with a lower conductivity and possibly an increased deposition rate. The outlier in figure 4.3, showing an increased growth rate yet similar conductivity levels at reduced heater temperatures, could reflect changes in both the substrate and gas phase temperatures, potentially affecting the growth rate without compromising grain size. As this observation is based on a single sample, further research is needed to deepen the understanding of the deposition process. However, the observed trend of higher deposition rates while maintaining conductivity levels is particularly interesting for industrial applications, where high deposition rates are essential for a high throughput.

The experimental findings presented earlier establish hydrogen radical etching as a key mechanism influencing the growth process, primarily because of its profound impact on the resulting conductivity of the material. This conclusion is drawn from observing the significant effects of the filament temperature and hydrogen dilution on the conductivity. Subsequently, the total flow rate emerges as the second most influential factor, suggesting that the concentration of reactive species on the sample is also crucial in determining the properties of the material. The lack of conductivity variation with changes in deposition pressure could be attributed to the limited experimental range tested, which may be too narrow to

result in any discernible effects. Additionally, the conductivity might already be in a saturated regime, which prevents any further improvements through fine-tuning of these deposition parameters. The substrate temperature, within the scope of this investigation, seems to yield only a minimal influence on the properties of the material. The doping effect with variations in F_{N2} on nc-SiC$_X$:H(n) has been previously discussed, where its limited impact within the tested range was related to the opposing phenomena of reduced crystallite size due to impurity incorporation and the consequent increase in impurity scattering of charge carriers, which effectively counterbalances the increase in charge carrier concentration, whereas doping activation could not factor in this minor variation as the T_f should be sufficiently high to have nearly complete dopant activation.

An additional parameter not explored in this context is the number of catalytic filaments utilized during deposition. A higher count of filaments not only improves the deposition rate through an increased generation of reactive species, but also intensifies the thermal radiation [112]. Given the observed inverse relationship between the deposition rate and σ, an increase in the number of filaments is anticipated to decrease the conductivity of nc-SiC$_X$:H(n). In parallel, the enhanced thermal radiation from more filaments could potentially elevate the substrate temperature. The increased deposition rate implies a higher decomposition rate of the precursor gases, possibly leading to an increased concentration of reactive species on the sample. Since both the material-depositing gas and the hydrogen dilution gas are decomposed, the ratio of hydrogen radicals to the decomposed depositing gas is expected to remain constant. However, an augmented molecular coverage on the sample, similar to an increased total gas flow, may result in a decline in conductivity, particularly given that the substrate temperature seems to have a negligible effect in this study. Therefore, it is reasonable to conclude that utilizing more catalytic filaments would lead to a decrease in the conductivity of the material, as the influence of the substrate temperature is considered negligible within the parameters of this investigation.

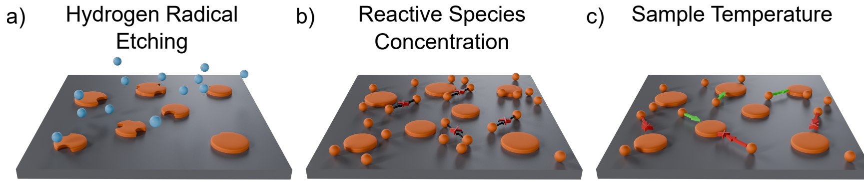

Figure 4.4.: *Visualization of the three discussed growth mechanisms a) hydrogen radical etching, b) number of reactive species on the substrate and c) sample temperature.*

4.1.2. Passivating Properties of Nanocrystalline Silicon Carbide

Beyond the opto-electrical attributes, the passivating properties of a contact material are crucial to achieve high device voltages. To attain a good passivation quality, the HWCVD-prepared n-type nc-SiC_X:H(n) needs an additional interfacial oxide between the crystalline silicon and nc-SiC_X:H(n). This oxide acts as a first passivating layer and as a protective layer to protect the crystalline silicon surface from the impacts during deposition of the HWCVD process [95, 111]. Nevertheless, the achieved passivation quality additionally relies strongly on the material properties and therefore deposition conditions of the nc-SiC_X:H(n). The layer stack utilized in the finished solar cell is introduced in section 4.2. The implied open-circuit voltage (iV_{OC}) serves as a direct indicator of the passivation quality and is analyzed in relation to the filament temperature for different filament-substrate distances, as illustrated in figure 4.5. In these experiments, crystalline silicon is symmetrically passivated on both sides with the SiO_X and nc-SiC_X:H(n) layer structure, as depicted in the inlet. It is observed that the iV_{OC} reaches saturation at lower T_f values and significantly declines with increasing T_f. A similar pattern is noted for larger $d_{f\text{-}s}$, albeit the decline in iV_{OC} shifts to higher temperatures. The effectiveness of nc-SiC_X:H(n)'s chemical passivation depends on hydrogen, which is introduced to the underlying SiO_X and saturates the dangling bonds at the crystalline silicon/SiO_X interface. Given the low solubility of hydrogen in crystalline silicon carbide, it is likely located outside of the crystalline grains [95]. Therefore, larger grains could potentially reduce the hydrogen content within the layer, as fewer larger grains result in a reduced grain boundary area,

and thus area in which hydrogen could be located. As a result, an increase in T_f leads to a larger grain size and, consequently, a lower hydrogen content, including in the SiO_X and the crystalline silicon/SiO_X interface, and passivation effectiveness. For an increased $d_{f\text{-}s}$, a reduction in hydrogen content is anticipated [95], yet this condition shifts the iV_{OC} curve to higher filament temperatures. In settings with larger $d_{f\text{-}s}$, the sample temperature is likely to be reduced, leading to smaller grains. However, the hydrogen radicals, being generated further from the sample, have an extended path to travel during which they could potentially react with other reactive species in the gas phase, reducing their availability for incorporation into the growing layer. This may result in an overall decrease in hydrogen concentration, and both effects may balance each other's influence. In such cases, the higher filament temperatures resulting in a decrease of iV_{OC} could be attributed to a reduction in the effusion of incorporated hydrogen during deposition, thus shifting the critical filament temperature for hydrogen effusion. Despite the expectations of a lower overall hydrogen concentration, the low-temperature iV_{OC} plateau appears consistent across different T_f levels, suggesting that the passivating capabilities of hydrogen might reach saturation, rendering the additional hydrogen content ineffective for further passivation.

A continuous increase in the hydrogen content in the layers, as shown in figure 4.6 a) and b), is observed when examining the intensity of FTIR silicon-hydrogen bond peak intensities ($I_{Si\text{-}H}$s) for varying T_fs and c_Hs, respectively. For the F_{total} in figure 4.6 c), no monotonous trend in $I_{Si\text{-}H}$ is observed. The $I_{Si\text{-}H}$ consistently increases with decreasing T_f and c_H, and peaks at intermediate values of F_{total} before decreasing at both lower and higher flow rates, more pronounced at lower rates. The $I_{Si\text{-}H}$ seems to plateau for low c_H and high F_{total}. The steady increase in the hydrogen content with lower filament temperatures can again be linked to the grain size, where smaller grains at lower temperatures promote higher hydrogen solubility within the layer. A similar trend is observed for low c_H. Here, the $I_{Si\text{-}H}$ may begin to reach saturation, indicating that the material is fully saturated with hydrogen and cannot incorporate any additional hydrogen, although future investigations regarding the grain size trends are necessary to confirm any saturation for small grain sizes. For a reduced F_{total}, the increase in grain size leads to a decrease in hydrogen solubility and therefore to a reduction

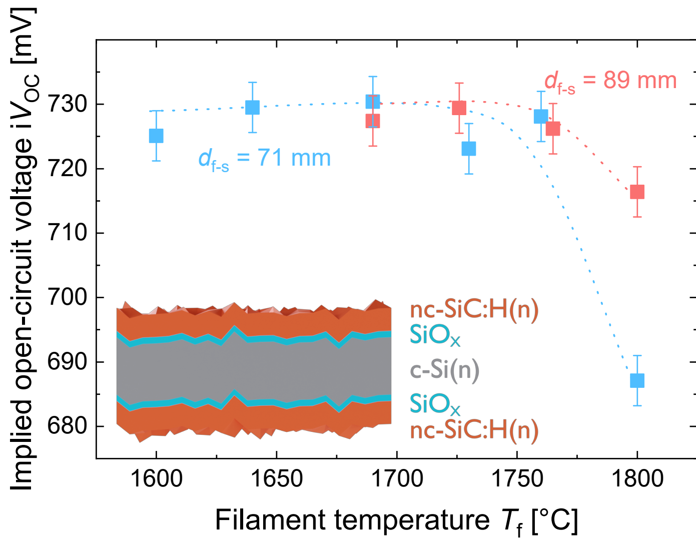

Figure 4.5.: *Variation in the implied open-circuit voltage (iV_{OC}) as a function of the filament temperature (T_f) for two distinct filament-substrate distances ($d_{f\text{-}s}$s). The inlet shows the sample structure featuring SiO_X and nc-SiC_X:H(n) layers on both sides. The lower T_f leads to an enhanced iV_{OC}, while a larger $d_{f\text{-}s}$ shifts the temperature of iV_{OC} decline to higher values. The dashed lines serve as visual guides.*

in hydrogen content. Conversely, for high F_{total}, an increase in hydrogen content could be anticipated, as the grain size is expected to decrease. However, the increased gas flow past the heated filaments might improve heat transfer to the substrate, thereby increasing the substrate temperature and potentially causing hydrogen to effuse from the layers during deposition. In such scenarios, intermediate flow rates may offer an optimal balance between minimizing hydrogen effusion and reducing grain size. Finally, by correlating the observed trends in iV_{OC} with those in $I_{\text{Si-H}}$, it is noticeable that while the hydrogen content continues to increase at low filament temperatures, the iV_{OC} reaches a plateau at lower temperatures. This could imply that the passivating capability of hydrogen in the layer and at the crystalline silicon/SiO_X interface has a maximum threshold beyond which additional hydrogen does not contribute to further chemical passivation, even if it is available. Unfortunately, a direct comparison between iV_{OC} and $I_{\text{Si-H}}$ is not feasible in this study, as the data for both studies have been generated using different systems. However, such a comparison could provide valuable

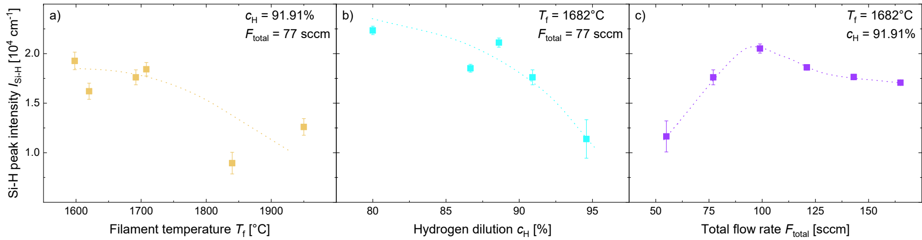

Figure 4.6.: *Variation in the FTIR silicon-hydrogen bond peak intensity ($I_{Si\text{-}H}$) in response to changes in the a) filament temperature (T_f), b) hydrogen dilution (c_H), and c) total gas flow rate (F_{total}). The other relevant deposition parameters are specified in each diagram. Low T_f and c_H elevate the hydrogen content, while an intermediate F_{total} maximizes it. The dashed lines provide guides to the eye.*

information on the passivation mechanisms of the nc-SiC$_X$:H(n) layers.

4.2. Nanocrystalline Silicon Carbide Layers in Double-Layer Transparent Passivating Contacts

The prior sections have shown that the ideal opto-electric and passivating characteristics of nc-SiC$_X$:H(n) require a careful optimization of material properties that are often opposite to each other. A single nc-SiC$_X$:H(n) layer alone cannot fulfill all the requirements for an optimal front contact; for example, high passivation quality demands a low filament temperature, whereas high conductivity requires a high filament temperature. To address these opposites, a double layer nc-SiC$_X$:H(n) stack, in combination with a tunnel oxide, is used in the TPC approach [29], as shown in figure 4.7. This layer stack begins with a wet-chemically grown silicon oxide layer, which serves as the initial passivating layer and a protective buffer to shield the crystalline silicon surface from the harsh HWCVD deposition environment. Subsequently, a thin layer of passivating nc-SiC$_X$:H(n) is deposited to ensure high voltages of the device, topped by a conductive nc-SiC$_X$:H(n) layer to enhance the electrical properties of the layer stack. To facilitate lateral conductivity and provide an anti-reflective coating, a TCO is applied over the conductive nc-SiC$_X$:H(n) layer, forming the base for screen-printed silver contacts.

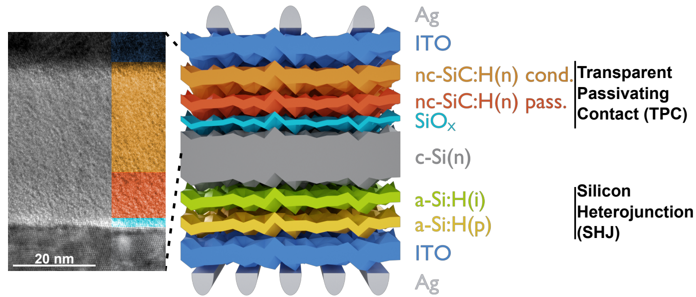

Figure 4.7.: *Schematic illustration of a solar cell featuring a transparent passivating contact (TPC) as front contact and a silicon heterojunction (SHJ) as rear contact. The TPC consists of a tunnel oxide layer combined with passivating and conductive nc-SiC$_X$:H(n) layers. The zoomed area displays a transmission electron microscope image of the layer stack. The inlet, courtesy of Xianlin Qu at Beijing University of Technology, showcases the thin layer structure.*

The rear side of the complete cell structure features a standard intrinsic and p-type a-Si:H heterojunction. The inset in figure 4.7 presents a high-resolution transmission electron microscope image of the SiO$_X$, passivating nc-SiC$_X$:H(n) and conducting nc-SiC$_X$:H(n) in the TPC layer stack, showing the ultra-thin nature of the tunnel oxide, crucial for efficient tunneling of the charge carrier into the nc-SiC$_X$:H(n) layers. The passivating nc-SiC$_X$:H(n) layer is intended to be thin due to its low conductivity, focusing on high hydrogen solubility to supply hydrogen for passivation purposes to the crystalline silicon/SiO$_X$ interface, which can be saturated during the deposition of the conductive layer. The thicker, conductive nc-SiC$_X$:H(n) layer not only supplies hydrogen to the passivating layer but also ensures a low-resistive contact to the TCO [29].

To gain further insights into this contact configuration, a systematic exploration of the layer thicknesses of the nc-SiC$_X$:H(n) layers is conducted. Beginning with the passivating nc-SiC$_X$:H(n) layer, as shown in figure 4.8, it is observed that a very thin passivating layer leads to sub-optimal solar cell parameters. While the pFF and FF maintain high levels, the iV_{OC}, V_{OC}, and J_{SC} experience significant reductions, accompanied by elevated ρ_c. Consequently, solar cells with exceedingly thin passivating nc-SiC:H(n) layer thicknesses ($d_{pass, SiC}$s) exhibit efficiencies typically below 20%, a direct consequence of the reduced V_{OC} and J_{SC}. With increasing $d_{pass, SiC}$, a sharp rise in iV_{OC} is noted, followed by a gradual increase

for even thicker layers. The V_{OC} mirrors this initial strong increase before stabilizing at thicker layer thicknesses. The J_{SC} behaves similarly, initially increasing in tandem with iV_{OC} and V_{OC} for a moderate increase in layer thickness, then plateauing at thicker layers. The p*FF* remains consistently high, irrespective of the passivating nc-SiC_X:H(n) layer thickness. In contrast, the *FF* exhibits a steady decline with increasing layer thickness, widening the gap between p*FF* and *FF* for thicker layers. A sharp decrease in ρ_c is noted from the initial levels for thin $d_{pass,\,SiC}$, followed by a subsequent increase for thicker layers. The η aligns with the *FF* trend, but displaying an initial boost for slightly larger $d_{pass,\,SiC}$.

The initially reduced iV_{OC}, V_{OC}, and J_{SC} can be primarily attributed to insufficient passivation resulting from an excessively thin $d_{pass,\,SiC}$ and thus low hydrogen availability, which negatively impacts both voltage and current due to intensive recombination at the interface. In the case of ultra-thin passivating layers, the hydrogen content soluble in the deposited material may be insufficient to fully saturate the dangling bonds at the c-Si/SiO_X interface. Furthermore, the minimal thickness of the layer could lead to incomplete substrate surface coverage by nc-SiC_X:H(n), potentially worsening damage to the c-Si due to the harsh deposition conditions marked by a high hydrogen radical density during the conductive nc-SiC_X:H(n) layer deposition. The pronounced difference between iV_{OC} and V_{OC} is likely influenced by a combination of passivation degradation induced by the sputter process, as elaborated in the following chapter, and perimeter recombination. Given that the solar cell represents only a fraction of the wafer used, as detailed in section 3.1, the charge carriers generated have the potential to recombine outside of the designated cell area [214–218]. The consistently high level of p*FF* suggests it is primarily dictated by the rear side junction, while *FF* also remains high, indicating a low series resistance for charge carriers that cross the layer stack. This observation seems contradicted by the significantly high ρ_c, which includes the series resistance. The increased ρ_c appears counter-intuitive; for extremely thin passivating nc-SiC_X:H(n) layers, the band bending at the oxide should intensify due to the closer proximity of the doped conductive nc-SiC_X:H(n) to the oxide [29, 219], which could improve the tunnel contact. Furthermore, if the substrate is unevenly covered by passivating nc-SiC_X:H(n), there might be a single layer-like contact between c-Si-SiO_X-conducting nc-SiC_X:H(n) that

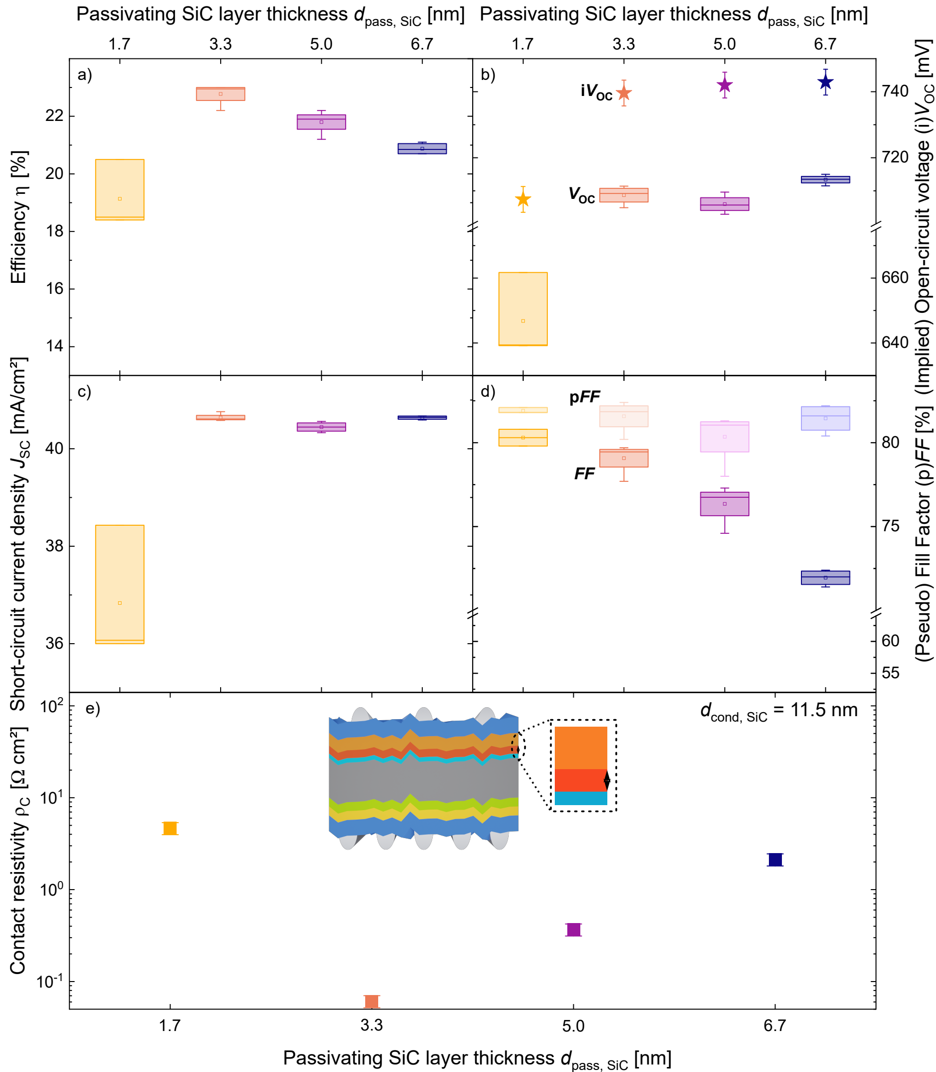

Figure 4.8.: *Impact of varying the passivating nc-SiC:H(n) layer thickness ($d_{pass,\ SiC}$) on a) power conversion efficiency (η), b) implied open-circuit voltage (iV_{OC}) and open-circuit voltage (V_{OC}), c) short-circuit current density (J_{SC}), d) pseudo Fill Factor (pFF) and Fill Factor (FF), and e) contact resistivity (ρ_c). Extremely thin $d_{pass,\ SiC}$ lead to an overall poor cell performance due to passivation challenges. Increased $d_{pass,\ SiC}$ enhances passivation but reduces FF. The inset illustrates the sample structure with the varying layer highlighted in the stack.*

is typically characterized by low contact resistivity [29]. Consequently, the high contact resistivity measured for a very thin $d_{\text{pass, SiC}}$ could be an anomaly and requires repetition for verification.

As $d_{\text{pass, SiC}}$ increases, the hydrogen content within the layer increases significantly, leading to enhanced passivation and consequently higher iV_{OC}, V_{OC}, and J_{SC}. For even thicker layers, with an abundance of hydrogen, only marginal improvements in iV_{OC} and V_{OC} are observed, suggesting that the passivating effect might reach saturation, as discussed in the previous section. Given that nc-SiC_X:H(n) maintains a high transparency and parasitic absorption is negligible in this thickness regime, J_{SC} remains constant once the majority of defects are passivated. The observed trend of decreasing *FF* with a widening gap between *FF* and p*FF* for thicker $d_{\text{pass, SiC}}$ aligns with the increase in ρ_c. The reduced conductivity of the passivating nc-SiC_X:H(n) layer progressively deters charge carrier conduction through the stack, thereby increasing the contact and series resistance. Following the initial increase, η mirrors the *FF* trend, as the decline in *FF* outweighs the slight increase in iV_{OC} for thicker $d_{\text{pass, SiC}}$. To optimize iV_{OC}, V_{OC}, and *FF*, and thereby maximize cell performance, an intermediate $d_{\text{pass, SiC}}$ thickness is most advantageous.

After examining the impact of the passivating nc-SiC_X:H(n) layer, attention is turned to the variations in the thickness of the conducting nc-SiC_X:H(n) layer, as presented in figure 4.9. Similarly to the observations with the passivating nc-SiC_X:H(n) layer, a minimal thickness in the conducting layer results in significantly lowered iV_{OC}, V_{OC}, J_{SC}, and a strong increase in ρ_c, coupled with reductions in both p*FF* and *FF*, cumulatively leading to diminished overall η. All these parameters improve rapidly with an increase in conducting nc-SiC:H(n) layer thickness ($d_{\text{cond, SiC}}$). Beyond the initial enhancement, iV_{OC} only slightly increases and V_{OC}, J_{SC}, and p*FF* stabilize, while *FF* continues to decrease and both the p*FF*-*FF* gap and ρ_c increase. The efficiency trend again mirrors that of *FF*.

The initial poor performance can be traced back to an exceptionally poor passivation quality, influencing all solar cell parameters. With a very thin conducting nc-SiC_X:H(n) layer, the hydrogen incorporation into the underlying passivating

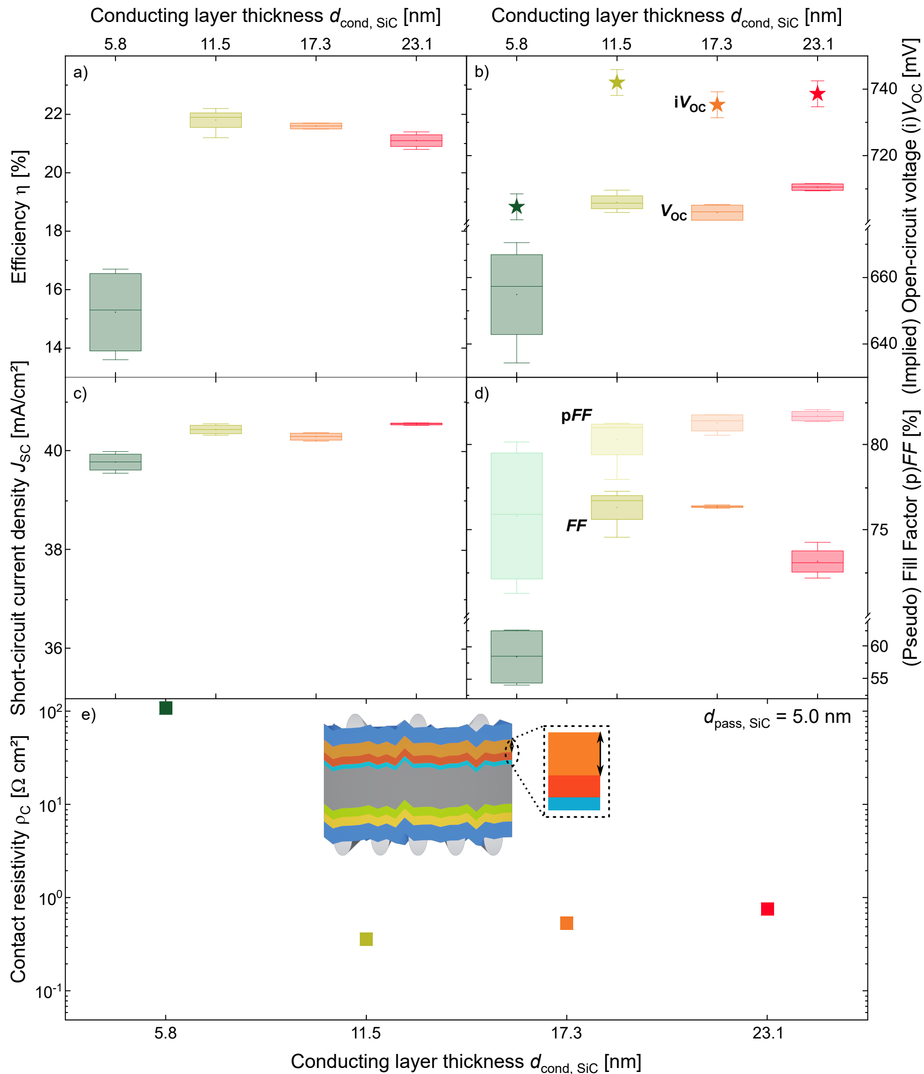

Figure 4.9.: *Effect of varying the conducting nc-SiC:H(n) layer thickness ($d_{cond,\,SiC}$) on a) power conversion efficiency (η), b) implied open-circuit voltage (iV_{OC}) and open-circuit voltage (V_{OC}), c) short-circuit current density (J_{SC}), d) pseudo Fill Factor (pFF) and Fill Factor (FF), and e) contact resistivity (ρ_c). Extremely thin $d_{cond,\,SiC}$ detrimentally affects most solar cell parameters. Thicker layers primarily reduce FF. The inset illustrates the sample with the varied layer within the stack.*

layer is limited. The passivating layer alone is not thick enough to provide the necessary hydrogen for a high-level chemical passivation, affecting even the p*FF*. Conversely, ρ_c is increased due to an insufficient charge carrier concentration in the doped layer, hindering effective band bending at the tunnel oxide and obstructing charge carrier transport from the crystalline silicon. As the thickness of the conducting layer increases, the stack acquires sufficient hydrogen for excellent passivation and band bending improves, leading to stable $\mathrm{i}V_{\mathrm{OC}}$, V_{OC}, J_{SC}, and p*FF*, along with low ρ_c and high *FF*. However, for even thicker $d_{\mathrm{cond,\,SiC}}$, the *FF* reduces and ρ_c increases, possibly due to the insufficient conductivity of the conducting nc-SiC$_X$:H(n), contributing to increased series resistance and resulting resistive losses.

The thickness variations in the nc-SiC$_X$:H(n) layers are anticipated to influence the J_{SC} by altering the reflective properties or parasitic absorption of the layer stack [142]. The measured reflection (*R*) curves and calculated reflection losses (J_{Refl}) for the $d_{\mathrm{cond,\,SiC}}$ variation, as seen in figure 4.10 a) and b), respectively, support this hypothesis. Indeed, *R* diminishes, particularly below wavelengths of 400 nm and above 600 nm, with a slight increase in reflection between 400 nm and 500 nm. Resulting from this, the calculated J_{Refl} decrease by approximately 0.5 $\frac{\mathrm{mA}}{\mathrm{cm}^2}$ for thicker $d_{\mathrm{pass,\,SiC}}$. This is not reflected in the J_{SC} observed in figure 4.9 c). The reductions in the blue and near-infrared spectrum could be compensated by absorption in the ITO layer, known for its higher absorption coefficient at these wavelengths [220]. Additionally, gains could partly be neutralized by the increased reflection in the 400 nm to 500 nm range or lost in the scattering of J_{SC} values due to process fluctuations, or parasitically absorbed in the nc-SiC$_X$:H(n) layers.

The visible reduction in the overall performance of solar cells observed in figure 4.8 and figure 4.9 is supported by the reduced *IQE* for either very thin passivating or conducting nc-SiC$_X$:H(n) layers, as shown in figure 4.11. In both cases, the *IQE* decreases throughout the whole wavelength spectrum. For thicker $d_{\mathrm{pass,\,SiC}}$ or $d_{\mathrm{cond,\,SiC}}$, the *IQE* remains high, regardless of further increases in layer thicknesses. A slight reduction in the range 350 nm to 500 nm is observed in the $d_{\mathrm{cond,\,SiC}}$ variation. The overall reduction in *IQE* for thin layers is indicative of

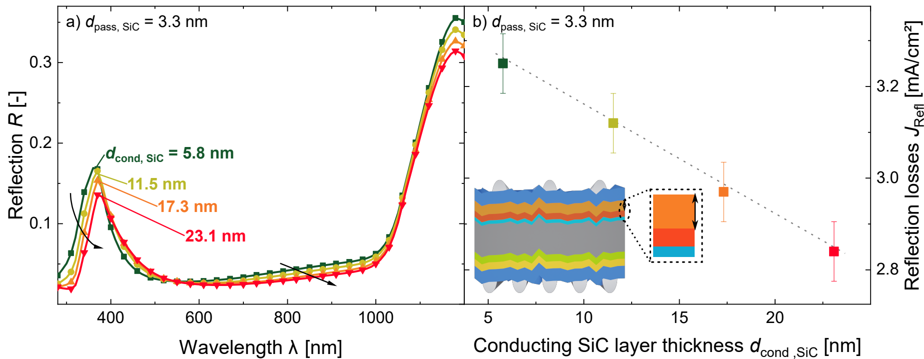

Figure 4.10.: *a) Reflection (R) curves for varying conducting nc-SiC:H(n) layer thicknesses ($d_{cond, SiC}$s) and b) the resulting calculated reflection losses (J_{Refl}) from a). A thicker $d_{cond, SiC}$ leads to a reduced reflection in the layer stack. The inset depicts the sample structure with the varied layer. Permission for use granted by John Wiley & Sons - Books, from [113] via Copyright Clearance Center, Inc.*

poor passivation at the front side of the rear-junction crystalline silicon solar cell, aligning with the previously noted reduced solar cell parameters. The decrease in low-wavelength response could be attributed to parasitic absorption in the nc-SiC_X:H(n), given its higher absorption coefficient in these regions [111].

The final aspect of this study investigates the interplay between V_{OC} with FF and pFF in relation to the variations in the thickness of the passivating and conducting nc-SiC_X:H(n) layers, as presented in figure 4.12 together with some calculated reference lines introduced in figure 2.6. For the $d_{cond, SiC}$ variation, the slight increase in pFF is visible for higher iV_{OC} as expected from the theoretical relations. For very low $d_{cond, SiC}$, a strong deviation to FF is visible, as discussed above. For thicker $d_{cond, SiC}$, the gap closes, but increases again for the thickest $d_{pass, SiC}$ used here. These trends are independent of iV_{OC} and related to changes in R_S, following the theoretically suggested lines. However, the impact of $d_{pass, SiC}$ variation is quite evident, showing the previously observed low iV_{OC} coupled with high FF for thinner $d_{pass, SiC}$. As $d_{pass, SiC}$ increases, iV_{OC} initially improves while maintaining a similar pFF and FF level, followed by a significant drop in FF even as iV_{OC} continues to increase slightly for thicker $d_{pass, SiC}$. For thicker $d_{pass, SiC}$, R_S increases as suggested by the theoretical calculations while maintaining a high-quality passivation. This observation indicates a direct trade-off between FF

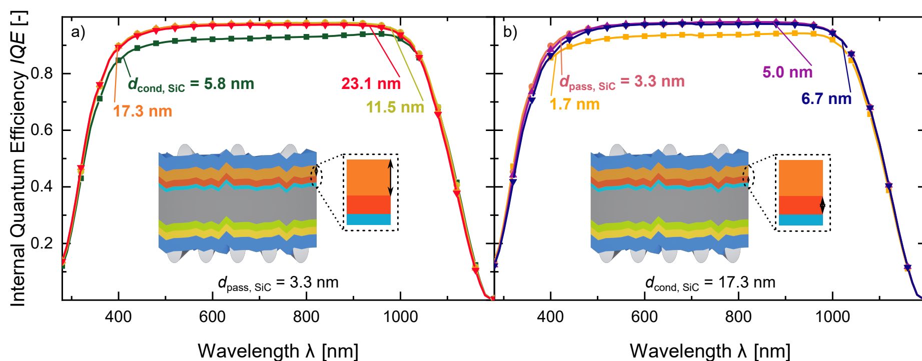

Figure 4.11.: *Internal quantum efficiencies (IQEs) for variations in a) conducting nc-SiC:H(n) layer thickness ($d_{cond, SiC}$) and b) $d_{pass, SiC}$. For very thin $d_{cond, SiC}$ or $d_{pass, SiC}$, the IQE is reduced due to poor passivation quality. Insets illustrate the varied layer within the sample stack. Permission for use granted by John Wiley & Sons - Books, from [113] via Copyright Clearance Center, Inc.*

and iV_{OC} depending on $d_{pass, SiC}$, where either efficient charge carrier extraction is achieved at the expense of passivation quality, or a high passivation quality is attained at the cost of a reduced *FF*. Optimal performance is observed at intermediate $d_{pass, SiC}$, where iV_{OC} is enhanced with only a modest *FF* reduction.

This trade-off can be illuminated by examining the schematic σ and $I_{Si\text{-}H}$ cross-sections through the nc-SiC_X:H(n) layers in figure 4.13. In the passivating nc-SiC_X:H(n) layer, a pronounced hydrogen concentration is accompanied by a noticeably low conductivity. This scenario is reversed in the conducting nc-SiC_X:H(n), where $I_{Si\text{-}H}$ is reduced, and σ increases by ten orders of magnitude. For optimal passivation, a substantial presence of hydrogen near the c-Si/SiO_X interface is essential to saturate the dangling bonds. In the transparent passivating contact structure, this hydrogen is made available by the passivating nc-SiC_X:H(n) layer, either during the deposition of the passivating nc-SiC_X:H(n), or the passivating nc-SiC_X:H(n) is enriched with hydrogen during the deposition of the conducting nc-SiC_X:H(n). Simultaneously, the passivating layer exhibits a significantly reduced conductivity, forming an almost insulating region near the interface. This low-conducting area contributes substantially to the series resistance, noticeable by the increase in ρ_c observed in figure 4.8 e) with thicker $d_{pass, SiC}$. Reducing this low-conductive area to decrease ρ_c simultaneously re-

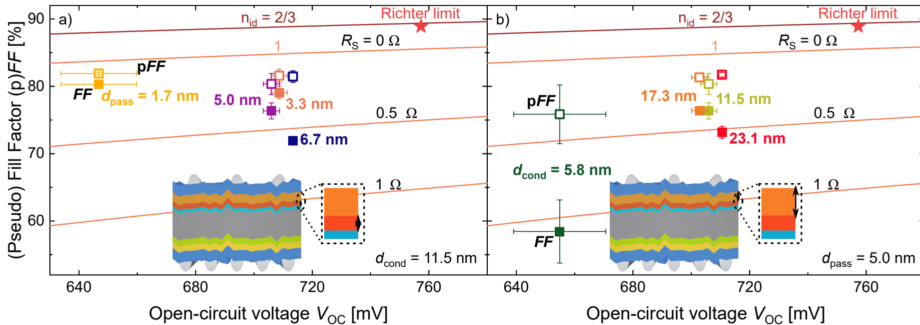

Figure 4.12.: *Correlation between the pseudo Fill Factor (pFF) or Fill Factor (FF) and implied open-circuit voltage (iV_{OC}) for a) various passivating nc-SiC:H(n) layer thicknesses ($d_{pass,\,SiC}$s) and b) conducting nc-SiC:H(n) layer thicknesses ($d_{cond,\,SiC}$s), with previously shown theoretical FF-V_{OC} dependencies for ideality factors of n_{id} =1 and n_{id} =2/3 with series resistances between $R_S = 0\,\Omega$ and $R_S = 1\,\Omega$. A clear trade-off between the FF and iV_{OC} is apparent with changing $d_{pass,\,SiC}$. The inset shows the sample structure with variations in both nc-SiC_X:H(n) layers.*

duces the hydrogen content near the c-Si/SiO_Xinterface, resulting in lower iV_{OC}. The challenge lies in achieving a high hydrogen content near the crystalline silicon while either maintaining or rapidly increasing the conductivity of the material.

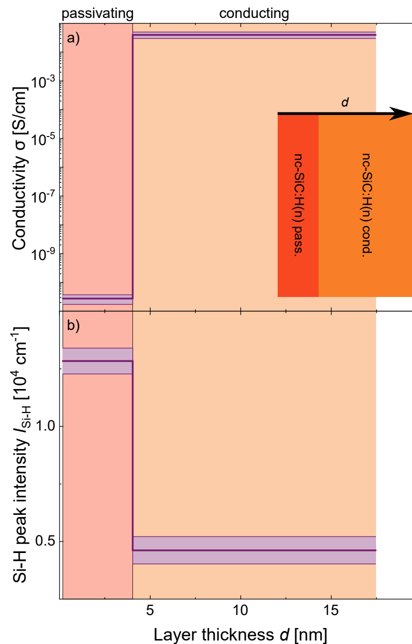

Figure 4.13.: *Schematic cross-section of a) the electrical conductivity (σ) and b) the FTIR silicon-hydrogen bond peak intensity ($I_{Si\text{-}H}$) through the nc-SiC_X:H(n) double layer stack. The passivating nc-SiC_X:H(n) layer exhibits a high hydrogen concentration and low σ, in contrast to the conducting nc-SiC_X:H(n), which has a high σ and low $I_{Si\text{-}H}$.*

4.3. Gradient Layer for Transparent Passivating Contacts

To enable a rapid increase in conductivity while preserving the high hydrogen content in the layer stack, a novel approach employing a graded nc-SiC_X:H(n) layer is explored in this section. This method eliminates the individual passivating nc-SiC_X:H(n) layer, transitioning its properties gradually from passivating to conducting nc-SiC_X:H(n) through a continuous increase in T_f. The rate of this transition, determined by the filament current ramp (R_{fil}), influences the properties of the layer, as depicted in figure 4.14. The figure illustrates iV_{OC} and p*FF* results with corresponding *FF*s for different R_{fil} settings. The upper inset of figure 4.14 a) shows the adjusted sample structure, highlighting the gradient layer as a color gradient in the illustration, while the lower inset in b) presents a typical

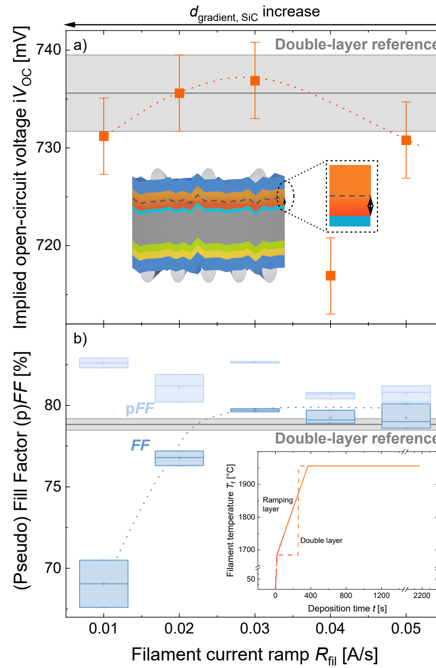

Figure 4.14.: *The a) implied open-circuit voltage (iV_{OC}) and b) pseudo Fill Factor (pFF) and Fill Factor (FF) for different filament current ramps (R_{fil}s), determining the graded nc-SiC:H(n) layer thickness ($d_{gradient,\ SiC}$). Lower R_{fil} leads to a reduced iV_{OC} and FF, which both improve towards intermediate R_{fil}. Higher R_{fil} yields lower iV_{OC}s but improved FFs.The pFFs remains consistently high. The insets in a) show the layer structure with the highlighted $d_{gradient,\ SiC}$ variation, and in b) the T_f profile. Dashed lines are visual aids.*

T_f profile for such a deposition, as well as for a double layer stack with two distinct nc-SiC_X:H(n) layers. As the T_f start at the passivating nc-SiC_X:H(n) level and needs to rise to the conducting nc-SiC_X:H(n) level for the gradient layers, the gradient layer thickness and total deposition time is dependent on the R_{fil}. The deposition time for the conducting nc-SiC_X:H(n) layer is constant for all solar cells.

The iV_{OC} starts at lower levels for smaller R_{fil}, improving for intermediate values above 735 mV before again decreasing at higher R_{fil}. Similarly, the *FF* starts with an initially low value, then increases as iV_{OC} improves, and finally plateaus at the higher R_{fil}. The p*FF* remains consistently high across different R_{fil}s. The low *FF* observed for the thick $d_{gradient,\ SiC}$ can be explained to the

presence of a substantial low-conductive region during the growth of the gradient layer, which prevents efficient extraction of charge carriers. The rate at which T_f increases does not produce a sufficiently fast change in the properties of the material, resulting in the thicker low-conductive part of the layer. This is additionally reflected in the large gap between pFF and FF, indicating a large series resistance. The gap narrows for a faster R_{fil}, as the low-conductive part of the gradient layer is reduced. When the thickness of the $d_{gradient, SiC}$ is minimal, the FF stabilizes since the resistance attributed to the low-conductive gradient layer is sufficiently reduced. In previous studies, it was established that for low conductive nc-SiC$_X$:H(n), a high hydrogen content is essential to achieve a significant increase in iV_{OC} [111]. However, this correlation does not appear to hold for scenarios with low R_{fil} settings. It is hypothesized that the prolonged deposition time, as a consequence of the slower ramping speed, may lead to increased heating of the substrate. This higher temperature potentially triggers the effusion of hydrogen during the deposition process. As a result, the freshly deposited material, which is less hydrogenated due to the higher filament temperatures, fails to compensate for this loss, thereby diminishing the layer's passivation quality. Conversely, with a quicker R_{fil}, the deposition time is reduced, thus reducing the thermal impact on the layer. This leads to the retention of more hydrogen within the layer stack, which further enhances the passivation. The real sample temperature during the deposition process needs to be investigated in the future. At the fast R_{fil}, the passivating part of the layer becomes very thin, preventing sufficient hydrogen incorporation to achieve a high passivation quality. It is notable that the low iV_{OC} observed at a R_{fil} of $0.04\,\frac{A}{s}$ appears to be an anomaly, probably attributable to variations in the deposition process or inconsistencies in the quality of the wafers.

Compared to the double layer approach, this method does not show a noticeable improvement in the iV_{OC}-FF trade-off. The best performing combination in this study demonstrates performances on par with the optimum configuration of the double layer stack. The pFF remains consistently high, which is expected as it is predominantly influenced by the junction side of the solar cell, the rear side in this context.

For a comprehensive understanding, a larger R_{fil} scan range is presented in

figure 4.15, revealing a consistent decrease in iV_{OC} with increasing R_{fil}. The pFF remains relatively stable, but a strong scattering is observed for a high R_{fil}. While the FF improves initially, aligning closer to pFF and diminishing the pFF-FF gap, it then mirrors pFF's scattering at higher R_{fil}. As previously clarified, the observed variations in iV_{OC} are largely attributed to the hydrogen incorporation within the layer. The R_{fil} employed in this process is designed to prevent the thermal effusion of hydrogen during deposition, implying that any notable changes are mostly due to the presence or absence of hydrogen integrated into the layer stack. In particular, the initial increase in R_{fil} results in a significant narrowing of the gap between the pFF and FF, with the latter subsequently aligning closely with the pFF. This behavior demonstrates the efficacy of this method in substantially decreasing the resistance throughout the stack. Consequently, the front contact stops to limit the series resistance of the solar cell, as evidenced by the relative constant pFF-FF gap. Scattering in the pFF and iV_{OC} can be ascribed to discrepancies in the quality of the wafer or to deviations inherent to the process. It is important to note that the inertia of the electronics of the deposition system exerts a considerable impact on the deposition durations, especially at higher R_{fil} values. Such inertia affects the $d_{gradient,\,SiC}$, which in turn significantly alters the material properties of the gradient layer. This interaction is likely responsible for the scattering patterns observed in the results.

In an effort to optimize the passivation and conductivity in TPCs, a hybrid approach is introduced that combines a double layer and a gradient layer strategy. This approach incorporates an ultra-thin passivating nc-SiC_X:H(n) seed layer beneath a graded nc-SiC_X:H(n) layer, topped with the usual conducting nc-SiC_X:H(n) layer. The effectiveness of this design is evaluated by varying the passivating seed nc-SiC:H(n) layer thickness ($d_{seed,\,SiC}$) while maintaining a constant R_{fil} in the gradient layer.

As shown in figure 4.16, the introduction of even a minimal $d_{seed,\,SiC}$ enhances the iV_{OC} compared to a configuration without a seed layer. The pFF remains consistently high across different seed layer thicknesses, while FF decreases with increasing $d_{seed,\,SiC}$, leading to a widening pFF-FF gap. However, a significant improvement in iV_{OC} is observed for intermediate $d_{seed,\,SiC}$ thicknesses,

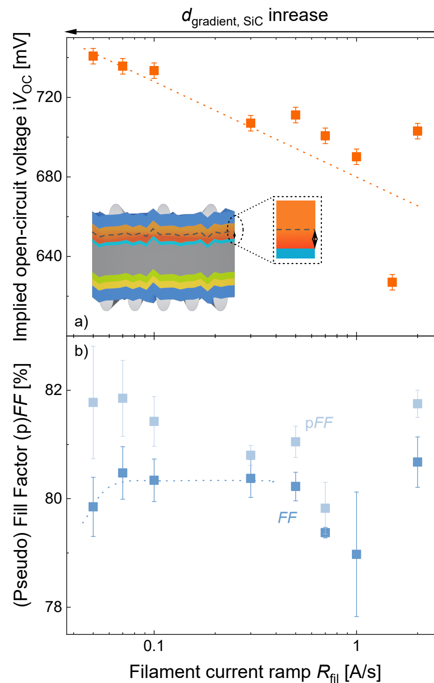

Figure 4.15.: *The a) implied open-circuit voltage (iV_{OC}) and b) Fill Factor (FF) and pseudo Fill Factor (pFF) for an extended range of filament current ramps (R_{fil}s), influencing the graded nc-SiC:H(n) layer thickness ($d_{gradient,\ SiC}$). The lowest R_{fil} in this figure equals the highest R_{fil} in figure 4.14. The iV_{OC} consistently declines with increasing R_{fil}, while the pFF is relatively constant. The FF initially converges towards pFF before following its fluctuation. The inset illustrates the sample setup with the varied layer thickness.*

indicating the benefit of the added hydrogen content of the seed layer. The selected R_{fil} rate aligns with the maximum rate presented in figure 4.14, also referenced by a $d_{seed,\ SiC}$ of 0 nm in figure 4.16. This particular rate is implemented because it maintains a high *FF* unaffected by an excessive layer thickness, yet it simultaneously reveals a degradation in iV_{OC}, primarily due to the restricted passivating capabilities of the nc-SiC_X:H(n) within the gradient layer. The criticality of choosing an optimal $d_{seed,\ SiC}$ lies in its impact on charge carrier extraction, preserving the *FF*, an effect already recognized from the passivating nc-SiC_X:H(n) variations in the double layer stack. Remarkably, even a minimal $d_{seed,\ SiC}$ induces a noticeable improvement in iV_{OC} compared to configurations

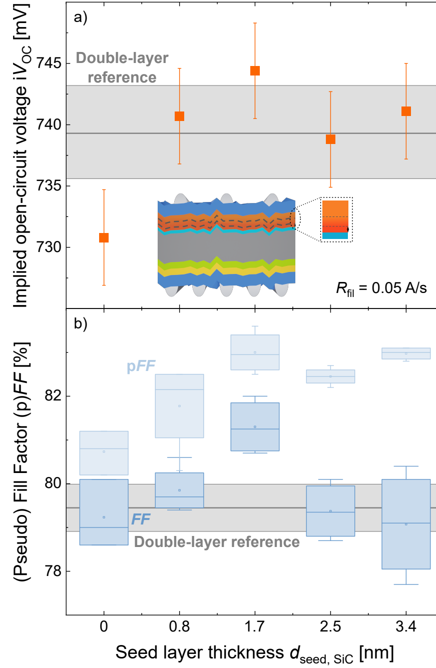

Figure 4.16.: *The a) implied open-circuit voltage (iV_{OC}) and b) pseudo Fill Factor (pFF) and Fill Factor (FF) for varying passivating seed nc-SiC:H(n) layer thickness ($d_{seed, SiC}$s). The filament current ramp (R_{fil}) of the seed layer is constant at 0.05 $\frac{A}{s}$. An increase in iV_{OC} with a growing pseudo Fill Factor (pFF)-FF gap is observed for increasing $d_{seed, SiC}$.*

without a seed layer.

This improved approach presents an initial boost in iV_{OC}, especially compared to configurations without a seed layer, ultimately reaching and stabilizing at an impressive level that exceeds 740 mV for variants with thicker $d_{seed, SiC}$. The introduction of the seed layer brings additional hydrogen into the layer stack, significantly enhancing the passivation quality of the layer stack. However, similar to the double layer stack approach, the addition of low-conductive material increases the resistance across the stack, which in turn decreases the *FF* and broadens the p*FF*-*FF* gap at first slightly for thinner $d_{seed, SiC}$, then more severe for larger $d_{seed, SiC}$. However, the anticipated rapid increase in conductivity throughout the layer stack, coupled with the maintained iV_{OC}, renders a well-balanced combination of a seed layer and gradient layer as a promising solution, potentially

surpassing the performance benchmarks set by the double layer stack approach.

It is relevant to note that the sample with a $d_{\text{seed, SiC}}$ of 0 nm, processed separately from the main series and originating from previous experiments, exhibits a marginally lower pFF. This variance can be attributed to process variations encountered during the a-Si:H rear side preparation. In a consistent series, the pFF is anticipated to remain relatively uniform, dependent on the prerequisite of sufficient front-side passivation, since it is predominantly influenced by the junction side of the cell.

In figure 4.17, further investigations on the interplay between R_{fil} and $d_{\text{seed, SiC}}$, considering their effects on iV_{OC} in a) and FF in b), are presented. This analysis helps to identify optimal combinations of these parameters to balance the passivation and conductivity. The heatmap shows that the higher iV_{OC} is favored by thicker $d_{\text{seed, SiC}}$ and lower R_{fil}, while opposite trends are observed for FF. Despite these conflicting trends, a range of parameter combinations offers promising results. The iV_{OC}-FF product shown in figure 4.17 c) reveals the best performance found for either high R_{fil} and lower $d_{\text{seed, SiC}}$ or both low $d_{\text{seed, SiC}}$ and R_{fil}.

In this combination, the integration of the seed and gradient layer approach led to notable enhancements in both the V_{OC} and the FF, surpassing the solar cell performance achieved by the double layer stack configuration, as detailed in table 4.1. This comparison also includes a standard SHJ reference solar cell. When compared, the TPCs demonstrate a superior J_{SC} relative to the SHJ, a result of the improved transparency offered by nc-SiC$_X$:H(n) as compared to a-Si:H. Although the double layer stack marginally outperforms the new approach in terms of J_{SC}, the layer thicknesses, especially with regard to $d_{\text{cond, SiC}}$, have not been adapted to the additional interlayer, and no significant statistics have been done yet. The iV_{OC} of this novel approach outshines both the TPC double layer and the SHJ references. However, it is observed that the V_{OC} of both TPC configurations lags slightly behind the SHJ reference, with the new approach improving upon the double layer stack by a surplus of 4.1 mV. This difference between the TPC and SHJ in V_{OC} can be attributed to factors such as sputter-induced degradation or inconsistencies in annealing between the nc-SiC$_X$:H(n)

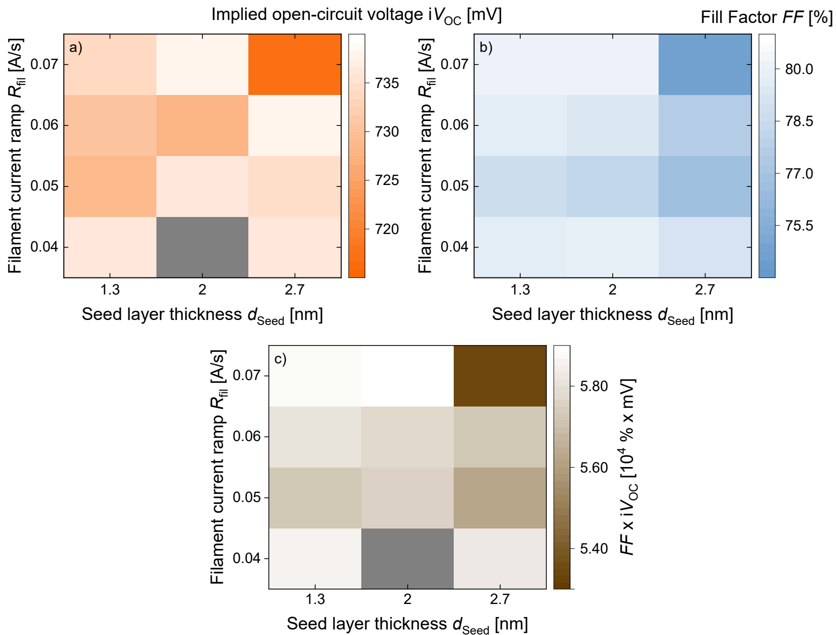

Figure 4.17.: *Heatmaps for varying filament current ramps (R_{fil}s) and passivating seed nc-SiC:H(n) layer thicknesss ($d_{seed,\ SiC}$s) for the a) implied open-circuit voltage (iV_{OC}) and b) Fill Factor (FF). c) shows the same heatmap for the product of iV_{OC} and FF to more easily identify optimal combinations. The iV_{OC} favors a thicker $d_{seed,\ SiC}$ and lower R_{fil}, while the opposite trend is visible for the FF. The highest combination can be achieved either for low $d_{seed,\ SiC}$ in combination with low R_{fil} or lower $d_{seed,\ SiC}$ with high R_{fil}.*

front side and the a-Si:H rear side, as will be discussed in the following chapter, and perimeter recombination, as discussed earlier. It should be noted that the V_{OC} for the SHJ reference surpasses its iV_{OC}, as this cell's a-Si:H layers are optimization for an additional light soaking process, a treatment applied post-fabrication, thereby elevating the V_{OC} beyond the precursor iV_{OC} measurement.

To achieve a V_{OC} comparable to the SHJ in the TPC structure, it is vital to scale from laboratory-sized 2x2 cm^2 cells to full-area, $M2^+$ cells, thus mitigating the effects of perimeter recombination. Additionally, the development of an effective light soaking treatment to recover sputter damage is ongoing, as discussed in subsequent chapters. Furthermore, the *FF* shows an improvement of $0.6\%_{abs}$ with the application of the seed and gradient layer approach, demonstrating the

Table 4.1.: *Comparison of the IV-parameters of a silicon heterojunction reference solar cell, the previous TPC double layer stack design, and the new TPC seed + gradient layer design. The new TPC design improves both the V_{OC} and FF, making them more comparable with the SHJ reference.*

	η [%]	J_{SC} [$\frac{mA}{cm^2}$]	iV_{OC} [mV]	V_{OC} [mV]	*FF* [%]	p*FF* [%]
SHJ reference [1] [221]	24.51	39.52	741.5	741.8	83.61	85.80
TPC double layer [2] [29]	23.99	40.90	738.4	725.5	80.90	84.00
TPC seed + gradient layer [2]	24.22	40.72	744.4	729.6	81.50	83.39

[1] M2+ cell area
[2] 4 cm^2 cell area

advantageous impact of the gradient layer. However, the SHJ reference still has a *FF* advantage of over 2%$_{abs}$ compared to the new TPC layer stack, indicating possibilities for further enhancements, such as tailoring the thickness of the conducting nc-SiC$_X$:H(n) layer to suit this new stack structure. Furthermore, exploring new techniques to increase the conductivity of nc-SiC$_X$:H(n) while maintaining high hydrogen solubility, such as light soaking or catalytic doping, could yield further advances.

Despite a slight decrease in J_{SC} compared to the double layer stack, the new seed and gradient layer approach facilitates an overall efficiency gain of 0.2%$_{abs}$, thanks to the combined improvements in V_{OC} and *FF*. Taking these enhancements into account and the potential to achieve a J_{SC} comparable to the double layer stack, an overall efficiency improvement of up to 0.5%$_{abs}$ is well within reach.

To further investigate the enhancements of the added gradient layer, a schematic comparison of the σ and $I_{Si\text{-}H}$ cross-sections between the gradient-layer approach and the traditional double layer stack is presented in figure 4.18 a) and b), respectively. This cross-sectional data is acquired by stopping the current ramp at different stages and depositing a layer with a thickness of 30 nm or more for conductivity or FTIR measurements. In both TPC approaches, the low-conductive passivating nc-SiC$_X$:H(n) layer is adjacent to the crystalline silicon, topped with the thicker, high-conductive nc-SiC$_X$:H(n) in the conducting layer. Unlike the previous approach where the conductivity remains reduced until the conducting nc-SiC$_X$:H(n) is applied, the gradient layer inserted between

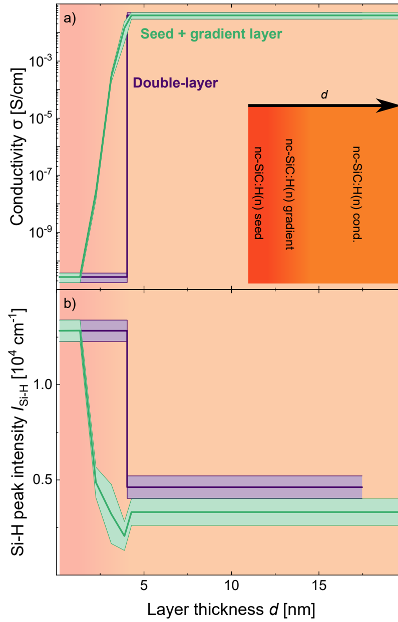

Figure 4.18.: *Updated schematic cross-section of the a) electrical conductivity (σ) and b) FTIR silicon-hydrogen bond peak intensity ($I_{Si\text{-}H}$) from figure 4.13. The profiles of the approach with the seed and gradient layer are added. An early and strong increase in σ is visible, while the $I_{Si\text{-}H}$ has an inverse profile. The inlet shows the nc-SiC$_X$:H(n) stack with the layer thickness d. The color gradient symbolizes the shift from passivating to conducting nc-SiC$_X$:H(n).*

the passivating and conducting nc-SiC$_X$:H(n) exhibits a steady increase in the conductivity. Inversely, the $I_{Si\text{-}H}$ initially reveals an amplified intensity in the passivating nc-SiC$_X$:H(n) layer, which gradually diminishes through the gradient layer before stabilizing at a lower intensity in the conducting nc-SiC$_X$:H(n). However, this configuration, featuring reduced thickness, yet high $I_{Si\text{-}H}$ seed layer in combination with the gradient layer nc-SiC$_X$:H(n), suffices to deliver plenty of hydrogen to the c-Si/SiO$_X$ interface of the crystalline silicon, thereby facilitating excellent passivation quality. This, coupled with the aforementioned rapid increment in σ, concludes in the enhancements described in table 4.1.

In the final segment of this section, SIMS profiles showing the distribution of hydrogen and nitrogen within the different single, double and gradient layers, as shown in figure 4.19 a) and b), are presented. Hydrogen was chosen as

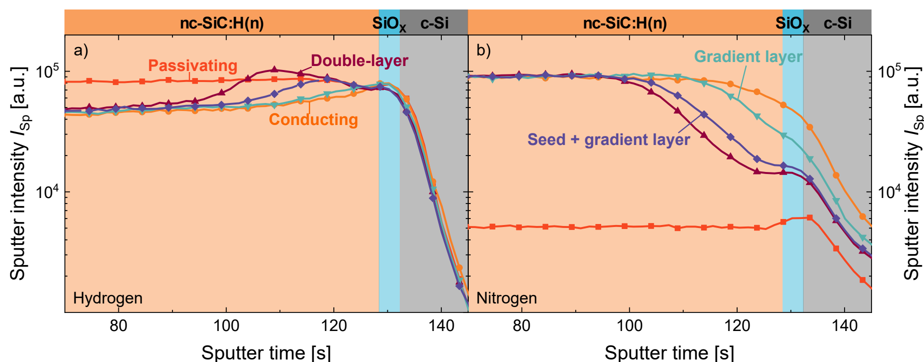

Figure 4.19.: *Secondary ion mass spectroscopy (SIMS) profiles for a) hydrogen and b) nitrogen of the passivating and conducting single layers, the double layer stack, the gradient layer, and the seed layer with the gradient layer on top. The seed and seed + gradient layer stacks are topped with a conductive nc-SiC$_X$:H(n) layer. In the passivating nc-SiC$_X$:H(n) parts of the samples, a high hydrogen concentration can be found, while a high nitrogen content is found for the conducting nc-SiC$_X$:H(n) parts.*

a high concentration close to the c-Si interface is necessary to acheive a high passivation quality, while nitrogen was chosen as an indication for crystallite sizes leading to high conductivities [95]. A uniform hydrogen concentration is observed across all layers within the SiO$_X$, decreasing towards the crystalline silicon. Notably, the passivating nc-SiC$_X$:H(n) layer exhibits the highest hydrogen presence, in contrast to the conducting nc-SiC$_X$:H(n), which shows the lowest. Intriguingly, the hydrogen intensity near the c-Si/SiO$_X$ interface of the conducting single layer slightly surpasses that of its bulk. The gradient nc-SiC$_X$:H(n) layer mirrors the hydrogen profile of its conducting counterpart. In the realm of the double layer stack, one can observe a gradual increase of hydrogen from the c-Si/SiO$_X$ interface, which diminishes sharply upon transition to the conducting material. The hydrogen intensity in the passivating region of the double layer is more pronounced than that in the single passivating layer. The hydrogen profile of the seed and gradient layer initially parallels that of the double layer, with a small reduction towards the conducting nc-SiC$_X$:H(n).

As for nitrogen, the passivating nc-SiC$_X$:H(n) single layer shows the lowest signal intensity, with a minor peak within the SiO$_X$. In contrast, the conducting nc-SiC$_X$:H(n) single layer shows a significant increase in nitrogen starting at the

c-Si interface, which maintains a consistently high level thereafter. The gradient layer exhibits a more gradual increase in nitrogen, similar so when a seed layer is integrated, even though it is shifted deeper into the nc-SiC_X:H(n) layer. Within the double layer stack, the nitrogen signal maintains a lower constant level near the c-Si interface, rising as in the conducting layer but situated deeper within the total nc-SiC_X:H(n) layer.

The observed hydrogen or nitrogen extensions into the crystalline silicon might come from ion beam mixing during the measurement process [222]. The ion beam used to sputter the sample layer could propel the layer atoms further into the sample, potentially shifting the signal to greater depths. The highest hydrogen concentration in the passivating nc-SiC_X:H(n) is attributed to the minimal size of its crystallites, which improves the solubility of hydrogen, as previously discussed. In contrast, the larger crystallites in the conducting layer correlate with a reduced hydrogen solubility. The subtle peak near the interface of the conducting layer is likely a result of its nucleation phase [173], leading to a less crystalline structure and therefore increased hydrogen absorption in the initial nanometers of the film. Additionally, the crystalline silicon interface is terminated by hydrogen during the hydrofluoric acid dip prior to the wet-chemical oxidation. This might also result in an enhanced hydrogen content close to the crystalline silicon interface. Given that both the conducting and gradient layers share a similar hydrogen profile, the nucleation and initial growth phase of the crystallites may align with or exceed the ramping speed of the filament temperature, potentially limiting the impact of the temperature gradient. The initially increased hydrogen signal in the double layer originates from the higher hydrogen solubility of the passivating material. Additional hydrogen incorporation toward the conducting layer might arise from enhanced hydrogenation during the nc-SiC_X:H(n) deposition process, which is also observed for intentional hydrogenation in literature for polycrystalline silicon [223, 224]. Molecular hydrogen might get decomposed at the filaments and, due to the increased T_f for the conducting nc-SiC_X:H(n) deposition, the hydrogen radical density can increase, leading to the observed larger crystallites from improved hydrogen radical etching during the deposition. But as the passivating nc-SiC_X:H(n) layer is already grown, the hydrogen radicals might not have enough energy to etch it. Its energy could still be high enough to implant or diffuse

the atomic hydrogen into the nc-SiC_X:H(n) network, incorporating itself into the already deposited material. This additional hydrogen in the layer may then also diffuse towards the SiO_X/c-Si interface at elevated sample temperatures present during the deposition, improving the passivation quality of the layer stack. The absence of a pronounced increase towards the conducting nc-SiC_X:H(n) in the seed and gradient layer approach could be offset by a more gradual decrease in hydrogen in the gradient nc-SiC_X:H(n) part of the stack, which could provide sufficient hydrogen for superior passivation, as demonstrated earlier. Considering the uniform hydrogen content across all layers in the SiO_X, yet the different passivating quality of, for example, the passivating and conducting nc-SiC_X:H(n) single layers, it becomes evident that the proximity of hydrogen to the c-Si/SiO_X interface is critical. However, the maximum of hydrogen in the double layer's passivating nc-SiC_X:H(n) is not directly at the interface to the crystalline silicon but between the passivating and conducting layers. This could hint at an indirect hydrogenation of the passivating layer by the new process conditions of the conducting layer, introducing an elevated hydrogen concentration at the transition from passivating to conducting nc-SiC_X:H(n). The filament temperature is increased, a higher hydrogen radical concentration with higher radical energies is expected. These higher-energy radicals could implant themselves in the already grown passivating silicon nitride (SiN)(n) layer, increasing the hydrogen content in the passivating layer close in proximity to the conducting nc-SiC_X:H(n).

In this context, nitrogen serves as an indicator of the crystallinity of the sample, given its high solubility in silicon carbide crystallites [225]. The lower nitrogen content in the passivating nc-SiC_X:H(n) layer might stem from reduced solubility in smaller crystallites or decreased nitrogen availability due to lower filament temperatures, and thus reduced nitrogen precursor breakdown, during deposition. Nitrogen accumulation in the SiO_X could result from either ambient nitrogen adsorption during storage of the substrates in the nitrogen chamber or a potential catalytic doping effect during the deposition process.

The nitrogen signal in the conducting nc-SiC_X:H(n) layer witnesses a distinct increase near the SiO_X interface. The decreased nitrogen signal at the interface can again be linked to the layer's nucleation phase, since both the

hydrogen decrease and nitrogen increase share similar depth dependencies in the nc-SiC_X:H(n). The similarity in hydrogen signals between the conducting and gradient layers, contrasted by their differing nitrogen signals, suggests that the lower nitrogen intensity might be attributed to a reduced nitrogen availability during deposition, a consequence of the lower filament temperature and initial slow ramping. The controlled increase of nitrogen in the nc-SiC_X:H(n) is substantially shifted by incorporating the seed layer with a lower nitrogen signal, a result of the smaller crystallites or the reduced availability of nitrogen in this layer segment. In the double layer stack, one would anticipate the nitrogen signal to increase deeper within the layer than observed, given the passivating layer's low nitrogen content. This earlier rise might partially be an artifact from ion-beam mixing during measurements or potentially some form of catalytic doping. When filament temperatures rise, greater decomposition of the nitrogen precursor gas may occur, allowing diffusion into the passivating part of the double layer stack, thus explaining this deep nitrogen extension from the conducting layer to the passivating layer. If true, the activation status of these dopants remains uncertain, considering the relatively low dopant activation of the as-deposited passivating layer [111]. Both catalytic doping hypotheses, whether related to SiO_X or passivating nc-SiC_X:H(n), warrant future investigations to validate these theories.

4.4. Summary of Optimized Silicon Carbide Layer Stacks for Enhanced Solar Cell Performance

This chapter begins by revisiting the opto-electrical properties and passivating capabilities of device-quality hydrogenated nanocrystalline silicon carbide (nc-SiC_X:H), focusing particularly on the influence of various hot wire chemical vapor deposition (HWCVD) parameters and various effects at play during layer growth. Subsequently, the chapter delves into the trends in solar cell characteristics influenced by the passivating and conductive layers of nc-SiC_X:H(n), emphasizing and closely examining the trade-off between the

open-circuit voltage (V_{OC}) and Fill Factor (FF). Building upon this, a novel layer structure is introduced, aimed at mitigating this trade-off and enhancing solar cell performance.

In the initial section, an in-depth analysis of the electrical conductivity (σ) and transparency, represented by the optical band gap (E_{04}), is undertaken. The filament temperature (T_f) and hydrogen dilution (c_H) emerge as most important factors influencing σ of nc-SiC_X:H(n), capable of altering it across nine orders of magnitude each. The total gas flow rate (F_{total}) is identified as the third most significant deposition parameter, affecting σ by five orders of magnitude, while other deposition parameters exert negligible impact within the scope of this study. The increase in conductivity is attributed to an increase in grain size of the silicon carbide crystallites in the layer. In addition, an increase in E_{04} is observed, which means that larger crystallites also enhance material transparency. Both improvements are traced back to the reduced growth rate during the deposition process. The main mechanism to alter grain size in nc-SiC_X:H(n) is increased hydrogen radical etching, which selectively removes weakly bonded material. This can be achieved through increased T_f, enhancing the radical yield from the hydrogen (H_2) dilution gas, or higher c_H, increasing the fraction of hydrogen radicals relative to the material-depositing gas. The second notable effect that influences material growth is the density of decomposed precursor molecules on the substrate; a reduction in reactive species enhances surface mobility, facilitating larger crystallite formation. Lowering F_{total}, for example, decreases the density of reactive species on the substrate. However, the substrate temperature has minimal impact on the grain size.

The next part of this chapter explores the passivating properties of nc-SiC_X:H(n) and its hydrogen content in the form of the FTIR silicon-hydrogen bond peak intensity ($I_{Si\text{-}H}$). A decrease in T_f enhances the passivating quality of nc-SiC_X:H(n), as hydrogen, crucial for passivating dangling bonds at the crystalline silicon/SiO_X interface, is hypothesized to be located at the grain boundaries. Consequently, smaller grains resulting from reduced T_f improve hydrogen solubility in the layer, thereby enhancing the iV_{OC}. An increase in the filament-substrate distance ($d_{f\text{-}s}$) shifts the V_{OC}-T_f curve towards higher

temperatures, possibly due to diminished sample heating from the hot filaments, leading to reduced hydrogen effusion. Generally, the hydrogen content in the layer can be increased by lowering T_f, reducing c_H, and maintaining an intermediate F_{total}. Although the $I_{Si\text{-}H}$ signal does not reach saturation at lower T_f, the V_{OC} does. However, directly correlating these values is challenging in this context, as the samples originate from separate deposition systems. It is speculated that the passivating potential of hydrogen might have an upper limit, beyond which additional hydrogen incorporation does not further improve passivation quality.

In the third section of this chapter, dependencies of the solar cell performance on each nc-SiC_X:H(n) layer within the double layer stack approach within transparent passivating contacts (TPCs) are investigated. Once a minimum thickness threshold is reached for the passivating nc-SiC_X:H(n) to obtain a sufficient passivation quality, primarily the iV_{OC} and FF are affected by the variations of the passivating nc-SiC:H(n) layer thickness ($d_{pass,\,SiC}$). There is a slight increase in iV_{OC} correlated with an increase in $d_{pass,\,SiC}$, yet FF decreases significantly, mainly due to the increase in contact resistivity (ρ_c). Regarding the adjustments in the $d_{cond,\,SiC}$, after surpassing a initial minimal thickness for improved hydrogen incorporation into the layer stack, the primary impact is again on FF. Here, an increase in ρ_c is found with a related decrease in FF. For exceedingly thin $d_{pass,\,SiC}$ or $d_{cond,\,SiC}$, a deterioration in all parameters of the solar cell is observed. This phenomenon can be predominantly ascribed to insufficient hydrogen incorporation within the layer stack during deposition, resulting in insufficient surface passivation of the crystalline silicon and thus impairing the overall solar cell performance. Furthermore, with variations in $d_{cond,\,SiC}$, a modification in the reflective behavior of the solar cell is expected. Calculations indicate a decrease in reflection losses by $0.5\,\frac{mA}{cm^2}$ with an increase in $d_{cond,\,SiC}$, yet the short-circuit current density (J_{SC}) of the solar cell does not mirror this trend. This discrepancy could be attributed to the strong parasitic absorption by the ITO in the same wavelength regions where gains are expected, potentially negating these improvements. Furthermore, for alterations in $d_{pass,\,SiC}$, a notable trade-off emerges between iV_{OC} and FF, presenting a significant limitation to improvements in solar cell efficiency. Given the relatively low conductivity of the passivating nc-SiC_X:H(n), a thicker

layer increases the overall resistance within the stack, yet this layer is essential to provide hydrogen for passivation at the crystalline silicon/SiO_X interface.

The fourth part of this chapter proposes a solution to mitigate the aforementioned trade-off. To increase the conductivity near the crystalline silicon surface, the passivating nc-SiC_X:H(n) layer is replaced with a graded layer, in which the deposition conditions are slowly transitioned from passivating-like to conducting-like. With this layout, thicker graded nc-SiC:H(n) layer thicknesses ($d_{\text{gradient, SiC}}$s) result in both a reduced *FF* and iV_{OC} due to the low conductive section of the gradient layer, coupled with increased sample temperatures from an extended deposition process leading to hydrogen effusion. Conversely, thinner $d_{\text{gradient, SiC}}$ layers yield a high *FF* but a reduced V_{OC}, attributed to an inadequate passivation quality of the layer. Intermediate $d_{\text{gradient, SiC}}$ deliver outcomes akin to the double layer stack approach. By integrating both strategies and incorporating an ultra-thin passivating seed layer alongside the graded layer, enhancements in both *FF* and iV_{OC}, as well as the overall V_{OC}, are achievable. This leads to a general increase in cell efficiency of 0.2%$_{\text{abs}}$, with a potential possible increase in power conversion efficiency (η) of up to 0.5%$_{\text{abs}}$ compared to the double layer approach.

5. Sputter Process-Induced Degradation in Nanocrystalline Silicon Carbide Passivation

This chapter dives into the systematic exploration of the ITO sputter deposition process and its impact on the passivating properties of nc-SiC$_X$:H(n). Previous studies have highlighted a severe deterioration in passivation quality after the ITO deposition, evident in the degradation of the V_{OC} in solar cells compared to the iV_{OC} of their precursors [111]. This phenomenon is one key limitation to the power conversion efficiency of TPC solar cells based on nc-SiC$_X$:H(n) functional layers. Through the combination of experimental and simulation approaches, this investigation aims to unravel the mechanisms behind sputter-induced degradation in transparent passivating contacts. Various possible contributing factors are discussed and a theory to understand the origins of such damage is suggested. Furthermore, the last section examines the annealing behavior of transparent passivating contact solar cells, with an focuses on assessing the possibilities with which annealing can cure sputter-induced damage. Results of sections section 5.2 and section 5.3 are also published in a peer-reviewed publication in [226] and finding from section 5.4 are published in a peer-review manuscript in [227].

5.1. Sputter Process-Induced Degradation in Passivating Contacts

The sputter deposition process, particularly when employing TCOs like ITO, exposes the sample to a multitude of potential damaging effects, as illustrated in figure 5.1. One such effect is substrate heating, which, if the sample temperature is too high, can degrade the passivation quality of the sample through, e.g. hydrogen effusion. However, beneficial results, such as in-situ annealing, may also arise. The interaction of the substrate with sputtering or doping gases, such as argon (Ar) or O, presents another potential influence through the reaction with the sample layer materials. The plasma generated during this process emits electromagnetic radiation, extending into the vacuum ultra-violet (VUV) regime [228, 229], capable of dissociating silicon-hydrogen and silicon-silicon bonds, which have binding energies of 2.35 eV and 2.5 eV, respectively [230, 231]. Additionally, the bombardment of ions, neutrals, and compounds plays a major role in the sputter process. These species, which may include ionized target atoms like indium (In), tin (Sn) and O, ionized sputter gas atoms like Ar and O, or ionized atmospheric residuals like molecular hydrogen (H), can impact the sample in both ionized and neutral states. The interaction of these elements in the gas phase can lead to the formation of charged compounds such as ArO^+, $InAr^+$, or $SnAr^+$, which also impinge on the sample. The distribution and intensity of these impinging particles are influenced by factors such as plasma excitation mode, target erosion, and process conditions. For instance, an increase in pressure during deposition can decrease the average energy of incident ions due to a reduced mean-free path in the gas phase. [232–235]. The acceleration of ions, neutrals and compounds towards the substrate is given by the voltage applied between the substrate and the target (V_T) and the charge state of the ion (c_s), giving the incident ion energy (E_{ion}) as

$$E_{ion} = V_T q c_s. \tag{5.1}$$

The charge state of the ion is typically assumed to be ± 1 unless specified otherwise. Furthermore, reactions and neutralization processes on the target surface

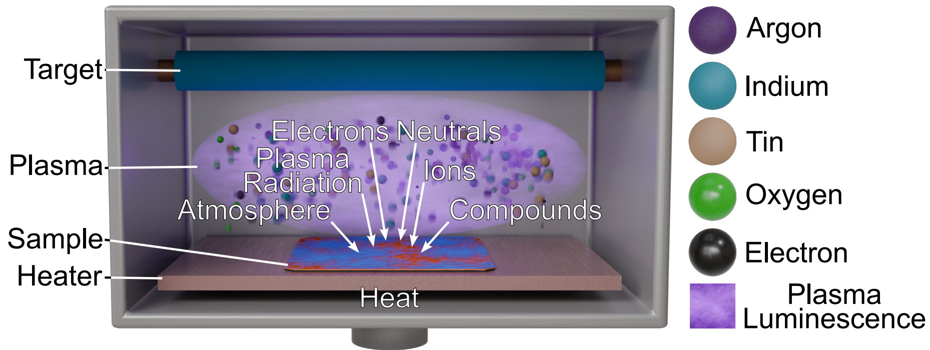

Figure 5.1.: *Schematic representation of the sputtering chamber, highlighting various factors influencing the sample, including the sputter atmosphere, electromagnetic emissions from the plasma, and the impact of ions, neutrals, and compounds from the target and sputter or doping gases, as well as electrons from the plasma. Reprinted under CC BY 4.0 from Ref. [226].*

can lead to potential variations in E_{ion}, which can produce higher-energy tails [236]. It is assumed that the behavior of reflected neutrals and compounds is similar to that of the ions. Furthermore, the direct current used to sustain the plasma enables the acceleration of electrons towards the sample with an maximum incident electron energy (E_{electron}) of

$$E_{\mathrm{electron}} = V_{\mathrm{T}} e, \tag{5.2}$$

where the elementary charge of an electron is e and if no collisions occur.

When ions impinge on the sample, they can be implanted within the layer, transferring their energy to the lattice through collisions with its atoms or to electrons through electronic interactions. This interaction can result in the sputtering or displacement of sample atoms, thereby creating vacancies within the nc-SiC_X:H(n) structure. Furthermore, the ions may excite electrons and ionize lattice atoms or generate phonons, that are quantized lattice vibrations, which propagate through the layer. Electrons, on the other hand, can induce secondary electrons by colliding with inner-shell electrons of lattice atoms. This process results in the ejection of a secondary electron and the subsequent emission of x-rays as an outer-shell electron fills the electron vacancy, releasing its energy as

x-rays. Furthermore, if primary electrons are deflected and decelerated by nuclei of layer lattice atoms, soft x-rays might be emitted as bremsstrahlung.

The deteriorating effects of the sputter deposition are not exclusive to nc-SiC_X:H(n). Similar phenomena have been observed in a-Si:H and poly-Si [237–241]. In the context of nc-SiC_X:H(n)-based passivating contacts, exposure to VUV radiation is detrimental, although its effect is mitigated during actual deposition processes by a protective growth of the ITO film. Ion bombardment, on the other hand, has been identified as a significant source of damage in this material. [29] In a-Si:H, studies suggest that damage from electromagnetic radiation saturates after a certain exposure duration, unlike the continuous damage from ion bombardment. Electromagnetic radiation, especially VUV radiation, is likely breaking the silicon-hydrogen bonds, while the latter is hypothesized to generate bound electron-hole pairs, referred to as excitons, that migrate and recombine non-radiatively at the crystalline silicon interface, in turn displacing hydrogen atoms and creating dangling bonds. Post-annealing processes can partially reverse this damage, but alterations in silicon-hydrogen bonding configurations are found, as observed by FTIR, indicating a change in the microstructure of the a-Si:H or at the crystalline silicon interface. [237–240]

For poly-Si passivating contacts, damaging mechanisms are expected to be similar to those in a-Si:H, with electromagnetic VUV radiation from the plasma and ion impact contributing to degradation. Again, non-radiative recombination of excitons at the crystalline silicon interface is suggested as a primary damaging mechanism. [241] In the case of hydrogenated nanocrystalline silicon (nc-Si:H), damage severity correlates with material density, where denser layers exhibit reduced damage. Unlike a-Si:H and poly-Si, electromagnetic radiation, including VUV, is not considered a significant damage factor for nc-Si:H. [242]

Across these types of materials, the extent of damage is influenced by deposition conditions, such as pressure and power. Higher pressure and lower power settings tend to reduce damage, likely due to decreased ion energy resulting from increased thermalization or reduced V_T. Furthermore, it is found that the initial damage in both the a-Si:H- and poly-Si-based passivating contacts depends on the thickness of the silicon layer, with thicker layers offering better resistance to

damage. In most cases, this damage is reversible, except in cases of extremely thin layers where irreparable damage is observed. [29, 241, 243]

Generally, the phenomenon of sputter process-induced damage in silicon-based materials to the passivation can be separated into recoverable and non-recoverable. In cases where non-recoverable damage occurs, particularly with extremely thin layers of a-Si:H or poly-Si, primary ions may implant near or at the crystalline silicon interface. This proximity can lead to material distortion and defect generation, either through the presence of an interstitial atom or a vacancy created by a displaced lattice atom. Such modifications increase the number of recombination centers at the interface, thereby reducing the passivation quality. These permanent defects, induced by implanted atoms, are unlikely to be restored at annealing temperatures that prevent hydrogen effusion, given the substantial activation energy required to mobilize the interstitial atoms or vacancies, as discussed later.

In the scenario of recoverable sputter-induced damage, different mechanisms are worth to consider. One such mechanism is the rupture of silicon-hydrogen or silicon-silicon bonds at the crystalline silicon interface, attributed to high-energy VUV radiation. These bond ruptures increase the number of interface defects, leading to a reduction in passivation quality. The specific mechanisms by which secondary effects of ion impact or implantation at a distance from the crystalline silicon interface, insufficient to directly impair passivation, cause damage remain somewhat elusive. The prevailing hypothesis for a-Si:H by Illiberi et al. [237], and adapted to poly-Si by Tutsch [241], involves the generation of an exciton by the impinging ion, which is believed to migrate to the crystalline silicon interface and recombine non-radiatively. This event is again thought to break a silicon-hydrogen bond, displacing the hydrogen atom in the process. However, the potential impact of electrons striking the sample surface has not been sufficiently explored to date, leaving a gap in our understanding of these secondary effects.

5.2. Impact of the Sputter Process on nc-SiC:H Material Properties and the Role of Sputter Atmosphere

This section examines the significant degradation in the passivation quality of TPC-passivated samples following the sputter deposition process. To negate any effects from a-Si:H layers, samples with symmetric TPC structures on both sides of the wafer are used. The focus is on the impact of this process on the material properties of nc-SiC_X:H(n) and the effect of the sputter atmosphere on degradation. The effective minority carrier lifetime (τ_{eff}) curves at various processing stages are depicted in figure 5.2. Initially (1), the TPC demonstrated an exceptional iV_{OC} of 747.3 mV. After ITO deposition (2), there was a significant reduction in the lifetime curve by two orders of magnitude in the entire minority carrier density (*n*) range. Subsequent annealing at 230 °C for 20 minutes in ambient atmosphere (3) reversed this damage to a large extent, although a reduction in the lower *n* regime persisted due to a field-effect or the band offset induced by the ITO [238, 244, 245], which alters the shape of the τ_{eff} curve in the low and medium minority charge carrier densities. For high minority charge carrier densities, enough charge carriers are generate to compensate the field-effect or band offset induced by the ITO. Remarkably, upon removal of the ITO, the lifetime curve aligned almost perfectly with the initial measurement. This indicated that the degradation in passivation quality of the transparent passivating contact was fully reversible, contrasting previous reports suggesting residual damage [29], and again underlined the excellent passivation properties of the TPC approach. The annealing behavior will be addressed again in section 5.4, where the reason for the previously though un-recoverable damage is highlighted. Upward kinks for very low minority charge carrier densities in curve (1) and (4) can be attributed to the trapping of minority charge carriers in traps, avoiding their recombination and artificially increasing τ_{eff}. Upward kinks at very high minority charge carrier lifetimes are a measurement artefact, as confirmed by Sinton Instruments.

The observed degradation in τ_{eff} and iV_{OC} suggested a significant alteration in the configuration of the silicon-hydrogen bonds at the crystalline silicon/SiO_X

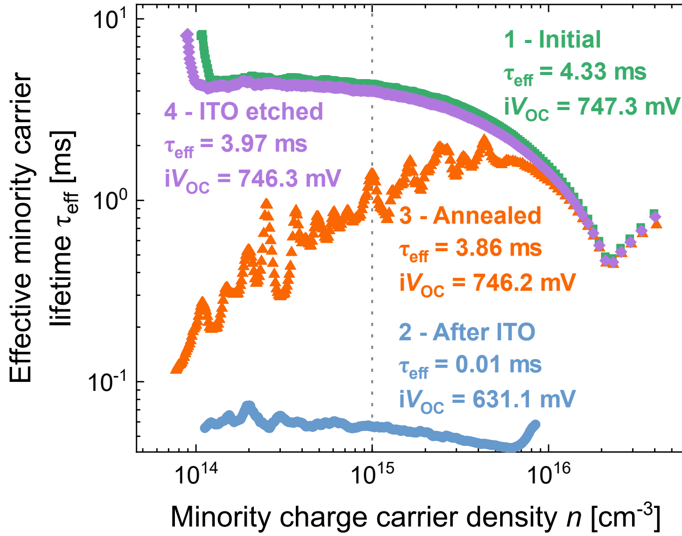

Figure 5.2.: *Measured lifetime curve for textured silicon wafers symmetrically passivated with the TPC structure. The initial effective minority carrier lifetime (τ_{eff}) (1) is strongly reduced after the sputter process (2), but recovers with an additional annealing (3) at 230 °C for 20 minutes in ambient atmosphere. After the ITO is removed (4), the lifetime curves nearly overlap again. The corresponding implied open-circuit voltage (iV_{OC}) values are given in the figure. The dashed line marks the minority carrier density (n) of 10^{15} cm^{-3}, at which τ_{eff} is defined. Reprinted under CC BY 4.0 from Ref. [226].*

interface. To illuminate this, the electrical properties and microstructural characteristics of the nc-SiC_X:H(n) were analyzed, as shown in figure 5.3. FTIR spectra of the silicon-carbon peak at 780 cm^{-1} and the silicon-hydrogen peak at approximately 2100 cm^{-1} [246] revealed no discernible changes in different processing steps. Similarly, Raman spectroscopy spectra and hydrogen effusion profiles remained unchanged within the measurement uncertainties, indicating that there were no substantial modifications in the crystallinity, grain size, or phase composition of the material. These observations suggested that the sputter process does not significantly affected the microstructure of the material, including damage to the grains or phase separation, as the silicon-carbon peak was undisturbed and no additional carbon or silicon peaks emerged. This was also shown by the unchanged electrical conductivity, as shown in the table inlet in figure 5.3 d), which was strongly correlated with the microstructure of the material [95]. Surprisingly, despite the maintained silicon-hydrogen bond configuration as

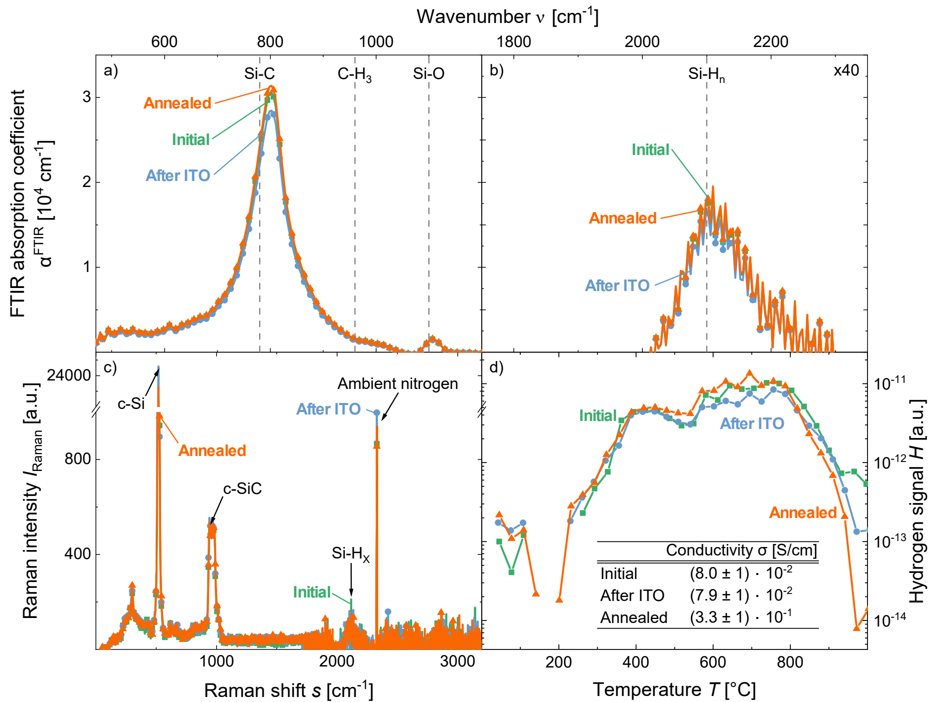

Figure 5.3.: *FTIR measurements of the a) silicon-carbon and b) silicon-hydrogen peak, c) Raman spectroscopy, and d) hydrogen effusion measurements with the inlet showing the electrical conductivity (σ) for the different processing steps. The FTIR, Raman spectroscopy, and σ samples have the ITO etched off, while the hydrogen effusion measurement sample is measured with the ITO still on the stack. For all different characterization methods, no deviation between the curves of different processing steps is found. The different peak positions [173, 174, 246] are marked by dashed lines.*

indicated by FTIR and Raman spectroscopy, as well as the overlapping hydrogen effusion profiles, there was a notable reduction in passivation quality post-sputter deposition. Since SiO_X did not provide a meaningful passivation itself and no significant field-effect passivation is known [111], this reduction was likely attributed to a reduced chemical passivation by hydrogen, albeit with potentially subtle changes at the c-Si/SiO_X interface that is most likely beyond the detection limits of the spectroscopic methods employed or obscured by signals from the bulk nc-SiC_X:H(n) material.

The presence of ITO appeared to distort parts of the lifetime curve even

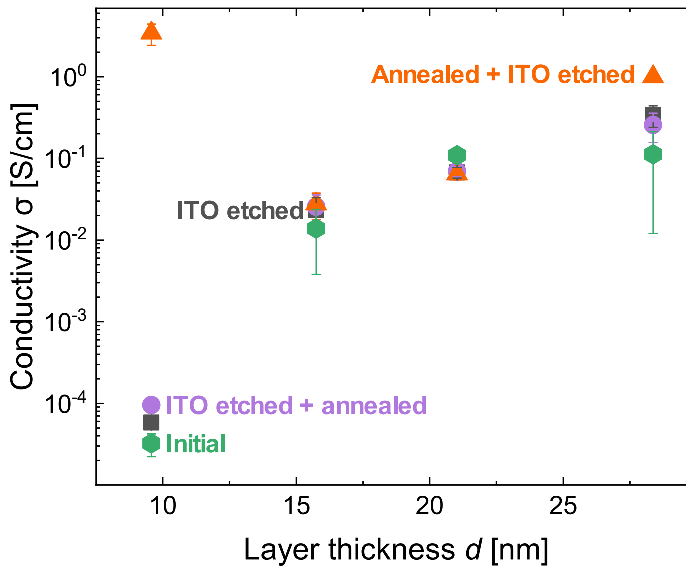

Figure 5.4.: *The layer thickness (d)-dependent electrical conductivity (σ) of hydrogenated nanocrystalline silicon carbide (nc-SiC$_X$:H) layers before and after indium tin oxide (ITO) deposition. To evaluate the damage to the material, the ITO is etched away, either before or after annealing at 230 °C for 20 minutes on a hot plate in ambient atmosphere. No significant alterations in σ are observed regardless of the sample processing method.*

after annealing, suggesting potential damage to the superficial nc-SiC$_X$:H(n) layer caused by the sputtering process, which could have resulted in reduced charge carrier concentrations. Although ITO was expected to induce only minor band bending in the initial nanometers at the ITO/nc-SiC$_X$:H(n) interface [219], any damage in this area could have affected the ability of the nc-SiC$_X$:H(n) to shield against field-effects from the ITO. To investigate this damage, thin films of nc-SiC$_X$:H(n) with varying thicknesses were prepared. The ITO was sputtered onto the nc-SiC$_X$:H(n) and subsequently etched away. The samples underwent annealing at 230 °C for 20 minutes either before or after the ITO etching. At these thin layer thicknesses, σ depends on d [95] as shown in figure 5.4 and any material damage, and thus reduction in charge carrier concentration, would have significantly affected the measured conductivity in this critical thickness interval.

As expected, the conductivity increased with d. In particular, a very high conductivity was observed for the thinnest layer if the sample was first annealed

and then the ITO was etched away. This σ was even higher than the highest recorded in section 4.1.1, suggesting that it might have been an outlier. Regardless of post-processing, no change in σ and thus charge carrier concentration relative to the pre-ITO deposition state was detected. Consequently, it was concluded that the nc-SiC_X:H(n) thin films were not significantly damaged by the sputtering process, and an extended field-effect from the ITO as a source of degradation in passivation quality was dismissed.

Figure 5.5 presents the iV_{OC} measurements for three distinct process variations: The standard reference process, a process involving sample exposure to process gases without plasma ignition and therefore no ITO deposition but with the sample being exposed to the deposition atmosphere, and a process with ignited plasma but deactivated sample heater resulting in an ITO deposition at lower sample temperatures. Each variation assesses the iV_{OC} in the initial state, after the ITO deposition and after the standard annealing step at 230 °C for 20 minutes.

For the reference process, a notable reduction in iV_{OC} was observed after ITO deposition, which was fully reversible upon annealing. In the absence of a plasma, there is no reduction in iV_{OC}, indicating that the mere presence of process gases or sample heating did not affect passivation quality. As the degradation of the reference process was reversible, it was expected that the additional energy intake of the sample through ion bombardment during the sputter process did not heat up the sample to a critical temperature and temperature indication tapes measured a temperature below 200 °C. In contrast, when the sample heater was off, the reduction in iV_{OC} was significantly greater than in the reference process, suggesting a detrimental effect of lower sample temperatures on passivation.

When comparing passivation damages in the reference process with reduced iV_{OC} in figure 5.2, it was evident that the samples in this study exhibit less deterioration. In this study, process conditions were used to minimize the damage to the passivation [29], while process conditions of the reference sputter process as used for silicon heterojunction were used for the lifetime curves shown previously. Despite similar opto-electrical properties, the less damaging ITO deposition employed higher pressures and lower powers, which reduces E_{ion}, as previously

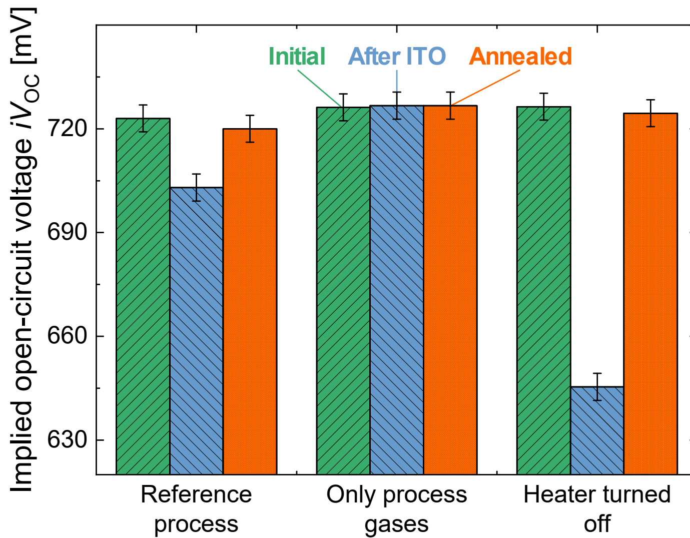

Figure 5.5.: *Implied open-circuit voltage (iV_{OC}) measurements for the initial sample stack, after ITO deposition, and after annealing at 230 °C for 20 minutes. The standard reference process is compared with a process variant without plasma ignition but with the sample heater and process gases active, resulting in no deposition but the sample being exposed to the deposition atmosphere, and another variant where the plasma is ignited but the sample heater is off, leading to an ITO deposition at lower temperatures. The process without plasma ignition shows no damage, while deactivating the sample heater results in significantly increased passivation damage.*

discussed. After confirming the reversibility of sputter-induced iV_{OC} reduction, all samples were processed using standard silicon heterojunction procedures to streamline sample preparation. As the damage of both processes was reversible, a valid comparison was possible across different experimental conditions in this study.

Given that the process variant without plasma ignition did not compromise the passivation quality, it was shown that neither the process gases nor the sample heater temperature alone could have caused the observed damage. Thus, the degradation was likely attributable to components of the plasma. The increased damage observed with a deactivated sample heater suggested a diminished effect of in-situ annealing or possibly an intensified damage mechanism at play. Considering that the estimated sample temperature during the reference process was around 170 °C, based on the temperature indication tapes, and even lower

with the sample heater off, it was unlikely that in-situ annealing significantly affected nc-SiC_X:H(n), which required higher temperatures for thermal restoration, as will be detailed in section 5.4. The possible relationship between the secondary effects of ion bombardment and the observed damage will be explored in the following sections.

5.3. Assessing the Role of Light, Electrons, and Ions in Sputter Process-Induced Degradation in nc-SiC:H

This section examines the various factors that might impact passivation quality during the sputter deposition process. As discussed previously, emissions from an oxygen plasma have been shown to affect passivation quality, although not significantly in actual deposition processes [29]. To confirm these findings, QSSPC-corrected PL images, taken after the sputtering process and after an additional annealing step, are presented in figure 5.6 a) and b), respectively. Different filter glasses with varying cut-off wavelengths were fixed on the sample using tape to isolate the effects of different parts of the light emitted from the plasma. Filter A transmitted only some part of the VUV emissions, while filter B transmitted all VUV emissions. Filter C cut all UV emissions off, and filter D blocked all blue and higher-energy light. The plasma emission spectra and filter transmissions are shown in figure 5.6 c). Radiation emitted from the argon or oxygen plasma includes light from the visible spectrum down to the wavelength in the VUV spectrum [228]. However, no passivation damage was observed under any filter, regardless of the cut-off wavelength or even the tape to fix them on the sample, confirming that plasma-emitted light was not a significant factor in degrading the passivation quality of TPCs and the degradation most likely originated from particle bombardment.

The role of electrons in the sputter process was first investigated through simulations, focusing on the maximum penetration depth (d_{max}) of electrons in the nc-SiC_X:H(n) layer. The simulations considered variations in crystalline volume

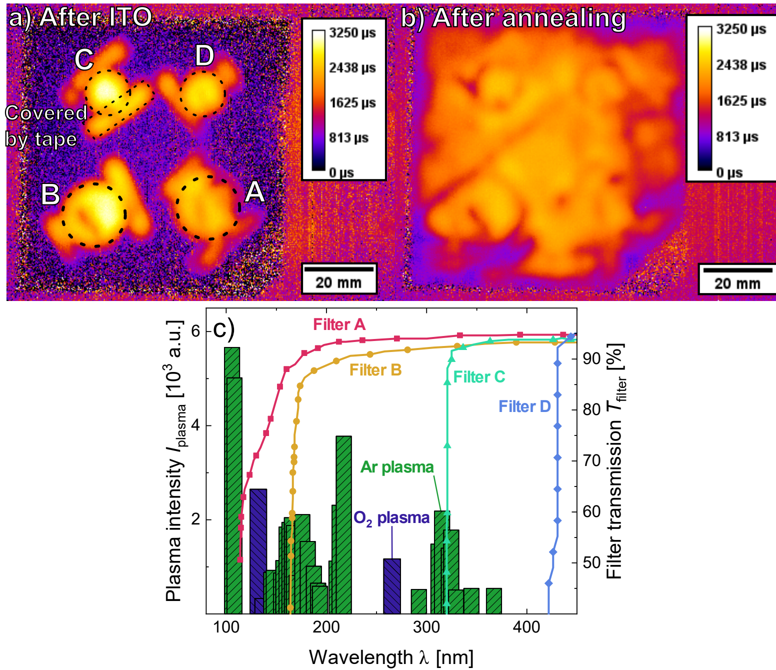

Figure 5.6.: *Quasy-Steady State Photoconductance (QSSPC)-corrected photoluminescent lifetime (PL) images of a symmetrical sample passivated with transparent passivating contact (TPC) a) before and b) after the ITO deposition process, with c) showing the transmission spectra of various filter glasses used during deposition, compared with plasma light emission data extracted from ref. [228]. Reprinted under CC BY 4.0 from Ref. [226].*

fraction (X_C), incident electron energy ($E_{electron}$), and hydrogen content (c_H), as illustrated in figure 5.7 a), b) and c), respectively. The results indicated that d_{max} was sensitive to the crystallinity of the material and incident electron energy, but remained relatively unaffected by the hydrogen content of the layers. d_{max} decreased from 5.0 nm to 3.7 nm for the amorphous to crystalline transition. For low $E_{electron}$, the electrons could not penetrate the layer, and electrons began to enter the layer at energies of approximately 50 eV. They could reach depths up to 9.4 nm for an $E_{electron}$ of 500 eV. Assuming the standard material properties and process conditions with a X_C of 80%, c_H of 13 at% and an $E_{electron}$ of 270 eV, the simulated d_{max} was 3.9 nm. A more amorphous material decreased the atomic order in the layer, increasing the spacing between the atoms. This reduced

the interaction probability of an electron with the layer material, increasing the maximum penetration depth. On the other hand, with a higher incident energy, the electrons had more energy they could lose through interactions with the layer atoms before they were stopped inside the layer. Hydrogen was the smallest atom available, so it could have been expected that it would have reduced the interaction probability with the electron since its small size. From the simulations, this seemed to be negligible because either the small size of the electron itself, or the effect was overshadowed by other energy-loss interactions of the electron. However, even at the highest energies, the electron was stopped within the first 10 nm and did not reach the crystalline silicon/SiO_X interface. Therefore, it was expected that it does not impact the passivation quality.

The simulations additionally explored x-ray generation within the nc-SiC_X:H-(n) layer, depending on its crystallinity and the incident electron energy in figure 5.7 c) and d), respectively. The findings suggested that, while x-ray generation occurred within the first angstroms at the generation threshold, it penetrated deeper with increasing electron energy, and x-ray generation could be found at a depth of up to 9 nm for an incident electron energy of 500 eV. For increasing X_C at the onset of x-ray generation, the generation depth did not change significantly and remained within 0.1 nm between the amorphous and crystalline cases. However, the target voltages and the resulting electron energies in the reference sputtering process were below the simulated threshold of 290 eV for the generation of x-rays, which implied that neither x-rays nor secondary electrons are likely to be significant contributors to passivation damage. The simulated onset was reasonable since the lowest-energy K transmission in silicon or carbon is the carbon K_α transition at 277 eV [247]. Moreover, the superficial nature of x-ray generation within the pathway of the electron in the layer and the behavior of secondary electrons, which did not penetrate deeply into the layer due to the lower energy or triggered further secondary electron generation, since they immediately lost energy due to breaking effects, which made cascading damage events which might have reached the crystalline silicon interface highly improbable. High energetic x-rays have a long attenuation length in silicon carbide, similarly so in silicon [248], so the x-rays might have been transmitted through the layer or whole sample. If the x-rays are instead absorbed in the layers or sample and since

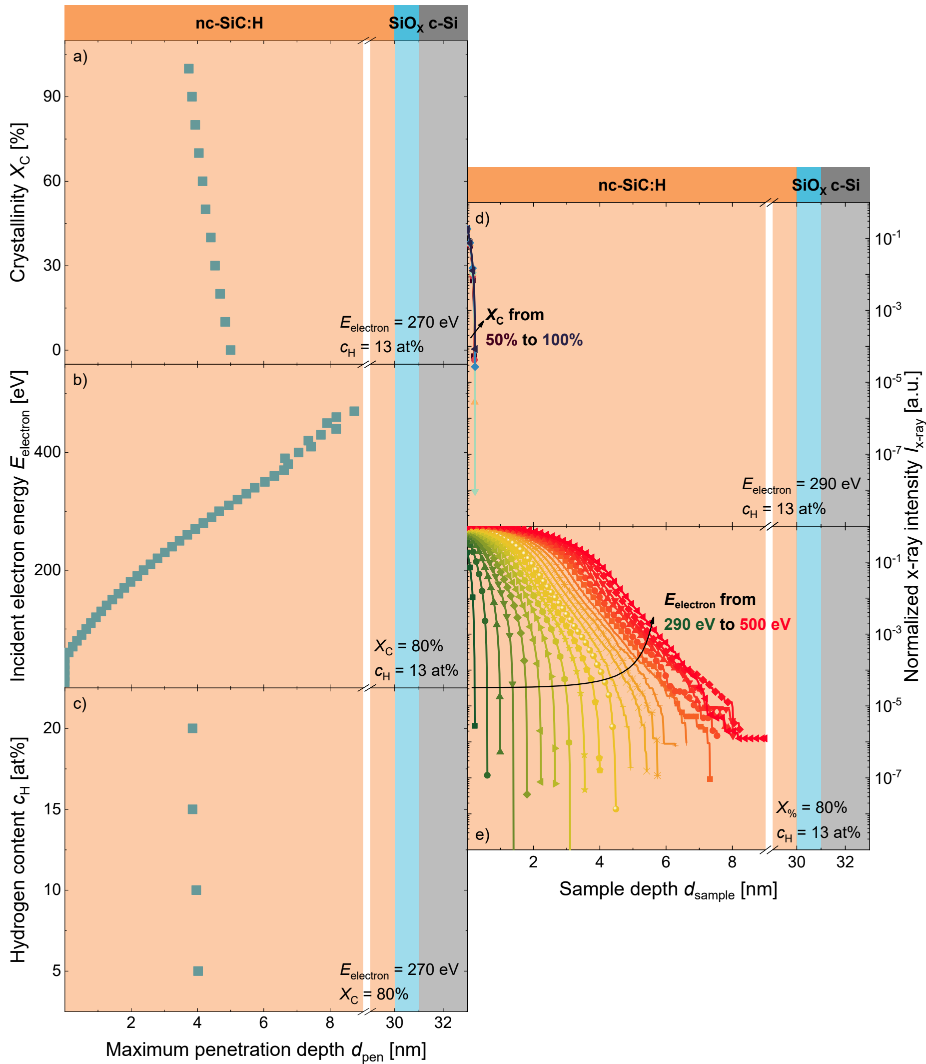

Figure 5.7.: *Simulated profiles of variations of a) crystalline volume fraction (X_C) of the nc-SiC$_X$:H(n), b) incident electron energy ($E_{electron}$) of the incident electron, and c) hydrogen content (c_H) of the nc-SiC$_X$:H(n) on maximum penetration depth (d_{max}), and x-ray generation profiles depending on d) X_C and e) $E_{electron}$. d_{max} increases for decreasing X_C and increasing $E_{electron}$. X-ray generation is superficial but increases for increasing $E_{electron}$.*

the VUV irradiation with energies higher than the energy of a silicon-hydrogen bond in the previous experiment did not damage the passivation quality, it was assumed that x-rays did not as well. When x-rays were generated, secondary electrons were additionally emitted. The energy of these electrons was assumed to be the minimum energy of 277 eV of the lowest x-ray emission line in carbon or silicon. With these energies, it was known that the penetration depth was only a few nanometers, and since there were interactions with the layer atoms, they would not have enough energy to create another secondary electron, which could have lead to electron cascades. Therefore, it was unlikely that a primary incident or secondary electron reached the crystalline silicon. X-rays were generated superficially, but the transmission through the material was not known. It was expected that, similar to VUV radiation, there was no degradation in passivation quality.

To experimentally validate the assumptions regarding the impact of electron irradiation and its secondary effects, a part of a symmetrically passivated sample with the TPC structure was exposed to an electron beam. This exposure occurred in a scanning electron microscope with an electron beam energy of 500 eV and a beam current of 1.6 nA. The QSSPC lifetime-corrected PL image, presented in figure 5.8, showed no detectable degradation in τ_{eff} within the irradiated area. Given that the electron energy was sufficient to generate x-rays and secondary electrons, it could be deducted that neither the primary electron impact nor its secondary effects compromised the passivation quality. This finding, along with the previous exclusion of electromagnetic radiation from the plasma and sputtering atmosphere as damaging factors, narrowed down the likely cause of sputter-induced degradation to ion bombardment.

Simulations of the ion bombardment process were carrier out to understand its influence. The results for d_{max} of primary incident ions are displayed in figure 5.9, considering variations in the X_C of nc-SiC_X:H(n) in a), the E_{ion} of the impinging oxygen ions in b), and the c_H of nc-SiC_X:H(n) in c). Oxygen ions, the smallest in the study, exhibited the deepest penetration depth because of their lower collision probability with layer atoms due to their small size compared to other investigated ion types. The maximum penetration depth for oxygen was

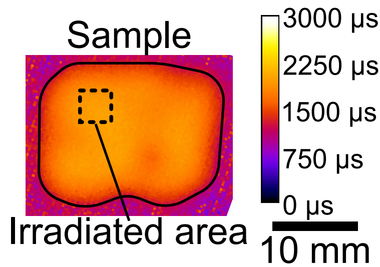

Figure 5.8.: *Quasy-Steady State Photoconductance-corrected photoluminescent lifetime (PL) image of a sample part irradiated with an electron beam in a scanning electron microscope. The beam energy is set at 500 eV, with a beam current of 1.6 nA. No degradation in the irradiated area is observed. Figure b) is reprinted under CC BY 4.0 from Ref. [226].*

4.8 nm, 3.7 nm for argon, 3.4 nm for tin and 3.2 nm for indium. Therefore, further discussions and investigations will focus on oxygen. The trends observed for ion penetration mimicked those for electron penetration; a more amorphous material structure lead to increased ion penetration from 4.3 nm in the crystalline to 5.8 nm in the amorphous case due to a larger atomic spacing and thus lower probability of ion-atom scattering events. Higher incident energies allowed ions to penetrate deeper before energy loss stopped their movement. An E_{ion} of 150 eV lead to a d_{max} of 3.6 nm, while an E_{ion} of 750 eV resulted in a d_{max} of 8.1 nm. Even with higher charge states, resulting in higher incident energies, it appeared implausible that direct ion penetration was the primary cause of passivation degradation at the crystalline silicon/SiO_X interface, as the deepest penetration depths for oxygen ions still fell within the first third of the sample depth. Even though the hydrogen was the smallest atom, c_H had a negligible effect on the maximum penetration depth.

Experimental validation of ion penetration depths, as suggested by the simulations, was performed using energy-dispersive x-ray spectroscopy (EDX). The results presented in figure 5.10 revealed that the interface between ITO and nc-SiC_X:H(n) was not sharply defined in the measurements, so the inflection point of the silicon signal was used as a reference point to determine the penetration depth. Within the ITO layer, indium exhibited the strongest signal, followed by oxygen, tin, argon, and silicon. The penetration depths of indium, argon, and tin in nc-SiC_X:H(n) were approximately 1.7 nm, while oxygen penetrated deeper,

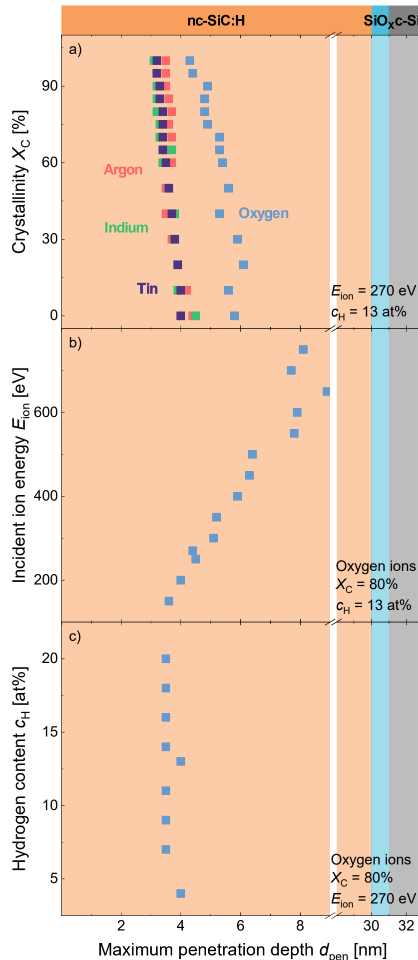

Figure 5.9.: *Simulated maximum penetration depth (d_{max}) for a) various ion types for different crystalline volume fractions (X_Cs), b) oxygen ions with varying incident ion energies (E_{ion}s) and c) oxygen ions for various c_Hs. Increasing d_{max} is observed with lower X_C and higher E_{ion}, with oxygen ions penetrating deeper than other ion species.*

reaching approximately 3.7 nm. The variation in signal intensity for the different elements was attributed to the differing capacities of these elements to ionize, which did not necessarily reflect their actual concentration in the layer. The similarity in the penetration depths of the larger ions, indium, argon, and tin, and the deeper penetration of the smaller oxygen ions aligned with the simulation predictions.

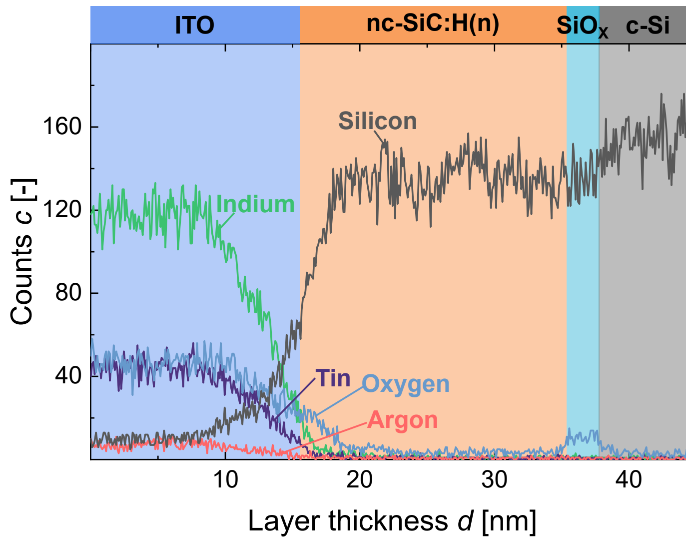

Figure 5.10.: *Energy-dispersive x-ray diffraction line scans across the full transparent passivating contact (TPC) stack including the indium tin oxide (ITO) layer after the sputter deposition process. The penetration depths of indium, tin, argon, and oxygen ions are compared. Reprinted under CC BY 4.0 from Ref. [226].*

The blurred interface in the EDX scans could have been due to depth effects during measurement or a sample alignment not perfectly perpendicular under the electron beam, possibly leading to x-ray information from below the surface layer. In general, the simulations slightly overestimated the measured penetration depths by one to two nanometers, which could have been due to the unclear definition of the ITO/nc-SiC_X:H(n) interface or deviations in the assumed material parameters. However, given the reasonable agreement between simulations and measurements within the uncertainties of the interface definition, these results offered valuable insight into the ion-bombardment and implantation process. With these shallow d_{max} within the first 5 nm of the nc-SiC_X:H(n), it was unlikely that ion implantation was a direct cause of the degradation in passivation quality of the crystalline silicon interface.

On penetrating the sample, ions interacted with layer atoms, primarily through collisions that transferred energy. If an ion collided with a lattice atom and sufficient energy was transferred, it could have displaced the atom, creating a recoiled atom and potentially a vacancy if the displaced atom was not replaced

by another recoiling atom. The transferred energy must have been greater than the energy needed to remove the atom from its lattice site and displace the lattice atom. The recoiling atom itself was then interacting with the layer atoms similarly to the incident ions. If there was not enough energy to displace the atom in the collision, the energy was given to the lattice as lattice vibration, called phonons. Additionally, incident ions interacted with the electrons of the layer atom, transferring energy and generating free electrons or electron-hole pairs [237]. This was summarized as ionization. The energy distribution for the assumed standard process, specifically focusing on the lightest ion, oxygen, and heaviest ion, tin, is illustrated in figure 5.11. Most of the incident energy with more than 60% was converted into phonons, with a significant portion of 30%-35% causing ionization of lattice atoms and a smaller fraction of 5% leading to vacancy creation. Lighter ions like oxygen tended to favor ionization, whereas heavier ions like tin contributed more to phonon generation, because the larger ions had a less-dense electron cloud and thus the interaction with the electrons of the layer atom might have been reduced [249, 250]. Vacancy generation appeared to be relatively unaffected by ion size, probably because this process required more energy than was available shortly after ions enter the nc-SiC_X:H(n) layer. Once the energy of the incident ion was insufficient for further movement in the lattice, it became an interstitial, observed as an implanted ion. The type of incident ion, and thus their energy distribution, could have potentially influenced the nature of the damage to passivation, depending on the underlying mechanism.

The energy loss (E_{loss}) additionally depended on the X_C of the layer and the E_{ion}, as shown in figure 5.12. Independent of X_C and E_{ion}, E_{loss} towards vacancy generation remained relatively constant in the nc-SiC_X:H(n) layer. An increase in either X_C or E_{ion} shifted the E_{loss} balance from the generation of phonons to the ionization of the layer atoms. For a higher X_C, this trend was plausible due to the increased density of a more crystalline material, which lead to a denser electron cloud and thus stronger interaction with the incident ion [249, 250]. Similarly, an increase in E_{ion} might have given more opportunities for interaction with electrons in the layer. With a higher incident energy, the chance that another interaction transferred sufficient energy to count towards either ionization or vacancy generation increased, as the E_{loss} towards phonons

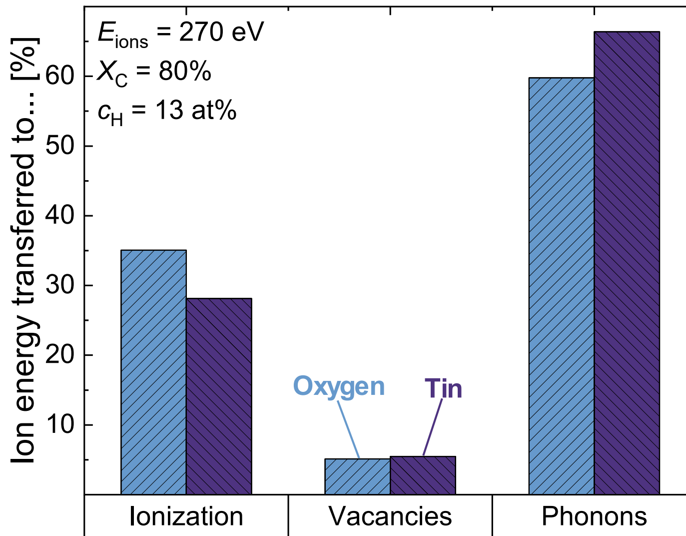

Figure 5.11.: *Simulated energy distribution for the primary incident ions and recoiling layer atoms, focusing on the lightest and heaviest ions, oxygen and tin, respectively, involved in the sputter process. The distribution highlights the relative contributions of phonons, ionization of lattice atoms, and vacancy generation.*

was the part insufficient for either interaction. These observations suggested that both the crystallinity of the material and the incident ion energy could have influenced the extent of damage to passivation, depending on the specific process and material conditions.

Figure 5.13 shows the generation depth profiles of ionization (*Io*) in a) and b), phonon (*P*) in c) and d) and vacancy (*Va*) in e) for different E_{ion} and X_C or vacancy types, respectively, in the nc-SiC_X:H(n) layer. The ionization and phonon generation were separated into contributions from the primary ions and recoiling atoms. In general, primary ions exhibited the highest ionization and phonon generation near the surface of the nc-SiC_X:H(n) layer. Recoiling atoms, however, displayed a higher maximum intensity at slightly deeper depths but decreased more rapidly. This resulted in a similar maximum depth for ionization and phonon generation between primary ions and recoils. The primary ions and recoiling atoms reached their ionization peak within the first few nanometers of the layer, with a subsequent decline and eventual disappearance within the

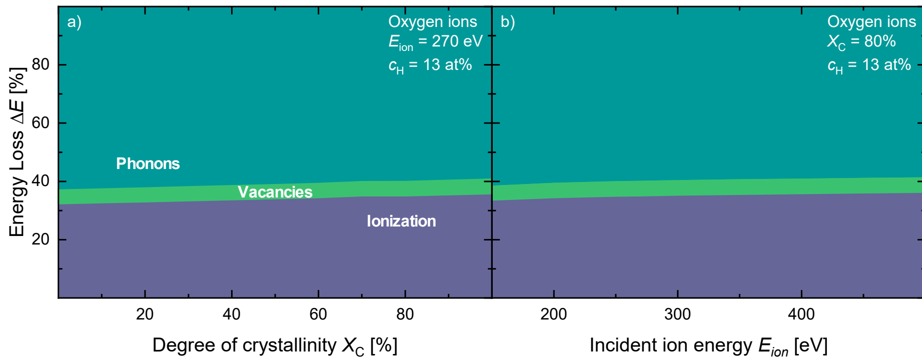

Figure 5.12.: *Simulated combined energy loss (E_{loss}) of incident oxygen ions and recoiling layer atoms depending on a) crystalline volume fraction (X_C) and b) E_{ion}. The E_{loss} towards vacancy generation remains constant, while a shift is observed favoring phonon generation over ionization of lattice atoms for both lower X_C and E_{ion}.*

initial four nanometers. While the intensity of the primary ions increased toward their maximum near the surface, the intensity of the ionization through recoiling atoms decreased first toward a local minimum, which was closer to the sample surface than the maximum of the ionization intensity of the primary ions. This local minimum was at similar depth than the maximum ionization intensity of the recoiling atoms. As the E_{ion} increased, the peak intensities increased and shift deeper into the sample. The shape of the distribution stayed similar, while only the intensity of *Io* increased. The X_{C} of the material also influenced the shape of the profiles, with a higher crystallinity intensifying the ionization peak with a slight shift towards the surface of the layer. The onset at the surface of the nc-SiC_X:H(n) increased to larger *Io* for a more crystalline material and the intensity of the local minimum observed for the recoiling atoms close to the surface increased, keeping the distance between the onset and minimum approximately constant. After a maximum intensity in *Io* was reached, *Io* falls off faster for higher X_{C} as the material is denser and the deepest ionization depth decreases.

Phonon generation exhibited similar trends, with a higher E_{ion} leading to higher generation depths. Phonons generated by primary ions penetrated approximately 1 nm deeper than ionization and the *P* maximum shifted further into the layer. Unlike the *Io* profiles, the peak *P* decreased and the curve flattened but reached deeper into the nc-SiC_X:H(n). The recoiling atoms on the other hand

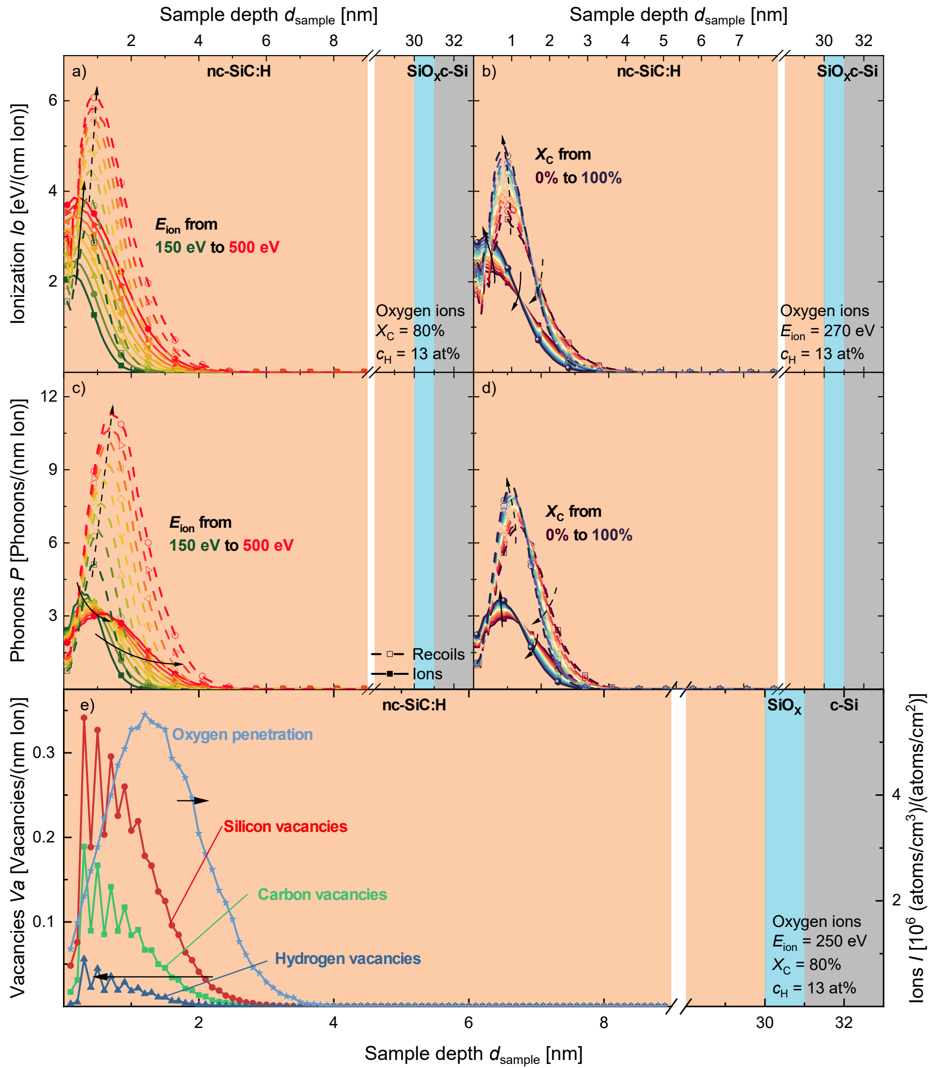

Figure 5.13.: *Simulated generation profiles for a) and b) ionization (Io), c) and d) phonon (P), and e) vacancy (Va), distinguishing between primary ions (solid lines) and recoiling atoms (dashed lines). a) and c) show the respective profile for a variation of E_{ion}, while b) and d) show the profiles for different X_C.*

maintained their P profiles shape for increasing E_{ion}, and the maximum P shifted further into the layer, resulting in an overall deeper maximum generation depth. The onset of P in the layer increased with E_{ion} from the incident ions, but was reduced for recoiling atoms. With decreasing X_C, the P profile generated by primary ions behaved similarly to higher E_{ion}. The peak position moved further into the layer, and the shape flattened. The P profile of the recoiling atoms changed in a similar way. Although the onset of P from recoiling atoms was approximately unchanged by X_C, a slight decrease for decreasing X_C was observed in the profiles generated by primary ions. Unlike the *Io* profiles, no local minimum was observed in the phonon generation of the recoiling atoms.

Vacancy generation profiles for silicon, carbon, and hydrogen showed that silicon generated the most vacancies, followed by carbon, with hydrogen showing the least vacancies. The general shape of the *Va* profile was similar for all elements. The depth of vacancy generation depended on the type of layer atom, with silicon vacancies occurring deepest in the layer, yet still within the initial 3 nm, far from the crystalline silicon interface. Furthermore, the implantation profile for oxygen ions is additionally shown. The previously d_{max} of 3.9 nm was found, while the profile peak was at 1.2 nm.

The depth profiles of these secondary effects, whether from primary ions or recoiling atoms, aligned closely with the implantation depth of oxygen ions, suggesting that these effects were confined within the path of the ion in the layer. Recoiling atoms shifted these effects slightly further into the nc-SiC$_X$:H(n), but still within the vicinity of the path of the primary ion. According to the simulations, no cascading events of recoiling atoms reached towards deeper sample depth (d_{sample}). Because the recoiling atoms were first generated by the primary ions, and then propagated in the layer, while the primary ions already lost a significant part of their energy through recoil generation and other interaction events, the generation profiles from the recoiling atoms were deeper in the layer than the ones from the primary ions. Phonons were the most abundantly generated per unit, followed by ionization and, lastly, vacancy generation. The peak positions of the *Va* profiles were closest to the nc-SiC$_X$:H(n) surface, followed by the peak of *Io* and finally P. The phonon generation and ionization from recoiling atoms were

higher than those from primary ions, as the ion might have generated multiple recoiling atoms. Furthermore, the recoiling atoms barely generated any vacancies, as the energy of the recoiling atoms might have been insufficient, and thus the interaction events were transferring the energy towards phonons or ionization.

The energy needed to generate a vacancy was largest and the collision event between the ion and layer atom must have transferred enough energy to knock the atom from its lattice position. Additionally, sufficient energy must have been supplied so that the knocked-off lattice atom could move from its previous position through the lattice. Close to the surface, additional surface energy was needed for the lattice atom to be sputtered from the sample. Deeper inside the layer, the incident ion had already lost a significant portion of its energy, so the fraction of energy transferred to the lattice atoms might have not been large enough to supply the lattice atoms with enough energy to be knocked from the lattice site and propagate inside the layer. Furthermore, the vacant lattice site might have been filled with an already generated recoiling atom, and the vacancy was filled. This effect resulted in the vacancy profiles being close to the layer surface. The silicon vacancy was the most abundant type of vacancy in the layer, as the given lattice and displacement energies of SRIM for silicon in silicon carbide were lower than those of carbon. As the silicon-silicon bond is weaker than the carbon-carbon or silicon-carbon bonds [251, 252], this was a reasonable assumption. Hydrogen had the lowest vacancy generation because the hydrogen concentration in the layer was low compared to that of silicon and carbon.

Larger E_{ion} lead to a shift in Io profiles to larger Io and deeper d_{sample}, since more energy of the incident ion was available. Therefore, the ion penetrates deeper into the layer and more energy was available for ion-electron interactions. A higher X_{C} on the other side resulted in a denser material, giving stronger interactions of the incident ion with the denser electron cloud. Consequently, more energy from the incident ion was transferred closer to the surface of the layers and the maximum depth of Io was reduced, while the intensity closer to the surface increased. The local minimum in the Io profile of the recoils close to the surface was approximately the same position as the maximum in vacancy generation. Thus, the recoils might have generated vacancies rather than transfer

energy to electrons.

The energy was transferred to phonons when the collision of the primary ion or a recoiling atom with a layer atom did not displace the layer atom. Therefore, the energy needed for phonons was small, and their quantity per unit was the largest. For larger X_C the same explanation as for the *Io* profiles held true with a denser material leading to a stronger interaction of the ion or recoils closer to the surface. The shape of the *P* profile from recoils did not change with increasing E_{ion}, like the primary ion profiles, since the energy of the recoils might have been similar for larger E_{ion}, but more recoils were generated. However, the *P* profile of the primary ions might have flattened because the ions still had a higher energy deeper inside the material and, therefore, collision events could have transferred enough energy for vacancy or recoil generation deeper inside the layer. This deeper generation of recoils might have also explained both the shift in *Io* and *P* profiles from the recoils deeper inside the layer.

In crystalline silicon carbide, silicon vacancies are harder to obtain than carbon vacancies, despite the lower bond energy of silicon-silicon bonds compared to carbon-carbon and silicon-carbon bonds [251, 252]. Therefore, carbon vacancies are found to be much more abundant than silicon vacancies [253]. The formation energy of a silicon vacancy is above 7.0 eV [254], while the formation energy of carbon vacancies is above 4.8 eV [255]. The activation energy for the carbon vacancy to migrate is greater than 3.6 eV [256], while it is greater than 2.0 eV for the silicon vacancy [257]. The activation energy for movement of carbon and silicon interstitials in silicon carbide is between 0.7 eV and 3.15 eV [258], lower than for vacancies. As a result of these high energies needed for the formation and propagation of vacancies, it was assumed that the number of vacancies in the material, in line with the simulation, is small. The ionization energy in silicon carbide is above 6.0 eV [259], while the exciton energy is between 2.4 eV and 3.4 eV [260]. From the dispersion relations of the phonons, their energy in crystalline silicon carbide is below 125 meV [261, 262]. With these energies, the energy distribution given by SRIM seemed reasonable, as the generation of vacancies together with their propagation, or interstitial movement, was mostly larger than the electronic effects, and the phonons possessed the lowest energy

and thus the largest fraction of energy from the incident ion.

In summary, with standard material and process parameters, the deepest ion penetration was observed with the smallest ion, oxygen, reaching a depth of 4.8 nm. These oxygen ions were capable of inducing the formation of silicon vacancies up to a depth of 4.0 nm, carbon vacancies extended to approximately 3.8 nm, and hydrogen vacancies up to 4.1 nm. The generation of phonons by primary ions occurred at depths that reached 4.8 nm, while recoils could induce phonons up to a slightly greater depth of 5.0 nm. The ionization depth approximately corresponded to the phonon generation depth. The microstructure of the nc-SiC_X:H(n) layers are nano-crystals in an amorphous matrix in the nucleation phase and a columnar grain structure for thicker layers [173]. Even in scenarios where there were amorphous channels between columnar-growing crystalline grains within the nc-SiC_X:H(n) material, the maximum penetration depth for oxygen ions was observed to be 5.8 nm. In such cases, the deepest formation of silicon vacancies occurred at 5.2 nm, while ionization of the lattice atoms and phonon generation by recoiling lattice atoms extended to 6.6 nm. When considering double-charged incident ions, the penetration depth for oxygen ions could reach 7.8 nm. At an E_{ion} of 500 eV, the highest energy level utilized in simulations of secondary effects, the depth at which silicon vacancies were generated could reach up to 6.7 nm, and the ionization and phonon generation processes occurred at depths that extended to approximately 8.9 nm. In extreme edge cases where an amorphous channel was impacted by a double-charged ion, the penetration depth of oxygen ions could reach 8.8 nm, with the deepest silicon vacancy observed at 8.4 nm, and ionization and phonon generation reached a maximum depth of 9.5 nm. However, it was critical to note that all these effects manifest within the initial 10 nm of the sample, significantly distant from the crystalline silicon interface.

In conclusion, extensive investigations had established that the various effects in this study were confined close to the surface of the nc-SiC_X:H(n) material. This was evidenced by the shallow implantation depths for ions and electrons, as well as their resulting secondary effects, all of which were restricted to the first nanometers of the nc-SiC_X:H(n), as depicted in figure 5.14. Notably, the potential

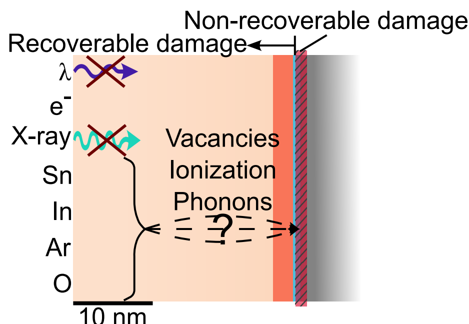

Figure 5.14.: *To-scale overview of various effects occurring during the sputtering process and their simulated depth of impact. All effects are either superficially or experimentally demonstrated to be non-damaging to the passivation of the sample.*

negative impacts of electrons, including secondary electron or x-ray generation, along with the influence of electromagnetic radiation emanating from the argon and oxygen plasma across different wavelengths, had been experimentally disproven as detrimental within the investigated process. The superficial nature of ion implantation was further verified by elemental analyses, which indicated that only the secondary effects of the implantation process were significant. As previously shown, phenomena such as the ionization of lattice atoms, the generation of different vacancy types and phonons were also confined to the implantation depth of the incident ions.

Although the passivation effect of the crystalline silicon wafer is depending on its interface, these superficial effects must have somehow extended their influence to this critical region. This made a mechanism for the propagation of the generated defects or introduced energies necessary. However, it was crucial to recognize that the damage induced are recoverable, so a lasting modification of the passivation quality at the crystalline silicon interface seemed improbable.

In a-Si:H and poly-Si, the degradation in passivation quality during the sputter process is often ascribed to the formation of a bound electron-hole pair, or exciton, resulting from the impact of ions. This exciton is assumed to migrate toward the crystalline silicon interface, where it recombined non-radiative, thereby displacing hydrogen atoms at the interface with its released energy [237, 241]. Contrary to free electrons, which did not compromise the passivation quality of

the sample, a portion of the ionizing energy in nc-SiC_X:H(n) might have also lead to the generation of excitons. Regardless of the material, nc-SiC_X:H(n), a-Si:H, or poly-Si, the exciton was required to traverse from the superficial few nanometers of the layer to the surface of the crystalline silicon. These silicon-based layers were very defective, with defects ranging from unsaturated bonds in amorphous structures, intergrain amorphous phases, or grain boundaries to imperfections in crystalline grain structures or strain within the layer and interstitial doping atoms. Because of these defects, there was a substantially probability of recombination of the electron-hole pair, given the proximity of charge carriers, and the reduced energy gap due to their bound state within the exciton. Consequently, it was highly improbable that the electron-hole pair would traverse significant distances without promptly recombining, given the abundance of available defects.

From this analysis, it was plausible to rule out additional effects from ionized lattice atoms, whether they be free electrons or bound electron-hole pairs, as potential sources of sputter-induced damage to the passivation quality. However, vacancies within the lattice could have caused disturbances and strain, potentially inducing defects. Although the energy required to break silicon-silicon, carbon-carbon, or silicon-carbon bonds is lower than the ionization energy of silicon, carbon, or silicon carbide [204, 251, 252, 259], sufficient energy transfer from the impinging ion to the lattice atom was necessary not only to break the bonds to other lattice atoms, but also to displace the atom from its lattice site. Both silicon and carbon vacancies could have propagated along the silicon carbide lattice, and their mechanisms of propagation will be discussed. The potential propagation mechanisms are illustrated in figure 5.15 a). For instance, a carbon vacancy (i) moved through nearest-neighbor hopping on the carbon sub-lattice, or alternatively, a vacancy-antisite complex could form, leading to the creation of a silicon vacancy with a carbon sitting on a silicon lattice site. However, this complex is unstable in silicon carbide, restricting propagation to nearest-neighbor hopping on the carbon sub-lattice. In contrast, the silicon vacancy (ii) could migrate through nearest-neighbor hopping on the silicon sub-lattice or via the formation of a carbon antisite-carbon vacancy complex. In particular, the activation energies for these movements were significantly high, several electron volts [256, 257], and the vacancy movement is observable only at elevated tem-

peratures of approximately 500 ℃ for carbon vacancies and 750 ℃ for silicon vacancies. Temperatures during the deposition process were insufficiently high to facilitate such movements; otherwise, substantial damage to the passivation quality of the a-Si:H rear side in a solar cell or nc-SiC_X:H(n) would have resulted from hydrogen effusion from the layers. Moreover, low-temperature annealing applied for complete recovery of degraded passivation would not be capable of curing damage, as these temperatures did not allow for vacancy migration. [253, 263–265]

Finally, the impacting ions could generate phonons, as schematically depicted in figure 5.15 b). Phonons, which are quantized lattice vibrations, require a lattice for propagation. According to their dispersion relation, the maximum energy that a phonon can possess in crystalline silicon carbide is approximately 125 eV [261, 262]. If multiple phonons dispersed simultaneously at a similar location, the released energy could have been high enough to damage the passivation quality at the c-Si/SiO_X interface by breaking silicon-hydrogen bonds. With the energy from the incident ions, the density of states of phonons increased, including the population of higher-energy optical phonons. Fewer of these optical phonons together were needed to supply the energy needed to break the silicon-hydrogen bond and displace the hydrogen. Therefore, the probability that enough optical phonons simultaneously dissipated at the crystalline silicon or silicon oxide interface and supply energy to break the silicon-hydrogen bond was increased. In crystalline silicon carbide, phonons have a mean-free path length exceeding 100 nm [266], which enabled ballistic transport through the layer. Given the vertical growth of grains in nc-SiC_X:H(n) [173], it was feasible for phonons to propagate through the layers to the c-Si/SiO_X interface. Similarly, in amorphous silicon, which lacks a crystal lattice, phonon-like modes exist and can have a comparable impact on material properties, including thermal conductivity, with mean-free path lengths also exceeding 100 nm [267, 268]. Thus, the energy from incident ions could have propagated through the layer towards the crystalline silicon. At the interface with crystalline silicon, or the SiO_X in TPC, which was in close proximity to crystalline silicon, the phonon scattered and dispersed. The energy carried by the phonon was then released, as illustrated in figure 5.16. This released energy of multiple phonons disrupted the silicon-hydrogen bond at the

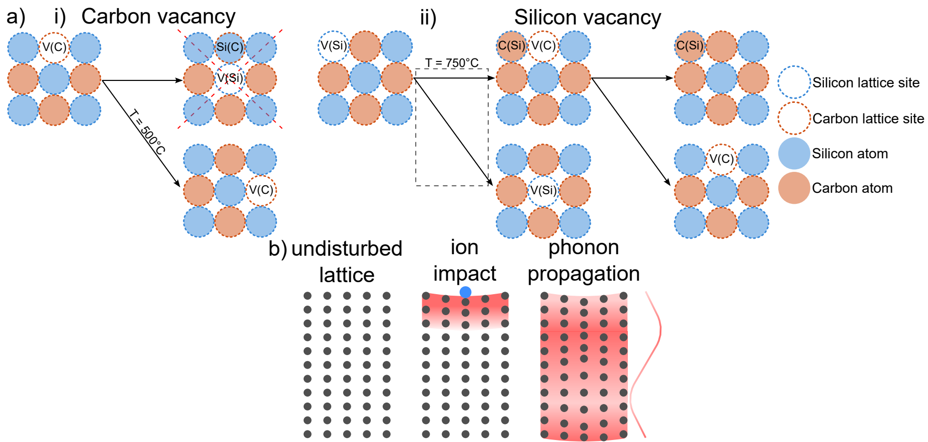

Figure 5.15.: *Schematic illustrations of a) mechanisms for the movement of carbon and silicon vacancies in the silicon carbide lattice, and b) phonon generation and propagation. Carbon vacancies move through direct hopping, while silicon vacancies can hop or create vacancy-antisite complexes. Phonons are quantized lattice vibrations. Reprinted under CC BY 4.0 from Ref. [226].*

crystalline silicon interface, degrading the passivation. However, because of the high thermal conductivity of crystalline silicon, the energy dissipated rapidly, and the duration of the energy pulse was short enough for hydrogen to be displaced without effusing from the sample. The lower-temperature annealing, which restored sputter-induced damage, subsequently allowed the displaced hydrogen to reattach to the previously broken bond, restoring the passivation quality of the crystalline silicon. In figure 5.5, a reduced sample temperature increased the mean-free path of phonons [266], potentially allowing more phonons to reach the SiO_X or crystalline silicon without dispersing, thus intensifying the damage. This could have explained the observed increase in damage, as the likelihood of in-situ annealing effects was deemed improbable, as previously discussed. Since the mean free path of a phonon is inversely proportional to the density of the material, the trend observed in nc-Si:H with reduced damage for denser layers still held true [269], making this explanation applicable to other materials than nc-SiC_X:H(n).

To mitigate the damage from the sputter process, several strategies were proposed. Increasing the sample temperature during sputter deposition could

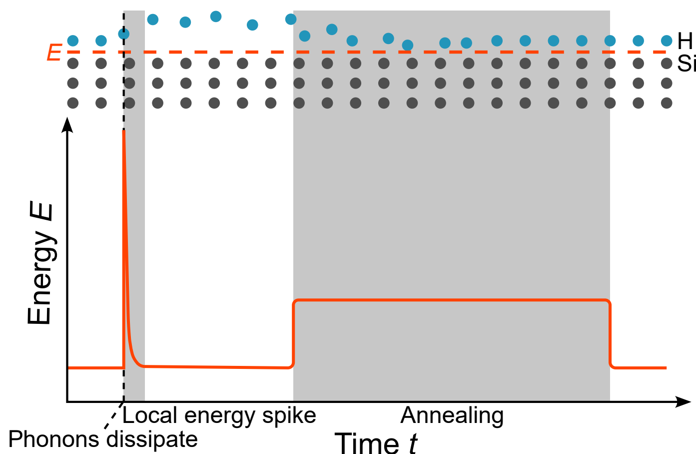

Figure 5.16.: *Schematic representation of hydrogen displacement at the silicon interface due to simultaneous multi-phonon dispersion. Subsequent low-temperature annealing can restore broken silicon-hydrogen bonds. Reprinted under CC BY 4.0 from Ref. [226].*

reduce the mean-free path length of phonons [266], but this must be balanced against the thermal stability of materials such as a-Si:H. Increasing the chamber pressure could thermalize the sputtered particles before they could reach the sample, potentially reducing the energy available for phonon generation. Lowering the sputtering power reduces the maximum energy of the incident particles. [29, 241] Although these approaches could minimize sputter damage, they also influenced the growth and opto-electrical properties of the TCO layer, necessitating careful optimization.

A more radical solution might be the introduction of phonon-blocking layers prior to sputtering. These layers would require a highly disordered structure with significant structural differences from the underlying silicon-based layer. Such layers could scatter and disperse phonons, preventing them from reaching the crystalline silicon or silicon oxide interface. For these layers to be feasible, they must possess electrical and optical properties similar to the applied TCO, ensuring they do not adversely affect other parameters of solar cells. Buffer layers have already shown promise in mitigating sputter damage in perovskite solar cells [270–272], and similar approaches could be effective for a-Si:H, poly-Si, and nc-SiC_X:H(n), consistent with the theory of phonon propagation as the primary

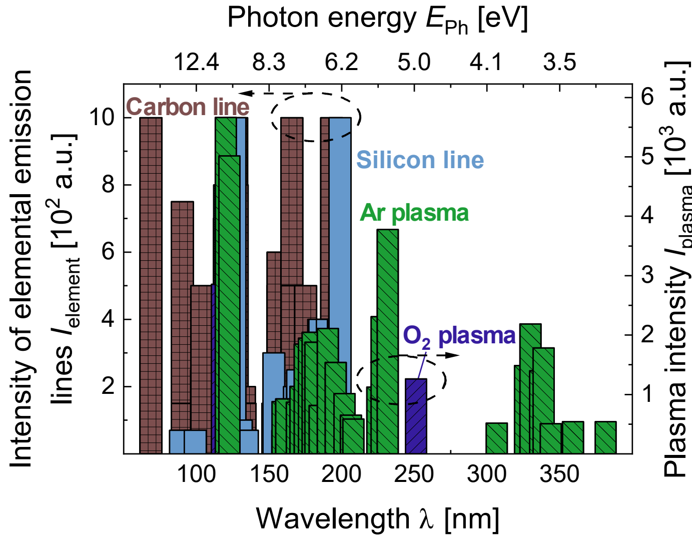

Figure 5.17.: *The Intensity of elemental emission lines ($I_{element}$) for the elements carbon and silicon and the plasma intensity (I_{plasma}) for radiation from an oxygen and argon plasma. Data of the plasma radiation taken from ref. [228] and from ref. [273] for the possible carbon and silicon emission lines.*

mechanism of sputter damage.

The damage induced by the sputter process might have also originated from UV emissions, which resulted from the relaxation of excited electrons within the material. As previously indicated in the incident ion energy distribution in figure 5.11, approximately one-third of the energy of an incident ion was transferred to electrons. When these electrons were excited but not ejected from the material, they could have released their energy as radiation when they relaxed back to their ground state. The potential emission lines, along with emissions from an argon and oxygen plasma, are shown in figure 5.17. The radiation emitted by silicon and, particularly, carbon, could have been significantly more energetic than that from the plasma. However, establishing a direct comparison of the intensities between the plasma radiation and element-specific emissions remained an open question, rendering a comparative analysis impractical.

Given the known degradation of the passivation quality of the TPC under VUV radiation from an oxygen plasma [111], it might have been that the intensity

of the VUV radiation generated from the excited electrons in the layers elements could have exceeded the plasma radiation, potentially leading to a decrease in the passivation quality of the TPC. This hypothesis underscored the need for further research on the specific effects of element-derived VUV emissions on sputter-induced damage, particularly in the context of TPC passivation.

In conclusion, while the superficial nature of the primary sputter effects and their secondary impacts suggested a minimal direct influence on the crystalline silicon interface passivation, the propagation of phonons and their subsequent energy dispersion presented a plausible mechanism for localized degradation. Understanding and mitigating these effects were crucial for optimizing the sputter deposition process and preserving the integrity of the passivation layer in solar cells. Nevertheless, the degradation of the passivation quality under VUV light generated from the relaxation of excited electrons in either silicon or carbon needed further investigation.

5.4. Annealing Behavior of Transparent Passivating Contact Solar Cells

In previous studies, solar cells underwent an annealing process at 220 °C for two periods of ten minutes each [29]. This procedure aimed to remove damage induced by the sputtering process, and was only partially successful in restoring the passivation quality of the solar cell, leading to a moderate V_{OC} in the device. On the contrary, this study implemented a single extended annealing session at 230 °C for 20 minutes. Despite this, a notable discrepancy persisted between the iV_{OC} and V_{OC} in the completed devices, as evidenced earlier in figure 4.8 and figure 4.9.

In contrast, samples passivated symmetrically with TPC structures, such as those depicted in figure 5.2, demonstrated a close alignment of iV_{OC} values pre- and post-sputtering plus post-annealing. This suggested an absence of residual damage after the annealing process. This observation was reinforced in figure 5.18, which compared iV_{OC} values of a wafer passivated symmetrically

with TPC structures and a solar cell precursor that has a TPC front and SHJ rear side across different processing stages. Initially, both types of sample exhibited comparable iV_{OC} values, nearing 740 mV. After sputtering of ITO, both types experienced significant degradation, with the solar cell precursor exhibiting a more pronounced decline in iV_{OC}. However, the subsequent 230 °C, 20 minutes annealing enabled the solar cell precursor to regain almost 30 mV in iV_{OC}, reaching approximately 720 mV, while the symmetrically passivated TPC sample completely recovered. Furthermore, the application of a light soaking step, typically integrated into the fabrication of SHJ reference samples and TPC solar cells, did not further enhance the iV_{OC} of the symmetrically passivated sample. Nevertheless, it increased the iV_{OC} of the solar cell precursor to 725 mV. This iV_{OC} aligned with the V_{OC} reported for TPC solar cells in the literature [29]. The observed variance in damage after ITO deposition agreed with the experimental scatter observed in previous studies on sputter-induced degradation. The full recovery of the symmetric sample after annealing, contrasted with the partial recovery of the solar cell precursor, suggested that the limitations in iV_{OC} primarily originate from the SHJ side of the solar cell. The residual damage, which persisted even after light soaking, mirrored the gap between iV_{OC} and V_{OC} observed in earlier solar cells, which was described as unrecoverable damage in previous work.

In figure 5.19 a) and b), the thermal stability of SHJ solar cells and the annealing behavior of symmetric TPC samples as a change in V_{OC} and iV_{OC} in the form of open-circuit voltage loss (ΔV_{OC}) and implied open-circuit voltage loss (ΔiV_{OC}), respectively, as a function of annealing temperature (T_{anneal}) are shown. ΔV_{OC} in a) compared the V_{OC} before and after the annealing step for the SHJ solar cells, while in b), ΔiV_{OC} depicted the difference in iV_{OC} after the sputtering process and after the annealing step for a symmetric TPC sample. The annealing time (t_{anneal}) was 20 minutes for all annealing steps. For the SHJ cells, an additional evaluation was conducted that includes a post-annealing light soak step.

In SHJ cells without light soaking, a marginal ΔV_{OC} was noted for T_{anneal} up to 190 °C. However, for T_{anneal} exceeding 190 °C, the deterioration in V_{OC} increased, reaching up to 20 mV at 230 °C. Implementing light soaking gener-

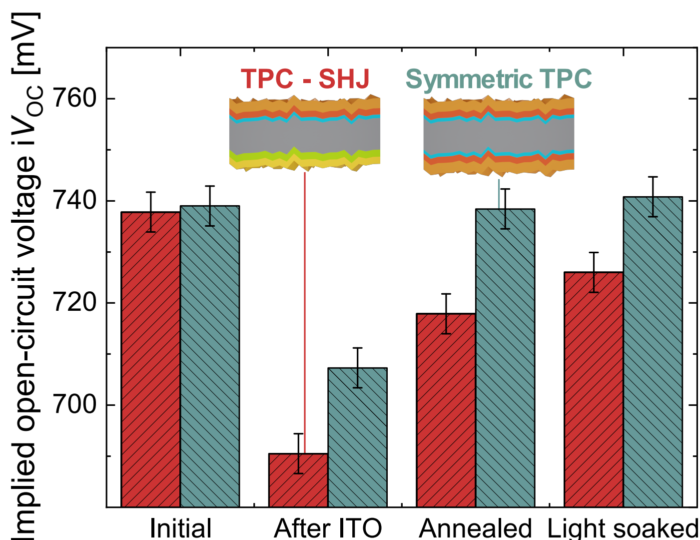

Figure 5.18.: *Comparison of implied open-circuit voltage (iV_{OC}) for symmetrically passivated wafers with the transparent passivating contact (TPC) and solar cell precursors with a TPC front side and silicon heterojunction (SHJ) rear side at different stages of the process. Although symmetrically passivated samples fully recover after annealing, the solar cell precursors do not, indicating limitations originating from the SHJ side.*

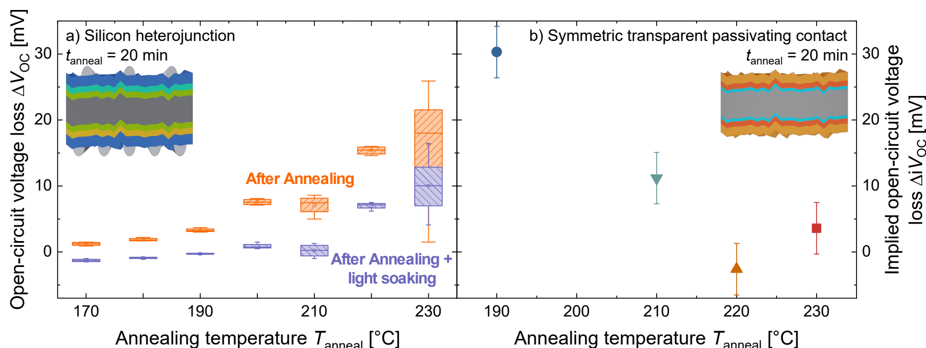

Figure 5.19.: *Analysis of a) open-circuit voltage loss (ΔV_{OC}) for a silicon heterojunction (SHJ) solar cell and b) ΔiV_{OC} a symmetrically passivated wafer with the transparent passivating contact (TPC) structure for varying annealing temperature (T_{anneal}). The constant annealing time (t_{anneal}) is 20 minutes for both cases. While the SHJ solar cell exhibits degradation at temperatures above 190 ℃, or 210 ℃ with light soaking, the symmetric TPC structure recovers at T_{anneal} of 220 ℃ or higher. Insets depict the sample structures of a SHJ solar cell and a symmetric TPC sample.*

ally restored this damage, improving the V_{OC} for T_{anneal} below 190 ℃. Damage became reversible with light soaking up to T_{anneal} of 210 ℃. Beyond this, light soaking did not fully recover ΔV_{OC}. The initial ΔV_{OC} fluctuations around 0 mV, observed before and after light soaking, could have been due to variations in the measurement system, ambient temperature or sample handling, which could have induced minor passivation degradation. This degradation appeared to be reversed by light soaking. Negative ΔV_{OC} values suggested additional recovery of degradation, caused by ambient storage prior to measurements.

The observed increase in ΔV_{OC} at higher T_{anneal} was likely due to the dissociation of silicon-hydrogen bonds at the c-Si interface, leading to hydrogen effusion. Light soaking partially reversed this degradation by re-establishing broken bonds. However, at elevated T_{anneal}, irreversible damage occurred, possibly due to excessive hydrogen effusion from the sample. Consequently, the optimal T_{anneal} for SHJ cells was determined to be 190 ℃ without light soaking, and 210 ℃ with light soaking.

For the nc-SiC_X:H(n)-based TPC samples, a 20-minute annealing at 190 ℃ resulted in a ΔiV_{OC} of approximately 30 mV. This value decreased to about 10 mV at 210 ℃ and vanishes at T_{anneal} of 220 ℃ or higher. Thus, TPC samples required a higher annealing temperature compared to SHJ cells for damage restoration. The hydrogen required for TPC damage repair must have originated from the nc-SiC_X:H(n) layers or been present in the SiO_X. The dissociation energy of hydrogen bonds with carbon or oxygen is higher than that with silicon [274]. Furthermore, the presence of carbon in the back bond of silicon in SiO_X strengthens the silicon-hydrogen bond, evidenced by a shift to higher wavenumbers in the FTIR silicon-hydrogen bond [275]. Therefore, TPC samples necessitated higher energy for hydrogen mobilization to saturate disrupted bonds, explaining the increased annealing temperatures compared to SHJ cells.

These findings highlighted a thermal incompatibility between the T_{anneal} required to repair sputter-induced damage in the TPC and the thermal tolerance of the SHJ rear side. The appropriate annealing temperatures to cure the TPC degraded the passivation quality of the SHJ side. In contrast, the suitable temperatures for SHJ did not fully restore the damage in TPCs, likely due to the more

robustly bonded hydrogen in nc-SiC_X:H(n) and SiO_X layer.

The ΔV_{OC}s for extended accumulated annealing times (t_{acc}s) of the previously investigated T_{anneal}s are shown in figure 5.20, where the annealing time on the hot plate was successively extended, if the sputter-induced damage was not restored. Initially, the degradation of passivation quality exhibited a scattering ranging from 48 mV to 95 mV for different samples. The ΔV_{OC} decreased to approximately 0 mV for T_{anneal} settings of either 230 ℃, as previously demonstrated, or 220 ℃ after the first annealing step. At a T_{anneal} of 210 ℃, ΔV_{OC} significantly reduces after the first annealing; however, it did not decrease substantially with further t_{acc} and, in some cases, even showed an increase. For this T_{anneal}, the ΔV_{OC} fluctuated around an average of 15 mV, which was consistent with the error margin of the measurement. At the lower T_{anneal} of 190 ℃, an exponentially decaying decrease in ΔV_{OC} with prolonged t_{acc} was observed, where ΔV_{OC} approached 10 mV. Once the passivation quality was degraded and the silicon-hydrogen bonds were disrupted, the released hydrogen atoms were displaced. The energy barrier for hydrogen migration to the now exposed silicon bond might have varied with the directly surrounding material in the layer. Although the higher annealing temperatures of 220 ℃ and 230 ℃ provided sufficient energy for hydrogen to overcome these barriers in the embedding layer and migrate towards the open silicon bond, thus recovering the passivation quality, the lower T_{anneal} might have not facilitated this movement for all hydrogen atoms. Insufficient hydrogen utilization prevented full ΔV_{OC} recovery. Prolonged t_{acc} might have enabled a 'hopping-like' movement of hydrogen, gradually migrating to the nearest favorable position. However, it appeared that some energy barriers remained impassable, preventing complete voltage recovery at lower temperatures.

In summary, degradation of passivation quality in TPC-passivated samples could be rapidly restored within the initial annealing step, or complete recovery of the damage might not be achievable. Increasing the annealing time could have further mitigated damage, but some residual degradation persisted, even after extended t_{acc}.

In a-Si:H, it has been established that performing an annealing step prior to the sputtering process can enhance passivation quality and amplify the effec-

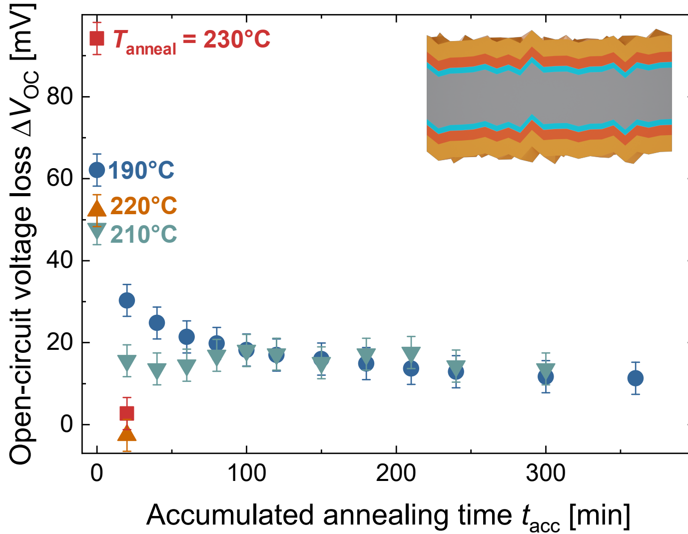

Figure 5.20.: *Evolution of open-circuit voltage loss (ΔV_{OC}) in symmetrically transparent passivating contact (TPC)-passivated samples over extended accumulated annealing times (t_{acc}s) for various annealing temperatures (T_{anneal}s). The increased annealing time further reduces ΔV_{OC} at lower T_{anneal}, but does not completely restore damaged passivation quality.*

tiveness of post-sputtering annealing [240]. Figure 5.21 describes the response of symmetrically TPC-passivated samples at various processing stages and t_{acc} for different pre-annealing times (t_{pre}s). For these experiments, the pre-annealing temperature (T_{pre}) was set at 230 ℃, a level determined to allow complete damage recovery in nc-SiC_X:H(n). Conversely, the post-annealing temperature (T_{post}) was maintained at 210 ℃, the maximum temperature a-Si:H could endure with additional light soaking. The initial pre-annealing phase did not affect the iV_{OC} of any sample, keeping it consistently above 740 mV. However, following the ITO deposition, a substantial reduction in iV_{OC} by up to 50 mV was observed across all samples. The sample with t_{pre} = 0 min exhibited the same pattern as previously described in the t_{acc} series with a significant initial increase in iV_{OC} but without complete recovery, followed by minor fluctuations around a steady value. The residual damage here was about 20 mV. All samples subjected to pre-annealing showed a noticeable improvement after the first annealing step, followed by an exponentially diminishing return in iV_{OC} with each subsequent

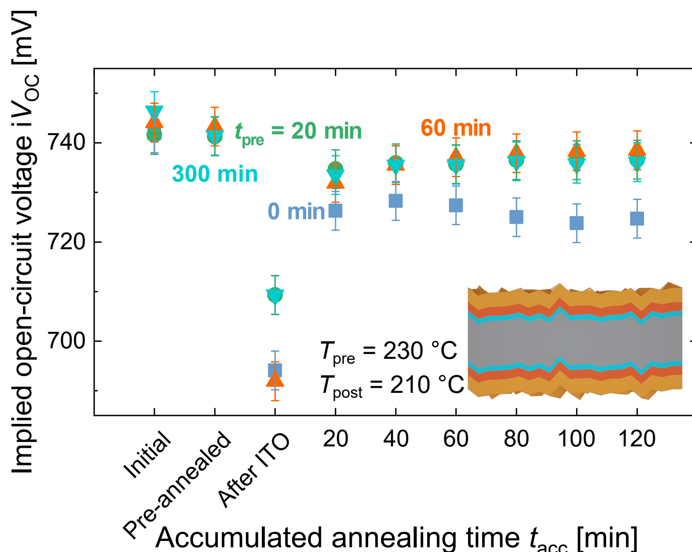

Figure 5.21.: *Implied open-circuit voltages (iV_{OC}s) of symmetrically transparent passivating contact (TPC)-passivated samples at different process stages and accumulated annealing times (t_{acc}s). Samples have varying t_{pre} before the sputter deposition. The pre-annealing temperature (T_{pre}) is 230 °C, and the post-annealing temperature (T_{post}) is 210 °C. The inlet depicts the sample structure.*

annealing step. The final iV_{OC} within the t_{acc} range explored in this study still lagged by approximately 5 to 10 mV behind the initial iV_{OC}.

The behavior of the reference sample with t_{pre} = 0 min could be attributed to an insufficient temperature, which did not provide enough energy for hydrogen to surpass the energy barriers necessary for migrating to the open silicon bonds. During the pre-annealing phase, hydrogen might have already repositioned within the material, settling in areas where the surrounding energy barriers for further movement were lower and thus the required T_{post} was reduced. Given the rapid nature of this movement, its effects were apparent across all investigated annealing durations.

This movement was essential for restoring the passivation quality that was compromised by the sputtering process. However, a part of the incomplete recovery of the degraded passivation quality could be attributed to the field-effect of the ITO, visible also in figure 5.2 at lower n [244, 245]. Additionally, this incom-

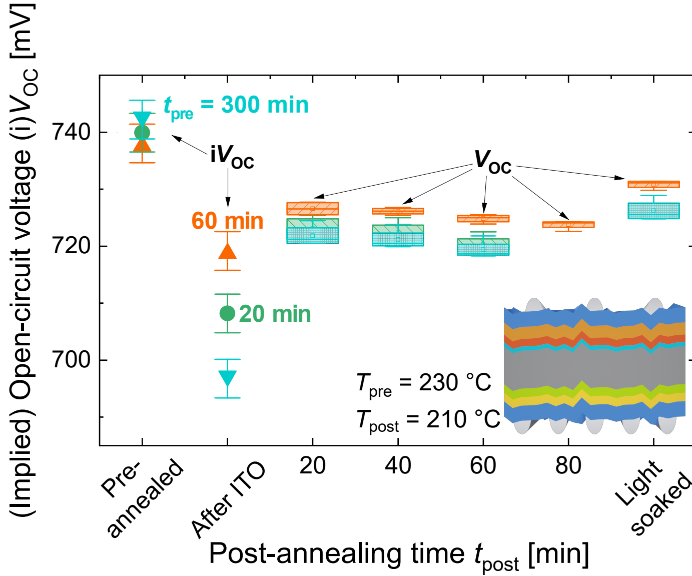

Figure 5.22.: *Implied open-circuit voltage (iV_{OC}) and open-circuit voltage (V_{OC}) of a transparent passivating contact (TPC) solar cell during various fabrication steps and with different pre-annealing time (t_{pre}). Pre-annealing, combined with a light soaking step, enhances the final V_{OC} compared to reference devices. The inlet depicts the sample structure.*

plete recovery could have been partly attributed to the restricted repositioning of hydrogen. Hydrogen displaced during the sputtering process might have still been confined behind energy barriers. This entrapment could have either blocked the hydrogen that was previously restructured during the pre-annealing phase or could have indicated that insufficient hydrogen in the surrounding material was present near the disrupted bonds. Consequently, this lead to the observed incomplete recovery of the passivation quality.

Finally, the pre-annealing treatment was incorporated into the fabrication of solar cells, as depicted in figure 5.22. Following the nc-SiC_X:H(n) deposition, the samples underwent pre-annealing on a hot plate in ambient atmosphere at T_{pre} of 230 °C for various t_{pre}. Subsequently, the a-Si:H rear side was deposited. Initially, all cell precursors exhibited a high iV_{OC} of around 740 mV. However, this value was notably reduced after the ITO deposition process, with considerable variance observed among the samples.

After the first annealing step, a substantial improvement in the V_{OC} was evident, elevating all samples to a comparable level of approximately 725 mV. With extended t_{acc}, a slight reduction in V_{OC} by approximately 5 mV was observed. The final light soaking step, designed to address the reduced V_{OC} resulting from the 210 °C annealing, successfully raised the V_{OC} above 730 mV. Although there remained a 10 to 15 mV discrepancy from the initial iV_{OC}, this pre-annealing approach significantly enhanced the V_{OC}, both in comparison to the previous champion device [29] and the solar cells discussed earlier in this work.

Implementing the light soaking step immediately after the first annealing phase could have potentially increased the final V_{OC} beyond 730 mV, as this could have prevented or reduced degradation in the a-Si:H layer, notable in the decreasing V_{OC} upon further post-annealing. Furthermore, the residual damage observed could have been attributed to perimeter recombination around the solar cell area on the silicon wafer [214–218]. Additionally, the incomplete recovery from the TPC, as previously noted, contributed to this residual damage.

5.5. Summary of Sputter Process-Induced Degradation and Annealing Effects in Transparent Passivating Contact Solar Cells

This chapter delves into the observed reduction in passivation quality after the sputter deposition of a transparent conductive oxide (TCO) layer, specifically indium tin oxide (ITO), and its annealing behavior. This phenomenon, not limited to hydrogenated nanocrystalline silicon carbide (nc-SiC_X:H)-based transparent passivating contacts (TPCs), is also observed in various other silicon-based contacts. Currently, a comprehensive theory that explains this damage remains elusive. This work utilized experimental and simulation studies to enhance the understanding of damaging mechanisms, focusing on electron and ion bombardment and the impact of radiation emitted from the plasma on the sample. Subsequently, the annealing behavior of TPC solar cells was examined, comparing the required temperature for damage recovery with the thermal stability of silicon heterojunc-

tion (SHJ) solar cells. A strategy to partly mitigate the identified incompatibilities was proposed.

The initial section of this chapter studied the impact of the sputter deposition process on the material properties of nc-SiC_X:H(n). The passivation properties of the TPC samples significantly deteriorated after sputter deposition, yet the implied open-circuit voltage (iV_{OC}) could be fully restored with an additional annealing step. Remarkably, the electrical conductivity (σ) of nc-SiC_X:H(n) remained unaffected by the TCO deposition. Comprehensive analysis using Fourier-Transform Infrared Spectroscopy (FTIR), Raman spectroscopy, and effusion experiments revealed no alterations in the microstructure of the material, specifically in respect to the silicon-carbon and silicon-hydrogen bonds. It was hypothesized that the overall microstructure remained intact during the sputtering process, and the changes at the crystalline silicon (c-Si)/silicon oxide (SiO_X) interface, essential in the degradation of the iV_{OC}, were masked by the properties of the bulk material. Although the gas atmosphere in the chamber was deemed non-detrimental to the sample, a decrease in sample temperature during the sputtering process amplified the damage. This increase in damage was not attributed to reduced in-situ annealing effects but was clarified later through an alternative mechanism.

The following part of this chapter delved deeper into identifying the root causes of the degraded iV_{OC}. This involved examining the impacts of plasma irradiation, electron bombardment, and ion bombardment on the sample. Initially, various filter glasses were employed to shield distinct segments of the electromagnetic spectrum emanating from the plasma. No damage was observed beneath any filtered region, while unshielded areas showed strong deterioration. This observation effectively ruled out plasma radiation as a contributor to passivation degradation in this process. The study then focused on the dynamics of electrons which were emitted from the plasma towards the sample. Simulations suggested that maximum penetration depth (d_{max}) for primary electrons was approximately 3.9 nm and that the generation of x-rays and secondary electrons was unlikely at incident electron energies ($E_{electron}$s) of the reference process. Even under conditions of increased incident energies or a completely amorphous material structure, d_{max} remained confined to the topmost 10 nm of the sample.

To further investigate this, a sample was subjected to electron beam irradiation at an $E_{electron}$ of 500 eV, which exceeded the expected energy during the sputter deposition process. This approach was designed to trigger potential secondary effects. However, post-irradiation analysis revealed no change in passivation quality, thus excluding electron bombardment and its associated secondary effects as sources of damage. Then, attention turned to ion irradiation. In this context, the incident ion energy (E_{ion}) significantly influenced the d_{max}, more so than the X_C. The impact of the hydrogen dilution (c_H) was found to be minor. Among the various ions, oxygen ions, being the smallest, showed the deepest penetration into the layer, with a simulated d_{max} of 4.8 nm, which was considerably distant from the crystalline silicon interface. This simulation was verified by energy dispersive x-ray spectroscopy scans, which indicated the deepest penetration by oxygen ions at 3.7 nm. Although the simulations slightly overestimated d_{max} due a diffuse ITO/nc-SiC_X:H(n) interface, they aligned well with the experimental findings. The study further revealed that incident ions primarily transferred their energy to phonons, followed by the ionization of lattice atoms and the creation of vacancies. Heavier ions exhibited a marginal preference for phonon generation over lattice atom ion-electron interactions. These secondary effects occurred at depths similar to the initial ion penetration, either from primary ions or recoiling lattice atoms. Theoretically, these effects could have propagated through the layer. However, vacancy-induced damage was deemed unlikely as a result of the high temperatures required for vacancy movement and the high energy barriers present, which exceeded both the tolerable sample temperatures and the applied annealing conditions. The hypothesis that the ion impact might have generated an electron-hole pair, leading to hydrogen displacement at the crystalline silicon interface from the recombination of the said electron-hole pair [237], was considered improbable. The defective nature of the layer material facilitated strong recombination, possibly preventing the electron-hole pair from reaching the crystalline silicon interface and instead causing recombination within the layer. In contrast, phonons, or phonon-like modes in amorphous silicon, could have travelled over 100 nm within the layers, potentially reaching the crystalline silicon interface. Here, multiple phonons could have simultaneously dissipated, releasing sufficient energy to break a silicon-hydrogen bond. This short and localized

energy spike might have displaced hydrogen, degrading the passivation, but not lasting long enough to induce hydrogen effusion, thereby keeping the hydrogen near the crystalline silicon interface. An additional annealing step might have provided the necessary energy for the hydrogen to migrate back to the crystalline silicon interface, thereby restoring passivation integrity. Another untested option was ultraviolet (UV) light generated by the excitation and relaxation of layer atoms hit by incident ions.

The concluding section of this chapter addressed the annealing behavior of TPC solar cells for curing damage induced by the sputter process. While the passivation of TPC structures was completely recoverable, the completed solar cells exhibited a diminished V_{OC}. The analysis identified the silicon heterojunction (SHJ) rear side as the bottleneck in the finished solar cell architecture. The a-Si:H layer demonstrated tolerance to temperatures up to 210 °C, if an additional light soaking step was employed. In contrast, the nc-SiC_X:H(n) layer needed a minimum curing temperature of 220 °C for a full recovery. This discrepancy in thermal requirements could not be resolved through prolonged annealing durations. The introduction of a pre-annealing step before the sputter process enhanced the recovery of the iV_{OC} at relatively lower temperatures, yet it failed to entirely reverse the sputter-induced damage. This improvement was hypothesized to originate from a re-organization of hydrogen within the nc-SiC_X:H(n), which reduced the energy barriers necessary to be overcome by the hydrogen to reach the crystalline silicon interface and recover the sputter process induced damage. When applied on a cell-level process, this pre-annealing step enabled the final V_{OC} of the device to surpass 730 mV, marking a substantial enhancement over the V_{OC} observed in solar cells previously discussed in this work, as well as the champion device reported in ref. [29]. This strategy, thus, not only contributed to a better understanding of the sputter-induced damage mechanisms but also offered a practical approach to mitigate their impact on solar cell performance.

6. Conclusion and Outlook

The aim of this thesis was on one hand to further enhance the power conversion efficiency (η) of the transparent passivating contact (TPC) solar cell structure, while also investigating the underlying reason for the sputter process induced degradation, limiting the open-circuit voltage (V_{OC}) of the device. It presented a comprehensive investigation of hydrogenated nanocrystalline silicon carbide (nc-SiC_X:H) in the realm of high-quality opto-electrical properties and its application in TPC solar cells. A detailed study had been conducted to understand the impact of various deposition parameters on the behavior of the material properties of nc-SiC_X:H, particularly focusing on its electrical conductivity (σ) and optical transparency. The current double layer structure encountered certain limitations which had been systematically identified and addressed through strategic modifications to the layer structure.

An additional notable limitation, as highlighted in previous research [29], was the pronounced discrepancy observed between the implied open-circuit voltage (iV_{OC}) of the solar cell precursor and the V_{OC} of the device, before and after the sputter deposition process. This discrepancy had been attributed to irreversible damage to the passivation quality caused by the sputtering process. In response, the latter part of this thesis delved into a detailed analysis, connecting both experimental procedures and simulation techniques, to shed light on the underlying mechanisms responsible for the sputter process-induced degradation. It was suggested that the degradation originated from the dissipation of phonons at the silicon oxide (SiO_X)/crystalline silicon (c-Si) interface, displacing hydrogen needed for passivation. Alternatively, the ion impact could excite electrons, which emit their excess energy while relaxing to their ground state as ultraviolet radiation. This segment of the thesis not only proposed an explanation, but also shed

light on the reasons behind the perceived irreversibility of the sputter process-induced damage in TPC solar cells.

Material Properties of nc-SiC:H(n)

The initial chapter of this research examined the impact of the deposition parameters on the material properties of nc-SiC_X:H. A notable finding was the strong correlation between the transparency of the material, as represented by the optical band gap (E_{04}), and its σ. An increase in σ was observed to correspond with an enhancement in E_{04}. The key deposition parameters essential to achieve superior opto-electrical properties included a high filament temperature (T_f) and hydrogen dilution (c_H), accompanied by a low total gas flow rate (F_{total}). These factors significantly influenced the deposition rate, where a slower rate tended to improve both σ and E_{04}. The dominant mechanism during material growth was hypothesized to be hydrogen radical etching, which served to increase the grain size of the material. A higher T_f increased the yield of hydrogen radicals, while an increased c_H augmented the hydrogen content in the precursor gas mixture, relative to the silicon carbide-depositing gas.

This effect was followed by the surface diffusion of precursor molecules on the surface of the substrate. An excess of molecules could cause cramming on the surface, leading to increased nucleation sites as the molecules were restricted in their movement. This resulted in the formation of more, yet smaller, grains that impeded each other during layer growth, ultimately reducing the overall grain size. The number of molecules present was influenced by F_{total} as more molecules could be decomposed at the filaments. This number was also likely to be affected to some extent by the deposition pressure (p_{depo}). The nucleation process might have also been influenced by the sample temperature, which affected the mobility of molecules on the sample surface. The sample temperature itself was likely dependent on factors such as chamber heater temperature (T_{heater}), filament-substrate distance ($d_{f\text{-}s}$), and possibly T_f. Within the studied range, the nitrogen flow rate (F_{N2}) appeared to have a negligible effect, possibly due to a trade-off between increased charge carrier concentration and smaller grains resulting from an increased defect density due to the presence of doping atoms.

In addition to the opto-electrical properties, the passivation quality of nc-SiC$_X$:H and its hydrogen content were analyzed. For high iV_{OC}s, a lower T_f was essential. Interestingly, the threshold temperature for a decrease in iV_{OC} appeared to shift to higher T_fs with a larger $d_{f\text{-}s}$. The enhancement in iV_{OC} was attributed to an increase in the hydrogen content in the layer, which was also achievable by reducing c_H or opting for an intermediate F_{total}. Smaller grain sizes were believed to increase the hydrogen content, thus improving the passivation capabilities of nc-SiC$_X$:H, as hydrogen was believed to reside at the grain boundaries within the material [95].

This segment of the investigation set the foundation for further detailed future analyses of the material properties of nc-SiC$_X$:H. With respect to its passivation quality potential, further examination of the hydrogen content across a broader range of deposition parameters is required. This investigation could establish a direct correlation between the hydrogen content and iV_{OC}, assessing whether an increase in the hydrogen content reaches a saturation point that limits the enhancement of iV_{OC}. Furthermore, hydrogen treatments via hot wire chemical vapor deposition (HWCVD), plasma-enhanced chemical vapor deposition (PECVD), or techniques like forming gas annealing and silicon nitride hydrogenation, might be employed post-deposition to elevate the passivation quality. Such treatments could minimize the required layer thickness to achieve a high iV_{OC}, or possibly improve the passivating capabilities of the material with an initially low hydrogen content, potentially achieving both high iV_{OC} and σ within the same material. If HWCVD or PECVD hydrogen treatments are applied to the conductive nc-SiC$_X$:H, it may be possible to improve σ by etching the amorphous phase or to facilitate grain growth by treating the nucleation zone at the beginning of layer growth. To further refine the electrical properties, exploratory investigations into dopant activation, such as light soaking, are necessary, as it is currently quite low for passivating nc-SiC$_X$:H [111]. Furthermore, research on catalytic doping processes to boost σ in either the passivating or conductive material are necessary, especially since some unintentional catalytic doping occurs in the double layer approach within the structure of the solar cell, as discussed in section 4.3. Lastly, a deeper understanding of the material could be achieved through molecular dynamic simulations, providing insights into the behavior of

hydrogen and dopants within the material and guiding how they can be used more effectively.

Double-layer and gradient layer nc-SiC:H(n) for Transparent Passivating Contact Solar Cells

In solar cell applications, nc-SiC_X:H was used in a double layer structure due to its ability to function either as a conducting material or a passivating material. The conducting nc-SiC_X:H, when used, reduced the reflective properties of the solar cell, optimized at a specific conducting nc-SiC:H(n) layer thickness ($d_{\mathrm{cond,\,SiC}}$). Contrary to expectations, this optimization did not similarly enhance the short-circuit current density (J_{SC}), likely due to parasitic absorption in the transparent conductive oxide (TCO) layer. Beyond a particular $d_{\mathrm{cond,\,SiC}}$ threshold, the V_{OC} remained stable, whereas the Fill Factor (*FF*) exhibited a minor decline with increased $d_{\mathrm{cond,\,SiC}}$, presumably owing to elevated resistances within the layer. In contrast, with variations of the passivating nc-SiC:H(n) layer thickness ($d_{\mathrm{pass,\,SiC}}$), a constant J_{SC} was maintained regardless of $d_{\mathrm{pass,\,SiC}}$, but a noticeable amplification in the iV_{OC} and a reduction in *FF* with increased $d_{\mathrm{pass,\,SiC}}$ was shown. This phenomenon could be attributable to a delicate equilibrium between the hydrogen concentration near the crystalline silicon interface, which was crucial for an optimal passivation quality, and the inherently low conductivity of the layer, thus creating a significant trade-off between these two pivotal solar cell parameters in this double layer structure.

To soften this trade-off, a gradient layer with a progressive transition in the material properties from a passivating to a conductive material was introduced. Replacing the passivating layer entirely with this gradient layer did not yield any efficiency gains in the solar cell, either due to the thick, low-conductive segment of the gradient layer that restricted the *FF*, or due to an insufficient hydrogen-rich part that diminished the iV_{OC}. A combined approach, which significantly thinned the passivating seed layer coupled with the introduction of a gradient layer, culminated in a 0.2$\%_{\mathrm{abs}}$ enhancement in efficiency of the champion solar cell, attributed to simultaneous gains in both V_{OC} and *FF* by relieving the previously identified trade-off.

To date, no comprehensive optimization of the seed, gradient, and conductive nc-SiC_X:H layers, considering their interdependence, has been performed. An optimized triple-layer configuration is expected to yield further advancements in V_{OC} and FF of the solar cell. Moreover, any material improvements proposed in the preceeding part are likely to also improve the overall performance of the device. Currently, complete recovery of the damage induced by the sputter process has not been achieved. The development of novel approaches, such as a light soaking procedure to fully restore the iV_{OC} to V_{OC} loss in the device, will significantly elevate the performance metrics of the solar cell.

Investigating Sputter-Induced Degradation in Transparent Passivating Contacts

The second part of the results in this thesis focused on examining the degradation in passivation quality due to the sputter deposition of TCO layers. A combination of experimental and simulation methodologies was employed to illuminate the core mechanisms of this phenomenon. It was established that the damage was entirely reversible, with no discernible alterations in the microstructure of the material. Neither the sputtering atmosphere nor the thermal effects of the sample heater altered the passivation quality. By deploying various optical filters to cut off different parts of the electromagnetic spectrum emitted by the sputtering plasma, it was observed that all shielded regions remain unaffected, even when portions of the vacuum ultra-violet (VUV) radiation were transmitted. This finding conclusively negated any detrimental impacts of plasma-emitted radiation. Subsequently, attention was directed towards the effects of electron bombardment. Simulations indicated that electrons were stopped within the initial 3.9 nm of the layer, and it was unlikely that characteristic x-ray radiation or secondary electrons would be generated. Experiments involving a 500 eV electron beam exposure underlined these findings, as no damage to the sample was detected, strengthening the simulation results. This observation effectively ruled out any detrimental effects arising from free electrons and x-rays, whether from bremsstrahlung or characteristic emissions from layer atoms, as all effects should have been present at these electron energies.

The investigation further extended to the simulation of ion bombardment. Penetration depths were assessed for various ions: Oxygen penetrated the deepest at 4.8 nm, followed by argon at 3.7 nm, tin at 3.4 nm, and indium at 3.2 nm. These estimations were slightly higher than those verified via energy-dispersive x-ray spectroscopy scans. The direct consequences from ion bombardment were thus disregarded as source for the degradation, as ions were implanted well away from the crystalline silicon interface. Any lasting impact close to the interface would have likely rendered the damage irreparable. Within the nc-SiC_X:H layer, the impinging ions initiated a cascade of secondary effects, including the generation of vacancies and phonons and the potential ionization of layer atoms. Given that vacancies in silicon carbide were immobile at lower temperatures, the efficacy of a low-temperature annealing for damage recovery was questionable. Ionized lattice atom electrons, as inferred from preceding investigations, are seemingly harmless.

Illiberi et al. propose that bound electron-hole pairs are generated, migrate towards the crystalline silicon interface, recombine, and displace hydrogen [237]. In the TPC, this would have required traversing over 20 nm, a distance at which the electron-hole pair was likely to recombine within the defect-rich layer. On the contrary, phonons, including phonon-like modes in amorphous silicon, possessed mean-free path lengths that exceeded 100 nm. Thus, an incident ion-excited phonon could have crossed the material, reaching an interface like the crystalline silicon interface, where it dissipated because of the perturbation in the lattice structure. The resultant energy from multiple phonons simultaneously dissipating might have broken a silicon-hydrogen bond, dislocating the hydrogen atom. This displaced hydrogen could then re-attach to the vacant bond during low-temperature annealing, reinstating passivation quality.

For a more comprehensive understanding, further exploration is crucial. Delving deeper into the microstructure, particularly the hydrogen arrangement within the material, using more sensitive techniques is essential to identify interface-level changes. Exploring how the damage correlates with the nc-SiC_X:H layer thickness and other material characteristics, such as grain size, is necessary to deepen the understanding of processes in the material. Moreover, the

consequences of ion bombardment warrants investigation in a more regulated setting, possibly using an ion implanter. Variations in ion sizes could influence the extend of the damage, and the impact of ion fluxes and energies must be considered and correlated with the reduction in passivation quality. Furthermore, further investigations are necessary regarding low-energy electrons, as these could penetrate deeper into the layer [276]. A direct comparison of these effects across different materials could yield unified conclusions. Comparing the sputter-induced damage with UV degradation effects may provide additional insight into the atomistic processes in the material. It is also crucial to examine whether this sputter-induced impairment affects field-effect passivation-based methods, as this study primarily discusses hydrogen-based chemical passivation. If phonons, as theorized, are the source of the damage, integrating additional layers to impede phonon propagation within the layer stack could be a viable solution. Additionally, the UV generation in nc-SiC_X:H layers needs to be assessed and the potential damaging effect needs deeper investigations.

Thermal Recovery of Transparent Passivating Contacts

Contrary to previous claims that the sputter-induced damage in transparent passivating contact solar cells was unrecoverable [29], this study presented a breakthrough that demonstrated complete recovery of the TPC. A notable thermal discrepancy between the TPC at the front side and the silicon heterojunction (SHJ) rear contact of the solar cell structure was identified, explaining the previously unrecoverable damage. The SHJ contact withstood temperatures of up to 190 °C, further enhanced to 210 °C with an additional light soaking step, whereas the TPC necessitated a minimum of 220 °C for full recovery. Prolonging the annealing duration did not lower this threshold temperature in the TPC structure. Interestingly, pre-annealing of the sample, beneficial in SHJ solar cells for mitigating sputter damage, improved the response of the TPC structure to lower temperature annealing, but fell short of complete damage recovery, leaving some residual damage. It was hypothesized that during pre-annealing, hydrogen within the SiO_X or nc-SiC_X:H layers underwent reconfiguration at elevated temperatures, thereby

reducing the energy barriers for hydrogen mobility, leading to this enhanced post-annealing behavior.

Research on the pre-annealing behavior of TPCs solar cells only just began. Future exploration is geared toward understanding how higher pre-annealing temperatures could potentially optimize the post-annealing performance of the TPC stack. Light soaking emerges as a promising technique to rectify sputter-induced damage in the TPC without adversely affecting the SHJ rear contact. Analyzing the annealing behavior of the TPC could reveal activation energies for various hydrogen-related processes within the TPC layer stack, providing deeper material insights. Lastly, the absence of a time dependency for complete damage restoration suggests that shorter annealing durations might suffice for recovery, posing minimal risk to the passivation quality of the SHJ side of the solar cell.

Further Advancements Strategies in Transparent Passivating Contacts for Solar Cells

Another layer within the TPC framework, the wet-chemical SiO_X layer, has not been the focus of this research. Preliminary findings indicated that the composition of the Piranha solution may influence the iV_{OC}, yet further experimentations are required to determine if this leads to an enhanced V_{OC} in the complete structure of the solar cell [277]. Alternative approaches, such as the use of a thermal silicon oxide, such as in tunnel oxide passivated contact (TOPCon) solar cells, or plasma oxidation, could potentially increase the passivation quality of the oxide layer, thus increasing the V_{OC} of the solar cell. Another strategy to improve the electrical conductivity through the oxide layer involves introducing dopants into the oxide, either during growth [278, 279] or in a post-growth catalytic doping step. Additionally, changes in the passivation quality could be attributed to alterations in stoichiometry and hydrogen solubility within the oxide, providing valuable information on the passivation mechanisms at work in the TPC.

Furthermore, previous work has exclusively explored wet-chemically grown SiO_Xs in relation to the TPC stack [111]. Exploring materials with lower band gaps, such as silicon nitride or hafnium oxide, might yield a higher tunnelling prob-

ability, enhancing the electrical contact. Materials that introduce fixed charges, such as hafnium or aluminum oxide, could introduce an additional field-effect passivation.

The high temperature stability of the HWCVD-grown nc-SiC_X:H remains unexamined. Identifying a high temperature stable nc-SiC_X:H could open opportunities for its application as a front-side passivation or contact layer in TOPCon solar cells. From a material perspective, the development of a p-type passivating contact is vital for the realization of a completely hot wire chemical vapor deposition-based nc-SiC_X:H solar cell.

Transitioning from laboratory-scale experiments to industrial-scale applications is another crucial step forward. The scalability of the process, particularly addressing layer inhomogeneities inherent in the HWCVD method, is vital for the industrial adaptation. The use of Piranha solution, while effective, generates substantial chemical waste, posing environmental and economic challenges for large-scale deployment. Moreover, as highlighted in the initial chapter of this study, the achievement of high conductivity requires low deposition rates, which conflicts with the demands for high throughput in industrial settings. Thus, revisiting the possibility of achieving higher electrical conductivity at improved deposition rates, as discussed earlier, becomes an essential consideration for practical application.

A. On the Lifetime of Hot Wire CVD Filaments

The selection of materials for the catalytic filaments in hot wire chemical vapor deposition (HWCVD) technology is a crucial aspect of the HWCVD chamber design. This choice balances the need for affordability, to minimize operational costs, and stability to reduce system downtime. In this study, rhenium filaments were used, a costly material priced at approximately 550 $\frac{\text{US\$}}{\text{m}}$ (as of November 2023). Tantalum, a less expensive alternative commonly used in the deposition of hydrogenated amorphous silicon (a-Si:H), is found to be less suitable during the nc-SiC_X:H deposition due to brittleness caused by carbon alloying of the filaments. Rhenium, despite its higher stability in regards to carbon alloying, also undergoes alloying with silicon, leading to eventual filament failure. The estimated total thickness of the deposited layer in relation to the changes of the filaments is investigated in figure A.1. A notable scattering in the thicknesses prior to filament breakage and replacement was observed, along with a discernible downward trend. A marked deviation from this trend occurred following an intensive cleaning of the filament holder and gas outlets.

This downward trend, coupled with improved filament stability after cleaning, suggested the potential benefits of incorporating a cleaning routine after every alternate filament change to improve the filament lifetime. Additionally, a non-invasive cleaning process implemented after certain deposition cycles may further extend the filament life. The considerable scattering in the data points could have most likely been attributed to the filament mounting technique. The filament ends were secured in ring-shaped holders using a screw, tightened on the top of the filament. The degree of tightness of this screw could have impacted

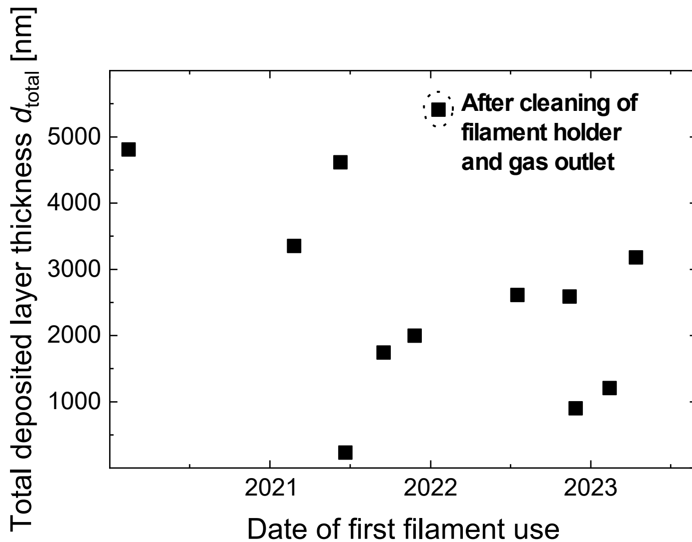

Figure A.1.: *Chronological representation of the estimated total layer thickness deposited per filament. A noticeable scattering with a general downward trend is evident.*

the integrity of the filament; an overly tightened screw compressed the filament, potentially reducing its diameter at the contact point, increasing electrical resistance, and consequently leading to accelerated ageing and premature breakage. Conversely, a loosely tightened screw might result in the filament slipping out of the holder. To gain more conclusive insights into the filament lifetime and implement effective maintenance strategies, a more repeatable method, such as a spring-loaded fixation, should be considered. Another challenge that may arise is the accumulation of deposited material at the contact points over time, which can lead to a degraded electrical contact between the holder and the filament. This could cause increasingly unreliable current management.

In conclusion, especially for industrial application considerations, extensive research is needed to enhance the longevity of the filaments. This includes exploring alternative contact techniques, filament materials, and cleaning protocols. Broader information on HWCVD technology and the dynamics at the filaments can be found in ref. [112].

B. Evaluation of SRIM Damage Calculation Models

The Stopping and Range of Ions in Matter (SRIM) presents three models to assess the damage to the layer, each of which will be evaluated and compared in this chapter. More comprehensive insights into the computational processes and the simulation framework can be found in ref. [206]. The *Kinchi-Pease* model stands out for its computational speed. However, its primary limitation lies in not monitoring the trajectories of recoiling atoms after creation. Consequently, it offers a general overview of vacancy distributions, which lacks element-specific distinctions. In contrast, the *Full Cascade* model provides a detailed tracking of each recoil at the cost of an increased computational time. This model delivers full data on element-specific vacancies and accounts for replacement collisions, although at the cost of extended computational time. It is also known for occasionally causing ion pile-up at interfaces in thinner layers, an issue circumvented by the *Monolayer* model. This latter model offers a compromise with intermediate computation time and includes replacement collisions, but, like the *Kinchi-Pease* model, it supplies only combined data on vacancies generated.

Variations in the simulation outcomes are primarily due to the different treatments of recoiling atoms. As illustrated in figure B.1, all models exhibited similar primary ion energy distributions, but diverged in their shares for recoiling layer atoms. The *Kinchi-Pease* model predominantly attributed recoil energy to phonons, a trend less pronounced in the *Full Cascade* and *Monolayer* models. Here, recoiling atoms played a more pronounced role in the creation of vacancies and in electron interactions. The similarity in primary ion results across models was reasonable, given that the absence of recoil tracking in the *Kinchi-Pease*

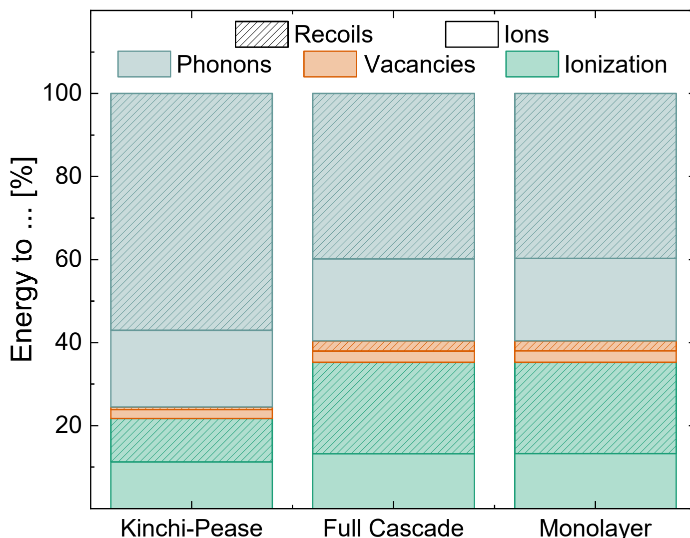

Figure B.1.: *Comparative energy distributions across the Kinchi-Pease, Full Cascade, and Monolayer models within the Stopping and Range of Ions in Matter (SRIM) framework. Although primary ion energy transfer remains consistent across models, the Kinchi-Pease model exhibits a higher fraction of energy from recoiling atoms to phonons. Discrepancies between the Full Cascade and Monolayer models are minimal.*

model limited its impact on vacancy generation and electron interaction, an aspect that changed in the other two models. With the predominant energy transfer to phonons observed across all models, the rapid computation offered by the *Kinchi-Pease* model appeared to be a pragmatic choice for time efficiency.

The differential treatment of recoiling atoms may also influence the depth distribution of various effects, as examined in figure B.2. The maximum penetration depth (d_{max}) for any ion or recoil, as depicted in figure B.2 a), showed a modest variance of only 1.1 nm, ranging from the oxygen ion in the *Kinchi-Pease* calculations to the hydrogen recoils in the *Full Cascade* calculations. This minor discrepancy, when considered in the context of the inherent statistical spread in Monte Carlo simulations, was deemed negligible. The vacancy generation profiles in figure B.2 b) were similar across models, indicating no significant variation in the general behavior of the simulated vacancies. The phonon and ionization calculations in figure B.2 c) and d), respectively, revealed a marginally deeper penetration in the layer from recoiling atoms in the *Full Cascade* and *Monolayer*

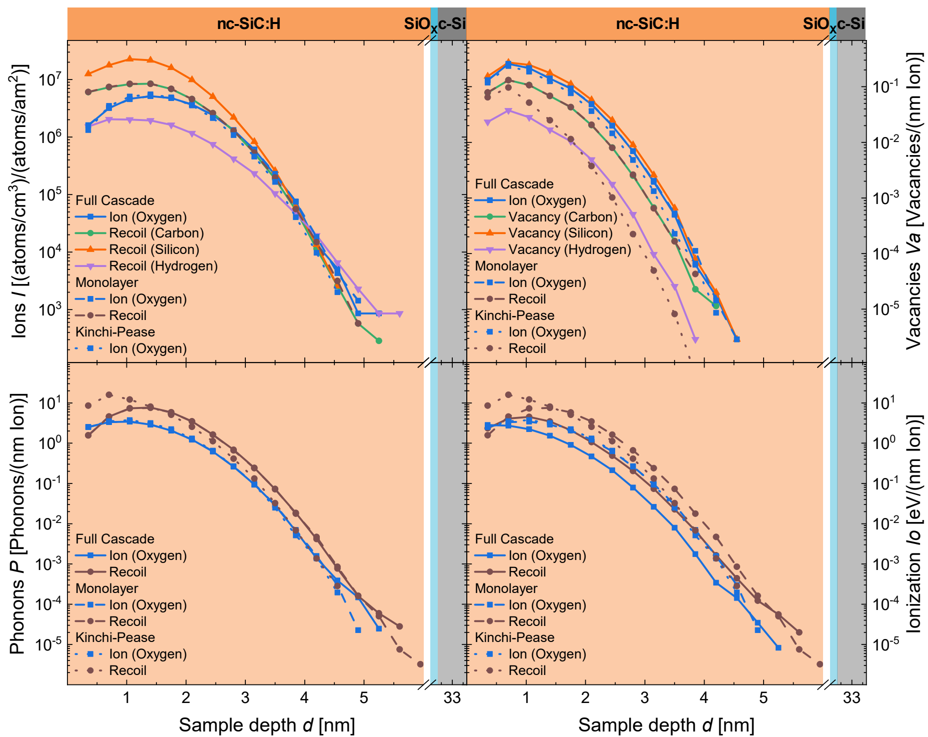

Figure B.2.: *Depictions of a) ion implantation and recoil atom profiles, b) vacancy generation profiles, c) phonon generation profiles, and d) electron interaction profiles for Full Cascade, Monolayer, and Kinchi-Pease models. The models demonstrate a commendable coherence in the various calculated profiles.*

models compared to the *Kinchi-Pease* model. However, since the difference was mainly around 0.2 nm, it was considered insignificant. The maximal generation depth of these effects from recoils in the *Full Cascade* and *Monolayer* model was up to 1.5 nm deeper than in the *Kinchi-Pease* model. However, given the overall alignment of results, this degree of uncertainty was acknowledged as a trade-off for computational time efficiency.

C. Evaluating the Optical Band Gap: Choosing an Appropriate Methodology

In the field of semiconductors, optical and electrical band gaps are critical parameters. The optical band gap signifies the minimal photon energy required to elevate an electron from the valence band to the conduction band. In contrast, the electrical band gap represents the theoretical minimum energy necessary to generate free electrons and holes, facilitating electrical conductivity. In particular, these band gaps may not necessarily correspond or behave in tandem. Often, the optical band gap exceeds the electrical band gap by several tenths of an electron volt. This discrepancy arises from various factors, such as the exciton binding energy, which necessitates additional energy to dissociate electron-hole pairs, the indirect nature of the band structure, or phenomena like the Burstein-Moss effect in heavily doped semiconductors. In the latter case, the Fermi level extends into the conduction band, filling the lower-energy states and necessitating higher excitation energies for the electron transition from the valence to the conduction band.

Various methods exist for determining the optical band gap, including reflectance/transmittance measurements, photoluminescence spectroscopy, ellipsometry, and photothermal deflection spectroscopy. These methods involve fitting a linear portion of the transmission or absorption coefficient data to interpolate the onset of light absorption. [280] However, calculating the absorption coefficient (α) can be challenging due to its multiple definitions.

A common definition of α employs the Bouguer-Lambert-Beer (BLB) law [280], expressed as:

$$\alpha_{BLB} = \frac{1}{d}\ln(\frac{1}{T}), \quad (C.1)$$

where d and T represent the layer thickness and transmission, respectively. This definition, however, overlooks the reflection (R), potentially overestimating absorption. Modifying this equation to include the external reflection yields:

$$\alpha_{corr} = -\frac{1}{d}\ln(\frac{T}{1-R}), \quad (C.2)$$

which accounts for the external reflection but still omits internal reflections. Further refinement for two-interface internal reflection leads to

$$\alpha_{simple} = \frac{1}{d}\ln(\frac{(1-R)^2}{T}) \quad (C.3)$$

and for multiple internal reflections to

$$\alpha_{complex} = \frac{1}{d}\ln(\frac{(1-R)^2}{2T}\sqrt{\frac{(1-R)^4}{2T}+R^2}). \quad (C.4)$$

The results for the different αs based on the example of a random sample of the investigations in section 4.1.1 measured with Ultraviolet/Visible spectroscopy (UV/VIS) can be found in figure C.1. The BLB approach yielded higher absorption coefficients, likely because of an overestimation from ignoring the reflection of the sample. The absorption coefficient decreased with more included reflections, reaching negative values for the reflection-corrected method at an photon energy (E_{photon}) of approximately 3.1 eV due to the limitations in sensitivity of the measurement system. The simple internal reflection-corrected α turned fully negative, as shown in the linear scaled graph of figure C.1 b). The multiple internal reflection-corrected α remained positive for higher E_{photon}s above roughly 3.9 eV. The incorporation of reflections into the calculation of the α significantly impacted the results, as observed in this study. The BLB model, which did not account for reflection, tended to considerably overestimate absorption in the layer. For the purposes of this work, the externally corrected absorption coefficient, α_{corr}, was employed. This model included some reflections and provided an

Table C.1.: *Different approaches for determining the optical band gap and the values for the optical band gap. Additionally, the energy range for the linear fit and the accuracy of the fit, as given by R^2, is presented.*

Method	Based on	Optical band gap [eV]	Linear energy range [eV]	R^2 [-]
Transmission	transmission (T)	4.65	0.54	0.998
Transmission derivative	$\frac{dT}{dE}$	2.77	0.82	0.919
Straight	α	3.63	0.26	0.990
Direct	α^2	3.84	0.19	0.985
Indirect	$\alpha^{\frac{1}{2}}$	3.18	0.73	0.995
Cody	$(\frac{\alpha}{E})^{\frac{1}{2}}$	3.23	0.12	0.997
Tauc	$(\alpha E)^{\frac{1}{2}}$	3.26	0.59	0.996
Tauc 2	$(\alpha E)^2$	3.86	0.19	0.981
E_{03}	$E(\alpha = 10^3)$	3.10	-	-
E_{04}	$E(\alpha = 10^4)$	3.25	-	-
E_{05}	$E(\alpha = 10^5)$	3.73	-	-

adequate extensive linear segment for subsequent fitting.

The selection of a suitable method for defining the optical band gap was the subsequent step. This study examined nine distinct methodologies, each based on either transmission curves, absorption coefficient curves, or their product with the E_{photon}. These methodologies, along with their corresponding linear energy bands for fitting and the accuracy of the fit, as indicated by the R^2 value, are detailed in table C.1. The respective figures, depicting the data and the fits, are presented in figure C.2 for transmission-based approaches, in figure C.3 for α-based and fixed energy approaches, and in figure C.4 for methods depending on both α and E_{photon}.

The smallest optical band gap was determined using the derivative of the transmission method, while the largest band gap was derived from the transmission method. The broadest energy range for fitting was observed in both the indirect and transmission derivative approaches. The most accurate fits, with values of R^2 greater than 0.990, were achieved using the transmission, indirect, Cody, and Tauc methods. The fit to the derivative of the transmission demonstrated a lower accuracy, likely due to significant data scattering and noise. The direct, Cody, and Tauc 2 methods exhibited the narrowest energy range

for fitting, which could potentially be further reduced by selecting a different α calculation method.

Most calculated optical band gaps fell within the 3 eV to 4 eV range. Figure C.5 compares the optical band gaps obtained from the various methods. It was observed that methods based on transmission data or its derivative tended to overestimate or underestimate the optical band gap, respectively. Methods such as straight, direct, Tauc 2, and $E(\alpha = 10^5)$ yielded similar results, with optical band gaps around 3.8 eV. Similarly, the indirect, Cody, Tauc, $E(\alpha = 10^3)$, and $E(\alpha = 10^4)$ methods indicated optical band gaps around 3.2 eV. For this research, given that most methods converged to an optical band gap of approximately 3.2 eV, one of these methods is selected. The $E(\alpha = 10^4)$ method was chosen to minimize evaluation time and to avoid dependence on data fitting and its associated quality. Further details on optical band gaps, the comparison of various methods, and their application to different materials are available in ref. [280].

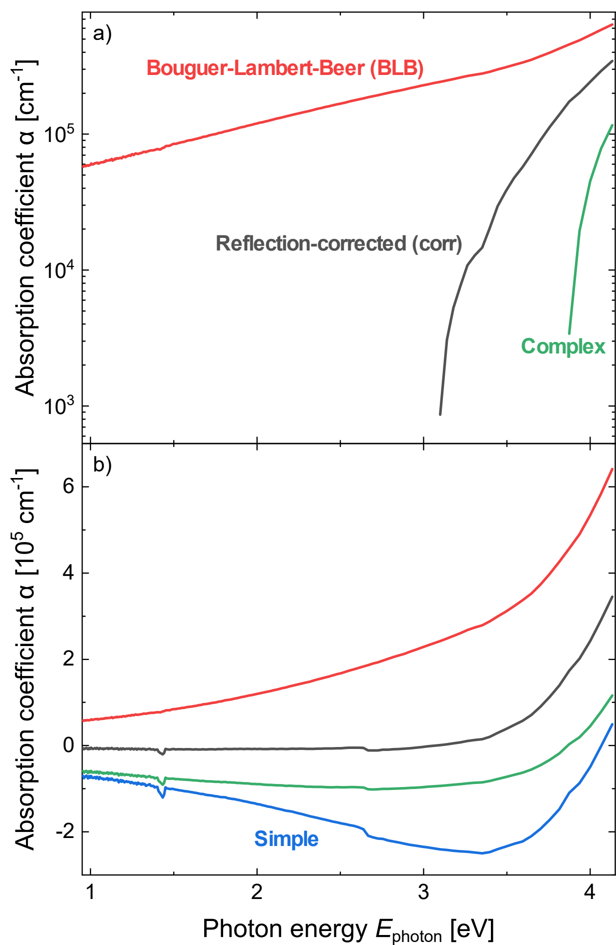

Figure C.1.: *The resulting absorption coefficient (α) from the different discussed equation equation* (C.1) *to equation* (C.4). *A trend with a decreasing α with more reflections is observable and can lead to completely negative αs due to measurement uncertainties.*

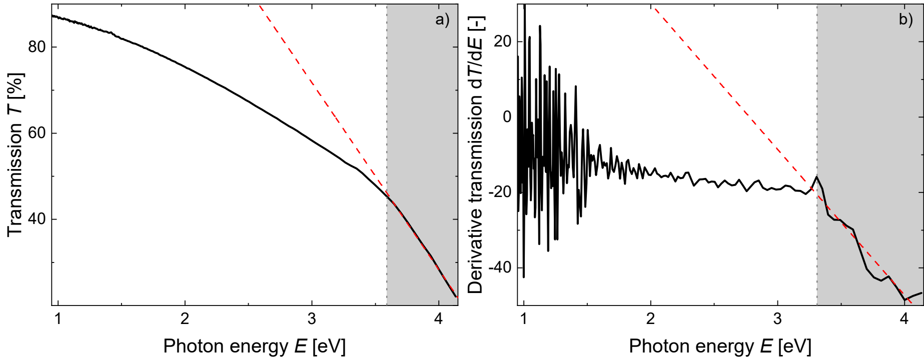

Figure C.2.: *Determination of the optical band gap, together with the values of the fit, given by the red dashed line, for the a) transmission and b) derivative of the transmission method. The shaded area visualizes the linear part of the data used for fitting.*

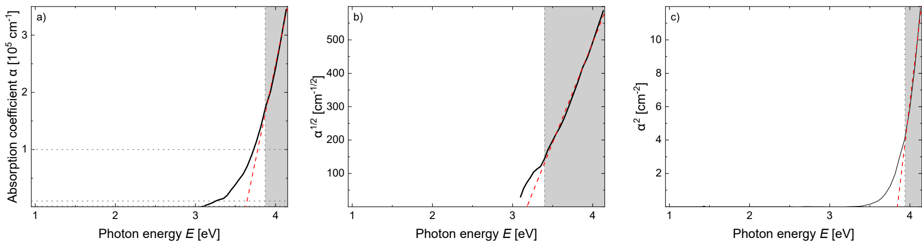

Figure C.3.: *Determination of the optical band gap, together with the values of the fit, given by the red dashed line, for the a) straight, b) indirect and c) direct method. The shaded area visualizes the linear part of the data used for fitting. The horizontal lines mark the absorption coefficient values at which the energies are evaluated for the fixed absorption coefficient approaches.*

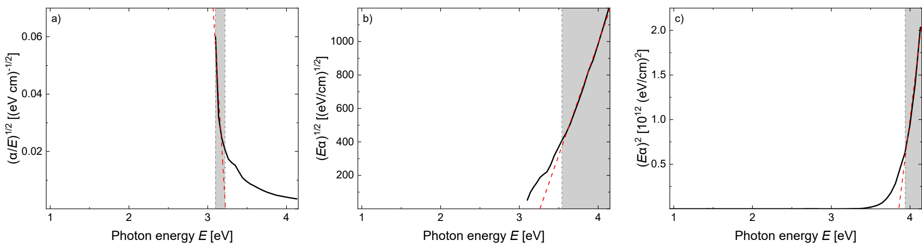

Figure C.4.: *Determination of the optical band gap, together with the values of the fit, given by the red dashed line, for the a) Cody, b) Tauc and c) Tauc 2 method. The shaded area visualizes the linear part of the data used for fitting.*

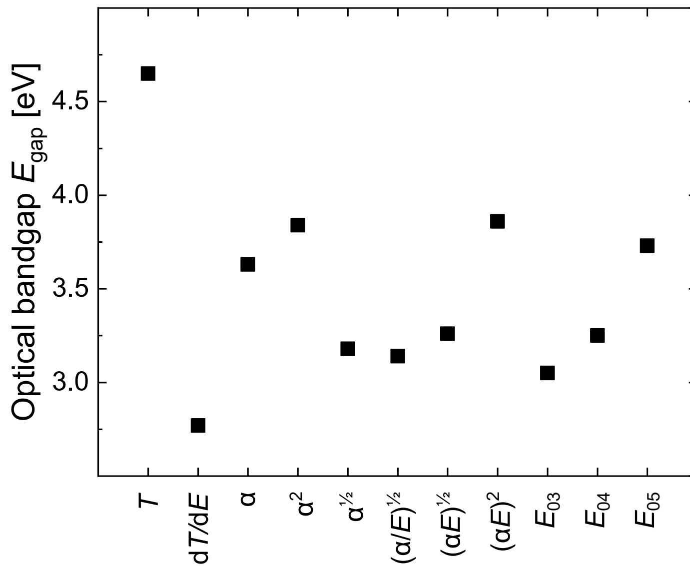

Figure C.5.: *The resulting optical band gaps for the various discussed methods. The transmission method gives the largest optical band gap, while the transmission derivative gives the smallest. The straight, direct, Tauc 2 and $E(\alpha = 10^5)$ give similar optical band gaps around 3.8 eV, while the indirect, Cody, Tauc, $E(\alpha = 10^3)$ and $E(\alpha = 10^4)$ give similar results around 3.2 eV.*

List of Abbreviations

This chapter lists all acronyms used in this thesis.

Nature Constants and Basic Acronyms:

Δn	excess charge carrier concentration
Δn_e	excess electron concentration
Δp	excess hole concentration
e	elementary charge of an electron
E	energy
E_{photon}	photon energy
E_{04}	optical band gap
E_C	conduction band energy
E_F	Fermi energy
$E_{F, e}$	quasi-Fermi level of electrons
$E_{F, h}$	quasi-Fermi level of holes
E_G	band gap
E_V	valence band energy
ω	frequency
G	generation rate
I_{Si-H}	FTIR silicon-hydrogen bond peak intensity
k_B	Boltzmann constant
μ_n	electron mobility
μ_p	hole mobility
n	minority carrier density
n_0	equilibrium electron concentration
N_C	density of states in the condution band
n_i	intrinsic charge carrier concentration

N_V	density of states in the valence band
p_0	equilibrium hole concentration
q	elemental charge
R_{Auger}	Auger recombination rate
R_{rad}	radiative recombination rate
R_{SRH}	Shockley-Read-Hall recombination rate
ρ_M	majority carrier resistance
ρ_m	minoriy carrier resistance
S	selectivity
σ	electrical conductivity
σ_L	photoconductance
UV	ultraviolet
VUV	vacuum ultra-violet
ν	wavenumber

Materials and Technologies:

Ar	argon
a-Si:H	hydrogenated amorphous silicon
B_2H_6	diborane
c-Si	crystalline silicon
H	molecular hydrogen
H_2	hydrogen
HCl	hydrochloric acid
HF	hydrofluoric acid
IBC	interdigitated back contact
In	indium
ITO	indium tin oxide
MgF_2	magnesium fluoride
MMS	monomethylsilane
N_2	nitrogen
nc-Si:H	hydrogenated nanocrystalline silicon
nc-SiC_X:H	hydrogenated nanocrystalline silicon carbide
O	oxygen
O_3	ozone

PERC	passivated emitter rear contact
POLO	polycrystalline silicon on oxide
poly-Si	polycrystalline silicon
SHJ	silicon heterojunction
SiH_4	silane
SiN	silicon nitride
SiO_X	silicon oxide
Sn	tin
TCO	transparent conductive oxide
TOPCon	tunnel oxide passivated contact
TPC	transparent passivating contact

Measurement and Sample Parameters:

A	absorption
α	absorption coefficient
c_H	hydrogen dilution

as used in chapter 3 and chapter 4

c_H	hydrogen content

as used in chapter 5

d	layer thickness
d_{sample}	sample depth
$d_{cond, SiC}$	conducting nc-SiC:H(n) layer thickness
d_{f-s}	filament-substrate distance
$d_{gradient, SiC}$	graded nc-SiC:H(n) layer thickness
d_{max}	maximum penetration depth
$d_{pass, SiC}$	passivating nc-SiC:H(n) layer thickness
$d_{seed, SiC}$	passivating seed nc-SiC:H(n) layer thickness
ΔiV_{OC}	implied open-circuit voltage loss
ΔV_{OC}	open-circuit voltage loss
E_{ion}	incident ion energy
$E_{electron}$	incident electron energy
E_{loss}	energy loss
EQE	external quantum efficiency

FF	Fill Factor
F_{N2}	nitrogen flow rate
F_{total}	total gas flow rate
η	power conversion efficiency
$I_{element}$	Intensity of elemental emission lines
Io	ionization
I_{plasma}	plasma intensity
IQE	internal quantum efficiency
$\mathrm{i}V_{OC}$	implied open-circuit voltage
J	current density
J_0	recombination current density
J_{gen}	light-generated current density
J_{mpp}	current density at the maximum power point
J_{rec}	current density from charge carrier recombination
J_{Refl}	reflection losses
J_{SC}	short-circuit current density
k	extincition coefficient
L_T	transfer length
n	refractive index
P	phonon
P_{in}	incident power
P_{MPP}	power at the maximum power point
p_{depo}	deposition pressure
$\mathrm{p}FF$	pseudo Fill Factor
r	deposition rate
R	reflection
R_{fil}	filament current ramp
R_S	series resistance
R_{sh}	shunt resistance
ρ_c	contact resistivity
T	transmission
T_{anneal}	annealing temperature
t_{acc}	accumulated annealing time

t_{anneal}	annealing time
T_f	filament temperature
T_{heater}	chamber heater temperature
T_{post}	post-annealing temperature
T_{pre}	pre-annealing temperature
t_{pre}	pre-annealing time
τ_{eff}	effective minority carrier lifetime
τ_{pulse}	duration of the light pulse
V	voltage
Va	vacancy
V_{imp}	implied voltage
V_{mpp}	voltage at the maximum power point
V_{OC}	open-circuit voltage
V_T	target voltage
X_C	crystalline volume fraction

Methods, Measurements and Tools:

CASINO	Monte Carlo Simulation of Electron Trajectory in Solid
CVD	chemical vapor deposition
FTIR	Fourier-Transform Infrared Spectroscopy
HWCVD	hot wire chemical vapor deposition
PECVD	plasma-enhanced chemical vapor deposition
PL	photoluminescent lifetime
PVD	physical vapor deposition
QSSPC	Quasy-Steady State Photoconductance
SE	spectral ellipsometry
SIMS	secondary ion mass spectroscopy
SRIM	Stopping and Range of Ions in Matter
TLM	transfer length method
UV/VIS	Ultraviolet/Visible spectroscopy

List of Figures

2.1. a) Sketch of continuum of energy bands depending on the interatomic spacing, adapted from [32] and b) snapshots for classifications of, from left to right, schematic representations of band structures for metals, semiconductors, and insulators, highlighting the band overlap in metals and the distinct band gaps in semiconductors and insulators. 8
2.2. Depiction of the Fermi-level positioning within the band gap for a) intrinsic, b) p-type doped, and c) n-type doped scenarios. 10
2.3. Depiction of a *pn*-junction in a non-illuminated state with a generated electron/hole pair in the p-type and n-type material. At the *pn*-junction, an electron can migrate from the p-type to n-type region, but not vice versa. The hole, on the other hand, can move from n-type to p-type material but is blocked to move from p-type material to n-type material. 12
2.4. Basic structure of a crystalline silicon solar cell consisting of an absorber material for light absorption and electron/hole pair generation, which can already be doped. On top needs to be a doped layer of different polarity for charge carrier separation and some contacts for charge carrier extraction. 13
2.5. Illustration of a *JV*-curve (blue) and the corresponding power (orange) of a solar cell under one sun illumination. Key solar cell parameters are highlighted. The curve is mirrored to positive currents for clarity. 14

2.6. Calculations of the dependence of FF on V_{OC} for n_{id} of 2/3 and 1 and different series resistance (R_S) of 0 Ω, 0.5 Ω and 1 Ω. The star marks the maximum achievable FF-V_{OC} combination for wafer thicknesses and dopant concentrations used in this thesis. The impact of shunt resistance (R_{sh}) is neglected. 18
2.7. From left to right, schematic representation of light absorption, radiative recombination, Auger recombination and Shockley-Read-Hall recombination. 23
2.8. Illustrations of prevalent solar cell technologies: a) The passivated emitter rear contact (PERC) structure, b) a tunnel oxide passivated contact (TOPCon) structure utilized on the rear side, and c) a hydrogenated amorphous silicon (a-Si:H)-based silicon heterojunction (SHJ) contact. An illustration of the structure is shown on the left side, while a sketch of the corresponding band diagrams is shown on the right side. 25
2.9. Optimization triangle for front passivating contacts, illustrating the interplay and trade-offs between the short-circuit current density (J_{SC}), open-circuit voltage (V_{OC}), and the Fill Factor (FF). 29
2.10. Evolution of the power conversion efficiency (η) of silicon carbide-based solar cells based on their publication date. High-temperature solar cells mostly employ a plasma-enhanced chemical vapor deposition (PECVD) silicon carbide with a crystalliaztion step and additional hydrogenation, while low-temperature solar cells employ either PECVD or hot wire chemical vapor deposition (HWCVD) to grow amorphous or nanocrystalline silicon carbide. The solar cells marked as 'Hydrogenation treatment' employ a low-temperature approach, but utilize an additional hydrogenation treatment of temperatures around 400 °C. The learning rate (LR) of the high- and low-temperature approach are given in the graph as well. Efficiency data taken from refs. [29, 89, 116, 117, 119, 120, 127, 128, 130, 131, 134–136, 143, 159–163] 38

3.1. Illustration of the hot wire chemical vapor deposition (HWCVD) chamber, pinpointing the key deposition parameters in bold. 44
3.2. Exemplary Fourier-Transform Infrared Spectroscopy (FTIR) spectrum of a hydrogen-rich nc-SiC_X:H. The peak positions were identified according to values given in literature. [170, 173–175] 51
3.3. Generation rate (G) and excess charge carrier concentration (Δn) during the illumination flash in a photoluminescent lifetime (PL) imaging setup. The time points for image capture were indicated, with broader marks denoting the integration of the image signal over time. 62

4.1. Dependence of the lateral electrical conductivity (σ) on various deposition parameters a) deposition pressure (p_{depo}), b) filament-substrate distance ($d_{\text{f-s}}$), c) chamber heater temperature (T_{heater}), d) hydrogen dilution (c_{H}), e) nitrogen flow rate (F_{N2}), f) total gas flow rate (F_{total}), and g) filament temperature (T_{f}). The parameters that most affect σ, with variations of more than nine orders of magnitude, are T_{f} and c_{H}, followed by a five orders of magnitude shift in σ due to F_{total}. Reproduced with permission from John Wiley & Sons - Books, from [113]; permission conveyed through Copyright Clearance Center, Inc. 70
4.2. Correlation between the optical band gap (E_{04}) and electrical conductivity (σ) for the previous series of deposition parameters. An increase in conductivity is usually accompanied by an increase in E_{04}. Reproduced with permission from John Wiley & Sons - Books, from [113]; permission conveyed through Copyright Clearance Center, Inc. 71
4.3. Dependence of electrical conductivity (σ) on the deposition rate (r) across various deposition parameter series. Lower r tends to yield higher σ, though the increased deposition rate from the chamber heater temperature (T_{heater}) series may be an exception. Reproduced with permission from John Wiley & Sons - Books, from [113]; permission conveyed through Copyright Clearance Center, Inc. 72

4.4. Visualization of the three discussed growth mechanisms a) hydrogen radical etching, b) number of reactive species on the substrate and c) sample temperature. 75
4.5. Variation in the implied open-circuit voltage (iV_{OC}) as a function of the filament temperature (T_f) for two distinct filament-substrate distances ($d_{f\text{-}s}$s). The inlet shows the sample structure featuring SiO_X and nc-SiC_X:H(n) layers on both sides. The lower T_f leads to an enhanced iV_{OC}, while a larger $d_{f\text{-}s}$ shifts the temperature of iV_{OC} decline to higher values. The dashed lines serve as visual guides. 77
4.6. Variation in the FTIR silicon-hydrogen bond peak intensity ($I_{Si\text{-}H}$) in response to changes in the a) filament temperature (T_f), b) hydrogen dilution (c_H), and c) total gas flow rate (F_{total}). The other relevant deposition parameters are specified in each diagram. Low T_f and c_H elevate the hydrogen content, while an intermediate F_{total} maximizes it. The dashed lines provide guides to the eye. 78
4.7. Schematic illustration of a solar cell featuring a transparent passivating contact (TPC) as front contact and a silicon heterojunction (SHJ) as rear contact. The TPC consists of a tunnel oxide layer combined with passivating and conductive nc-SiC_X:H(n) layers. The zoomed area displays a transmission electron microscope image of the layer stack. The inlet, courtesy of Xianlin Qu at Beijing University of Technology, showcases the thin layer structure. . . . 79
4.8. Impact of varying the passivating nc-SiC:H(n) layer thickness ($d_{pass,\,SiC}$) on a) power conversion efficiency (η), b) implied open-circuit voltage (iV_{OC}) and open-circuit voltage (V_{OC}), c) short-circuit current density (J_{SC}), d) pseudo Fill Factor (pFF) and Fill Factor (FF), and e) contact resistivity (ρ_c). Extremely thin $d_{pass,\,SiC}$ lead to an overall poor cell performance due to passivation challenges. Increased $d_{pass,\,SiC}$ enhances passivation but reduces FF. The inset illustrates the sample structure with the varying layer highlighted in the stack. 81

4.9. Effect of varying the conducting nc-SiC:H(n) layer thickness ($d_{\text{cond, SiC}}$) on a) power conversion efficiency (η), b) implied open-circuit voltage (iV_{OC}) and open-circuit voltage (V_{OC}), c) short-circuit current density (J_{SC}), d) pseudo Fill Factor (p*FF*) and Fill Factor (*FF*), and e) contact resistivity (ρ_c). Extremely thin $d_{\text{cond, SiC}}$ detrimentally affects most solar cell parameters. Thicker layers primarily reduce *FF*. The inset illustrates the sample with the varied layer within the stack. 83

4.10. a) Reflection (R) curves for varying conducting nc-SiC:H(n) layer thicknesses ($d_{\text{cond, SiC}}$s) and b) the resulting calculated reflection losses (J_{Refl}) from a). A thicker $d_{\text{cond, SiC}}$ leads to a reduced reflection in the layer stack. The inset depicts the sample structure with the varied layer. Permission for use granted by John Wiley & Sons - Books, from [113] via Copyright Clearance Center, Inc. 85

4.11. Internal quantum efficiencies (*IQE*s) for variations in a) conducting nc-SiC:H(n) layer thickness ($d_{\text{cond, SiC}}$) and b) $d_{\text{pass, SiC}}$. For very thin $d_{\text{cond, SiC}}$ or $d_{\text{pass, SiC}}$, the internal quantum efficiency (*IQE*) is reduced due to poor passivation quality. Insets illustrate the varied layer within the sample stack. Permission for use granted by John Wiley & Sons - Books, from [113] via Copyright Clearance Center, Inc. 86

4.12. Correlation between the pseudo Fill Factor (p*FF*) or Fill Factor (*FF*) and implied open-circuit voltage (iV_{OC}) for a) various passivating nc-SiC:H(n) layer thicknesses ($d_{\text{pass, SiC}}$s) and b) conducting nc-SiC:H(n) layer thicknesses ($d_{\text{cond, SiC}}$s), with previously shown theoretical FF-V_{OC} dependencies for ideality factors of $n_{id}=1$ and $n_{id}=2/3$ with series resistances between $R_S = 0\,\Omega$ and $R_S = 1\,\Omega$. A clear trade-off between the *FF* and iV_{OC} is apparent with changing $d_{\text{pass, SiC}}$. The inset shows the sample structure with variations in both nc-SiC_X:H(n) layers. 87

4.13. Schematic cross-section of a) the electrical conductivity (σ) and b) the FTIR silicon-hydrogen bond peak intensity ($I_{\text{Si-H}}$) through the nc-SiC$_X$:H(n) double layer stack. The passivating nc-SiC$_X$:H(n) layer exhibits a high hydrogen concentration and low σ, in contrast to the conducting nc-SiC$_X$:H(n), which has a high σ and low $I_{\text{Si-H}}$. . . 88
4.14. The a) implied open-circuit voltage (iV_{OC}) and b) pseudo Fill Factor (p*FF*) and Fill Factor (*FF*) for different filament current ramps (R_{fil}s), determining the graded nc-SiC:H(n) layer thickness ($d_{\text{gradient, SiC}}$). Lower R_{fil} leads to a reduced iV_{OC} and *FF*, which both improve towards intermediate R_{fil}. Higher R_{fil} yields lower iV_{OC}s but improved *FF*s.The p*FF*s remains consistently high. The insets in a) show the layer structure with the highlighted $d_{\text{gradient, SiC}}$ variation, and in b) the T_f profile. Dashed lines are visual aids. . . 89
4.15. The a) implied open-circuit voltage (iV_{OC}) and b) Fill Factor (*FF*) and pseudo Fill Factor (p*FF*) for an extended range of filament current ramps (R_{fil}s), influencing the graded nc-SiC:H(n) layer thickness ($d_{\text{gradient, SiC}}$). The lowest R_{fil} in this figure equals the highest R_{fil} in figure 4.14. The iV_{OC} consistently declines with increasing R_{fil}, while the p*FF* is relatively constant. The *FF* initially converges towards p*FF* before following its fluctuation. The inset illustrates the sample setup with the varied layer thickness. 92
4.16. The a) implied open-circuit voltage (iV_{OC}) and b) pseudo Fill Factor (p*FF*) and Fill Factor (*FF*) for varying passivating seed nc-SiC:H(n) layer thicknesss ($d_{\text{seed, SiC}}$s). The filament current ramp (R_{fil}) of the seed layer is constant at 0.05 $\frac{A}{s}$. An increase in iV_{OC} with a growing pseudo Fill Factor (p*FF*)-*FF* gap is observed for increasing $d_{\text{seed, SiC}}$. 93

4.17. Heatmaps for varying filament current ramps (R_{fil}s) and passivating seed nc-SiC:H(n) layer thicknesss ($d_{seed, SiC}$s) for the a) implied open-circuit voltage (iV_{OC}) and b) Fill Factor (FF). c) shows the same heatmap for the product of iV_{OC} and FF to more easily identify optimal combinations. The iV_{OC} favors a thicker $d_{seed, SiC}$ and lower R_{fil}, while the opposite trend is visible for the FF. The highest combination can be achieved either for low $d_{seed, SiC}$ in combination with low R_{fil} or lower $d_{seed, SiC}$ with high R_{fil}. 95
4.18. Updated schematic cross-section of the a) electrical conductivity (σ) and b) FTIR silicon-hydrogen bond peak intensity (I_{Si-H}) from figure 4.13. The profiles of the approach with the seed and gradient layer are added. An early and strong increase in σ is visible, while the I_{Si-H} has an inverse profile. The inlet shows the nc-SiC$_X$:H(n) stack with the layer thickness d. The color gradient symbolizes the shift from passivating to conducting nc-SiC$_X$:H(n). 97
4.19. Secondary ion mass spectroscopy (SIMS) profiles for a) hydrogen and b) nitrogen of the passivating and conducting single layers, the double layer stack, the gradient layer, and the seed layer with the gradient layer on top. The seed and seed + gradient layer stacks are topped with a conductive nc-SiC$_X$:H(n) layer. In the passivating nc-SiC$_X$:H(n) parts of the samples, a high hydrogen concentration can be found, while a high nitrogen content is found for the conducting nc-SiC$_X$:H(n) parts. 98

5.1. Schematic representation of the sputtering chamber, highlighting various factors influencing the sample, including the sputter atmosphere, electromagnetic emissions from the plasma, and the impact of ions, neutrals, and compounds from the target and sputter or doping gases, as well as electrons from the plasma. Reprinted under CC BY 4.0 from Ref. [226]. 107

5.2. Measured lifetime curve for textured silicon wafers symmetrically passivated with the TPC structure. The initial effective minority carrier lifetime (τ_{eff}) (1) is strongly reduced after the sputter process (2), but recovers with an additional annealing (3) at 230 °C for 20 minutes in ambient atmosphere. After the indium tin oxide (ITO) is removed (4), the lifetime curves nearly overlap again. The corresponding implied open-circuit voltage (iV_{OC}) values are given in the figure. The dashed line marks the minority carrier density (n) of 10^{15} cm^{-3}, at which τ_{eff} is defined. Reprinted under CC BY 4.0 from Ref. [226]. 111
5.3. FTIR measurements of the a) silicon-carbon and b) silicon-hydrogen peak, c) Raman spectroscopy, and d) hydrogen effusion measurements with the inlet showing the electrical conductivity (σ) for the different processing steps. The FTIR, Raman spectroscopy, and σ samples have the ITO etched off, while the hydrogen effusion measurement sample is measured with the ITO still on the stack. For all different characterization methods, no deviation between the curves of different processing steps is found. The different peak positions [173, 174, 246] are marked by dashed lines. 112
5.4. The layer thickness (d)-dependent electrical conductivity (σ) of hydrogenated nanocrystalline silicon carbide (nc-SiC_X:H) layers before and after indium tin oxide (ITO) deposition. To evaluate the damage to the material, the ITO is etched away, either before or after annealing at 230 °C for 20 minutes on a hot plate in ambient atmosphere. No significant alterations in σ are observed regardless of the sample processing method. 113

5.5. Implied open-circuit voltage (iV_{OC}) measurements for the initial sample stack, after ITO deposition, and after annealing at 230 °C for 20 minutes. The standard reference process is compared with a process variant without plasma ignition but with the sample heater and process gases active, resulting in no deposition but the sample being exposed to the deposition atmosphere, and another variant where the plasma is ignited but the sample heater is off, leading to an ITO deposition at lower temperatures. The process without plasma ignition shows no damage, while deactivating the sample heater results in significantly increased passivation damage. 115

5.6. Quasy-Steady State Photoconductance (QSSPC)-corrected photoluminescent lifetime (PL) images of a symmetrical sample passivated with transparent passivating contact (TPC) a) before and b) after the ITO deposition process, with c) showing the transmission spectra of various filter glasses used during deposition, compared with plasma light emission data extracted from ref. [228]. Reprinted under CC BY 4.0 from Ref. [226]. 117

5.7. Simulated profiles of variations of a) crystalline volume fraction (X_C) of the nc-SiC$_X$:H(n), b) incident electron energy ($E_{electron}$) of the incident electron, and c) hydrogen content (c_H) of the nc-SiC$_X$:H(n) on maximum penetration depth (d_{max}), and x-ray generation profiles depending on d) X_C and e) $E_{electron}$. d_{max} increases for decreasing X_C and increasing $E_{electron}$. X-ray generation is superficial but increases for increasing $E_{electron}$. 119

5.8. Quasy-Steady State Photoconductance-corrected photoluminescent lifetime (PL) image of a sample part irradiated with an electron beam in a scanning electron microscope. The beam energy is set at 500 eV, with a beam current of 1.6 nA. No degradation in the irradiated area is observed. Figure b) is reprinted under CC BY 4.0 from Ref. [226]. 121

5.9. Simulated maximum penetration depth (d_{max}) for a) various ion types for different crystalline volume fractions (X_Cs), b) oxygen ions with varying incident ion energies (E_{ion}s) and c) oxygen ions for various c_Hs. Increasing d_{max} is observed with lower X_C and higher E_{ion}, with oxygen ions penetrating deeper than other ion species. . 122
5.10. Energy-dispersive x-ray diffraction line scans across the full transparent passivating contact (TPC) stack including the indium tin oxide (ITO) layer after the sputter deposition process. The penetration depths of indium, tin, argon, and oxygen ions are compared. Reprinted under CC BY 4.0 from Ref. [226]. 123
5.11. Simulated energy distribution for the primary incident ions and recoiling layer atoms, focusing on the lightest and heaviest ions, oxygen and tin, respectively, involved in the sputter process. The distribution highlights the relative contributions of phonons, ionization of lattice atoms, and vacancy generation. 125
5.12. Simulated combined energy loss (E_{loss}) of incident oxygen ions and recoiling layer atoms depending on a) crystalline volume fraction (X_C) and b) E_{ion}. The E_{loss} towards vacancy generation remains constant, while a shift is observed favoring phonon generation over ionization of lattice atoms for both lower X_C and E_{ion}. 126
5.13. Simulated generation profiles for a) and b) ionization (*Io*), c) and d) phonon (*P*), and e) vacancy (*Va*), distinguishing between primary ions (solid lines) and recoiling atoms (dashed lines). a) and c) show the respective profile for a variation of E_{ion}, while b) and d) show the profiles for different X_C. 127
5.14. To-scale overview of various effects occurring during the sputtering process and their simulated depth of impact. All effects are either superficially or experimentally demonstrated to be non-damaging to the passivation of the sample. 132

5.15. Schematic illustrations of a) mechanisms for the movement of carbon and silicon vacancies in the silicon carbide lattice, and b) phonon generation and propagation. Carbon vacancies move through direct hopping, while silicon vacancies can hop or create vacancy-antisite complexes. Phonons are quantized lattice vibrations. Reprinted under CC BY 4.0 from Ref. [226]. . . . 135
5.16. Schematic representation of hydrogen displacement at the silicon interface due to simultaneous multi-phonon dispersion. Subsequent low-temperature annealing can restore broken silicon-hydrogen bonds. Reprinted under CC BY 4.0 from Ref. [226]. . . . 136
5.17. The Intensity of elemental emission lines (I_{element}) for the elements carbon and silicon and the plasma intensity (I_{plasma}) for radiation from an oxygen and argon plasma. Data of the plasma radiation taken from ref. [228] and from ref. [273] for the possible carbon and silicon emission lines. 137
5.18. Comparison of implied open-circuit voltage ($\mathrm{i}V_{\mathrm{OC}}$) for symmetrically passivated wafers with the transparent passivating contact (TPC) and solar cell precursors with a TPC front side and silicon hetero-junction (SHJ) rear side at different stages of the process. Although symmetrically passivated samples fully recover after annealing, the solar cell precursors do not, indicating limitations originating from the SHJ side. 140
5.19. Analysis of a) open-circuit voltage loss (ΔV_{OC}) for a silicon hetero-junction (SHJ) solar cell and b) implied open-circuit voltage loss ($\Delta \mathrm{i}V_{\mathrm{OC}}$) a symmetrically passivated wafer with the transparent passivating contact (TPC) structure for varying annealing temperature (T_{anneal}). The constant annealing time (t_{anneal}) is 20 minutes for both cases. While the SHJ solar cell exhibits degradation at temperatures above 190 ℃, or 210 ℃ with light soaking, the symmetric TPC structure recovers at T_{anneal} of 220 ℃ or higher. Insets depict the sample structures of a SHJ solar cell and a symmetric TPC sample. 140

5.20. Evolution of open-circuit voltage loss (ΔV_{OC}) in symmetrically transparent passivating contact (TPC)-passivated samples over extended accumulated annealing times (t_{acc}s) for various annealing temperatures (T_{anneal}s). The increased annealing time further reduces ΔV_{OC} at lower T_{anneal}, but does not completely restore damaged passivation quality. 143
5.21. Implied open-circuit voltages (iV_{OC}s) of symmetrically transparent passivating contact (TPC)-passivated samples at different process stages and accumulated annealing times (t_{acc}s). Samples have varying pre-annealing time (t_{pre}) before the sputter deposition. The pre-annealing temperature (T_{pre}) is 230 ℃, and the post-annealing temperature (T_{post}) is 210 ℃. The inlet depicts the sample structure. 144
5.22. Implied open-circuit voltage (iV_{OC}) and open-circuit voltage (V_{OC}) of a transparent passivating contact (TPC) solar cell during various fabrication steps and with different pre-annealing time (t_{pre}). Pre-annealing, combined with a light soaking step, enhances the final V_{OC} compared to reference devices. The inlet depicts the sample structure. 145

A.1. Chronological representation of the estimated total layer thickness deposited per filament. A noticeable scattering with a general downward trend is evident. 162

B.1. Comparative energy distributions across the *Kinchi-Pease*, *Full Cascade*, and *Monolayer* models within the Stopping and Range of Ions in Matter (SRIM) framework. Although primary ion energy transfer remains consistent across models, the *Kinchi-Pease* model exhibits a higher fraction of energy from recoiling atoms to phonons. Discrepancies between the *Full Cascade* and *Monolayer* models are minimal. 164

B.2. Depictions of a) ion implantation and recoil atom profiles, b) vacancy generation profiles, c) phonon generation profiles, and d) electron interaction profiles for *Full Cascade*, *Monolayer*, and *Kinchi-Pease* models. The models demonstrate a commendable coherence in the various calculated profiles. 165

C.1. The resulting absorption coefficient (α) from the different discussed equation equation (C.1) to equation (C.4). A trend with a decreasing α with more reflections is observable and can lead to completely negative αs due to measurement uncertainties. 171

C.2. Determination of the optical band gap, together with the values of the fit, given by the red dashed line, for the a) transmission and b) derivative of the transmission method. The shaded area visualizes the linear part of the data used for fitting. 172

C.3. Determination of the optical band gap, together with the values of the fit, given by the red dashed line, for the a) straight, b) indirect and c) direct method. The shaded area visualizes the linear part of the data used for fitting. The horizontal lines mark the absorption coefficient values at which the energies are evaluated for the fixed absorption coefficient approaches. 172

C.4. Determination of the optical band gap, together with the values of the fit, given by the red dashed line, for the a) Cody, b) Tauc and c) Tauc 2 method. The shaded area visualizes the linear part of the data used for fitting. 172

C.5. The resulting optical band gaps for the various discussed methods. The transmission method gives the largest optical band gap, while the transmission derivative gives the smallest. The straight, direct, Tauc 2 and $E(\alpha = 10^5)$ give similar optical band gaps around 3.8 eV, while the indirect, Cody, Tauc, $E(\alpha = 10^3)$ and $E(\alpha = 10^4)$ give similar results around 3.2 eV. 173

List of Tables

2.1. Key solar cell parameters for each technology type as of December 2024. Data taken from ref. [52]. 30

3.1. Overview of the deposition parameter series presented in section 4.1.1. The variation of each series was marked in bold letters. 45

4.1. Comparison of the *IV*-parameters of a silicon heterojunction reference solar cell, the previous TPC double layer stack design, and the new TPC seed + gradient layer design. The new TPC design improves both the V_{OC} and *FF*, making them more comparable with the SHJ reference. 96

C.1. Different approaches for determining the optical band gap and the values for the optical band gap. Additionally, the energy range for the linear fit and the accuracy of the fit, as given by R^2, is presented.169

List of Publications

Publications related to this work

1. **A. Eberst**, B. Xu, K. Bittkau, A. Lambertz, U. Rau and K. Ding, *Performance improvements through gradient layers in transparent passivating contact solar cells*, Cell Reports Physical Science, **6 (7)**, 102658 (2025)
2. B. Xu and **A. Eberst**, P. Fall, M. A. Yaqin, V. Lauterbach, K. Bittkau, A. Lambertz, U. Rau and K. Ding, *Restoring sputter damage by light soaking in silicon carbide-based transparent passivating contact solar cells*, Cell Reports Physical Science, **6 (5)**, 102552 (2025)
3. **A. Eberst**, B. Xu, K. Bittkau, W. Duan, A. Lambertz, A. Meise, M. Heggen, R. E. Dunin-Borkowski, U. Rau and K. Ding, *Deeper Insight into the Mechanisms Behind Sputter Damage in Silicon Solar Cells Based on the Example of Nanocrystalline Silicon Carbide*, Adv. Phys. Res., **3 (9)**, 2400036 (2024)
4. **A. Eberst**, B. Xu, W. Duan, A. Lambertz, U. Rau and K. Ding, *Development of Gradient Layers to Improve the Efficiency of Transparent Passivating Contact Solar Cells*, 2023 IEEE 50th Photovoltaic Specialists Conference (PVSC), San Juan, PR, USA, **1 (1)**, (2023)
5. **A. Eberst**, A. Lambertz, W. Duan, V. Smirnov, U. Rau and K. Ding, *Material Properties of Nanocrystalline Silicon Carbide for Transparent Passivating Contact Solar Cells*, Sol. RRL, **7 (7)**, 2300013 (2023)

Other publications

1. S. Alkhereibi, M.A. Yaqin, **A. Eberst**, B. Xu, J. Jo, H. Alsamamra, A.

Lambertz, U. Rau, K. Ding and J. Mayer, *Resolving the microstructure of aluminum-doped zinc oxide thin films grown on different silicon heterojunction solar cell structures by advanced transmission electron microscopy*, Thin Solid Films, 140744 (2025)

2. B. Xu, K. Bittkau, **A. Eberst**, K. Zhang, Y. Liu, J. Yang, W. Duan, M. A. Yaqin, V. Smirnov, C. Zhou, W. Wang, X. Xu, A. Lambertz, U. Rau and K. Ding, *Downshifting Encapsulant: Optical Simulation Evaluation of the Solution to Ultraviolet-Induced Degradation in Silicon Heterojunction Solar Cells*, Advanced Energy and Sustainability Research, **6 (1)**, 2400227 (2024)
3. Q. Yang, K. Bittkau, **A. Eberst**, U. Rau and K. Ding, *The impact of interface recombination on the external quantum efficiency of silicon solar cells*, Solar Energy Materials and Solar Cells **273**, 112953 (2024)
4. Q. Yang, W. Duan, **A. Eberst**, B. Klingebiel, Y. Wang, A. Kulkarni, A. Lambertz, K. Bittkau, Y. Zhang, S. Vitusevich, U. Rau, T. Kirchartz and K. Ding, *Origin of sputter damage during transparent conductive oxide deposition for semitransparent perovskite solar cells*, Journal of Materials Chemistry A, **12**, 14816 (2024)
5. W. Duan, G. Mains, H. T. Gebrewold, K. Bittkau, A. Lambertz, B. Xu, V. Lauterbach, **A. Eberst**, N. Nicholson, L. Korte, M. A. Yaqin, K. Zhang, Q. Yang, U. Rau and K. Ding, *Enhancing the Selectivity and Transparency of the Electron Contact in Silicon Heterojunction Solar Cells by Phosphorus Catalytic Doping*, Adv. Funct. Mater. **34**, 2310552 (2024)
6. D. Qiu, W. Duan, A. Lambertz, **A. Eberst**, K. Bittkau, U. Rau and K. Ding, *Transparent Conductive Oxide Sputtering Damage on Contact Passivation in Silicon Heterojunction Solar Cells with Hydrogenated Nanocrystalline Silicon*, Sol. RRL **6**, 2200651 (2022)
7. **A. Eberst**, A. Zamchiy, K. Qiu, P. Winkel, H.T. Gebrewold, A. Lambertz, W. Duan, S. Li, K. Bittkau, T. Kirchartz, U. Rau and K. Ding, *Optical Optimization Potential of Transparent-Passivated Contacts in Silicon Solar Cells*, Sol. RRL **6**, 2101050 (2022)
8. **A. Eberst**, A. Zamchiy, K. Qiu, A. Lambertz, W. Duan, S. Li, K. Bittkau, S.

Haas, F. Finger, T. Kirchartz, U. Rau, K. Ding, *Achieving a high Short Circuit Current Density of 40.9 mA/cm² for Two-Side Contacted Silicon Heterojunction Solar Cells by using SiC-based Transparent Passivating Contacts*, 2021 IEEE 48th Photovoltaic Specialists Conference (PVSC), Fort Lauderdale, FL, USA, 0300 – 0302 (2021)

9. M. Köhler, M. Pomaska, P. Procel, R. Santbergen, A. Zamchiy, B. Macco, A. Lambertz, W. Duan, P. Cao, B. Klingebiel, S. Li, **A. Eberst**, M. Luysberg, K. Qiu, O. Isabella, F. Finger, T. Kirchartz, U. Rau, K. Ding, *A silicon carbide-based highly transparent passivating contact for crystalline silicon solar cells approaching efficiencies of 24%*, Nat. Energy **6**, 529 – 537 (2021)

10. M. Pomaska, M. Köhler, P. Procel, A. Zamchiy, A. Singh, D.Y. Kim, O. Isabella, M. Zeman, S. Li, K. Qiu, **A. Eberst**, V. Smirnov, F. Finger, U. Rau, K. Ding, *Transparent silicon carbide/tunnel SiO^2 passivation for c-Si solar cell front side: Enabling J_{sc} > 42 mA/cm^2 and iVoc of 742 mV*, Prog Photovolt Res Appl. **28**, 321 – 327 (2020)

Curriculum Vitae

Personal information	
Name	Alexander Eberst
Date of Birth	11.01.1995
Place of Birth	Hannover
Citizenship	German
Education	
2020 – 2025	PhD candidate at the Forschungszentrum Jülich GmbH Institute for Energy Materials and Devices - Photovoltaics (IMD-3)
2018 – 2020	Master of Science in Materials Science at the RWTH Aachen University Main Subjects: Electronic Materials & Nanoelectronics Master Thesis at the IEK-5 Photovoltaics, Forschungszentrum Jülich
2014 – 2018	Bachelor of Science in Materials Science at the RWTH Aachen University Bachelor Thesis at GaN Device Technology, RWTH Aachen University
2005 – 2013	Marion-Dönhoff-Gymnasium, Nienburg (Weser)
2001 – 2005	Grundschule Schünebusch, Estorf (Weser)

References

[1] H. Bauer, F. Liebach, L. Gigliotti, T. Gruenewald, B. Smeets, C. Tryggestad, R. Winter, Unlocking opportunities from industrial electrification, tech. rep., **2022**.

[2] IEA, World energy outlook 2023, tech. rep., IEA Paris, **2023**.

[3] IEA, Global EV outlook 2023, tech. rep., IEA Paris, **2023**.

[4] IEA, The future of heat pumps, IEA Paris, **2022**.

[5] IRENA, World Energy Transitions Outlook 2023: 1.5 °C Pathway, tech. rep., International Renewable Energy Agency, **2023**.

[6] M. Wei, C. A. McMillan, S. de la Rue du Can, *Current Sustainable/Renewable Energy Reports* **2019**, *6*, 140–148.

[7] J. L. Barton, *Science* **2020**, *368*, 1181–1182.

[8] U. Nations, United Nations: Paris Agreement, United Nations, New York, **2016**.

[9] C. Analytics, N. Institute, Warming Projections Global Update - November 2022, tech. rep., Climate Action Tracker, **2022**.

[10] C. Analytics, N. Institute, Paris Agreement turning point, tech. rep., Climate Action Tracker, **2020**.

[11] H. Lund, *Renewable energy systems*, Elsevier, **2010**.

[12] B. Ćosić, G. Krajačić, N. Duić, *Energy* **2012**, *48*, 80–87.

[13] M. Ram, D. Bogdanoc, A. Aghahosseini, O. A. Solomon, A. Gulagi, M. Child, Fell-Hans-Josef, C. Breyer, Global energy system based on 100% renewable energy-power sector, tech. rep., Global Renewable Energy Solutions Showcase, **2017**.

[14] M. Fischer, J. Zhang, P. Ni, A. Metz, G. Erfurt, C.-C. Li, W. Jooss, M. Woodhouse, F. Jiang, I. Saha, International Technology Roadmap for Photovoltaic (ITRPV), tech. rep., vdma, **2023**.

[15] S. Phillips, W. Warmuth, Photovoltaic Report, tech. rep., Fraunhofer Institute for Solar Energy Systems, PSE Projekt GmbH, **2023**.

[16] C. Kost, S. Shammugam, V. Fluri, D. Peper, A. D. Memar, T. Schlegl, Stromgestehungskosten Erneuerbare Energien, tech. rep., Fraunhofer Institute for Solar Energy Systems, **2021**.

[17] W. Shockley, H. J. Queisser, *Journal of applied physics* **1961**, *32*, 510–519.

[18] L. C. Hirst, N. J. Ekins-Daukes, *Progress in Photovoltaics: Research and Applications* **2011**, *19*, 286–293.

[19] A. Richter, M. Hermle, S. W. Glunz, *IEEE journal of photovoltaics* **2013**, *3*, 1184–1191.

[20] E. Comission, Critical Raw Materials Resilience: Charting a Path towards greater Security and Sustainability, tech. rep., European Comssion, **2020**.

[21] D. M. Chapin, C. S. Fuller, G. L. Pearson, Solar Energy Converting Apparatus, Patent, Patent No. 2,780,765, **1954**.

[22] T. G. Allen, J. Bullock, X. Yang, A. Javey, S. De Wolf, *Nature Energy* **2019**, *4*, 914–928.

[23] M. A. Green, *Solar Energy Materials and Solar Cells* **2015**, *143*, 190–197.

[24] M. Fischer, Z. Ouyang, A. Metz, G. Erfurt, C.-C. Li, W. Jooss, M. Woodhouse, F. Jiang, Y. Chen, I. Saha, P. Ni, International Technology Roadmap for Photovoltaic (ITRPV), tech. rep., vdma, **2024**.

[25] H. Lin, M. Yang, X. Ru, G. Wang, S. Yin, F. Peng, C. Hong, M. Qu, J. Lu, L. Fang, et al., *Nature Energy* **2023**, 1–11.

[26] M. Green, Fundamental Advantages of Silicon Heterojunction Cells and The Path to 28% Efficiency, 6th Silicon Heterojunction Workshop, **2023**.

[27] G. Nogay, J. P. Seif, Y. Riesen, A. Tomasi, Q. Jeangros, N. Wyrsch, F.-J. Haug, S. De Wolf, C. Ballif, *IEEE Journal of Photovoltaics* **2016**, *6*, 1654–1662.

[28] D. Qiu, A. Lambertz, W. Duan, L. Mazzarella, P. Wagner, A. B. Morales-Vilches, G. Yang, P. Procel, O. Isabella, B. Stannowski, et al., *Advanced Science* **2024**, *11*, 2403728.

[29] M. Köhler, M. Pomaska, P. Procel, R. Santbergen, A. Zamchiy, B. Macco, A. Lambertz, W. Duan, P. Cao, B. Klingebiel, et al., *Nature Energy* **2021**, *6*, 529–537.

[30] A. Einstein, *Annalen der Physik* **1905**, *4*, 17.

[31] P. Würfel, U. Würfel, *Physics of solar cells: from basic principles to advanced concepts*, John Wiley & Sons, **2016**.

[32] S. H. Simon, *The Oxford solid state basics*, OUP Oxford, **2013**.

[33] R. Gross, A. Marx, *Festkörperphysik*, De Gruyter, **2018**.

[34] M. A. Green et al., *Third generation photovoltaics*, Springer, **2006**.

[35] J. A. Nelson, *The physics of solar cells*, World Scientific Publishing Company, **2003**.

[36] R. A. Sinton, A. Cuevas, *Applied Physics Letters* **1996**, *69*, 2510–2512.

[37] M. A. Green, *Silicon solar cells: advanced principles & practice*, Centre for Photovoltaic Devices and Systems, **1995**.

[38] A. Razzaq, T. G. Allen, S. De Wolf, *ACS Energy Letters* **2023**, *8*, 4438–4440.

[39] A. Richter, S. W. Glunz, F. Werner, J. Schmidt, A. Cuevas, *Physical review B* **2012**, *86*, 165202.

[40] T. Ahmad, S. Sobhan, M. F. Nayan, *Journal of power and Energy Engineering* **2016**, *4*, 31–46.

[41] S. B. Prakash, G. Singh, S. Singh, *Frontiers in Physics* **2021**, *9*, 690588.

[42] X. Ma, S. Bader, B. Oelmann, *IEEE Access* **2020**, *9*, 1350–1361.

[43] C. Kittel, *Einführung in die Festkörperphysik*, Oldenbourg Wissenschaftsverlag, **2013**.

[44] R. Brendel, R. Peibst, *IEEE Journal of photovoltaics* **2016**, *6*, 1413–1420.

[45] W. Li, Z. Xu, Y. Yan, J. Zhou, Q. Huang, S. Xu, X. Zhang, Y. Zhao, G. Hou, *Advanced Energy Materials* **2024**, 2304338.

[46] D. Macdonald, L. Geerligs, *Applied Physics Letters* **2004**, *85*, 4061–4063.

[47] S. W. Glunz, B. Steinhauser, J.-I. Polzin, C. Luderer, B. Grübel, T. Niewelt, A. M. Okasha, M. Bories, H. Nagel, K. Krieg, et al., *Progress in Photovoltaics: Research and Applications* **2023**, *31*, 341–359.

[48] M. A. Leilaeioun, A. Onno, S. Manzoor, J. Shi, K. C. Fisher, J. Y. Zhengshan, Z. C. Holman, *IEEE Journal of Photovoltaics* **2019**, *10*, 326–334.

[49] J. Yu, J. Li, Y. Zhao, A. Lambertz, T. Chen, W. Duan, W. Liu, X. Yang, Y. Huang, K. Ding, *Solar Energy Materials and Solar Cells* **2021**, *224*, 110993.

[50] Q. Tang, W. Duan, A. Lambertz, K. Bittkau, M. A. Yaqin, Y. Zhao, K. Zhang, Q. Yang, D. Qiu, F. Gunkel, et al., *Solar Energy Materials and Solar Cells* **2023**, *251*, 112120.

[51] N. Aqab, H. Riaz, A. Nayfeh, *IEEE 43rd Photovoltaic Specialists Conference (PVSC)* **2016**, 0598–0601.

[52] M. A. Green, E. D. Dunlop, M. Yoshita, N. Kopidakis, K. Bothe, G. Siefer, X. Hao, *Progress in Photovoltaics: Research and Applications* **2024**, *32*, 3–13.

[53] K. Gao, Q. Bi, X. Wang, W. Liu, C. Xing, K. Li, D. Xu, Z. Su, C. Zhang, J. Yu, et al., *Advanced Materials* **2022**, *34*, 2200344.

[54] D. K. Ghosh, S. Bose, G. Das, S. Acharyya, A. Nandi, S. Mukhopadhyay, A. Sengupta, *Surfaces and Interfaces* **2022**, *30*, 101917.

[55] H. Ullah, S. Czapp, S. Szultka, H. Tariq, U. B. Qasim, H. Imran, *Energies* **2023**, *16*, 715.

[56] M. Q. Khokhar, S. Q. Hussain, S. Kim, S. Lee, D. P. Pham, Y. Kim, E.-C. Cho, J. Yi, *Transactions on Electrical and Electronic Materials* **2020**, *21*, 138–143.

[57] M. Sharma, J. Panigrahi, V. K. Komarala, *Nanoscale Advances* **2021**, *3*, 3373–3383.

[58] Y. Jiao, J. Q. Zhang, P. Liu, *19th China International Forum on Solid State Lighting & 2022 8th International Forum on Wide Bandgap Semiconductors* **2023**, 8–12.

[59] C. Langpoklakpam, A.-C. Liu, K.-H. Chu, L.-H. Hsu, W.-C. Lee, S.-C. Chen, C.-W. Sun, M.-H. Shih, K.-Y. Lee, H.-C. Kuo, *Crystals* **2022**, *12*, 245.

[60] S. Zhao, X. Zhao, Y. Wei, Y. Zhao, H. A. Mantooth, *IEEE Journal of Emerging and Selected Topics in Power Electronics* **2021**, *9*, 4096–4114.

[61] M. Ostling, H.-S. Lee, M. Domeij, C.-M. Zetterling, *Proceedings of the International Conference Mixed Design of Integrated Circuits and System 2006. MIXDES 2006.* **2006**, 34–42.

[62] D. P. Urciuoli, V. Veliadis, H. C. Ha, V. Lubomirsky, *2011 Twenty-Sixth Annual IEEE Applied Power Electronics Conference and Exposition (APEC)* **2011**, 354–358.

[63] L. A. G. Rodriguez, L. Gill, J. A. Mueller, J. Neely, G. Baker, J. D. Flicker, E. Schrock, G. Pickrell, R. J. Kaplar, *IEEE Transactions on Industry Applications* **2023**, *59*, 2326–2339.

[64] R. Ghosh, S. Mondal, S. K. Ghorui, *2017 International Conference on Computer Electrical & Communication Engineering (ICCECE)* **2017**, 1–5.

[65] K. Jacobs, S. Heinig, D. Johannesson, S. Norrga, H.-P. Nee, *IEEE Transactions on Power Electronics* **2021**, *36*, 8887–8906.

[66] V. Vervisch, F. Issa, S. Biondo, L. Ottaviani, W. Vervisch, D. Szalkai, L. Vermeeren, A. Klix, A. Hallen, A. Kuznetsov, et al., *MRS Online Proceedings Library (OPL)* **2014**, *1693*, mrss14–1693–dd03–09.

[67] M. Andersson, B. Hammarlund, A. L. Spetz, D. Puglisi, *Fourth Scientific Meeting EuNetAir* **2015**, 32–35.

[68] I. A. Sassi, M. B. E. H. Rhouma, M. G. Daher, *Optical and Quantum Electronics* **2023**, *55*, 1–17.

[69] Y. Tawada, H. Okamoto, Y. Hamakawa, *Applied Physics Letters* **1981**, *39*, 237–239.

[70] I. A. Yunaz, K.-i. Hashizume, S. Miyajima, A. Yamada, M. Konagai, *Solar Energy Materials and Solar Cells* **2009**, *93*, 1056–1061.

[71] S. Sreejith, J. Ajayan, S. Kollem, B. Sivasankari, *Silicon* **2022**, *14*, 8277–8293.

[72] E. T. Efaz, M. M. Rhaman, S. Al Imam, K. L. Bashar, F. Kabir, M. E. Mourtaza, S. N. Sakib, Mozahid, FA, *Engineering Research Express* **2021**, *3*, 032001.

[73] A. Tabata, M. Mori, *Thin Solid Films* **2008**, *516*, 626–629.

[74] A. Pawbake, A. Mayabadi, R. Waykar, R. Kulkarni, A. Jadhavar, V. Waman, J. Parmar, S. Bhattacharyya, Y.-R. Ma, R. Devan, et al., *Materials Research Bulletin* **2016**, *76*, 205–215.

[75] T. Chen, F. Köhler, A. Heidt, Y. Huang, F. Finger, R. Carius, *Thin Solid Films* **2011**, *519*, 4511–4515.

[76] K. Chokawa, Y. Daigo, I. Mizushima, T. Yoda, K. Shiraishi, *Japanese Journal of Applied Physics* **2021**, *60*, 085503.

[77] Y. Onuma, K. Kamimura, Y. Nagura, K. Koike, S. Yonekubo, *Materials Science Engineering Physics* **1992**.

[78] T. Kaneko, N. Miyakawa, H. Sone, H. Yamazaki, *Thin Solid Films* **2002**, *409*, 74–77.

[79] M. G. Park, W. S. Choi, J.-H. Boo, Y.-J. Kim, D. H. Yoon, B. Hong, *Journal De Physique Iv* **2002**, *12*, 155–160.

[80] C. S. Roper, V. Radmilovic, R. T. Howe, R. Maboudian, *Journal of the Electrochemical Society* **2006**, *153*, C562.

[81] I. Ferreira, M. E. V. Costa, L. Pereira, E. Fortunato, R. Martins, A. R. Ramos, M. F. da Silva, *Applied Surface Science* **2001**, *184*, 8–19.

[82] K. K. Nussupov, N. B. Beisenkhanov, S. Keiinbay, A. T. Sultanov, *Optical Materials* **2022**, *128*, 112370.

[83] P. Kaminski, A. Abbas, K. Bass, G. Claudio, *Energy Procedia* **2011**, *10*, 71–75.

[84] Y.-H. Joung, F.-S. Kang, H. I. Kang, W. S. Choi, J. Yoo, *Thin Solid Films* **2015**, *587*, 160–162.

[85] M. Oujja, K. Tabakkouht, M. Sanz, E. Rebollar, M. Sánchez-Arenillas, J. F. Marco, M. Castillejo, R. de Nalda, *Applied Physics A* **2022**, *128*, 375.

[86] M. A. Ahmed, M. F. M. Sabri, W. R. Abed, *ARO-The Scientific Journal of Koya University* **2021**, *9*, 46–50.

[87] E. Paneerselvam, V. K. L. Narayanan, N. J. Vasa, M. Higashihata, D. Nakamura, H. Ikenoue, M. S. R. Rao, *Journal of Electronic Materials* **2019**, *48*, 3468–3478.

[88] J. Steffens, S. Weit, J. Rinder, R. Glatthaar, S. Möller, G. Hahn, B. Terheiden, *IEEE Journal of Photovoltaics* **2020**, *10*, 1624–1631.

[89] Y. Lin, Z. Yang, Z. Liu, J. Zheng, M. Feng, Y. Zhi, L. Lu, M. Liao, W. Liu, D. Ma, et al., *Energy & Environmental Science* **2021**, *14*, 6406–6418.

[90] S. Janz, S. Reber, S. Glunz, *Proceedings of the 21st EUPVSEC* **2006**, 660.

[91] R. Ferre, A. Orpella, D. Munoz, I. Martin, F. Recart, C. Voz, J. Puigdollers, P. Roca i Cabarrocas, R. Alcubilla, *Progress in Photovoltaics* **2008**, *16*, 123–127.

[92] T. Rajagopalan, X. Wang, B. Lahlouh, C. Ramkumar, P. S. Dutta, S. Gangopadhyay, *Journal of Applied Physics* **2003**, *94*, 5252–5260.

[93] W. Beyer, *Journal of Non-Crystalline Solids* **1987**, *97*, 1027–1034.

[94] K. J. Kim, S. Lee, J. H. Lee, M.-H. Roh, K.-y. Lim, Y.-W. Kim, *Journal of the American Ceramic Society* **2009**, *92*, 424–428.

[95] M. B. Pomaska, PhD thesis, Forschungszentrum Jülich, **2017**.

[96] J. Y. Seto, *Journal of Applied Physics* **1975**, *46*, 5247–5254.

[97] F. Demichelis, C. Pirri, E. Tresso, *Journal of Applied Physics* **1992**, *72*, 1327–1333.

[98] T. Chen, A. Schmalen, J. Wolff, D. Yang, R. Carius, F. Finger, *physica status solidi c* **2010**, *7*, 754–757.

[99] M. Vetter, I. Martín, A. Orpella, C. Voz, J. Puigdollers, R. Alcubilla, *MRS Online Proceedings Library (OPL)* **2002**, *715*.

[100] S. Miyajima, A. Yamada, M. Konagai, *Japanese journal of applied physics* **2007**, *46*, 1415.

[101] S. Kerdiles, A. Berthelot, F. Gourbilleau, R. Rizk, *Applied physics letters* **2000**, *76*, 2373–2375.

[102] G. Chen, S. Chen, Z. Lin, R. Huang, Y. Guo, *Micromachines* **2022**, *13*, 2043.

[103] M. Mirzaei, M. Mirzaei, *Journal of Molecular Modeling* **2011**, *17*, 527–531.

[104] C. G. Rodrigues, *Semiconductors* **2021**, *55*, 625–632.

[105] W. Thurber, R. Mattis, Y. Liu, J. Filliben, *Journal of the Electrochemical Society* **1980**, *127*, 1807.

[106] R. Ferre, I. Martin, M. Vetter, M. Garin, R. Alcubilla, *Applied Physics Letters* **2005**, *87*, 202109.

[107] R. Sharma, A. Alleva, A. Hajjiah, H. Sivaramakrishnan Radhakrishnan, J. Poortmans, *ACS Applied Energy Materials* **2022**, *5*, 9994–10001.

[108] I. Martín, M. Vetter, M. Garín, A. Orpella, C. Voz, J. Puigdollers, R. Alcubilla, *Journal of Applied Physics* **2005**, *98*, 10.

[109] A. Gaufrès, F. Husser, E. Fourmond, R. Monna, M. Lemiti, *28th European Photovoltaic Solar Energy Conference* **2013**, hal–0189056.

[110] A. Gaufrès, F. Husser, E. Fourmond, M. Lemiti, *Energy Procedia* **2013**, *38*, 823–832.

[111] M. Köhler, PhD thesis, Forschungszentrum Jülich, **2020**.

[112] H. Matsumura, H. Umemoto, K. K. Gleason, R. E. Schropp, *Catalytic chemical vapor deposition: technology and applications of Cat-CVD*, John Wiley & Sons, **2019**.

[113] A. Eberst, A. Lambertz, W. Duan, V. Smirnov, U. Rau, K. Ding, *Solar RRL* **2023**, *7*, 2300013.

[114] J. Irikawa, S. Miyajima, T. Watahiki, M. Konagai, *Applied Physics Express* **2011**, *4*, 3.

[115] W. Yu, W. Lu, X. Teng, W.-g. Ding, L. Han, G.-s. Fu, *Journal of Vacuum Science and Technology* **2010**, *28*, 1234–1239.

[116] D. Hamashita, S. Miyajima, M. Konagai, *Solar energy materials and solar cells* **2012**, *107*, 46–50.

[117] C. Ehling, D. Treptow, G. Bilger, F. Einsele, M. B. Schubert, *35th IEEE Photovoltaic Specialists Conference* **2010**, 001368–001373.

[118] M. Boccard, Z. C. Holman, *Journal of Applied Physics* **2015**, *118*, 065704.

[119] H. Du, Y. Lin, Z. Wang, M. Liao, Z. Liu, X. Luo, Y. Cao, L. Fu, W. Liu, B. Yan, et al., *Materials Science in Semiconductor Processing* **2024**, *170*, 107969.

[120] J. Zheng, Z. Yang, L. Lu, M. Feng, Y. Zhi, Y. Lin, M. Liao, Y. Zeng, B. Yan, J. Ye, *Solar Energy Materials and Solar Cells* **2022**, *238*, 111586.

[121] D. Suwito, PhD thesis, Universität Konstanz, **2011**.

[122] A. Ingenito, G. Nogay, Q. Jeangros, E. Rucavado, C. Allebé, S. Eswara, N. Valle, T. Wirtz, J. Horzel, T. Koida, et al., *Nature Energy* **2018**, *3*, 800–808.

[123] A. Ingenito, G. Nogay, J. Stuckelberger, P. Wyss, L. Gnocchi, C. Allebe, J. Horzel, M. Despeisse, F.-J. Haug, P. Löper, et al., *IEEE Journal of Photovoltaics* **2018**, *9*, 346–354.

[124] M. Singh, R. Santbergen, L. Mazzarella, A. Madrampazakis, G. Yang, R. Vismara, Z. Remes, A. Weeber, M. Zeman, O. Isabella, *Solar Energy Materials and Solar Cells* **2020**, *210*, 110507.

[125] Z. Xu, K. Tao, S. Jiang, R. Jia, W. Li, Y. Zhou, Z. Jin, X. Liu, *Solar Energy Materials and Solar Cells* **2020**, *206*, 110329.

[126] L. Xiao, O. Astakhov, T. Chen, M. Stutzmann, F. Finger, *Thin solid films* **2011**, *519*, 4519–4522.

[127] D. Zhang, D. Deligiannis, G. Papakonstantinou, R. A. van Swaaij, M. Zeman, *IEEE Journal of Photovoltaics* **2014**, *4*, 1326–1330.

[128] S. Miyajima, K. Haga, A. Yamada, M. Konagai, *Japanese Journal of Applied Physics Part 2-Letters & Express Letters* **2006**, *45*, L432–L434.

[129] K. Ding, M. Pomaska, A. Singh, F. Lentz, F. Finger, U. Rau, *physica status solidi (RRL)–Rapid Research Letters* **2016**, *10*, 233–236.

[130] D. Pysch, J. Ziegler, J.-P. Becker, D. Suwito, S. Janz, S. Glunz, M. Hermle, *34th IEEE Photovoltaic Specialists Conference (PVSC)* **2009**, 000794–000799.

[131] R. Sharma, H. S. Radhakrishnan, L. Tous, J. Poortmans, *Solar Energy Materials and Solar Cells* **2022**, *238*, 111637.

[132] M. Köhler, M. Pomaska, A. Zamchiy, A. Lambertz, W. Duan, F. Lentz, S. Li, V. Smirnov, T. Kirchartz, F. Finger, *IEEE journal of photovoltaics* **2019**, *10*, 46–53.

[133] R. Petres, J. Libal, T. Buck, R. Kopecek, M. Vetter, R. Ferre, I. Martín, D. Borchert, P. Fath, *2006 IEEE 4th World Conference on Photovoltaic Energy Conference*, *1*, 1012–1015.

[134] G. Nogay, J. Stuckelberger, P. Wyss, E. Rucavado, C. Allebé, T. Koida, M. Morales-Masis, M. Despeisse, F.-J. Haug, P. Löper, et al., *Solar Energy Materials and Solar Cells* **2017**, *173*, 18–24.

[135] M. Van Cleef, F. Rubinelli, R. Schropp, *MRS Online Proceedings Library* **1998**, *507*, 125–130.

[136] C. Banerjee, K. L. Narayanan, K. Haga, J. Sritharathikhun, S. Miyajima, A. Yamada, M. Konagai, *Japanese Journal of Applied Physics* **2007**, *46*, 1–6.

[137] G. Nogay, A. Ingenito, E. Rucavado, Q. Jeangros, J. Stuckelberger, P. Wyss, M. Morales-Masis, F.-J. Haug, P. Löper, C. Ballif, *IEEE Journal of Photovoltaics* **2018**, *8*, 1478–1485.

[138] M. Van Cleef, R. Schropp, F. Rubinelli, *Applied physics letters* **1998**, *73*, 2609–2611.

[139] V. Šály, M. Perný, J. Packa, F. Janíček, M. Váry, M. Mikolášek, J. Huran, *18th International Scientific Conference on Electric Power Engineering (EPE)* **2017**, 1–4.

[140] M. Perný, V. Šály, F. Janíček, M. Mikolášek, M. Váry, J. Huran, *Journal of Electrical Engineering* **2018**, *69*, 52–57.

[141] T.-H. Chang, Y.-H. Chu, C.-C. Lee, J.-Y. Chang, *Applied Physics Letters* **2012**, *101*, 241601.

[142] M. Pomaska, M. Köhler, P. Procel Moya, A. Zamchiy, A. Singh, D. Y. Kim, O. Isabella, M. Zeman, S. Li, K. Qiu, et al., *Progress in Photovoltaics: research and applications* **2020**, *28*, 321–327.

[143] S. Glunz, A. Grohe, M. Hermle, M. Hofmann, S. Janz, T. Roth, O. Schultz, M. Vetter, I. Martin, R. Ferré, *20th European Photovoltaic Solar Energy Conference and Exhibition* **2005**, *6*, 10.

[144] R. Ferre, I. Martin, P. Ortega, M. Vetter, M. Garin, R. Alcubilla, *Spanish Conference on Electron Devices* **2007**, 238–241.

[145] R. Ferre, I. Martín, P. Ortega, M. Vetter, I. Torres, R. Alcubilla, *Journal of applied physics* **2006**, *100*, 073703.

[146] M. Vetter, I. Martin, R. Ferre, M. Garín, R. Alcubilla, *Solar Energy Materials and Solar Cells* **2007**, *91*, 174–179.

[147] I. Martín, M. Vetter, A. Orpella, C. Voz, J. Puigdollers, R. Alcubilla, *Applied Physics Letters* **2002**, *81*, 4461–4463.

[148] D. Pysch, J. Ziegler, J.-P. Becker, D. Suwito, S. Janz, S. W. Glunz, M. Hermle, *Applied Physics Letters* **2009**, *94*, 093510.

[149] I. Martın, M. Vetter, A. Orpella, J. Puigdollers, A. Cuevas, R. Alcubilla, *Applied Physics Letters* **2001**, *79*, 2199–2201.

[150] I. Martín, M. Vetter, M. Garín, A. Orpella, C. Voz, J. Puigdollers, R. Alcubilla, *Journal of Applied Physics* **2005**, *98*, 10.

[151] R. Ferré Tomàs, Thesis, Universitat Politècnica de Catalunya, **2008**.

[152] M. Pomaska, W. Beyer, E. Neumann, F. Finger, K. Ding, *Thin Solid Films* **2015**, *595*, 217–220.

[153] M. Köhler, A. Zamchiy, M. Pomaska, A. Lambertz, F. Lentz, W. Duan, V. Smirnov, F. Finger, U. Rau, K. Ding, *IEEE 7th World Conference on Photovoltaic Energy Conversion* **2018**, 3468–3472.

[154] M. Boccard, C. Ballif, Z. C. Holman, *IEEE 44th Photovoltaic Specialist Conference (PVSC)* **2017**, 1220–1221.

[155] R. Ferre, I. Martín, M. Vetter, D. Baetzner, J. Tan, A. Cuevas, R. Alcubilla, *21st European Photovoltaic Solar Energy Conference* **2006**, *16*, 176.

[156] M. Boccard, A. Jackson, Z. C. Holman, *IEEE 43rd Photovoltaic Specialists Conference (PVSC)* **2016**, 1179–1181.

[157] A. Eberst, A. Zamchiy, K. Qiu, P. Winkel, H. T. Gebrewold, A. Lambertz, W. Duan, S. Li, K. Bittkau, T. Kirchartz, *Solar RRL* **2022**, *6*, 2101050.

[158] K. Qiu, M. Pomaska, S. Li, A. Lambertz, W. Duan, A. Gad, M. Geitner, J. Brugger, Z. Liang, H. Shen, et al., *ACS applied materials & interfaces* **2020**, *12*, 29986–29992.

[159] S. Glunz, S. Janz, M. Hofmann, T. Roth, G. Willeke, *IEEE 4th World Conference on Photovoltaic Energy Conference* **2006**, *1*, 1016–1019.

[160] D. Suwito, U. Jäger, J. Benick, S. Janz, M. Hermle, R. Preu, S. Glunz, *relation* **2010**, *2*, 1.

[161] D. Pysch, M. Bivour, M. Hermle, S. W. Glunz, *Thin Solid Films* **2011**, *519*, 2550–2554.

[162] P. Ortega, I. Martín, G. Lopez, M. Colina, A. Orpella, C. Voz, R. Alcubilla, *Solar Energy Materials and Solar Cells* **2012**, *106*, 80–83.

[163] G. Nogay, J. Stuckelberger, P. Wyss, Q. Jeangros, C. Allebé, X. Niquille, F. Debrot, M. Despeisse, F.-J. Haug, P. Löper, et al., *ACS applied materials & interfaces* **2016**, *8*, 35660–35667.

[164] M. Pomaska, A. Richter, F. Lentz, T. Niermann, F. Finger, U. Rau, K. Ding, *Japanese Journal of Applied Physics* **2017**, *56*, 022302.

[165] M. Köhler, M. Pomaska, F. Lentz, F. Finger, U. Rau, K. Ding, *ACS applied materials & interfaces* **2018**, *10*, 14259–14263.

[166] Q. Wang in *High-Throughput Analysis: A Tool for Combinatorial Materials Science*, Springer, **2003**, pp. 395–413.

[167] K. Cole, B. S. Levine in *Principles of Forensic Toxicology*, Springer, **2020**, pp. 127–134.

[168] A. A. Edwards, B. D. Alexander in *Encyclopedia of Spectroscopy and Spectrometry*, Elsevier, **2017**, pp. 511–519.

[169] P. R. Griffiths, *Science* **1983**, *222*, 297–302.

[170] V. P. Tolstoy, I. Chernyshova, V. A. Skryshevsky, *Handbook of infrared spectroscopy of ultrathin films*, John Wiley & Sons, **2003**.

[171] A. Langford, M. Fleet, B. Nelson, W. Lanford, N. Maley, *Physical Review B* **1992**, *45*, 13367.

[172] G. Lucovsky, *Solid State Communications* **1979**, *29*, 571–576.

[173] F. Köhler, PhD thesis, Forschungszentrum Jülich, **2013**.

[174] T. Chen, Y. Huang, H. Wang, D. Yang, A. Dasgupta, R. Carius, F. Finger, *Thin Solid Films* **2009**, *517*, 3513–3515.

[175] J. Luna-López, G. García-Salgado, T. Díaz-Becerril, J. C. López, D. Vázquez-Valerdi, H. Juárez-Santiesteban, E. Rosendo-Andrés, A. Coyopol, *Materials Science and Engineering: B* **2010**, *174*, 88–92.

[176] K. J. Stout, L. Blunt, *Three dimensional surface topography*, Elsevier, **2000**.

[177] H. Fujiwara, *Spectroscopic Ellipsometry: Principles and Applications*, John Wiley & Sons, **2007**.

[178] P. Van der Heide, *Secondary ion mass spectrometry: an introduction to principles and practices*, John Wiley & Sons, **2014**.

[179] C. V. Raman, K. S. Krishnan, *Nature* **1928**, *121*, 711–711.

[180] I. R. Lewis, H. Edwards, *Handbook of Raman spectroscopy: from the research laboratory to the process line*, CRC press, **2001**.

[181] S. Veprek, F.-A. Sarott, Z. Iqbal, *Physical Review B* **1987**, *36*, 3344.

[182] J. Kiefer, M. F. Stodt, U. Fritsching, *Journal of Raman Spectroscopy* **2021**, *52*, 1582–1588.

[183] R. A. Sinton, A. Cuevas, M. Stuckings, *Conference Record of the Twenty Fifth IEEE Photovoltaic Specialists Conference-1996* **1996**, 457–460.

[184] G. Masetti, M. Severi, S. Solmi, *IEEE Transactions on electron devices* **1983**, *30*, 764–769.

[185] F. Dannhäuser, *Solid-State Electronics* **1972**, *15*, 1371–1375.

[186] A. Kimmerle, P. Rothhardt, A. Wolf, R. A. Sinton, *Energy Procedia* **2014**, *55*, 101–106.

[187] S. Instruments, *WTC-120 Photoconductance Lifetime Tester and Optional Suns-Voc User Manual*, www.sintoninstruments.com.

[188] B. Turan, PhD thesis, Forschungszentrum Jülich, **2016**.

[189] S. Eidelloth, R. Brendel, *IEEE Electron Device Letters* **2013**, *35*, 9–11.

[190] D. K. Schroder, *Semiconductor material and device characterization*, John Wiley & Sons, **2015**.

[191] U. Rau, *IEEE Journal of Photovoltaics* **2012**, *2*, 169–172.

[192] T. Trupke, R. Bardos, M. Schubert, W. Warta, *Applied Physics Letters* **2006**, *89*.

[193] K. Ramspeck, S. Reißenweber, J. Schmidt, K. Bothe, R. Brendel, *Applied Physics Letters* **2008**, *93*.

[194] S. Herlufsen, K. Bothe, J. Schmidt, R. Brendel, S. Siegmund, *Solar energy materials and solar cells* **2012**, *106*, 42–46.

[195] S. Herlufsen, K. Ramspeck, D. Hinken, A. Schmidt, J. Müller, K. Bothe, J. Schmidt, R. Brendel, *physica status solidi (RRL)–Rapid Research Letters* **2011**, *5*, 25–27.

[196] S. Herlufsen, J. Schmidt, D. Hinken, K. Bothe, R. Brendel in Proc. 24th EU PVSE Conf., 2AO, *Vol. 1*, **2009**.

[197] A. Aberle, S. Wenham, M. Green in Conference Record of the Twenty Third IEEE Photovoltaic Specialists Conference-1993 (Cat. No. 93CH3283-9), IEEE, **1993**, pp. 133–139.

[198] A. Kumar, S. Singh, S. Tomer, S. K. Srivastava, M. Dutta, P. Pathi, et al., *Physica Scripta* **2023**, *98*, 090001.

[199] R. Handy, *Solid-State Electronics* **1967**, *10*, 765–775.

[200] M. A. Green, *Englewood Cliffs* **1982**.

[201] B. Fischer, G. Heintz, *User Manual - LOANA Solar Cell Analysis System*, pv tools, **2017**.

[202] G. L. Harris, *Properties of silicon carbide*, Institute of Electrical Engineers of Japan, **1995**.

[203] Y. Awad, PhD thesis, Universite de Sherbrooke, **2006**.

[204] W. M. Haynes, *CRC handbook of chemistry and physics*, CRC press, **2014**.

[205] N. N. Greenwood, A. Earnshaw, *Chemie der Elemente*, Viley-VCH, **1988**.

[206] J. F. Ziegler, J. P. Biersack, M. D. Ziegler, *SRIM : the stopping and range of ions in matter*, SRIM Co., **2008**.

[207] P. Hovington, D. Drouin, R. Gauvin, *Scanning* **1997**, *19*, 1–14.

[208] D. Drouin, P. Hovington, R. Gauvin, *Scanning* **1997**, *19*, 20–28.

[209] P. Hovington, D. Drouin, R. Gauvin, D. C. Joy, N. Evans, *Scanning* **1997**, *19*, 29–35.

[210] D. Drouin, A. R. Couture, D. Joly, X. Tastet, V. Aimez, R. Gauvin, *Scanning* **2007**, *29*, 92–101.

[211] B. Paviet-Salomon, A. Tomasi, A. Descoeudres, L. Barraud, S. Nicolay, M. Despeisse, S. De Wolf, C. Ballif, *IEEE Journal of Photovoltaics* **2015**, *5*, 1293–1303.

[212] Z. C. Holman, A. Descoeudres, L. Barraud, F. Z. Fernandez, J. P. Seif, S. De Wolf, C. Ballif, *IEEE Journal of Photovoltaics* **2012**, *2*, 7–15.

[213] A. Eberst, B. Xu, K. Bittkau, A. Lambertz, U. Rau, K. Ding, *Cell Reports Physical Science* **2025**, *6*, 102658.

[214] F. Haase, S. Schäfer, C. Klamt, F. Kiefer, J. Krügener, R. Brendel, R. Peibst, *IEEE Journal of photovoltaics* **2017**, *8*, 23–29.

[215] K. C. Fong, M. Padilla, A. Fell, E. Franklin, K. R. McIntosh, T. C. Kho, A. W. Blakers, Y. Nebel-Jacobsen, S. R. Surve, *IEEE Journal of Photovoltaics* **2015**, *6*, 244–251.

[216] P. P. Altermatt, G. Heiser, M. A. Green, *Progress in Photovoltaics: Research and Applications* **1996**, *4*, 355–367.

[217] E. Franklin, K. Fong, K. McIntosh, A. Fell, A. Blakers, T. Kho, D. Walter, D. Wang, N. Zin, M. Stocks, et al., *Progress in Photovoltaics: research and applications* **2016**, *24*, 411–427.

[218] M. Abbott, J. Cotter, T. Trupke, R. Bardos, *Applied physics letters* **2006**, *88*, 114105.

[219] H. T. Gebrewold, K. Bittkau, K. Qiu, U. Rau, K. Ding, *Solar RRL* **2023**, *7*, 2201051.

[220] Z. C. Holman, M. Filipič, A. Descoeudres, S. De Wolf, F. Smole, M. Topič, C. Ballif, *Journal of Applied Physics* **2013**, *113*, 013107.

[221] W. Duan, A. Lambertz, K. Bittkau, D. Qiu, K. Qiu, U. Rau, K. Ding, *Progress in Photovoltaics: Research and Applications* **2022**, *30*, 384–392.

[222] J. Likonen, M. Hautala, I. Koponen, *Nuclear Instruments and Methods in Physics Research Section B: Beam Interactions with Materials and Atoms* **1992**, *64*, 149–152.

[223] R. Plieninger, H. Wanka, J. Kühnle, J. Werner, *Applied physics letters* **1997**, *71*, 2169–2171.

[224] K. Shimizu, N. Kohama, T. Tani, J.-i. Hanna, *Journal of non-crystalline solids* **2004**, *338*, 403–407.

[225] A. Lebedev, *Semiconductors* **1999**, *33*, 107–130.

[226] A. Eberst, B. Xu, K. Bittkau, W. Duan, A. Lambertz, A. Meise, M. Heggen, R. E. Dunin-Borkowski, U. Rau, K. Ding, *Advanced Physics Research* **2024**, *3*, 2400036.

[227] B. Xu, A. Eberst, P. Fall, M. A. Yaqin, V. Lauterbach, K. Bittkau, A. Lambertz, U. Rau, K. Ding, *Cell Reports Physical Science* **2025**, *6*, 102552.

[228] Y. Kuang, B. Macco, B. Karasulu, C. K. Ande, P. C. Bronsveld, M. A. Verheijen, Y. Wu, W. M. Kessels, R. E. Schropp, *Solar Energy Materials and Solar Cells* **2017**, *163*, 43–50.

[229] H. Profijt, P. Kudlacek, M. Van de Sanden, W. Kessels, *Journal of The Electrochemical Society* **2011**, *158*, G88.

[230] C. G. Van de Walle, *Physical Review B* **1994**, *49*, 4579.

[231] R. Wehrspohn, S. Deane, I. French, I. Gale, J. Hewett, M. Powell, J. Robertson, *Journal of Applied Physics* **2000**, *87*, 144–154.

[232] A. Plagemann, K. Ellmer, K. Wiesemann, *Journal of Vacuum Science & Technology A: Vacuum Surfaces and Films* **2007**, *25*, 1341–1350.

[233] K. Ellmer, T. Welzel, *Journal of Materials Research* **2012**, *27*, 765–779.

[234] B. Chapman, *Glow Discharge Processes: Sputtering and Plasma Etching*, Wiley, **1980**.

[235] T. Welzel, K. Ellmer, *Vakuum in Forschung und Praxis* **2013**, *25*, 52–56.

[236] Y. Takagi, Y. Sakashita, H. Toyoda, H. Sugai, *Vacuum* **2006**, *80*, 581–587.

[237] A. Illiberi, P. Kudlacek, A. Smets, M. Creatore, M. Van De Sanden, *Applied Physics Letters* **2011**, *98*, 242115.

[238] B. Demaurex, S. De Wolf, A. Descoeudres, Z. Charles Holman, C. Ballif, *Applied Physics Letters* **2012**, *101*, 171604.

[239] M. Tamakoshi, N. Matsuki, *Japanese Journal of Applied Physics* **2015**, *54*, 08KD09.

[240] T. Konishi, K. Ohdaira, *Thin Solid Films* **2017**, *635*, 73–77.

[241] L. Tutsch, PhD thesis, Albert-Ludwigs-Universität Freiburg, **2020**.

[242] D. Qiu, W. Duan, A. Lambertz, A. Eberst, K. Bittkau, U. Rau, K. Ding, *Solar RRL* **2022**, *6*, 2200651.

[243] W. Duan, G. Mains, H. T. Gebrewold, K. Bittkau, A. Lambertz, B. Xu, V. Lauterbach, A. Eberst, N. Nicholson, L. Korte, et al., *Advanced Functional Materials* **2024**, *34*, 2310552.

[244] B. Demaurex, J. P. Seif, S. Smit, B. Macco, W. Kessels, J. Geissbühler, S. De Wolf, C. Ballif, *IEEE Journal of Photovoltaics* **2014**, *4*, 1387–1396.

[245] R. Rößler, C. Leendertz, L. Korte, N. Mingirulli, B. Rech, *Journal of Applied Physics* **2013**, *113*, 144513.

[246] A. Kleinová, J. Huran, V. Sasinková, M. Pernỳ, V. Šály, J. Packa, *Reliability of Photovoltaic Cells Modules Components and Systems VIII* **2015**, *9563*, 166–173.

[247] J. A. Bearden, *Reviews of Modern Physics* **1967**, *39*, 78.

[248] S. Nida, A. Tsibizov, T. Ziemann, J. Woerle, A. Moesch, C. Schulze-Briese, C. Pradervand, S. Tudisco, H. Sigg, O. Bunk, et al., *Journal of synchrotron radiation* **2019**, *26*, 28–35.

[249] R. Chang, *Physical chemistry for the biosciences*, University Science Books, **2005**.

[250] R. H. Petrucci, F. G. Herring, J. D. Madura, C. Bissonnette, *General chemistry: principles and modern applications*, Prentice Hall, **2010**.

[251] J. Dong, A.-B. Chen in *SiC Power Materials: Devices and Applications*, Springer, **2004**, pp. 63–87.

[252] T. L. Cottrell, *The strengths of chemical bonds*, Butterworths Scientific Publications, **1958**.

[253] M. Bockstedte, A. Mattausch, O. Pankratov, *Physical Review B* **2003**, *68*, 205201.

[254] F. Bruneval, G. Roma, *Physical Review B* **2011**, *83*, 144116.

[255] X. Wang, J. Zhao, Z. Xu, F. Djurabekova, M. Rommel, Y. Song, F. Fang, *Nanotechnology and Precision Engineering (NPE)* **2020**, *3*, 211–217.

[256] M. E. Bathen, J. Coutinho, H. Ayedh, J. U. Hassan, I. Farkas, S. Öberg, Y. K. Frodason, B. G. Svensson, L. Vines, *Physical Review B* **2019**, *100*, 014103.

[257] R. K. Defo, X. Zhang, D. Bracher, G. Kim, E. Hu, E. Kaxiras, *Physical Review B* **2018**, *98*, 104103.

[258] S. Zhao, G. Ran, F. Gao, S. Ma, D. Cui, G. Yang, *Journal of Nuclear Materials* **2021**, *557*, 153255.

[259] D. Gobrecht, *Frontiers in Astronomy and Space Sciences* **2021**, *8*, 662545.

[260] A. Lebedev, *Semiconductor science and technology* **2006**, *21*, R17.

[261] B. Dorner, H. Schober, A. Wonhas, M. Schmitt, D. Strauch, *The European Physical Journal B-Condensed Matter and Complex Systems* **1998**, *5*, 839–846.

[262] S. Al Smairat, J. Graham, *Journal of Applied Physics* **2021**, *130*, 125902.

[263] R. Rurali, E. Hernández, P. Godignon, J. Rebollo, P. Ordejón, *Computational materials science* **2003**, *27*, 36–42.

[264] G. Roma, F. Bruneval, L. A. Ting, O. N. Bedoya Martínez, J. P. Crocombette in Defect and Diffusion Forum, *Vol. 323*, Trans Tech Publ, **2012**, pp. 11–18.

[265] E. Rauls, T. Frauenheim, A. Gali, P. Deák, *Physical Review B* **2003**, *68*, 155208.

[266] K. Watari, H. Nakano, K. Sato, K. Urabe, K. Ishizaki, S. Cao, K. Mori, *Journal of the American Ceramic Society* **2003**, *86*, 1812–1814.

[267] K. T. Regner, D. P. Sellan, Z. Su, C. H. Amon, A. J. McGaughey, J. A. Malen, *Nature communications* **2013**, *4*, 1640.

[268] T. Zhan, Y. Xu, M. Goto, Y. Tanaka, R. Kato, M. Sasaki, Y. Kagawa, *Applied Physics Letters* **2014**, *104*, 071911.

[269] S. N. Ahmed, *Physics and engineering of radiation detection*, Academic Press, **2007**.

[270] H. H. Park, *Electronic Materials Letters* **2021**, *17*, 18–32.

[271] E. Magliano, P. Mariani, A. Agresti, S. Pescetelli, F. Matteocci, B. Taheri, A. Cricenti, M. Luce, A. Di Carlo, *ACS Applied Energy Materials* **2023**, *6*, 10340–10353.

[272] K. Liu, B. Chen, J. Y. Zhengshan, Y. Wu, Z. Huang, X. Jia, C. Li, D. Spronk, Z. Wang, Z. Wang, et al., *Journal of Materials Chemistry A* **2022**, *10*, 1343–1349.

[273] J. E. Sansonetti, W. C. Martin, *Journal of physical and chemical reference data* **2005**, *34*, 1559–2259.

[274] T. L. Brown, H. E. LeMay, B. E. Bursten, *Chemistry: the central science*, Pearson Educación, **2002**.

[275] H. Wieder, M. Cardona, C. Guarnieri, *physica status solidi (b)* **1979**, *92*, 99–112.

[276] M. El-Desawy, PhD thesis, Universität Duisburg, **2007**.

[277] A. Eberst, Forschungszentrum Jülich, Germany, master thesis, **2020**.

[278] H. Nakajima, H. T. C. Tu, K. Ohdaira, *Japanese Journal of Applied Physics* **2023**, *62*, SK1040.

[279] H. Nakajima, H. T. C. Tu, K. Ohdaira, *physica status solidi (RRL)–Rapid Research Letters* **2022**, *16*, 2200052.

[280] A. R. Zanatta, *Scientific reports* **2019**, *9*, 11225.

Acknowledgements

This journey, with all its challenges and achievements, would not have been possible without the support and inspiration of many. I am grateful to each individual who contributed to this effort, and I extend my deepest appreciation to:

Prof. Dr. Uwe Rau, for his exemplary guidance and scholarly insights throughout this research. His expertise and encouragement have been invaluable in shaping this thesis.

Prof. Dr. Arthur Weeber, for his encouragement and effort as secondary assessor of this thesis.

Dr. Kaining Ding, whose mentorship was instrumental in sharpening my analytical skills and broadening my perspectives. His thoughtful advice and stimulating discussions have greatly enriched my research experience.

Dr. Karsten Bittkau, for his expertise in measurement techniques and for offering fresh perspectives during our discussions. His many reviews of my manuscripts and abstracts have been crucial in refining my work.

Dr. Andreas Lambertz, for his support in tackling various challenges and for his role in organizing the silicon heterojunction baseline at IEK-5 Photovoltaic, which has been essential to this research.

Dr. Weiyuan Duan, for her insightful inputs and probing questions during discussions, continually motivating me to strive for more.

Dr. Vladimir Smirnov, for his many comments on abstracts and manuscripts, including this thesis, and for giving insightful inputs during discussions.

Dr. Joon Ho Oh, for his exceptional support during his visits and for being an outstanding host during my time in South Korea. His company and assistance have been greatly appreciated.

Andreas Schmalen and Johannes Wolff, for their technical support with the deposition systems, and their prompt and efficient resolution of numerous challenges encountered during my experimental work.

The entire *baseline team* at IEK-5 Photovoltaics, whose collective efforts and support with sample processing and measurement setups were much needed. Special thanks to *Volker Lauterbach* for his quick and reliable help with many sample processing steps and the LOANA system, *Hildegard Siekmann* for her many sputter depositions and sharing her broad technical knowledge about the sputtering process, *Alain Doumit* for his support with the wet-chemistry and always making sure there are enough wafers in stock, *Silke Lynen* for her support with the magnesium fluoride depositions, amorphous silicon depositions and help with the conductivity measurement setup, and *Andreas Mück* for his support with the amorphous silicon deposition.

Binbin Xu, my fellow Ph.D. student, for enriching discussions on silicon carbide, his assistance with numerous experiments, and being a great and encouraging office mate.

My other fellow PhD colleagues, particularly *Benedikt Fischer*, *Timon Vaas*, *Toby Rudolph*, *Sergey Shcherbachenko*, *Seçil Güler*, *Yanxin Liu*, and *Gaosheng Huang*, for their companionship and the countless coffee breaks shared during this journey.

Jonathan Werner, for being an excellent office mate, assisting with Python-related questions, and listening to my complaints.

Dr. Wolfhard Beyer, whose deep understanding of hydrogen and invaluable experiences have been fundamental for this work. His passing is a great loss, and his contributions are deeply missed.

My beloved wife, *Alexandra Eberst*, for her unending patience, moral support, and encouragement throughout these years.

My *family*, whose support and motivation have been the foundation of my journey. Their belief in me has been my constant source of strength.

My heartfelt thanks to everyone mentioned, and to those unnamed, who have been part of this journey. Your contributions and support have been the

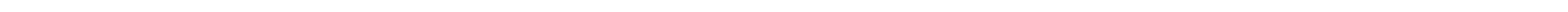

pillars of this accomplishment.

Band / Volume 684
Europäische Energiewende – Deutschland im Herzen Europas
T. Klütz, P. Dunkel, T. Busch, J. Linssen, D. Stolten (2025), IV, 56 pp
ISBN: 978-3-95806-870-4

Band / Volume 685
Performance and stability of solar cells and modules: From laboratory characterization to field data analysis
T. S. Vaas (2025), xvii, 146 pp
ISBN: 978-3-95806-871-1

Band / Volume 686
From Soil Legacy to Wheat Yield Decline: Studying the Plant-Soil Feedback Mechanisms in Wheat Rotations
N. Kaloterakis (2025), XXIX, 188 pp
ISBN: 978-3-95806-874-2

Band / Volume 687
Entwicklung von Beschichtungsverfahren für die Herstellung von Wärmedämmschichten auf additiv gefertigten Komponenten
M. Rüßmann (2026), ix, 188 pp
ISBN: 978-3-95806-877-3

Band / Volume 688
Model Perovskite Oxide Electrocatalysts for the Oxygen Evolution Reaction and their Material Sustainability Evaluation
L. Heymann (2026), vi, 174 pp
ISBN: 978-3-95806-878-0

Band / Volume 689
Development of an oxygen ion conducting solid oxide electrolysis cell based on gadolinium-doped cerium oxide as fuel electrode and electrolyte material
D. Ramler (2026), ix, 162 pp
ISBN: 978-3-95806-879-7

Band / Volume 690
Design of Local Multi-Energy Systems: Impact of Coupled Energy Vector Integration and Grid Service Participation
P. S. Glücker (2026), xxviii, 145 pp
ISBN: 978-3-95806-880-3

Band / Volume 691
A Parallel-in-Space Simulator for Accelerating Power System Simulation on Graphics Processing Units
J. Zhang (2026), 112 pp
ISBN: 978-3-95806-882-7

Band / Volume 692
Entwicklung von Reparaturmethoden für einkristalline Bauteile mittels thermischer Spritzverfahren
M. L. Létang (2026), X, 211 pp
ISBN: 978-3-95806-883-4

Band / Volume 693
Assessing the Environmental Implications of Offshore Wind Energy Advancements on the Future German Electricity Sector
A. Benitez (2026), xi, 176 pp
ISBN: 978-3-95806-885-8

Band / Volume 694
Entwicklung von Korrosionsschutzschichten für Protonen-Austausch-Membran-Wasserelektrolyseure
T. Sievert (2026), 201 pp
ISBN: 978-3-95806-888-9

Band / Volume 695
Hierarchical Modeling of Electrocatalytic Reactions from a Local Perspective
X. Zhu (2026), ix, 121 pp
ISBN: 978-3-95806-889-6

Band / Volume 696
Nanocrystalline Silicon Carbide in Transparent Passivating Contact Solar Cells
A. Eberst (2026), xiii, 225 pp
ISBN: 978-3-95806-891-9

Weitere ***Schriften des Verlags im Forschungszentrum Jülich*** unter
http://wwwzb1.fz-juelich.de/verlagextern1/index.asp

Energie & Umwelt / Energy & Environment
Band / Volume 696
ISBN 978-3-95806-891-9

Mitglied der Helmholtz-Gemeinschaft